Optical Nanoantennas and Their Use as Perfect Absorbers

Rasoul Alaee

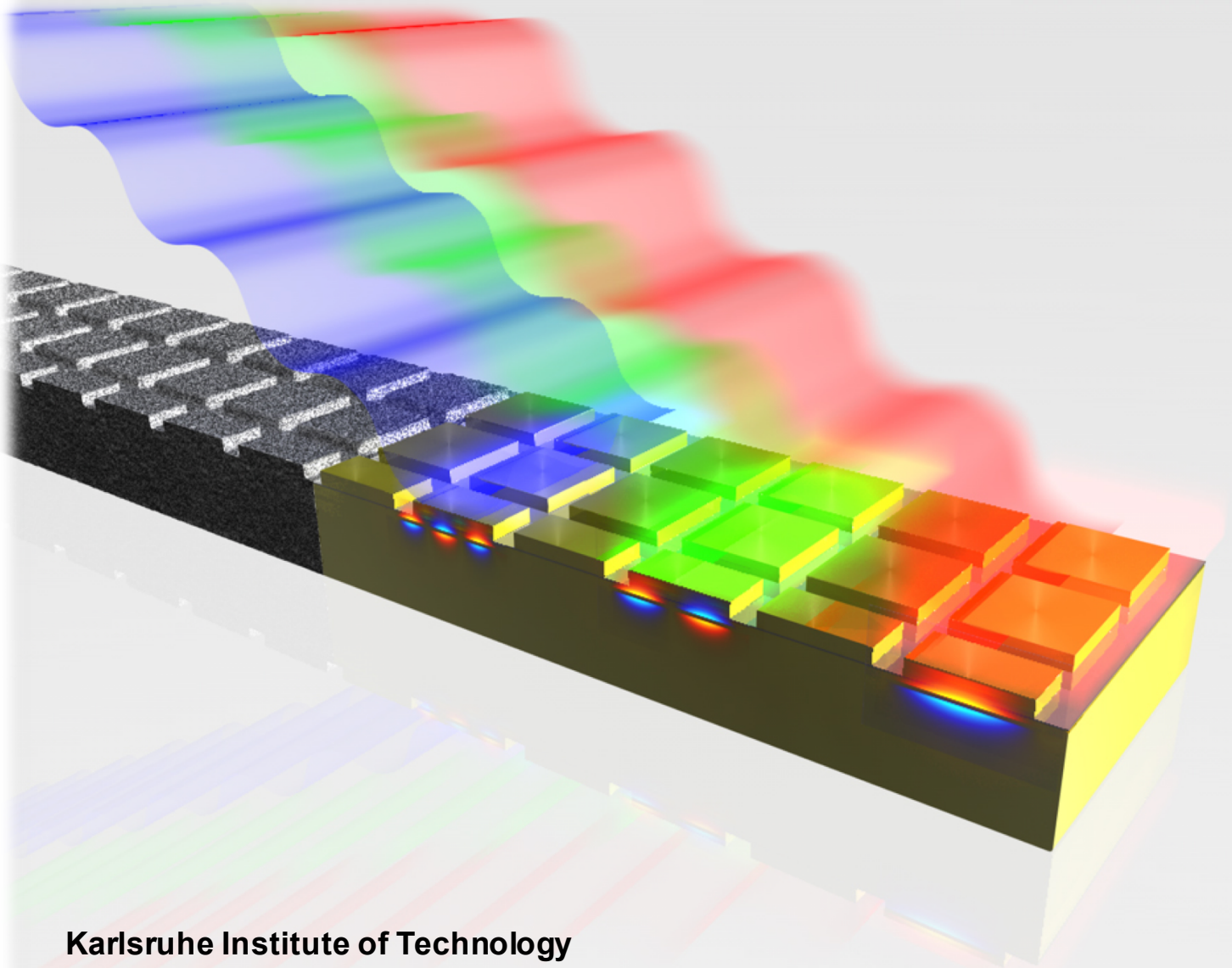

Karlsruhe Institute of Technology

Karlsruhe Institute of Technology

Optical Nanoantennas and Their Use as Perfect Absorbers

Zur Erlangung des akademischen Grades eines

DOKTORS DER NATURWISSENSCHAFTEN

von der Fakultät für Physik des

Karlsruher Instituts für Technologie (KIT)

genehmigte

DISSERTATION

von

MS in Electrical Engineering, Rasoul Alaee Khanghah

aus Iran

Tag der mündlichen Prüfung: 04.12.2015

Referent: Prof. Dr. Carsten Rockstuhl

Institut für Theoretische Festkörperphysik

Korreferent: Prof. Dr. Martin Wegener

Institut für Angewandte Physik

Publications

Publications whose contents are a part of this thesis have been highlighted in bold.

Peer-reviewed Journals

1. **R. Alaee, M. Albooyeh, M. S. Mirmoosa, Y. Kivshar, C. Rockstuhl, All-dielectric reciprocal bianisotropic nanoparticles, Phys. Rev. B, 92 , 245130 (2015).**

2. **R. Alaee, D. Lehr, R. Filter, F. Lederer, E.-B. Kley, C. Rockstuhl, and A. Tünnermann, Scattering dark states in multi-resonant concentric plasmonic nanorings, ACS Photonics, 2, 1085–1090 (2015).**

3. **R. Alaee, R. Filter, D. Lehr, F. Lederer, C. Rockstuhl, A generalized Kerker condition for highly directive nanoantennas, Opt. Lett. 40, 2645-2648 (2015).**

4. **R. Alaee, M. Albooyeh, M. Yazdi, N. Komjani C. Simovski, F. Lederer and C. Rockstuhl, Magneto-electric coupling in plasmonic nanoparticles: Theory and applications, Phys. Rev. B 91, 115119 (2015).**

5. M. Albooyeh, R. Alaee, C. Rockstuhl, and C. Simovski, Revisiting substrate-induced bianisotropy in metasurfaces, Phys. Rev. B 91, 195304 (2015).

6. **M. Yazdi, M. Albooyeh, R. Alaee, V. Asadchy, C. Rockstuhl, N. Komjani, and C. Simovski, A bianisotropic metasurface absorber with asymmetric resonant response, IEEE Transactions on Antennas and Propagation, 63, 3004, (2015).**

7. 2. I. Fernandez-Corbaton, S. Nanz, R. Alaee, C Rockstuhl, Exact dipolar moments of a localized electric current distribution, Opt. Express, 23 , 33044-33064 (2015).

8. **D. Lehr, R. Alaee, R. Filter, K. Dietrich, T. Siefke, C. Rockstuhl, F. Lederer, E-B. Kley, A. Tünnermann, Plasmonic nanoring fabrication**

tuned to pitch: Efficient, deterministic, and large scale realization of ultra-small gaps for next generation plasmonic devices, Appl. Phys. Lett. 105, 143110, (2014).

9. R. Yu, R. Alaee, F. Lederer, and C. Rockstuhl, Manipulating the Interaction between Localized and Delocalized Surface Plasmon Polaritons in Graphene, Phys. Rev. B 90, 085409, (2014).

10. C. Menzel, E. Hebestreit, R. Alaee, M. Albooyeh, S. Mühlig, S Burger, C. Rockstuhl, C. Simovski, S. Tretyakov, F. Lederer, T. Pertsch, Extreme coupling: A route towards local magnetic metamaterials, Phys. Rev. B 89, 155125, (2014).

11. R. Filter, M. Farhat, M. Steglich, R. Alaee, C. Rockstuhl, and F. Lederer, Tunable graphene antennas for selective enhancement of THz-emission, Opt. Express 21, 3737-3745, (2013).

12. R. Alaee, C. Menzel, A. Banas, K. Banas, S. Xu, H. Chen, H. O. Moser, F. Lederer, and C. Rockstuhl, Propagation of electromagnetic fields in bulk terahertz metamaterials: A combined experimental and theoretical study, Phys. Rev. B 87, 075110, (2013).

13. **R. Alaee, C. Menzel, U. Huebner, E. Pshenay-Severin, S. Bin Hasan, C. Rockstuhl, T. Pertsch, and F. Lederer, Deep-subwavelength plasmonic nanoresonators exploiting extreme coupling, Nano Lett. 13, 3482-3486, (2013).**

14. **U. Huebner, E. Pshenay-Severin, R. Alaee, C. Menzel, M. Ziegler, C. Rockstuhl, F. Lederer, T. Pertsch, H-G. Meyer, and J. Popp, Exploiting extreme coupling to realize a metamaterial perfect absorber, Microelectronic Eng. 111, 110-113, (2013).**

15. R. Alaee, C. Menzel, C. Rockstuhl, and F. Lederer, Perfect absorbers on curved surfaces and their potential applications, Opt. Express 20, 18370-18376, (2012).

16. R. Alaee, M. Farhat, C. Rockstuhl, and F. Lederer, A perfect absorber made of a graphene micro-ribbon metamaterial, Opt. Express 20, 28017-28024, (2012).

17. C. Menzel, R. Alaee, E. Pshenay-Severin, C. Helgert, A. Chipouline, C. Rockstuhl, T. Pertsch, and F. Lederer, Genuine effectively biaxial left-handed metamaterials due to extreme coupling, Opt. Lett. 37, 596-598, (2012).

Conference Contributions

1. R. Alaee, M. Albooyeh, M. S. Mirmoosa, Y. Kivshar, C. R. Simovski, F. Lederer, and C. Rockstuhl, "Magneto-Electric Coupling in All-Dielectric Nanoantennas," The 9th International Congress on Advanced Electromagnetic Materials in Microwaves and Optics, (2015).

2. C. Rockstuhl, R. Alaee, M. Albooyeh, R. Filter, D. Lehr, and C. Simovski, "Nanoantennas with a Tunable Response: Single Particle and Array Properties," The 9th International Congress on Advanced Electromagnetic Materials in Microwaves and Optics, (2015).

3. C. Rockstuhl, S. Nanz, R. Alaee, I. Fernandez-Corbaton, M. Albooyeh and C. Simovski, "Meta-atoms with tunable response," SPIE Optics and Optoelectronics conference in Prague, (2014).

4. R. Alaee, M. Albooyeh, C. Menzel, S. Fasold, N. Janunts, M. Falkner, T. Pertsch, C. R. Simovski, F. Lederer, and C. Rockstuhl, "Magneto-electric Response in Coupled Plasmonic Nanoparticles," The 8th International Congress on Advanced Electromagnetic Materials in Microwaves and Optics, (2014).

5. M. Albooyeh, R. Alaee, C. Rockstuhl, and C. R. Simovski, "Bianisotropy in metasurface," The 8th International Congress on Advanced Electromagnetic Materials in Microwaves and Optics, (2014).

6. D. Lehr, R. Filter, R. Alaee, K. Dietrich, C. Rockstuhl, F. Lederer, E-B. Kley, A. Tünnermann, "Enhancing the efficiency of up-conversion by double-resonant plasmonic nanorings," Light, Energy and the Environment Congress, (2014).

7. R. Alaee,M. Albooyeh, C. Simovski, F. Lederer, C.Rockstuhl, "Novel optical features in asymmetric nanoparticle systems," META'14, Singapore, (2014). List Item: R. Alaee, M. Farhat, R. Yu, C. Rockstuhl, and F. Lederer, "A coherent perfect absorber made from graphene," Graphene Nanophotonics , Benasque, Spain, (2013).

8. C. Rockstuhl, R. Alaee, C. Menzel, U. Huebner, E. Pshenay-Severin, S. Bin Hasan, T. Pertsch, and F. Lederer, "Exploiting extreme coupling in nanoplasmonic elements," NOMA Cetraro, Italy, (2013).

9. F. Lederer, S. Mühlig, C. Rockstuhl, R. Alaee, and C. Menzel , "Tailoring meta-atoms for specific metamaterial applications," OWTNM, Twente, The Netherlands, (2013).

10. R. Alaee, R. Yu, F. Lederer, and C. Rockstuhl, "Complete light absorption in extremely graphene plasmonic nanostructure," DOKDOK, (2013).

11. R. Alaee, M. Farhat, C. Rockstul, and F. Lederer, "Graphene Based Fabry-Perot Cavity as a Perfect Absorber," ETOPIM 9, (2012).

12. C. Menzel, R. Alaee, E. Pshenay-Severin, C. Helgert, T. Paul, A. Chipouline, C. Rockstuhl, T. Pertsch, and F. Lederer, "Extreme coupling as a key to achieve homogenous metamaterials"," The 6th International Congress on Advanced Electromagnetic Materials in Microwaves and Optics, (2012).

13. R. Alaee, C. Menzel, U. Huebner, E. Pshenay-Severin, T. Pertsch, H.-G. Meyer, J. Popp, C. Rockstuhl, and F. Lederer, "Complete light absorption in extremely coupled plasmonic nanostructure," DOKDOK, (2012).

14. U. Huebner, E. Pshenay-Severin, R. Alaee, C. Menzel, C. Rockstuhl, F. Lederer, T. Pertsch , H.-G. Meyer and J. Popp, "Exploiting extreme coupling to realize a metamaterial perfect absorber," MNE, (2012).

Contents

1 Introduction

Light carries energy. In many applications, e.g. optical sensors, thermal emitters, optical modulators, or solar cells, it is desirable to absorb as much as possible the energy of the impinging light. This requires to fully suppress the transmission and reflection. Hence, the energy will be dissipated in the absorbing layer. In principle, perfect absorption occurs if two conditions are satisfied. The first condition requires the absorbing layer to be impedance matched with the free space impedance. This fully suppresses the reflection. In general, in order to satisfy the second condition (i.e. zero transmission), the absorbing layer should be sufficiently thick (compared to the wavelength). Then, the incoming electromagnetic energy is fully absorbed before reaching to the end of the layer. However, the necessary thickness will limit the application of the absorbing layer in highly integrated nanophotonic devices. To overcome this problem (i.e. achieving thin layer perfect absorbers) there are many practical approaches that can be used to design a considerably thin perfect absorber. They often come at the price at operating only in a narrow spectral range, but for many application perspectives this is permissible. In the following, we chronologically will review various mechanism and approaches to achieve thin perfect absorbers for light.

Research on how electromagnetic waves can be efficiently absorbed potentially started with the invention of radar in the 1930's. At that time, it was important to disguise an object (e.g. an airplane) from radars. Therefore, various approaches have been introduced to reduce the reflected waves from the object [1]. The most important inventions among them are Dallenbach, Jaumann [2], and Salisbury perfect absorbers [3]. Dallenbach perfect absorbers consist of a homogeneous lossy dielectric layer on top of a metallic ground plate [Fig. 1.0.1 (a)]. The thickness of the layer and the properties of material (permittivity and permeability) have to be carefully chosen such that the reflected light is totally suppressed via impedance matching. The thickness of the layer d should be roughly a quarter wavelength $d \simeq \lambda/4n$ (n is the refractive index of the layer). In fact, such a layer can absorb the light in a narrow bandwidth. By increasing the number of the layers the absorption bandwidth can be broadened. On the hand, a Salisbury perfect absorber consists of a resistive sheet on top of a metallic ground plate separated by a dielectric spacer (no Ohmic losses).

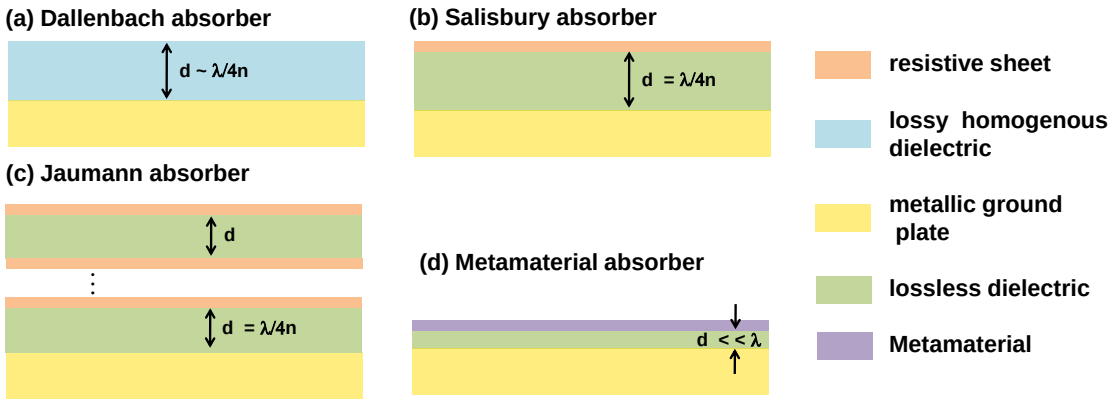

Figure 1.0.1: Schematic view of three well-known microwave perfect absorbers: a) The Dallenbach perfect absorber, b) the Salisbury perfect absorber, and c) the Jaumann perfect absorber. d) Perfect metamaterial absorber.

Such perfect absorber sometimes called stealth technology. This perfect absorber mainly relies on the absorption in the resistive sheet. The refractive index of the dielectric spacer plays an important role on choosing the thickness of the layer. The Jaumann perfect absorber is a generalized Salisbury perfect absorber that helps to increase the bandwidth [4]. Jaumann suggested multi-layers of resistive sheets on top of the metallic ground plate separated by dielectric spacers of equal thickness. Therefore, the wave can resonate at distinct frequencies which provides a multi-band perfect absorber. The basic principle of the Jaumann as well as the Salisbury perfect absorbers can be understood by a destructive interference of the reflected light and a suppression of the transmitted light. Therefore, as already mentioned they all require a notable thickness ($\simeq \lambda/4n$) to fully absorb the impinging wave which renders them impractical for some applications. The metamaterial based perfect absorbers can solve this limitation [5,6]. In this thesis, we will provide a guideline to achieve considerably thin perfect absorbers compared to the aforementioned perfect absorbers. In addition, the structures under consideration are shown to possess further interesting optical effects

In the past years, optically thin perfect absorbers, known as *perfect metamaterial absorbers,* have been introduced based on periodic subwavelength metallic particles (sometimes called meta-atoms or nanoantennas) [6, 7]. Note that, in this thesis, we prefer to use the term *nanoantenna* for any optically small particle that might possesses an arbitrary shape and it can be made from arbitrary materials. We only require from these nanoantennas that an external field can induce currents (either conductive or displacement currents) that reradiate. Tailoring the geometry of the nanoantenna allows to control their scattering characteristics. This will be at the heart of the various functional devices we discuss in this thesis, for which the perfect

absorber is a prominent example. Perfect metamaterial absorbers attracted considerable attentions at microwave [5,6], terahertz, and especially near-infrared [8,9] and visible [10–14] frequencies. These perfect absorbers have potential applications, e.g. optical filters, optical sensors, thermal emitters, and solar cells. In this thesis, we present our contributions to this field and aim to properly address the following questions:

a) Most aforementioned perfect absorbers required a metallic ground plate. This restricts their optical response for an illumination with a plane wave propagating such that it first interacts with the metallic ground plate, i.e. acting as a reflector. Therefore, it would be interesting to design an optically thin perfect absorber without a metallic ground plate. The question is: *Is it possible to achieve perfect absorption without a metallic ground plate?*

b) The optical response of the majority of the aforementioned perfect absorbers depends strongly on the incident angle of impinging light. In fact, this is related to the thickness of dielectric spacer. For perfect absorbers with large dielectric spacers (e.g. Salisbury screen), the absorption changes strongly when illuminated at oblique incidence. This can be explained by exploring the underlying mechanism of absorption, i.e. coherent interference. Therefore, in order to overcome this limitation, an ideal solution relies on decreasing the thickness of the dielectric spacer. *What kinds of interesting physical features can be achieved for perfect absorbers with extremely thin dielectric spacers?*

c) As already noted, most of the common perfect absorbers consist of an array of small resonant nanoantennas,. Therefore, it is essential to understand the optical response of these individual building blocks. To understand the scattering properties of an individual nanoantenna, we rely on a well established approach known as multipole expansion [15,16]. This approach allows to calculate the dominating multipole moments supported by an arbitrary nanoantenna. However, for most pertinent nanoantennas the optical response can be fully described with the electric/magnetic dipole moment. The question therefore is: *Is there any universal limitation on the scattering, absorption, and extinction properties of a nanoantenna which exhibits electric/magnetic dipole moment?*

d) Basic nanoantennas, e.g. metallic nanospheres, nanodisks, and nanopatches, can only support an electric response [17–19]. In fact, this electric response limits their scattering performance and they can only scatter light identically in forward and backward directions. To have a better control on the scattering property, Kerker suggested to use a magnetic response in addition to the electric response for a dielectric sphere [20]. This extra magnetic response can be used as an extra degree of freedom to have further control on the scattering of nanoantennas. In particular, nanoanten-

nas with zero- forward/backward scattering can be achieved by tailoring the electric and magnetic responses; known as the Kerker condition (or the balanced condition). This is achieved by a constructive or destructive interference of the radiated far-fields of the induced electric and magnetic dipole moments in either direction. In general, nanoantennas can support higher order multipole moments besides electric and magnetic dipole moments. Therefore, an interesting questions would be: *Is it possible to have even better control over the scattering properties of nanoantennas while exploiting higher order electromagnetic multipole moments? What kind of novel scattering effects can be obtained from such nanoantennas?*

e) Finally, it is important to have an analytical tool available to predict the optical response of an array of nanoantennas based on the response of the individual nanoantenna. The questions are: *Is it possible to achieve complete light absorption by an array of nanoantennas which exhibit only electric/magnetic dipoles? What about nanoantennas which exhibit both electric and magnetic dipoles*? *Which conditions should be satisfied in order to fully absorb the light? What about an array of nanoantennas beyond the dipole approximation?*

1.1 Aim and structure of the thesis

In this thesis, we focus on the scattering properties of individual nanoantennas as well as of array thereof. The thesis can be divided into two parts. In the first part, we explore remarkable scattering properties for individual nanoantennas such as Fano resonances, scattering dark states, a possible bianisotropic response, directional radiation pattern and so on. This is done with the help of a very powerful semi-analytical tool known as multipole expansion. In the second part, we explore the optical responses of an array made of such nanoantennas by a simple analytical model. Results are also fully supported by full wave simulations. We focus on different physical mechanisms in order to enhance and control the interaction of light with the array. This allows to achieve a complete light absorption, an asymmetric optical response, and an enhanced transmission.

The content of this thesis has been published in more than 15 publications and has been presented at the occasion of several invited and contributed conference contributions. In the following chapters of the thesis, we will focus on fundamental and important achievements of those contributions in a broad, consistent, and complete context. The thesis consists of six chapters and is organized as follows:

In Chapter 2, we introduce an analytical framework to discuss the scattering properties of individual nanoantennas. We discuss some universal limitations of the scat-

tering/absorption properties of an individual nanoantenna, which supports only an electric/magnetic dipole moment. We also explore some interesting optical features for a nanoantenna, which exhibits both electric and magnetic dipole moments in balanced condition. Moreover, we describe the optical response of a periodic array of such nanoantennas. We show that there is a universal limitation on the absorption of an array of electric/magnetic dipole scatterers (i.e. the maximum absorption is limited to 50 percent). Finally, we discuss various potential theoretical approaches to enhance the absorption towards the ultimate goal of complete light absorption.

In Chapter 3, we focus on two types of bianisotropic nanoantennas, namely plasmonic and high-index dielectric bianisotropic nanoantennas. For both of these nanoantennas, the bianisotropic coupling is obtained by breaking the geometrical symmetry of the nanoantennas. In principle, the chapter is divided into two main parts. The first part of this chapter is related to plasmonic nanoantennas consisting of gold nanopatches. We start with a simple nanopatch that supports only an electric dipole moment. We show that the absorption of an array of such nanoantennas is limited to 50 percent. In order to obtain a nanoantenna with a strong magnetic dipolar response in addition to the electric one, we use two identical coupled nanopatches separated with thin dielectric spacer. Eventually, in order to propose a nanoantenna with a pronounced bianisotropic coupling, we break the geometrical symmetry of the coupled nanopatches, i.e. using two nonidentical nanopatches with different lateral dimensions. We show that such nanoantennas possess remarkable optical features as individual structure as well as upon periodic arrangement in an array, e.g. zero backscattering and complete light absorption. The bianisotropic coupling leads to an entirely different optical response (asymmetric reflection/absorption) when the nanoantenna is illuminated from opposite directions. Finally, we propose a novel nanoantenna with tunable radiation patterns by utilizing a phase change material (PCM) as a dielectric spacer. This allows to switch the radiation of the nanoantenna from a directional pattern to a dipole-like one. In the second part of this chapter, we introduce a lossless bianisotropic nanoantenna made of a high-index dielectric material. We start with a cylindrical high-index dielectric nanoantenna that supports strong electric and magnetic dipole moments due to Mie resonances. By breaking the symmetry of such nanoantennas, we introduce a strong magneto-electric coupling that leads to various interesting optical features such as different backward scattering response when illuminated from opposite directions.

In Chapter 4, we present two different schemes for a complete light absorption, namely a near-field coupling and a far-field interference scheme. The investigated structure is an array of nanopatch nanoantennas on top of a metallic ground plate separated by a dielectric spacer. In the near-field scheme (thin dielectric spacer), we

introduce the concept of the *extreme coupling* in order to achieve deep-subwavelength perfect absorbers. The thin dielectric spacer, in the order of few nanometers, is experimentally achieved by an atomic layer deposition (ALD). By using a simple analytical approach, we predict the resonance position of the perfect absorber that is in a good agreement with numerical as well as experimental results. Finally, we investigate the far-field scheme (where the thickness of the dielectric spacer is comparable to the wavelength). In this scheme, we use a simple Fabry-Perot (FP) cavity model to predict the optical response of the investigated structure. The structure acts as a perfect absorber and the underlying physical mechanism of the absorption can be fully understood from a destructive interference between the direct and multiply reflected waves inside the FP cavity.

In Chapter 5, we investigate the optical properties of nanoantennas consisting of gold nanorings. The aim of this chapter is to introduce novel nanoantennas with remarkable optical features, e.g. uniform field enhancement, directional light radiation by using a generalized Kerker condition, Fano resonances, and scattering dark states. The work is done theoretically but supporting experimental results conducted by colleagues are presented as well. We start with a single nanoring which supports only an electric dipole moment. This allows to obtain a noticeable uniform field enhancement. We introduce a generalized Kerker condition beyond the dipole approximation to design a gold nanoring with a zero backscattering field. The directional radiation pattern can be achieved when the electric dipole and quadrupole moments are in balanced condition. We also present a complete light absorption for an array of such nanoantennas by introducing a simple condition for the supported modes, i.e. electric dipole and quadrupole modes (beyond the dipole approximation). In the end, we explore the optical properties of multi-rings which allows to obtain scattering dark states and Fano features.

Finally, in Chapter 6, we give a brief summary of all the theoretical results and important achievements of this thesis and discuss the possible research directions in the future.

2 Analytical framework

When light interacts with a small object (e.g. a nanoantenna), two basic processes are encountered. First, scattering might occur. The scattering cross section is defined to describe how strong the object (nanoantenna) scatters the light with respect to its geometrical cross section during the scattering process [15]. The second process is absorption. In this process, the energy of the incoming light is converted into an internal energy of the nanoantenna (e.g. thermal energy). The absorption is measured in terms of the absorption cross section. These two processes, i.e. scattering and absorption, will remove a part of the energy of the incoming light. In other words, the incoming light is attenuated by the nanoantenna and this attenuation is known as extinction. It can be measured in terms of the extinction cross section. Some fundamental questions that arise in the interaction of light with nanoantenna which motivated this field of research are as follows: *Is there a universal limitation on the scattering/absorption cross section of a nanoantenna in dipole approximation? If yes, how to overcome these limitations? Is it possible to entirely suppress the scattering? What about controlling the direction of scattering (directional radiation pattern)? How does light interact with an array of nanoantennas?*

All the aforementioned questions are important to understand various interesting phenomenons, e.g. super-scattering, super-absorption, super-directivity, scattering dark states, asymmetric Fano line-shape, electromagnetically induced transparency (EIT), complete light absorption, and much more. To be able to discuss such phenomena, a theoretical formalism is needed. In this chapter, we briefly introduce at first such a formalism. It is known as the multipole expansion of the scattered field of an arbitrary nanoantenna. Such expansion allows to characterize the scattering objects in terms of multipole moments. Furthermore, experimentally observable quantities such as scattering, absorption, and extinction cross sections can be deduced from the multipole moments. Note that they are the most important measured quantities that allows to discuss all the aforementioned physical processes. Next we apply this formalism to study the potentially simplest nanoantenna, i.e. a nanoantenna characterized only by an electric or magnetic dipole moment. We will derive some interesting consequences on the possible cross sections for an electric or magnetic dipole moment that are shown to be bound by some universal limits. We show

that there are some universal limitations on the scattering, absorption, and extinction cross sections of such nanoantennas. We also indicate several strategies that allow to overcome these limitations on the absorption or scattering properties of a nanoantenna. In general they require to consider nanoantennas that sustain also higher order electromagnetic multipole moments and/or terms that describe a possible bianisotropy. Thereafter we derive analytical expressions to calculate the optical response of an array of nanoantennas, which can be described by electric/magnetic dipole moments. This allows to discuss some universal limitations on the absorption of such an array of nanoantennas. Finally, we propose some practical approaches to overcome this limitation, which will be discussed in the following chapters.

2.1 Multipole expansion

In general, there are two basic approaches to calculate the multipole moments of an arbitrary nanoantenna. They either rely on an expansion of the scattered field or on an expansion of the induced current densities. Both approaches provide identical results. In this section, we briefly introduce these approaches. Next, we compare them for the case of a coupled nanopatch antenna which exhibits the electric, magnetic dipole and electric quadrupole moments. We will show that these approaches lead to similar results. In general, the extracted multipole moments using scattered field approach are exact and there is no approximation. However, the electric current approach is only valid if the size of the nanoantenna is small compared to the wavelength. Therefore, in the entire thesis we use the scattered field approach to retrieve all the dominated multipole moments of the nanoantenna.

2.1.1 Scattered field approach

In this subsection, we briefly introduce the multipole expansion of the scattered field of an arbitrary nanoantenna which is embedded in a homogeneous and isotropic medium. The basic approach to calculate the multipole moments of an arbitrary nanoantenna can be deduced from Mie Theory. In 1908, Gustav Mie proposed an analytical approach to calculate the light scattering by spheres [15]. This theory relies on the expansion of the incident, scattered, and internal fields in terms of vector spherical harmonics. The amplitudes of the incident fields are fixed upon choosing an illumination. The amplitudes of the scattered and internal fields are given by enforcing governing boundary conditions [15]. To quantify the scattering response of an arbitrary nanoantenna, the scattered ($\mathbf{E}_{\mathrm{sca}}$) field [Fig. 2.1.1] has to be calculated at first numerically. In the this thesis, we used COMSOL Multiphysics to

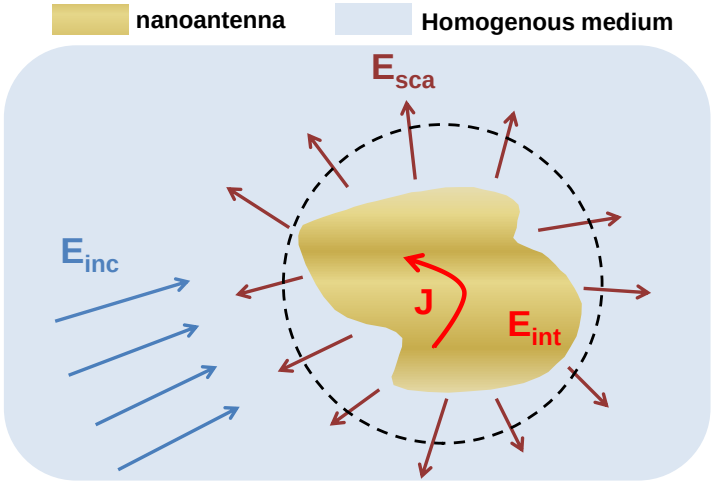

Figure 2.1.1: Schematic view of the scattering problem of an arbitrary nanoantenna. $\mathbf{E}_{\text{sca}}$ and $\mathbf{E}_{\text{int}}$ are scattered and internal electric fields, respectively. These fields are induced by an incident electric field (i.e. $\mathbf{E}_{\text{inc}}$). $\mathbf{J}$ represents the induced electric current density. The field inside the nanoantenna is defined as an internal field (i.e. $\mathbf{E}_{\text{int}}$). The dashed line shows where the scattered fields are numerically calculated.

simulate the scattering response of the investigated nanoantennas [21]. Afterwards the scattered field can be expanded in terms of vector spherical harmonics (VSHs). The expansion of the numerically calculated scattered field will be

$$\mathbf{E}_{\text{sca}}(\mathbf{r},\omega) = \sum_{n=1}^{\infty}\sum_{m=-n}^{n} k^2 E_{nm}\left[a_{nm}\mathbf{N}_{nm}^{(3)}(\mathbf{r},\omega) + ib_{nm}\mathbf{M}_{nm}^{(3)}(\mathbf{r},\omega)\right], \quad (2.1.1)$$

where ω is the angular frequency. a_{nm}, b_{nm} are the multipole coefficients in a spherical base and they are representing the strength of different electric and magnetic multipole moments, respectively. Here, $n = 1$ represents the dipole response, $n = 2$ for the quadrupole and the rest (i.e. $n \geqslant 3$) for the higher order multipoles. k is the wavenumber in the ambient medium. $\mathbf{N}_{nm}^{(3)}(\mathbf{r},\omega)$ and $\mathbf{M}_{nm}^{(3)}(\mathbf{r},\omega)$ are the vector spherical harmonics. $\mathbf{E}_{\text{sca}}(\mathbf{r},\omega)$ is the numerically calculated scattered field on a sphere with radius a which includes the entire nanoantenna [see dashed lines in Fig. 2.1.1]. The prefactor is defined as

$$E_{nm} = |\mathbf{E}_{\text{inc}}|\sqrt{\frac{2n+1}{4\pi}}\sqrt{\frac{(n-m)!}{(n+m)!}}(-1)^m, \quad (2.1.2)$$

where $|\mathbf{E}_{\text{inc}}|$ is the amplitude of the incident electric field. The electric and magnetic

multipole coefficients (a_{nm}, b_{nm}) can be easily extracted from the orthogonality of the vector spherical harmonics and read as

$$a_{nm} = \frac{\int_0^{2\pi}\int_0^{\pi}\mathbf{E}_{\text{sca}}\left(r=a,\theta,\varphi,\omega\right)\left[\mathbf{N}_{nm}^{(3)}\left(r=a,\theta,\varphi,\omega\right)\right]^{*}\sin\theta\mathrm{d}\theta d\varphi}{k^2E_{nm}\int_0^{2\pi}\int_0^{\pi}\left|\mathbf{N}_{nm}^{(3)}\left(r=a,\theta,\varphi,\omega\right)\right|^2\sin\theta\mathrm{d}\theta d\varphi}, \quad (2.1.3)$$

$$b_{nm} = \frac{\int_0^{2\pi}\int_0^{\pi}\mathbf{E}_{\text{sca}}\left(r=a,\theta,\varphi,\omega\right)\left[\mathbf{M}_{nm}^{(3)}\left(r=a,\theta,\varphi,\omega\right)\right]^{*}\sin\theta\mathrm{d}\theta d\varphi}{ik^2E_{nm}\int_0^{2\pi}\int_0^{\pi}\left|\mathbf{M}_{nm}^{(3)}\left(r=a,\theta,\varphi,\omega\right)\right|^2\sin\theta\mathrm{d}\theta d\varphi}. \quad (2.1.4)$$

Here, the integration is performed on a sphere with radius $r = a$. Finally, the Cartesian multipole moments can be calculated using the well-known expression for the electric field generated from the electric/magnetic multipoles. The electric $\mathbf{p} = \begin{pmatrix} p_{\text{x}}, & p_y, & p_{\text{z}} \end{pmatrix}^T$ and magnetic $\mathbf{m} = \begin{pmatrix} m_{\text{x}}, & m_y, & m_{\text{z}} \end{pmatrix}^T$ moments are given by

$$\mathbf{p} = C_0\begin{pmatrix} (a_{11}-a_{1-1}) \\ i\,(a_{11}+a_{1-1}) \\ -\sqrt{2}a_{10} \end{pmatrix}, \quad \mathbf{m} = cC_0\begin{pmatrix} (b_{11}-b_{1-1}) \\ i\,(b_{11}+b_{1-1}) \\ -\sqrt{2}b_{10} \end{pmatrix}, \quad (2.1.5)$$

where $C_0 = \frac{\sqrt{6\pi i}}{cZk}$ with c is the speed of light in vacuum and Z is the impedance of the ambient material. The symbol T denotes the transpose of the matrix. Similarly, the electric quadrupole moment can be calculated as

$$\mathbf{Q} = \begin{pmatrix} Q_{xx} & Q_{xy} & Q_{xz} \\ Q_{yx} & Q_{yy} & Q_{yz} \\ Q_{zx} & Q_{zx} & Q_{zz} \end{pmatrix} \quad (2.1.6)$$

$$= D_0\begin{pmatrix} i\,(a_{22}+a_{2-2})-\frac{i\sqrt{6}}{2}a_{20} & (a_{2-2}-a_{22}) & i\,(a_{2-1}-a_{21}) \\ (a_{2-2}-a_{22}) & -i\,(a_{22}+a_{2-2})-\frac{i\sqrt{6}}{2}a_{20} & (a_{2-1}+a_{21}) \\ i\,(a_{2-1}-a_{21}) & (a_{2-1}+a_{21}) & i\sqrt{6}a_{20} \end{pmatrix},$$

with prefactor $D_0 = \frac{6\sqrt{30\pi}}{icZk^2}$. By replacing the a_{nm} with b_{nm} and modifying the perfactor D_0, a similar expression as shown in Eq. 2.1.6 can be found for the magnetic quadrupole moment **MQ**.

Finally, the scattering cross section reads as

$$\begin{aligned} C_{\text{sca}} &= k^2 \sum_{n=1}^{\infty} \sum_{m=-n}^{n} n\,(n+1)\left[|a_{nm}|^2 + |b_{nm}|^2\right] \\ &= C_{\text{sca}}^{p} + C_{\text{sca}}^{m} + C_{\text{sca}}^{Q} + ..., \end{aligned} \tag{2.1.7}$$

which is the sum of the different multipole contributions. Note that, in the entire thesis, this approach is used to retrieve the dominated multipole moments of the investigated nanoantennas.

2.1.2 Electric current approach

In this subsection, we briefly discuss an alternative approach which allows to calculate Cartesian multipole moments. In fact, the electric and magnetic multipole moments can be calculated from a volume integration over the charge density ρ or the induced electric current distribution $\mathbf{J}$ and read as [22–24]

$$p_\alpha = \int r_\alpha \rho \mathrm{d}v = \frac{1}{-i\omega}\int J_\alpha \mathrm{d}v, \tag{2.1.8}$$

$$m_\alpha = \frac{1}{2}\int \left(\mathbf{r}\times\mathbf{J}\right)_\alpha \mathrm{d}v, \tag{2.1.9}$$

$$Q_{\alpha\beta} = \frac{1}{-2i\omega}\int \left[r_\alpha J_\beta + r_\beta J_\alpha - \frac{2}{3}\delta_{\alpha\beta}\left(\mathbf{r}\cdot\mathbf{J}\right)\right]\mathrm{d}v, \tag{2.1.10}$$

$$QM_{\alpha\beta} = \frac{1}{3}\int \left[\left(\mathbf{r}\times\mathbf{J}\right)_\alpha r_\beta + \left(\mathbf{r}\times\mathbf{J}\right)_\beta r_\alpha\right]\mathrm{d}v, \tag{2.1.11}$$

where α, $\beta = x$, y, z. Note that the integration is across the volume occupied by the nanoantenna. By using the electric field distribution inside the nanoantenna, i.e. $\mathbf{E}_{\text{int}}$, the current distribution $\mathbf{J} = -i\omega\epsilon_0\left(\epsilon_r - 1\right)\mathbf{E}_{\text{int}}$ can be calculated. ϵ_r is the generalized complex dielectric permittivity, which can describe material properties of both dielectric and metallic nanoantennas. The physical origin of the induced current is either a conduction current or a displacement current; depending on the material that the nanoantenna is made of, i.e. metals or dielectrics, respectively. Note that Eqs. 2.1.8 till 2.1.11 are approximated expressions and only valid for optically small nanoantennas. In contrast, Eqs. 2.1.5and 2.1.6 are exact expressions and are valid for nanoantennas with any sizes.

2.1.3 Comparison: Practical example

In the previous subsections, we briefly introduced two different approaches to extract the Cartesian multipole moments of an arbitrary nanoantenna embedded in a homogeneous and isotropic media. In this subsection, we apply these formalisms to study a canonical nanoantenna made of coupled nanopatches as shown in Fig. 2.2.1 (a). The nanoantenna is illuminated by a plane wave with an electric field polarized along the x-axis that propagates in the positive z-direction. The antennas supports two distinct modes. They occur due to the hybridization of the localized surface plasmon polaritons that are sustained by the individual metallic nanopatch. The resonance frequencies of these localized surface plasmon polaritons depend on the size of the nanopatch and the material from which they are made. The resonance frequencies, therefore, can be tuned across an extended spectral domain. The first mode is a symmetric mode, which leads to an induced electric dipole moment p_{x} as shown in Fig. 2.2.1 (a). In this mode, the induced current densities in the nanopatches oscillate both in phase. The second mode is an antisymmetric mode that leads to a magnetic dipole as well as electric quadrupole moment [Fig. 2.2.1 (c) and (d)]. This mode is characterized by an induced current density in both nanopatches that are out of phase. Note that we will investigate this nanoantenna more extensively in the following chapter. It can be seen that there is a good agreement between two approaches. In the following chapters, we only use the scattered field approach to calculate the Cartesian multipole moments.

2.2 Scattering properties of nanoantennas: Universal limitations

Nanoantennas are canonical elements in nanooptics, which can be used to control light-matter interaction at the nanoscale. In this section, we want to present some universal limitations (in the dipole approximation) on their interaction with light. In general, nanoantennas can be made from two types of materials, i.e. a) metals b) dielectrics. In the case of metals, nanoantennas support a localized surface plasmon resonance. This is a collective oscillation of the conduction electrons of the metallic antenna resonantly coupled to the electromagnetic wave at visible or near-infrared frequencies [25]. In the case of dielectric nanoantennas, Mie resonances can be excited. They are also known as whispering gallery resonances [26]. In this section, we want to explore scattering properties of the aforementioned nanoantennas from a theoretical point of view. In the following Chapters, we will investigate different types of plasmonic as well as dielectric nanoantennas.

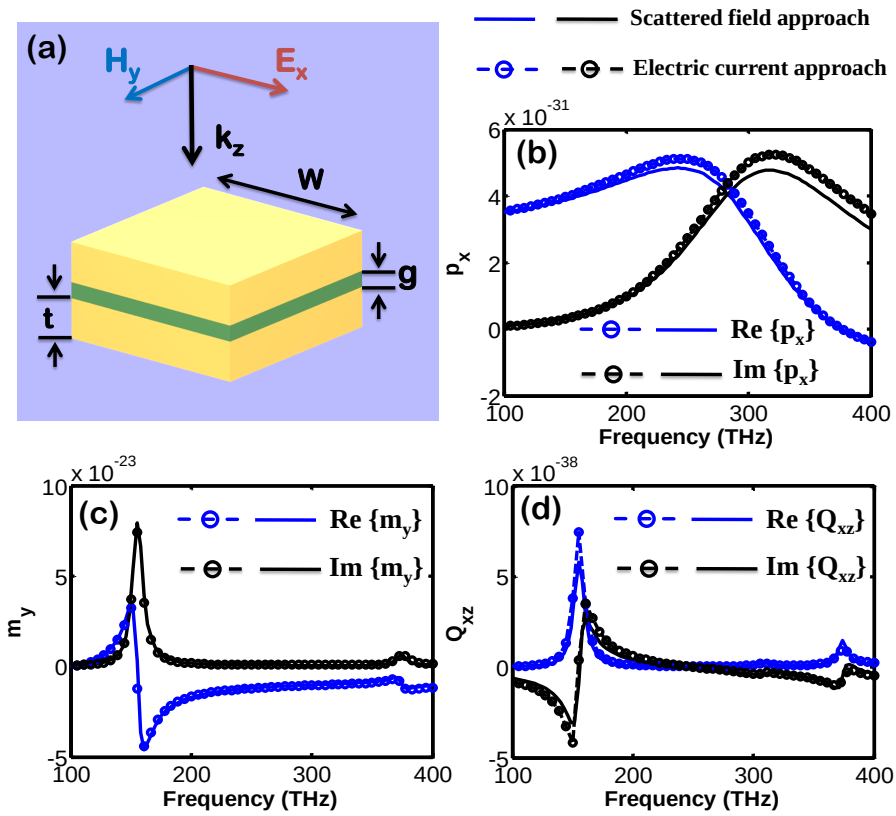

Figure 2.2.1: (a) The geometry of the investigated nanoantenna. The width and thickness of the nanopatches are $W = 250$ nm, and $t = 50$ nm, respectively. The dielectric spacer has a refractive index of $n = \sqrt{\epsilon_r} = 1.46$ and its thickness is $g = 8$ nm. The surrounding material is assumed to be air. (b)-(d) The corresponding Cartesian multipole moments calculated from two approaches. p_x is the induced electric dipole moment, m_y is the induced magnetic dipole moment, Q_{xz} is the induced electric quadrupole moment. All other moments are negligible in the expansion.

2.2.1 Nanoantennas: Electric/magnetic dipole

In this subsection, we explore some universal limitations on the scattering properties of nanoantennas in dipole approximation [27–29]. We show that there is a universal limitation on the absorption, scattering, and extinction cross sections of a nanoantenna, which supports only an electric/magnetic dipole moment. Let us start with the simplest case, i.e. a nanoantenna that only supports an electric dipole moment $\mathbf{p}$. Now, for an incident plane wave with an electric field polarized along the x-axis that propagates in z-direction ($E_{\mathrm{x}}^{\mathrm{inc}}$, $H_{\mathrm{y}}^{\mathrm{inc}}$), the induced electric dipole moment p_{x} can be expressed as

$$p_{\mathrm{x}} = \epsilon_0 \alpha_{\mathrm{ee}} E_{\mathrm{x}}^{\mathrm{inc}},$$

where α_{ee} is the electric polarizability. It is a scalar here and constitutes the sole component that matters in the context of the present configuration. Generally, the electric polarizability is a tensor. In the far-field, the scattered fields ($\mathbf{E}_{\mathrm{sca}}$, $\mathbf{H}_{\mathrm{sca}}$) by the induced electric dipole moment p_{x} are given by [22]

$$\mathbf{E}_{\mathrm{sca}} = Z\mathbf{H}_{\mathrm{sca}} \times \mathbf{n} = \frac{ck}{4\pi} Z \left(\mathbf{n} \times \mathbf{p}\right) \times \mathbf{n} \frac{e^{ikr}}{r}, \tag{2.2.1}$$

$$\mathbf{H}_{\mathrm{sca}} = \frac{ck}{4\pi} \left(\mathbf{n} \times \mathbf{p}\right) \frac{e^{ikr}}{r}, \tag{2.2.2}$$

where $\mathbf{n}$ is the normal unit vector. The dependency of the fields on the spatial coordinate and the frequency is omitted here for brevity. By using the above expressions, scattered power (i.e. the surface integral of the outward flowing flux of the Poynting vector of scattered fields) of the induced electric dipole moment can be written as

$$P_{\mathrm{sca}} = \frac{1}{2}\mathrm{Re} \oiint_S \left(\mathbf{E}_{\mathrm{sca}} \times \mathbf{H}_{\mathrm{sca}}^*\right) \cdot \mathbf{n} \, \mathrm{d}s = \frac{c^2 Z_0 k^4}{12\pi} |\mathbf{p}|^2 = \frac{k^4}{6\pi} |\alpha_{\mathrm{ee}}|^2 \frac{|E_{\mathrm{x}}^{\mathrm{inc}}|^2}{2Z}. \tag{2.2.3}$$

Now by using the definition of the time-averaged Poynting vector for the illumination plane wave, i.e.

$$I_0 = \frac{1}{2}\mathrm{Re}\left(\mathbf{E}_{\mathrm{inc}} \times \mathbf{H}_{\mathrm{inc}}^*\right) = \frac{|E_{\mathrm{x}}^{\mathrm{inc}}|^2}{2Z},$$

and Eq. 2.2.3, the total scattering cross section of the induced electric dipole moment can be expressed as

$$C_{\mathrm{sca}} = \frac{P_{\mathrm{sca}}}{I_0} = \frac{k^4}{6\pi} |\alpha_{\mathrm{ee}}|^2. \tag{2.2.4}$$

On the other hand, the extracted power is defined as

$$\begin{aligned} P_{\text{ext}} &= -\frac{1}{2}\text{Re}\oiint_S (\mathbf{E}_{\text{inc}} \times \mathbf{H}^*_{\text{sca}} + \mathbf{E}_{\text{sca}} \times \mathbf{H}^*_{\text{inc}}) \cdot \mathbf{n}\, \text{d}s, \\ &= -\frac{\omega}{2}\text{Im}\left(\mathbf{p}^* \cdot \mathbf{E}_{\text{inc}}\right) = \frac{1}{2}\omega\epsilon_0\alpha''_{\text{ee}}|\mathbf{E}_{\text{inc}}|^2, \end{aligned} \tag{2.2.5}$$

where α''_{ee} is the imaginary part of the electric polarizability (i.e. $\alpha_{\text{ee}} = \alpha'_{\text{ee}} + i\alpha''_{\text{ee}}$). The extinction cross section can be defined as $C_{\text{ext}} = \frac{P_{\text{ext}}}{I_0} = k\text{Im}\left(\alpha_{\text{ee}}\right) = k\alpha''_{\text{ee}}$. It is well-known that the extracted power $P_{\text{ext}} = P_{\text{sca}} + P_{\text{abs}}$ is a sum of the scattered power P_{sca} and the absorbed power P_{abs} [15]. The same is valid for the cross sections, i.e. $C_{\text{ext}} = C_{\text{sca}} + C_{\text{abs}}$. Therefore, the absorption cross section can be written as

$$\begin{aligned} C_{\text{abs}} &= \frac{P_{\text{abs}}}{I_0} = \frac{P_{\text{ext}} - P_{\text{sca}}}{I_0}, \\ &= \frac{-\frac{1}{2}\text{Re}\oiint_S \left[(\mathbf{E}_{\text{inc}} + \mathbf{E}_{\text{sca}}) \times (\mathbf{H}_{\text{sca}} + \mathbf{H}_{\text{inc}})^*\right] \cdot \mathbf{n}\text{d}s}{I_0}, \qquad (2.2.6) \\ &= \left(k\alpha''_{\text{ee}} - \frac{k^4}{6\pi}|\alpha_{\text{ee}}|^2\right). \qquad (2.2.7) \end{aligned}$$

Note that the absorbed power can be defined by a surface integral of the inward flowing flux of the Poynting vector of the total field through the surface S surrounding the nanoantenna [see Eq. 2.2.6]. Now we can calculate the maximum absorption cross section by differentiating C_{abs} with respect to the real and imaginary parts of the polarizability, i.e. α'_{ee} and α''_{ee}. The final results can be written as

$$\frac{\text{d}C_{\text{abs}}}{\text{d}\alpha'_{\text{ee}}} = 0 \quad \rightarrow \quad \alpha'_{\text{ee}} = 0, \tag{2.2.8}$$

$$\frac{\text{d}C_{\text{abs}}}{\text{d}\alpha''_{\text{ee}}} = 0 \quad \rightarrow \quad \alpha''_{\text{ee}} = \frac{3\pi}{k^3}. \tag{2.2.9}$$

This suggests that in order to achieve maximum absorption for a nanoantenna, which supports only an electric dipole response, the nanoantenna should be in resonance, i.e. the real part of the polarizability should be zero. By substituting Eq. 2.2.8 and Eq. 2.2.9 into Eq. 2.2.7, the maximum absorption cross section can be calculated

$$C^{\text{max}}_{\text{abs}} = \frac{3\pi}{2k^2}.$$

Similarly, by substituting Eq. 2.2.8 and Eq. 2.2.9 into Eq. 2.2.4 the maximum

scattered power will be

$$C_{\mathrm{sca}}^{\mathrm{max}} = \frac{3\pi}{2k^2}.$$

Therefore, we can conclude that *a nanoantenna which exhibits only an electric dipole response is most absorptive if the absorbed power is identical to the scattered power*, i.e. $C_{\mathrm{abs}}^{\mathrm{max}} = C_{\mathrm{sca}}^{\mathrm{max}} = \frac{3\pi}{2k^2}$. This condition is known as *critical coupling* [10, 27, 30, 31]. Moreover, it is important to mention that for such a nanoantenna the scattering/absorption cross section ($C_{\mathrm{abs}}^{\mathrm{max}}$ or $C_{\mathrm{sca}}^{\mathrm{max}}$) can exceed the geometrical cross section (A) by an order of magnitude. To exemplify these thoughts, let us assume a nanodisk antenna with a finite height, radius a and geometrical cross section of $A = \pi a^2$. The nanoantenna shall be sufficiently small compared to the wavelength ($ka << 1$). Hence, the absorption/scattering cross section can be much bigger than the geometrical cross section at critical coupling, i.e.

$$\frac{C_{\mathrm{sca}}^{\mathrm{max}}}{A} = \frac{C_{\mathrm{abs}}^{\mathrm{max}}}{A} = \frac{3}{2(ka)^2} >> 1.$$

Note that for metallic nanoantennas the enhanced absorption is associated with the excitation of surface plasmons, which leads to a huge near-field enhancement. This field enhancement will play a crucial rule to achieve promising applications. For lossy dielectric nanoantennas at infrared wavelengths the absorption is associated with the excitation of surface phonons [32]. We wish to stress that the underlying physical mechanism usually cannot be explained in the context of Maxwell's equations, since material properties are introduced on phenomenological grounds. However, physical reasoning using e.g. solid state theory, can explain the origin of the resonance.

Now let us focus on a lossless case, i.e. the absorbed power is zero ($P_{\mathrm{abs}} = 0$). This means that the impinging energy of the illuminating plane wave on the nanoantenna will be scattered backed to the surrounding media. Therefore, the extracted and scattered power should be identical, i.e. $P_{\mathrm{ext}} = P_{\mathrm{sca}}$. This equality leads to a well-known expression for the imaginary part of the polarizability

$$\mathrm{Im}\left(\frac{1}{\alpha_{\mathrm{ee}}}\right) = -\frac{\alpha_{\mathrm{ee}}''}{|\alpha_{\mathrm{ee}}|^2} = -\frac{k^3}{6\pi}. \tag{2.2.10}$$

Equation 2.2.10 presents an important physical quantity that is known as the *scattering losses*; also called *radiation losses* [27, 33]. Note that this quantity is

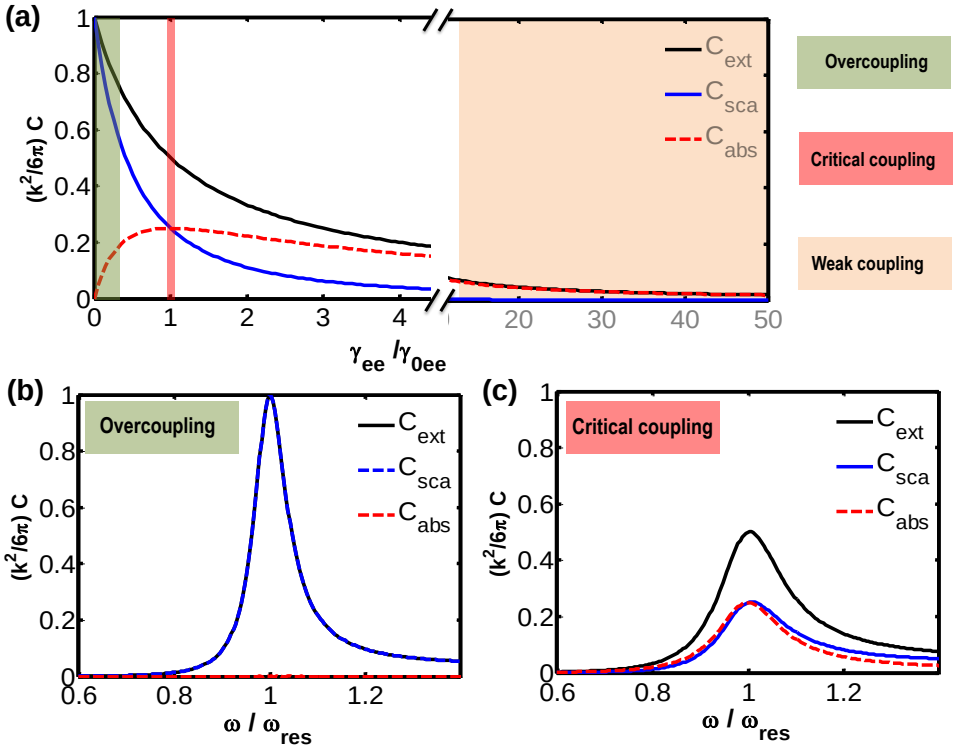

Figure 2.2.2: (a) Normalized extinction, absorption, and scattering cross sections at resonance as a function of the normalized Ohmic losses (i.e. γ_{ee}/γ_{ee0}). (b) Normalized extinction, absorption, and scattering cross sections as a function of the normalized frequency for the lossless case (i.e. $\gamma_{ee} = 0$). (c) The same plot as (b) but for the case of maximum absorption cross section or critical coupling (i.e. $\gamma_{ee} = \gamma_{ee0}$).

independent of the geometrical parameters and materials the nanoantenna is made of. These radiation losses only depend on the wavelength. In the next chapter, we will investigate these scattering losses in detail for a high-index dielectric nanoantenna.

Now, to better understand the aforementioned results, let us assume that the polarizability of the nanoantenna α_{ee} can be expressed by a Lorentzian line-shape that reads as [33]

$$\frac{1}{\alpha_{ee}} = \frac{\omega_{0ee}^2 - \omega^2 - i\omega\gamma_{ee}}{\alpha_{0ee}} - i\frac{k^3}{6\pi}, \tag{2.2.11}$$

where ω_{0ee} is the resonance frequency, γ_{ee} express the Ohmic losses (also called non-radiative losses), α_{0ee} is the strength of resonance. The last term, i.e. $\frac{k^3}{6\pi}$, is related to the scattering losses. Note that Eq. 2.2.11 fulfills Eq. 2.2.10 if the Ohmic losses are zero, i.e. $\gamma_{ee} = 0$.

By using Eq. 2.2.10, Eq. 2.2.5, and Eq. 2.2.4, the scattering and extinction cross

sections can be calculated and they are given by

$$C_{\text{sca}} = \frac{k^4}{6\pi}|\alpha_{\text{ee}}|^2 \;=\; \frac{k^4}{6\pi}\frac{\alpha_{0\text{ee}}^2}{\left(\omega_{0\text{ee}}^2-\omega^2\right)^2+\left(\omega\gamma_{\text{ee}}+\frac{k^3}{6\pi}\alpha_{0\text{ee}}\right)^2}, \tag{2.2.12}$$

$$C_{\text{ext}} = k\text{Im}\left(\alpha_{\text{ee}}\right) \;=\; \frac{k\alpha_{0\text{ee}}\left(\omega\gamma_{\text{ee}}+\frac{k^3}{6\pi}\alpha_{0\text{ee}}\right)}{\left(\omega_{0\text{ee}}^2-\omega^2\right)^2+\left(\omega\gamma_{\text{ee}}+\frac{k^3}{6\pi}\alpha_{0\text{ee}}\right)^2}. \tag{2.2.13}$$

To get a broader picture and to be able to explain and understand Eq. 2.2.12 and Eq. 2.2.13 in detail, we calculated the scattering, absorption, and extinction cross sections as a function of the normalized Ohmic losses at the resonance frequency [Fig. 2.2.2 (a)]. Note that the scattering, absorption, and extinction cross sections are normalized to $\frac{6\pi}{k^2}$, which is the maximum extinction cross section. This occurs whenever the nanoantenna is lossless, i.e. $C_{\text{ext}}^{\text{max}} = \frac{6\pi}{k^2}$. Moreover, the Ohmic losses are normalized to the scattering losses in Fig. 2.2.2 (a). In principle, three different coupling regime can be distinguished:

a) *Overcoupling* ($\gamma_{\text{ee}} << \gamma_{0\text{ee}}$): This occurs if the Ohmic losses (i.e. γ_{ee}) of the nanoantenna are much smaller than the scattering losses (i.e. $\gamma_{0\text{ee}}$). Note the scattering losses are defined as $\gamma_{0\text{ee}} = \frac{k^3}{6\pi}\left(\frac{\alpha_{0\text{ee}}}{\omega_0}\right)$. Figure 2.2.2 (b) shows the normalized the scattering, absorption, and extinction cross sections as a function of normalized frequency (i.e. $\omega/\omega_{\text{res}}$) for the lossless case, i.e. $\gamma_{\text{ee}} = 0$. It can be seen that the scattering and extinction cross sections are identical, i.e $C_{\text{ext}} = C_{\text{abs}}$.

b) *Critical coupling* ($\gamma_{\text{ee}} = \gamma_{0\text{ee}}$): This occurs whenever the Ohmic losses (γ_{ee}) are identical to the scattering losses ($\gamma_{0\text{ee}}$). This condition allows to achieve maximum absorption. It can be seen that the maximum absorption cross section occurs whenever $\gamma_{\text{ee}} = \gamma_{0\text{ee}} = \frac{k^3}{6\pi}\left(\frac{\alpha_{0\text{ee}}}{\omega_0}\right)$ [Fig. 2.2.2 (a) and (c)]. Figure 2.2.2 (c) shows the same plot as Fig. 2.2.2 (b) for the case of critical coupling. In this case, the absorption cross section is identical to the scattering cross section, i.e. $C_{\text{abs}} = C_{\text{sca}}$. Therefore, the extinction cross section will be $C_{ext} = 2C_{\text{abs}} = 2C_{\text{sca}}$.

c) *Weak coupling* ($\gamma_{\text{ee}} >> \gamma_{0\text{ee}}$): This occurs if the Ohmic losses (γ_{ee}) are much larger than the scattering losses ($\gamma_{0\text{ee}}$). At extremely large Ohmic losses, i.e. $\gamma_{\text{ee}} >> \gamma_{0\text{ee}}$, the scattering cross section is considerably small with respect to the absorption cross section, i.e. $C_{\text{sca}} << C_{\text{abs}}$. In other words, the absorption cross section is identical to the extinction cross section, i.e. $C_{\text{ext}} \simeq C_{\text{abs}}$. This occurs whenever the nanoantenna is considerably small with respect to the wavelength. The frequency dependency of the scattering, absorption, and extinction cross sections for the weak

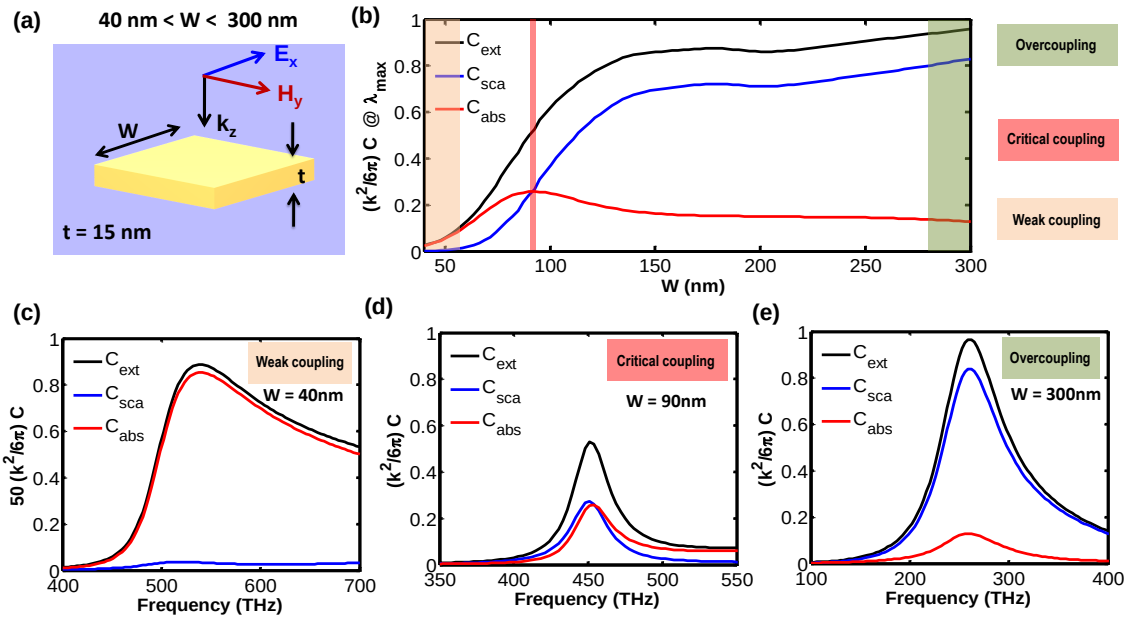

Figure 2.2.3: (a) Schematic of the nanopatch antenna. (b) Normalized extinction, scattering, absorption cross sections at resonance frequency ($\lambda_{\max}$) as a function of width of the investigated patch nanoantenna (i.e. W). (c) Normalized extinction, scattering, absorption cross sections as a function of frequency when the width of nanoantenna is $W = 50$ nm. In this case the $C_{\text{ext}} \approx C_{\text{abs}}$. This occurs for really small nanoantenna compare to the wavelength. (d) Same as (c) whenever the nanoantenna is at critical coupling, i.e. $C_{\text{abs}}|_{\lambda_{\max}} = C_{\text{ext}}|_{\lambda_{\max}}$. This occurs if the width of nanoantenna is $W = 90$ nm. (e) Same as (d) when the scattering cross section is dominated $W = 40$ nm.

coupling regime is not shown here. However, we will investigate that in the following for a nanopatch antenna.

The aforementioned theoretical results can be applied to an arbitrary plasmonic nanoantenna as long as it supports only an electric dipole response. In order to confirm that, we investigate possibly the simplest nanoantenna, i.e. a gold nanopatch [Fig. 2.2.3 (a)]. The height of the nanopatch is assumed to be $t = 15$ nm and its width W is varying from 40 nm to 300 nm. It can be seen that by varying the width W of the nanoantenna, it is possible to tune the Ohmic losses. This is shown in Fig. 2.2.3 (a). For small nanoantennas, i.e. $W < 60$ nm, the absorption cross section is much larger than the scattering cross section, i.e. $C_{\text{abs}} \simeq C_{\text{ext}}$ [Fig. 2.2.3 (c)]. In principle, this is always valid for a nanoantenna much smaller than the operating wavelength. By increasing the width of the nanopatch, the critical coupling (maximum absorption regime) can occur. In the chosen example this happens at for W =90 nm [Fig. 2.2.3(c)]. Finally, for considerably large nanoantenna, scattering losses dominate and the extinction cross section might reach its maximum value, i.e.

Table 2.1: Analytical expression for absorption, scattering, and extinction cross sections of a nanoantenna which exhibits an electric or a magnetic dipole moment. An analytical expression for the scattering losses of such nanoantenna; known as Sipe-Kranendonk condition.

Moments / polarizabilities	**Scattering cross section (C_{sca})**	**Extinction cross section (C_{ext})**	**Sipe-Kranendonk condition (scattering losses)**
electric dipole $\mathbf{p} = \epsilon_0 \alpha_{\mathrm{ee}} \mathbf{E}$	$C_{\mathrm{sca}} = \frac{k^4}{6\pi} \lvert\alpha_{\mathrm{ee}}\rvert^2$	$C_{\mathrm{ext}} = k\mathrm{Im}\left(\alpha_{\mathrm{ee}}\right)$	$\mathrm{Im}\left(\frac{1}{\alpha_{\mathrm{ee}}}\right) = -\frac{k^3}{6\pi}$
magnetic dipole $\mathbf{m} = \alpha_{\mathrm{mm}} \mathbf{H}$	$C_{\mathrm{sca}} = \frac{k^4}{6\pi} \lvert\alpha_{\mathrm{mm}}\rvert^2$	$C_{\mathrm{ext}} = k\mathrm{Im}\left(\alpha_{\mathrm{mm}}\right)$	$\mathrm{Im}\left(\frac{1}{\alpha_{\mathrm{mm}}}\right) = -\frac{k^3}{6\pi}$

Table 2.2: Universal limitation on the absorption, scattering and extinction cross sections of a nanoantenna which exhibit electric/magnetic dipole moment.

Nanoantennas (electric/magnetic dipole)	**Maximum scattering cross section ($C_{\mathrm{sca}}^{\mathrm{max}}$)**	**Maximum absorption cross section ($C_{\mathrm{abs}}^{\mathrm{max}}$)**	**Maximum extinction cross section ($C_{\mathrm{ext}}^{\mathrm{max}}$)**
lossless (dielectric)	$\frac{6\pi}{k^2}$	0	$\frac{6\pi}{k^2}$
Lossy (metallic)	$< \frac{6\pi}{k^2}$	$\frac{1}{4}\left(\frac{6\pi}{k^2}\right)$	$< \frac{6\pi}{k^2}$

$C_{\mathrm{ext}} \approx \frac{k^2}{6\pi}$. In other words, the absorption cross section is small compared to the scattering cross section, i.e. $C_{\mathrm{ext}} \simeq C_{\mathrm{sca}} >> C_{\mathrm{abs}}$.

All the findings in this subsection are also valid for a nanoantenna which supports only a magnetic dipole moment. This is briefly reflected in Table. 2.1. As one can see from the table, all the equations for a magnetic dipole moment are analogous, or dual, to those for an electric dipole moment. In fact, this can be understood from the duality of Maxwell's equations. Note that a similar expression of Eq. 2.2.10 also holds for the scattering losses of a magnetic dipole, i.e. $\mathrm{Im}\left(\frac{1}{\alpha_{\mathrm{mm}}}\right) = -\frac{k^3}{6\pi}$. This expression is also called Sipe-Kranendonk condition that can be obtained from conservation of energy [27]. In chapter 3, we will investigate this expression for a lossless high-index dielectric nanoantenna. Moreover, we also summarized all our findings in this subsection in Table. 2.2. Note that these findings are valid as long as the nanoantenna exhibits only an electric/magnetic dipole moment. It is also interesting to mention that these universal limitations are independent of the shape and material of the nanoantenna. Experimental verification of some of these claims can be found in [34–36].

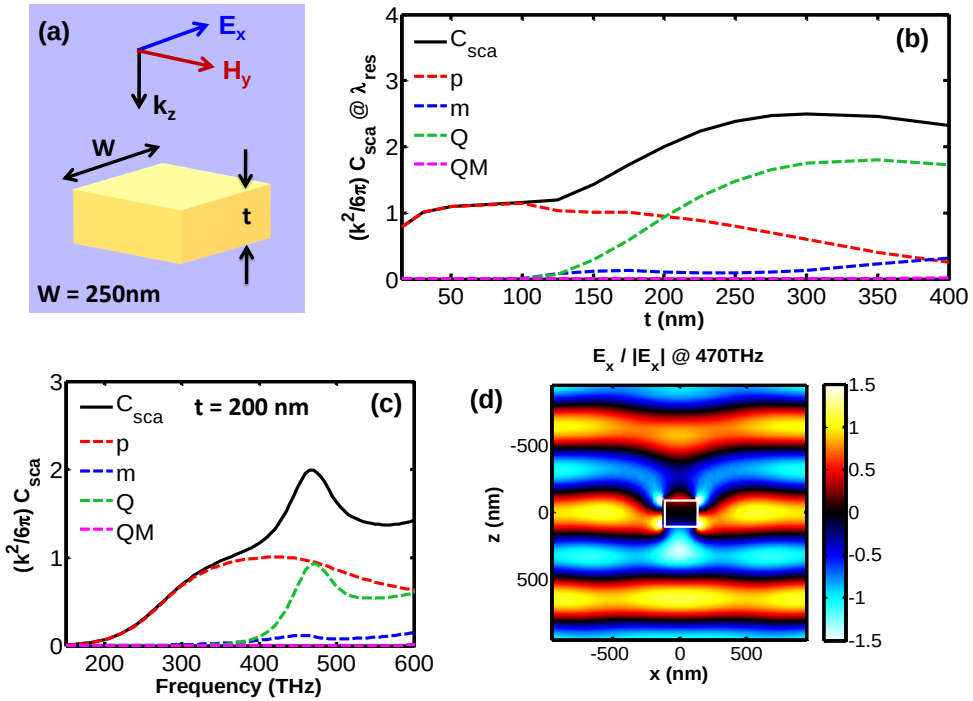

Figure 2.2.4: (a) Schematic of the nanoantenna. (b) Normalized scattering cross section at resonance as a function of thickness of nanoantenna. (c) Normalized scattering cross section as a function of frequency for $t = 200$ nm. (d) Field distributions (E_x) at 470 THz.

2.2.2 Nanoantennas: Beyond dipole approximation

In the previous subsection, we have shown that there are upper bounds for the absorption, extinction, and scattering cross sections of a nanoantenna, which supports only an electric or a magnetic dipole moment. In general, these upper bounds do not apply if the size of the nanoantenna approaches the wavelength of operation. In other words, if the nanoantenna supports other multipole moments than just an electric or a magnetic dipole moment. These higher order multipoles allow to achieve remarkable scattering features such as super-scattering, super-backscattering, super-directivity, and super-absorption [28, 37–39]. In this thesis, we investigate some of these unconventional optical features for different nanoantennas. In particular, in this section, we present a simple nanopatch that allows to observe a super-scattering feature. The term super-scattering applies whenever the maximum scattering cross section, which can be obtained by an electric dipole moment, i.e. $C_\mathrm{sca}^\mathrm{max} = \frac{k^2}{6\pi}$, is exceeded.

In principle, super-scattering can be achieved if a nanoantenna supports multipole resonances in the same frequency range. It also should operate in the overcoupling regime, i.e. the absorption losses should be much smaller than the scattering losses.

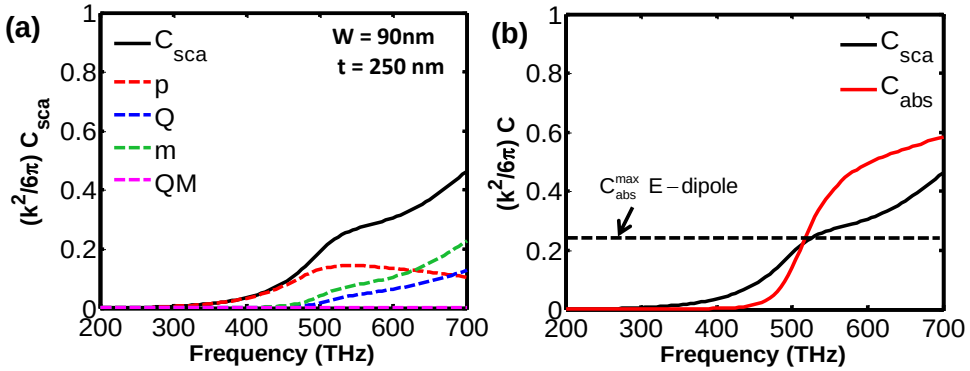

Figure 2.2.5: (a) Normalized scattering cross section for a nanopatch with a width of $W = 90\,\text{nm}$ and thickness of $t = 250\,\text{nm}$. (b) Normalized scattering and absorption cross sections.

In the previous subsection, we have shown that a nanopatch antenna with considerably small thickness possesses only an electric dipole response. In order to excite higher order modes for such a nanoantenna, we propose a nanopatch with a larger thickness. As already shown in Fig. 2.2.3 (a), in order to operate in the overcoupling regime, the width of the nanoantenna should also be large, e.g. $W = 250$ nm [Fig. 2.2.3]. Figure 2.2.4 (a) shows the schematic of the investigated nanoantenna. It is illuminated by a plane wave with an electric field polarized along the x-axis that propagates in the z-direction. The normalized total scattering cross section as a function of thickness of the nanopatch is shown in Fig. 2.2.4 (b). The contributions of different Cartesian mulipole moments are equally shown in the same plot. For the thin nanopatch (i.e. $t < 100$ nm), the contributions from the electric dipole moment dominate. Therefore, the scattering cross section should be $C_{\text{sca}} \leq \frac{k^2}{6\pi}$. By increasing the thickness of the nanopatch, the electric quadrupole and magnetic dipole moments tend to contribute notably to the scattering response. This enhances the total scattering cross section. Figure 2.2.4 (c) depicts the scattering cross section as a function of frequency for a nanopatch with thickness $t = 200$ nm. It can be seen that the total scattering cross section is considerably enhanced around 470 THz. This occurs due to the excitation of electric and magnetic dipole moments as well as electric quadrupole moment at the same frequency range. The field distribution also confirms that the nanopatch hugely scatters the impinging light [Fig. 2.2.4 (b)]. In the following chapters, we will discuss various nanoantennas with super-directive patterns. We will show that a super-directive antenna can be realized if the amplitude and phase of different multipoles are properly balanced.

Furthermore, it is also possible to overcome the absorption limit of an electric dipole, i.e. $\frac{1}{4}\left(\frac{6\pi}{k^4}\right)$ which is sometimes called the super-absorption regime. In prin-

ciple, this regime of absorption can be achieved if the nanoantenna supports more than one mode (i.e. higher order mulipoles) in the same frequency range and also operate at the critical coupling regime. To verify this we also calculate the scattering and absorption cross sections of a nanopatch which supports electric and magnetic dipole moments as well as electric quadrupole moment [Fig. 2.2.5 (a)]. It can be seen that the nanoantenna absorbs more than an electric dipole $C_{\text{abs}} > \frac{1}{4}\left(\frac{6\pi}{k^4}\right)$, which is shown in Fig. 2.2.5 (d) with a black dashed line.

2.3 Optical properties of an array of nanoantennas: Dipole approximation

In this section, we shortly introduce an analytical approach to calculate the optical response in terms of reflection and transmission of of a periodic array of nanoantennas. We assume that the nanoantenna is considerably small with respect to the wavelength such that it only supports electric and magnetic dipole moments. We start with the generalized boundary conditions (interface conditions) for such an array of nanoantennas. By using these boundary conditions, we calculate the reflected and transmitted electric fields. Finally, we discuss the optical response of an array of nanoantennas sustaining electric dipole moments and show that its absorption is limited to 50 percent. This is a universal limitation for an array of nanoantennas which support only electric dipole moments. Due to the symmetry in Maxwell's equations, the same limitation holds for an array of nanoantennas sustaining magnetic dipole moments. We also propose various approaches to overcome this limitations, e.g. using an array of nanoantennas that exhibit both electric and magnetic dipole moments, an array of nanoantennas that exhibit electric or magnetic dipole moment deposited on top of a metallic ground plate, and also an array of nanoantennas that sustain an electric dipole and quadrupole moments. Eventually, we wish to note that in the following we speak synonymously about an array of nanoantennas that sustain, e.g., an electric dipole moment and an arrays of electric dipole moments. In the description this is indistinguishable.

2.3.1 Generalized boundary conditions and reflected and transmitted fields

The aim of this subsection is to establish the relation between the reflected and transmitted electric and magnetic fields with the transverse induced electric and magnetic surface polarizations ($\mathbf{P}_t^s$, $\mathbf{M}_t^s$) at normal incidence. Note that the subscript t refers

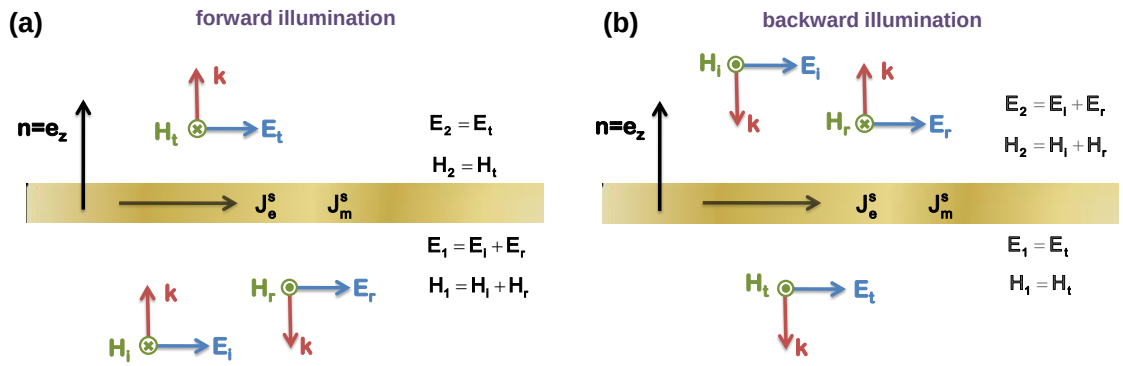

Figure 2.3.1: A surface consists of an electric $\mathbf{J}_e^s$ and a magnetic $\mathbf{J}_m^s$ current densities, which is illuminated by forward (a) and backward (b) incident plane wave.

to the transverse components of the the induced electric and magnetic surface polarizations ($\mathbf{P}^s$, $\mathbf{M}^s$). The normal components ($\mathbf{P}_n^s$, $\mathbf{M}_n^s$) are only important for an oblique incidence which will not be investigated in this thesis. Afterwards it will be shown that how the surface polarizabilities depend on the polarizabilities of the individual nanoantennas. This allows a closed form expression for the reflection and transmission of a nanoantenna array in terms of the properties of the individual constituents. Let us start with the generalized boundary conditions at normal incidence. They are given by [27, 40–43]:

$$\mathbf{n} \times \mathbf{E}|_{z=0^-}^{0^+} = \mathbf{n} \times (\mathbf{E}_2 - \mathbf{E}_1) = i\omega\mu \mathbf{M}_t^s, \tag{2.3.1}$$

$$\mathbf{n} \times \mathbf{H}|_{z=0^-}^{0^+} = \mathbf{n} \times (\mathbf{H}_2 - \mathbf{H}_1) = -i\omega \mathbf{P}_t^s. \tag{2.3.2}$$

$\mathbf{E}(z = 0^+) = \mathbf{E}_2$ and $\mathbf{E}(z = 0^-) = \mathbf{E}_1$ are the total transverse electric fields at the interface in the upper (i.e. $z = 0^+$) and lower ($z = 0^-$) half space relative to the array. The same holds for the transverse magnetic fields ($\mathbf{H}_1$ and $\mathbf{H}_2$) [Fig. 2.3.1]. The induced averaged surface electric and magnetic current densities are defined as $\mathbf{J}_e^s = -i\omega\mathbf{P}_t^s$ and $\mathbf{J}_m^s = -i\omega\mu\mathbf{M}_t^s$. By using these definitions, the boundary (interface) condition can be expressed as

$$\mathbf{n} \times (\mathbf{E}_2 - \mathbf{E}_1) = -\mathbf{J}_m^s, \tag{2.3.3}$$

$$\mathbf{n} \times (\mathbf{H}_2 - \mathbf{H}_1) = \mathbf{J}_e^s. \tag{2.3.4}$$

Note that we explicitly consider two different illumination directions: a) forward and b) backward [Fig. 2.3.1]. This is only important when the array shows a different

optical response with respect to the illumination directions. In principle, this occurs if the array is made of bianisotropic nanoantennas. In Chapter 3 we will discuss such nanoantennas in detail. In Fig. 2.3.1, the array is illuminated by a plane wave for which the following relation holds

$$\mathbf{n}\times\mathbf{H}_i \;=\; \mp\frac{1}{Z}\mathbf{E}_i. \tag{2.3.5}$$

Here, $\mathbf{E}_i$ and $\mathbf{H}_i$ are the electric and magnetic incident fields and the Z is the impedance of the medium. We assume here for simplicity that the upper and lower medium have the same impedance (i.e. the nanoantennas are embedded in uniform medium). Extensions to an asymmetric optical environment can easily be made. The $\mp$ sign in Eq. 2.3.5 denotes a forward/backward incident plane wave. They do propagate in the positive/negative z-direction. According to Fig. 2.3.1 (a), the electric and magnetic fields *at the interface* in the upper ($z = 0^+$) and lower ($z = 0^-$) half space for the forward illumination direction are given by

$$\mathbf{E}_1 = \mathbf{E}_i + \mathbf{E}_r \qquad \mathbf{H}_1 = \mathbf{H}_i + \mathbf{H}_r, \tag{2.3.6}$$

$$\mathbf{E}_2 = \mathbf{E}_t \qquad \mathbf{H}_2 = \mathbf{H}_t, \tag{2.3.7}$$

where $\mathbf{E}_r$ and $\mathbf{H}_r$ are the reflected fields and $\mathbf{E}_t$ and $\mathbf{H}_t$ are the transmitted fields. By substituting Eq. 2.3.6 and Eq. 2.3.7 into Eq. 2.3.3 and Eq. 2.3.4 and using the relation between electric and magnetic fields for a plane wave, i.e. Eq. 2.3.5, the following expression for the fields can be found:

$$\mathbf{E}_t - \mathbf{E}_i - \mathbf{E}_r \;=\; \mathbf{n}\times\mathbf{J}^s_m, \tag{2.3.8}$$

$$\frac{-\mathbf{E}_t + \mathbf{E}_i - \mathbf{E}_r}{Z} \;=\; \mathbf{J}^s_e. \tag{2.3.9}$$

By a simple algebra, we can find the relation between reflected/transmitted field and the induced electric and magnetic surface currents densities

$$\mathbf{E}_r = -\frac{1}{2}\left(Z\mathbf{J}_e^s + \mathbf{n}\times\mathbf{J}_m^s\right), \tag{2.3.10}$$

$$\mathbf{E}_t = \mathbf{E}_i - \frac{1}{2}\left(Z\mathbf{J}_e^s - \mathbf{n}\times\mathbf{J}_m^s\right). \tag{2.3.11}$$

Similar expressions can be found for a backward illumination. The electric and magnetic fields *at the interface* in the upper ($z = 0^+$) and lower ($z = 0^-$) half space for a backward illumination are given by [Fig. 2.3.1(b)]

$$\mathbf{E}_2 = \mathbf{E}_i + \mathbf{E}_r, \qquad \mathbf{H}_2 = \mathbf{H}_i + \mathbf{H}_r,$$

$$\mathbf{E}_1 = \mathbf{E}_t, \qquad \mathbf{H}_1 = \mathbf{H}_t,$$

and finally, by using the same procedure, the reflected and transmitted fields for the backward illumination will be

$$\mathbf{E}_r = -\frac{1}{2}\left(Z\mathbf{J}_e^s - \mathbf{n}\times\mathbf{J}_m^s\right), \tag{2.3.12}$$

$$\mathbf{E}_t = \mathbf{E}_i - \frac{1}{2}\left(Z\mathbf{J}_e^s + \mathbf{n}\times\mathbf{J}_m^s\right). \tag{2.3.13}$$

In the following sections, we use Eqs. 2.3.10, till 2.3.13 to calculate the reflection and transmission coefficients of an array of nanoantennas.

2.3.2 Array of nanoantennas: Universal limitations

In this section, we focus on the optical properties of periodic array of nanoantennas in dipole approximation [27, 44–48]. In particular, we start with an array of nanoantennas which exhibits only an electric or a magnetic dipole moment. We will show that the absorption of such an array is fundamentally limited to 50 percent. In fact, this holds for an arbitrary nanoantenna, independent of shape and material, as along as its scattering response is properly described by an electric or magnetic dipole moment. To overcome this limitation, i.e. to enhance the absorption, we explore different approaches. We show that an array of nanoantennas which exhibits both electric and magnetic dipole moments can be used to achieve complete light absorption. This occurs if the electric and magnetic dipoles are in a balanced condition. Another approach to enhance the absorption is by using an array of nanoantennas (with induced electric/magnetic dipoles) on top of a metallic ground plate. This will be discussed in length in Chapter 4.

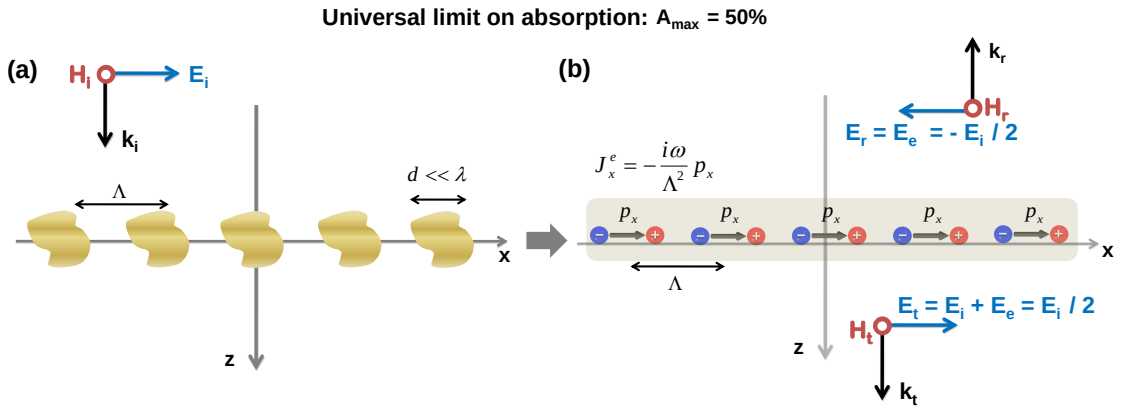

Figure 2.3.2: (a) Geometry of an infinite periodic array of nanoantennas which supports only electric dipole moment. The array is embedded in a uniform homogeneous host medium and excited by a plane wave. The two-dimensional array is periodic in x-y plane. (b) The radiated fields by the average electric current density J_x in the case of maximum absorption, i.e. $A_{max} = 0$.

2.3.2.1 Periodic array of electric/magnetic dipole moments

The interaction of light with a periodic array of optically small nanoantennas is an interesting and fundamental problem which attracts tremendous interests and leads to promising applications [49–51]. These arrays are also called metasurfaces. In this section, we will investigate a limitation concerning the optical properties of such an array of nanoantennas. We assume that nanoantennas are optically small such that the external incidence field can only excite electric dipole moments. We show that a periodic array of electric dipole moments can only absorb 50 percent of the impinging light. Afterwards we also briefly consider in analogy the situation of an array of magnetic dipole moment.

Let us consider an infinite planar array of optically small nanoantennas, which supports only an electric dipole moment. The dipole moment shall be oriented along the x-axis. The array is excited by a plane wave (normal incidence) with an electric field polarized along the x-axis that propagating in the positive z-direction [Fig. 2.3.2]. We assume that the array of nanoantennas is situated in the xy-plane and embedded in a homogeneous lossless medium. The period Λ of the array is sufficiently small compared to the wavelength $d << \lambda$. d is a measure for the spatial extent of the individual nanoantenna. The shape of the nanoantennas can be arbitrary, e.g. nanopatches, nanodiscs, nanostrips, nanospheres, or nanocylinders. We require an illumination to induce only a co-polarized an electric dipole moment, i.e. p_x. All the higher order multipole moments should be negligible. Now, in order to calculate the optical response of a periodic array of electric dipole moments [Fig. 2.3.2 (b)], let

us start to express the induced electric dipole moment p_x excited by an x-polarized external plane wave. It reads as

$$p_x = \epsilon_0 \alpha_{ee} E_x^{loc}, \tag{2.3.14}$$

where α_{ee} is the electric polarizability, E_x^{loc} is the local electric field at the dipole position. It is defined as $E_x^{loc} = E_x^{inc} + E_x^{int}$. E_x^{inc} is the incident electric field and E_x^{int} is the interaction field created by the rest of the electric dipole moments in the array [27]. The interaction field is proportional to p_x and can be expressed by $E_x^{int} = \frac{\beta_{ee} p_x}{\epsilon_0}$. Here, the interaction constant β_{ee} is given by [27, 44]

$$\beta_{ee} = \frac{ik}{4\Lambda^2}\left(1 + \frac{1}{ikR_0}\right)e^{ikR_0}, \tag{2.3.15}$$

where $R_0 = \Lambda/1.438$ is the effective inter-particle distance. This is calculated for the quasi-static case [44] and it is a good approximation as long as the nanoantennas are small compared to the wavelength. Details about the derivation of the interaction constant β_{ee} can be found in Ref. [27, 44]. Note that the imaginary part of the interaction constant for a periodic array can be calculated without any approximation by using a conservation of energy [27] and can be written as

$$\mathrm{Im}\left(\beta_{ee}\right) = \mathrm{Im}\left(\frac{1}{\alpha_{ee}}\right) + \frac{k}{2\Lambda^2} = -\frac{k^3}{6\pi} + \frac{k}{2\Lambda^2}, \tag{2.3.16}$$

where, the first term corresponds to the scattering losses (i.e. $-\frac{k^3}{6\pi}$) and the second term (i.e. $\frac{k}{2\Lambda^2}$) is related to the plane wave created by the induced averaged electric surface current. Finally, the interaction constant can be written as

$$\begin{aligned}\beta_{ee} &= \mathrm{Re}\left(\beta_{ee}\right) + i\mathrm{Im}\left(\beta_{ee}\right) \\ &= \mathrm{Re}\left[\frac{ik}{4\Lambda^2}\left(1 + \frac{1}{ikR_0}\right)e^{ikR_0}\right] + i\left(-\frac{k^3}{6\pi} + \frac{k}{2\Lambda^2}\right).\end{aligned} \tag{2.3.17}$$

By using Eq. 2.3.14 and the local field definition, the induced electric dipole moment can be written as

$$p_x = \epsilon_0 \frac{\alpha_{ee}}{1 - \alpha_{ee}\beta_{ee}} E_x^{inc} = \epsilon_0 \alpha_{eff} E_x^{inc}, \tag{2.3.18}$$

where $\alpha_{\mathrm{ee}}^{\mathrm{eff}} = \frac{\alpha_{\mathrm{ee}}}{1-\alpha_{\mathrm{ee}}\beta_{\mathrm{ee}}}$ is the so-called effective or renormalized electric polarizability of the array. To calculate the reflection and transmission coefficients, we use the generalized boundary condition Eq. 2.3.11, i.e. $E_{\mathrm{x}}^{\mathrm{r}} = -\frac{1}{2}ZJ_{\mathrm{x}}$ and the induced averaged electric surface current density, i.e. $J_{\mathrm{x}}^{\mathrm{e}} = -i\omega\frac{p_{\mathrm{x}}}{\Lambda^2}$. Note that the average magnetic surface current is zero. Therefore, the induced reflected electric field is given as

$$\begin{aligned} E_{\mathrm{x}}^{\mathrm{r}} &= -\frac{1}{2}ZJ_{\mathrm{x}}^{\mathrm{e}} = \frac{i\omega}{2\Lambda^2}Zp_{\mathrm{x}} \\ &= \frac{ik}{2\Lambda^2}\frac{\alpha_{\mathrm{ee}}}{1-\alpha_{\mathrm{ee}}\beta_{\mathrm{ee}}}E_{\mathrm{x}}^{\mathrm{inc}}, \end{aligned} \tag{2.3.19}$$

and finally the reflection and transmission coefficients can be calculated

$$r = \frac{E_{\mathrm{x}}^{\mathrm{r}}}{E_{\mathrm{x}}^{\mathrm{inc}}} = \frac{ik}{2\Lambda^2}\frac{\alpha_{\mathrm{ee}}}{1-\alpha_{\mathrm{ee}}\beta_{\mathrm{ee}}}, \tag{2.3.20}$$

$$t = 1 + r \tag{2.3.21}$$

$$= 1 + \frac{ik}{2\Lambda^2}\frac{\alpha_{\mathrm{ee}}}{1-\alpha_{\mathrm{ee}}\beta_{\mathrm{ee}}}. \tag{2.3.22}$$

Note that Eq. 2.3.20 and Eq. 2.3.22 hold only for an optically thin layer of nanoantennas (metasurface). From the reflection and transmission coefficient the absorption can be calculated. It read as

$$A = 1 - |r|^2 - |t|^2 = 1 - |r|^2 - |1+r|^2. \tag{2.3.23}$$

The reflection coefficient is a complex number and can be written as $r = r_r + ir_i$. Here, r_r is the real part and r_i is the imaginary part of the complex reflection coefficient r. Thus, the absorption can be written as

$$A = -2\,(1+r_r)\,r_r - 2r_i^2. \tag{2.3.24}$$

Now we can find the condition for maximum absorption for an array of electric dipole moments by differentiating the absorption A with respect to r_r and r_i and searching for the roots, identifying extremal points in the absorption, i.e.

$$\frac{\mathrm{d}A}{\mathrm{d}r_r} = 0 \rightarrow r_r = -\frac{1}{2}, \tag{2.3.25}$$

$$\frac{\mathrm{d}A}{\mathrm{d}r_i} = 0 \rightarrow r_i = 0. \tag{2.3.26}$$

Therefore, in order to obtain maximum absorption, the reflection and transmission coefficients of the array should be $r = -\frac{1}{2}$, $t = 1 + r = \frac{1}{2}$. By substituting these values of r and t into Eq. 2.3.23, we can prove that *an array of electric dipole moments can only absorb 50 percent of an impinging light*, i.e. $A_{\max} = \frac{1}{2}$. This is a universal limitation that holds for nanoantenna as long as it supports only an electric dipole moment. In order to cancel the incident field, the array of electric dipole moments should radiate a plane wave with the same amplitude in both forward and backward directions. The optimum case occurs when only half of the incident field is canceled as shown in Fig. 2.3.2. In the case of the maximum absorption, the induced averaged electric surface current density will be $J_{\mathrm{x}}^{\mathrm{e}} = \frac{E_{\mathrm{x}}^{\mathrm{inc}}}{Z}$. The corresponding individual polarizability is given by

$$\alpha_{\mathrm{ee}} = \frac{1}{\beta_{\mathrm{ee}} - \frac{ik}{\Lambda^2}}. \tag{2.3.27}$$

For a dense array of lossless (no Ohmic losses) nanoantennas, it can be easily shown that the reflection coefficient at resonance will reach $r = -1$, therefore, the transmission coefficient should be zero $t = 1 + r = 0$. As a result, the corresponding individual polarizability can be expressed as

$$\alpha_{\mathrm{ee}} = \frac{1}{\beta_{\mathrm{ee}} - \frac{ik}{2\Lambda^2}}. \tag{2.3.28}$$

Note that by using Babinet's principle, all the aforementioned findings can be applied to a metallic film with an array of holes. This explains why an array of holes possesses a total transmission at the resonance known as an extraordinary optical transmission (EOT) [52–54].

In order to quantitatively understand the fundamental limitation of absorption for an array of electric dipole moments, let us now assume that polarizability of an individual nanoantenna possesses a Lorentzian line-shape given by Eq. 2.2.11. By using Eq. 2.3.20 and the inter-particle interaction constant, i.e. $\beta_{\mathrm{ee}} = \mathrm{Re}\,(\beta_{\mathrm{ee}}) - i\frac{k^3}{6\pi} + i\frac{k}{2\Lambda^2}$ [27], the reflection coefficient can be written as

$$r = \frac{ik}{2\Lambda^2}\left(\frac{1}{\frac{1}{\alpha_{ee}}-\beta_{ee}}\right) = \frac{ik}{2\Lambda^2}\left(\frac{\alpha_{0ee}}{\omega_0'^2-\omega^2-i\omega\left(\gamma_{ee}+\frac{\alpha_0}{2\Lambda^2 c_0}\right)}\right), \quad (2.3.29)$$

where $\omega_0^{'} = \omega_0 - \mathrm{Re}\left(\beta_{ee}\right)\alpha_{0ee}$ is the resonance frequency of the array which is slightly red-shifted compared to the resonance of an individual nanoantenna (i.e. ω_0). The reflection coefficient at the resonance frequency $\omega = \omega_0^{'}$ is given by

$$r\left(\omega=\omega_0^{'}\right) = -\frac{\frac{\alpha_0}{2\Lambda^2 c_0}}{\left(\gamma_{ee}+\frac{\alpha_0}{2\Lambda^2 c_0}\right)} = -\frac{\gamma_{0ee}}{\left(\gamma_{ee}+\gamma_{0ee}\right)}. \quad (2.3.30)$$

γ_{0ee} is defined as $\gamma_{0ee} = \frac{\alpha_0}{2\Lambda^2 c_0}$. Moreover, the transmission coefficient will be $t\left(\omega=\omega_0^{'}\right) = 1 + r\left(\omega=\omega_0^{'}\right)$.

To better understand all the aforementioned results, the reflection, transmission, and absorption of an array of electric dipole moments at the resonance frequency as a function of the normalized dissipation losses (i.e. γ_{ee}/γ_{ee0}) are shown in Fig. 2.3.3 (a). It can be seen that the maximum reflection (i.e. $R_{\max} = |r_{\max}|^2 = 1$, $r_{\max} = -1$) occurs if the nanoantennas in the array are lossless, i.e. $\gamma_{ee} = 0$ [Fig. 2.3.3 (a)-(c)]. The transmission ($t = 1 + r$) for such a lossless array goes to zero at resonance frequency [Fig. 2.3.3 (b) and (c)].

The array will achieve its maximum absorption, i.e. $A_{\max} = \frac{1}{2}$, if the dissipation loss is equal to $\gamma_{ee} = \gamma_{0ee} = \frac{\alpha_0}{2\Lambda^2 c_0}$. This point of operation is shown with red line in Fig. 2.3.3 (a) and (d). In this case, the reflection and transmission coefficients will be $r = -1/2$, $t = 1/2$. This can be easily seen in Fig. 2.3.3 (e). As a practical example of the theoretical findings of this section, in the beginning of chapter 3, we investigate an array of gold nanopatches which exhibits only an electric dipole moment. We will show that it is possible to achieve the point of maximal absorption for the array by proper varying the geometrical parameters of the nanopatches and the periodicity such that it satisfies Eq. 2.3.27. The optical response of the array will be similar to the Fig. 2.3.3 (d) and (e).

The optical response of a periodic array of magnetic dipoles can be found by using a similar approach explained above. Here, we briefly explain it. The schematic of the array of nanoantennas which is illuminated by a plane wave with an electric field polarized along the x-axis is shown in Fig. 2.3.4 (a)-(b). We assume the induced magnetic dipole moments are in y-direction, i.e. $m_y = \alpha_{mm} H_y^{loc}$, where α_{mm} is the magnetic polarizability, $H_y^{loc} = H_y^{inc} + H_y^{int}$ is the local magnetic field at the dipole

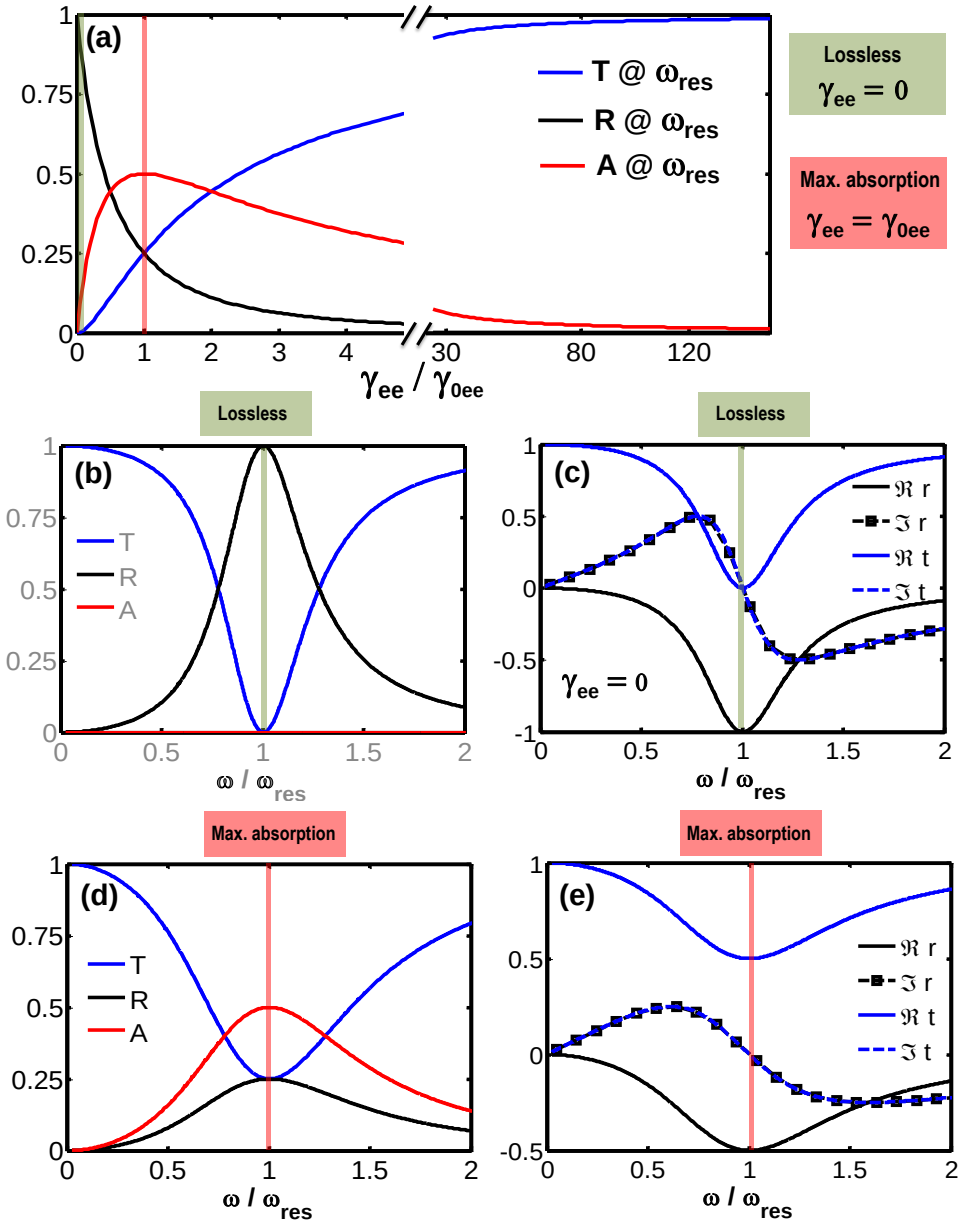

Figure 2.3.3: (a) Transmission, reflection, and absorption at resonance frequency as a function of normalized dissipation losses (i.e. γ_{ee}/γ_{0ee}). Maximum absorption (i.e. $A_{\max} = 0.5$) occurs whenever $\gamma_{ee} = \gamma_{0ee}$ (red line). (b) The transmission, reflection, and absorption as a function of normalized frequency for the lossless case, i.e. $\gamma_{ee} = 0$. (c) The same plot as (b) for the reflection and transmission coefficients. (d) -(e) Same plots as (b) and (c) for the case of maximal absorption (i.e. $\gamma_{ee} = \gamma_{0ee}$).

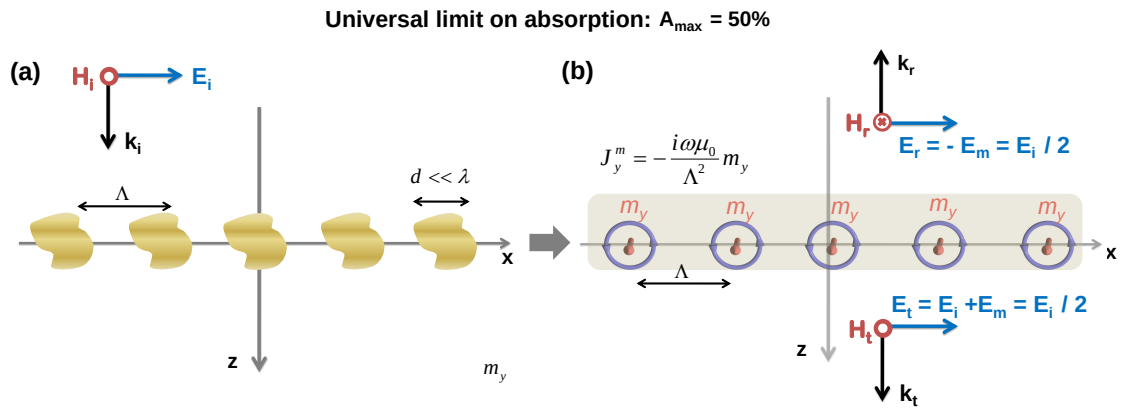

Figure 2.3.4: (a) Geometry of an infinite periodic array of magnetic dipoles in a uniform host medium excited by plane wave. The two-dimensional array is periodic in x-y plane. (b) The radiated field by the average magnetic current density in the case of maximum absorption.

position. $H_{\mathrm{y}}^{\mathrm{inc}}$ is the incident magnetic field and $H_{\mathrm{y}}^{\mathrm{int}}$ is the interaction field created by the rest of magnetic dipole moments in the array [27]. The interaction field is proportional to m_{y} and can be expressed by $H_{\mathrm{y}}^{\mathrm{int}} = \beta_{\mathrm{mm}} m_{\mathrm{y}}$. The magnetic interaction constant is identical to the electric one (i.e. $\beta_{\mathrm{mm}} = \beta_{\mathrm{ee}}$). Now by considering the averaged magnetic surface current density, i.e. $J_{\mathrm{y}}^{m} = -i\omega\mu_0 \frac{m_{\mathrm{y}}}{\Lambda^2}$ and the corresponding boundary condition (i.e. Eq. 2.3.11), we can find the reflected electric field as

$$E_{\mathrm{x}}^{\mathrm{r}} = \frac{1}{2} J_{\mathrm{y}}^{m} = -\frac{ik}{2\Lambda^2} \left(\frac{\alpha_{\mathrm{mm}}}{1 - \alpha_{\mathrm{mm}}\beta_{\mathrm{mm}}} \right) E_{\mathrm{x}}^{\mathrm{inc}},$$

and consequently, the reflection is given by

$$r = -\frac{ik}{2\Lambda^2} \left(\frac{\alpha_{\mathrm{mm}}}{1 - \alpha_{\mathrm{mm}}\beta_{\mathrm{mm}}} \right).$$

The transmission coefficient can be found from the reflection coefficient that is $t = 1 - r$. To find the maximum absorption of the array, we start with the absorption definition $A = 1 - |r|^2 - |1 - r|^2$ and using the complex reflection coefficient, i.e. $r = r_r + i r_i$. This allows us to write the absorption as

$$A = 2\,(1 - r_r)\, r_r - 2 r_i^2. \tag{2.3.31}$$

Now by differentiating the absorption A with respect to r_r and r_i we can find the condition for maximum absorption for an array of magnetic dipole moments. The reflection and transmission coefficients should be $r = \frac{1}{2}$, $t = 1 - r = \frac{1}{2}$. Finally, the

Table 2.3: Analytical expressions for transmission , reflection, absorption of a nanoantenna which exhibit electric/magnetic dipole.

Moments / polarizability	**Reflection** $R = \|r\|^2$	**Transmission** $T = \|t\|^2$	**Absorption** $A = 1 - \|t\|^2 - \|r\|^2$
electric dipole $\mathbf{p} = \epsilon_0 \alpha_{\mathrm{ee}} \mathbf{E}$	$r = \frac{ik}{2\Lambda^2} \alpha_{\mathrm{ee}}^{\mathrm{eff}}$	$t = 1 + r$	$A \leq \frac{1}{2}$
magnetic dipole $\mathbf{m} = \alpha_{\mathrm{mm}} \mathbf{H}$	$r = -\frac{ik}{2\Lambda^2} \alpha_{\mathrm{mm}}^{\mathrm{eff}}$	$t = 1 - r$	$A \leq \frac{1}{2}$

maximum absorption ($A_{\max} = \frac{1}{2}$) can be obtained for an array of magnetic dipoles in a homogeneous lossless media. The induced averaged magnetic surface current density is $J_{\mathrm{y}}^{m} = E_{\mathrm{x}}^{\mathrm{inc}}$ for case of the maximum absorption.

We briefly summarize all the finding of this section in Table 2.3. In principle it shows that due to the duality of Maxwell's equations, the response of an array of magnetic dipole moments is similar to the electric one. One of the important finding of this section is that *an array of electric/magnetic dipole moments can only absorb 50 percent of impinging light.* This is a universal limitation and is true for an array of arbitrary nanoantennas which only support electric/ magnetic dipole moments. In the following section, we will show that we can exceed this limit by using an array of nanoantennas that are characterized simultaneously by an electric and magnetic dipole moments. Eventually, complete light absorption is possible.

2.3.2.2 Periodic array of electric and magnetic dipole moments

In previous subsections, we have shown that there is an upper limit for the absorption by an array of nanoantennas that supports either an electric or a magnetic dipole moment. Here, we want to investigate the optical response of a periodic array of nanoantennas which supports both electric and magnetic dipole moments. The array is located in the xy-plane and illuminated by a plane wave with an electric field polarized along the x-axis that propagates in the positive z-direction [Fig. 2.3.5]. The period of the array is Λ which is sufficiently small compared to the wavelength λ. The relation between the induced dipole moments $(p_{\mathrm{x}}, m_{\mathrm{y}})$ and incident fields ($E_{\mathrm{x}}^{\mathrm{inc}}$,$H_{\mathrm{y}}^{\mathrm{inc}}$) can be written as

$$\begin{pmatrix} \frac{p_{\mathrm{x}}}{\epsilon_0} \\ Z m_{\mathrm{y}} \end{pmatrix} = \begin{pmatrix} \alpha_{\mathrm{xx}}^{\mathrm{ee}} & \alpha_{\mathrm{xy}}^{\mathrm{em}} \\ \alpha_{\mathrm{yx}}^{\mathrm{me}} & \alpha_{\mathrm{yy}}^{\mathrm{mm}} \end{pmatrix} \begin{pmatrix} E_{\mathrm{x}}^{\mathrm{loc}} \\ Z H_{\mathrm{y}}^{\mathrm{loc}} \end{pmatrix},$$

where $E_{\mathrm{x}}^{\mathrm{loc}} = E_{\mathrm{x}}^{\mathrm{inc}} + E_{\mathrm{x}}^{\mathrm{int}}$ and $H_{\mathrm{x}}^{\mathrm{loc}} = H_{\mathrm{x}}^{\mathrm{inc}} + H_{\mathrm{x}}^{\mathrm{int}}$. For simplicity, we assume here

in the following that the nanoantenna is not bianisotropic, i.e. $\alpha_{\mathrm{xy}}^{\mathrm{em}} = \alpha_{\mathrm{yx}}^{\mathrm{me}} = 0$. A bianisotropic nanoantenna will be investigated in detail in the next chapter. By using the generalized boundary condition and the averaged electric and magnetic current density (i.e. Eq. 2.3.11), we can write the reflected $E_{\mathrm{x}}^{\mathrm{r}}$ and transmitted $E_{\mathrm{x}}^{\mathrm{t}}$ electric fields in terms of electric and magnetic dipole moments as

$$E_{\mathrm{x}}^{\mathrm{r}} = \frac{i\omega}{2\Lambda^2}\left(Zp_{\mathrm{x}} - \mu_0 m_{\mathrm{y}}\right), \tag{2.3.32}$$

$$E_{\mathrm{x}}^{\mathrm{t}} = E_{\mathrm{x}}^{\mathrm{inc}} + \frac{i\omega}{2\Lambda^2}\left(Zp_{\mathrm{x}} + \mu_0 m_{\mathrm{y}}\right). \tag{2.3.33}$$

Now by employing the relation between local fields and incident fields, we can simply calculate the dipole moments as a function of the incident fields

$$p_{\mathrm{x}} = \epsilon_0 \frac{\alpha_{\mathrm{xx}}^{\mathrm{ee}}}{1 - \alpha_{\mathrm{xx}}^{\mathrm{ee}}\beta^{\mathrm{ee}}} E_{\mathrm{x}}^{\mathrm{inc}} = \epsilon_0 \widehat{\alpha}_{\mathrm{xx}}^{\mathrm{ee}} E_{\mathrm{x}}^{\mathrm{inc}}, \tag{2.3.34}$$

$$m_y = \frac{\alpha_{\mathrm{yy}}^{\mathrm{mm}}}{1 - \alpha_{\mathrm{yy}}^{\mathrm{mm}}\beta^{\mathrm{mm}}} H_{\mathrm{y}}^{\mathrm{inc}} = \widehat{\alpha}_{\mathrm{yy}}^{\mathrm{mm}} H_{\mathrm{y}}^{\mathrm{inc}}, \tag{2.3.35}$$

where $\widehat{\alpha}_{\mathrm{xx}}^{\mathrm{ee}}$ and $\widehat{\alpha}_{\mathrm{yy}}^{\mathrm{mm}}$ are the effective polarizability of the array. By substituting Eqs. 2.3.34 and 2.3.35 into Eq. 2.3.32 and Eq. 2.3.33, the reflection and transmission coefficients for the array can be found as

$$r = \frac{E_{\mathrm{x}}^{\mathrm{r}}}{E_{\mathrm{x}}^{\mathrm{i}}} = \frac{ik}{2\Lambda^2 \Delta_{\mathrm{ee}} \Delta_{\mathrm{mm}}} \left(\alpha_{\mathrm{xx}}^{\mathrm{ee}} - \alpha_{\mathrm{yy}}^{\mathrm{mm}}\right), \tag{2.3.36}$$

$$t = \frac{E_{\mathrm{x}}^{\mathrm{r}}}{E_{\mathrm{x}}^{\mathrm{i}}} = 1 + \frac{ik}{2\Lambda^2 \Delta_{\mathrm{ee}} \Delta_{\mathrm{mm}}} \left(\alpha_{\mathrm{xx}}^{\mathrm{ee}} + \alpha_{\mathrm{yy}}^{\mathrm{mm}} - \alpha_{\mathrm{xx}}^{\mathrm{ee}} \alpha_{\mathrm{yy}}^{\mathrm{mm}} \left[\beta_{\mathrm{ee}} + \beta_{\mathrm{mm}}\right]\right), \tag{2.3.37}$$

where $\Delta_{\mathrm{ee}} = 1 - \alpha_{\mathrm{xx}}^{\mathrm{ee}}\beta^{\mathrm{ee}}$ and $\Delta_{\mathrm{mm}} = 1 - \alpha_{\mathrm{yy}}^{\mathrm{mm}}\beta^{\mathrm{mm}}$. Note that $\beta_{\mathrm{ee}} = \beta_{\mathrm{mm}}$. Finally, the absorption can be expressed as

$$\begin{aligned} A &= 1 - |r|^2 - |t|^2, \\ &= 1 - |r_{\mathrm{ee}} - r_{\mathrm{mm}}|^2 - |1 + r_{\mathrm{ee}} + r_{\mathrm{mm}}|^2, \end{aligned} \tag{2.3.38}$$

where $r_{\mathrm{ee}} = \frac{ik}{2\Lambda^2}\widehat{\alpha}_{\mathrm{xx}}^{\mathrm{ee}}$ and $r_{\mathrm{mm}} = \frac{ik}{2\Lambda^2}\widehat{\alpha}_{\mathrm{xx}}^{\mathrm{ee}}$. In order to maximize the absorption, we can differentiate r_{ee} as well as r_{mm} with respect to its the real and imaginary parts. The optimum value will be

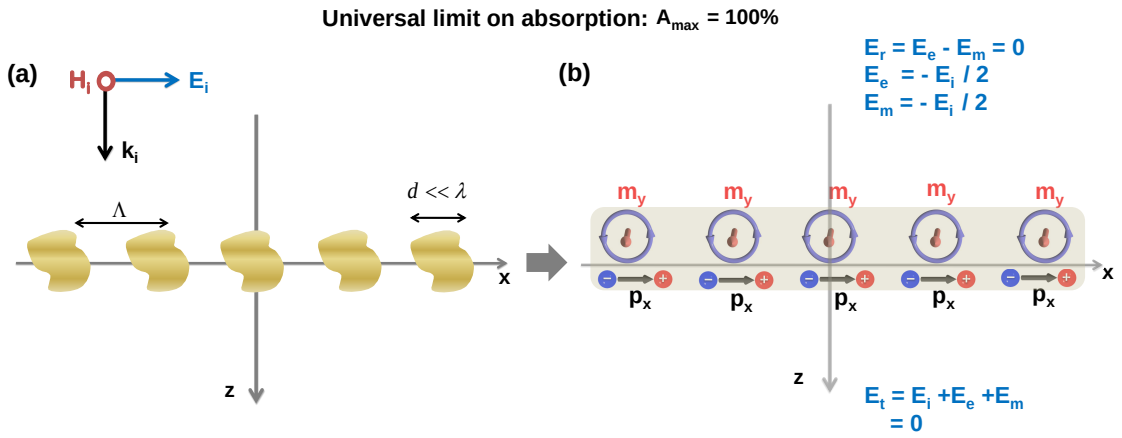

Figure 2.3.5: (a) Geometry of an infinite periodic array of nanoantennas that support electric and magnetic dipole moments in a uniform host medium excited by a plane wave. The two-dimensional array is periodic in x-y plane. (b) show the radiated field by the average magnetic current density in the case of maximum absorption.

$$r_{\mathrm{ee}} = r_{\mathrm{mm}} = -\frac{1}{2} \quad \Rightarrow \quad \widehat{\alpha}_{\mathrm{xx}}^{\mathrm{ee}} = \widehat{\alpha}_{\mathrm{yy}}^{\mathrm{mm}}. \tag{2.3.39}$$

The above condition, i.e. $\widehat{\alpha}_{\mathrm{xx}}^{\mathrm{ee}} = \widehat{\alpha}_{\mathrm{yy}}^{\mathrm{mm}}$, is called balanced condition for the effective polarizabilities. Hence, the balanced condition for the individual polarizabilities is given by

$$\alpha_{\mathrm{xx}}^{\mathrm{ee}} \quad = \quad \alpha_{\mathrm{xx}}^{\mathrm{mm}} = \frac{1}{\beta^{\mathrm{ee}} - \frac{ik}{\Lambda^2}}. \tag{2.3.40}$$

Note that the maximum absorption for an array of electric and magnetic dipoles (i.e. $A_{\mathrm{max}} = 1$) is twice the absorption that can be obtained for the array of electric/magnetic dipoles. At maximum absorption, the array will completely cancel the incident field in the forward direction without generating any backward wave, i.e. reflection [Fig. 2.3.5 (b)]. Moreover, the relation between the induced averaged electric and magnetic surface current densities in this case will be

$$\frac{J_{\mathrm{y}}^{\mathrm{m}}}{J_{\mathrm{x}}^{\mathrm{e}}} \quad = \quad \frac{E_{\mathrm{x}}^{\mathrm{inc}}}{E_{\mathrm{x}}^{\mathrm{inc}}/Z} = Z, \tag{2.3.41}$$

which simply means that the array is impedance matched with the embedded medium. On the other hand, we can also find the relation between electric and magnetic dipole moments at total absorption, i.e. $p_{\mathrm{x}} = \frac{m_{\mathrm{y}}}{c}$.

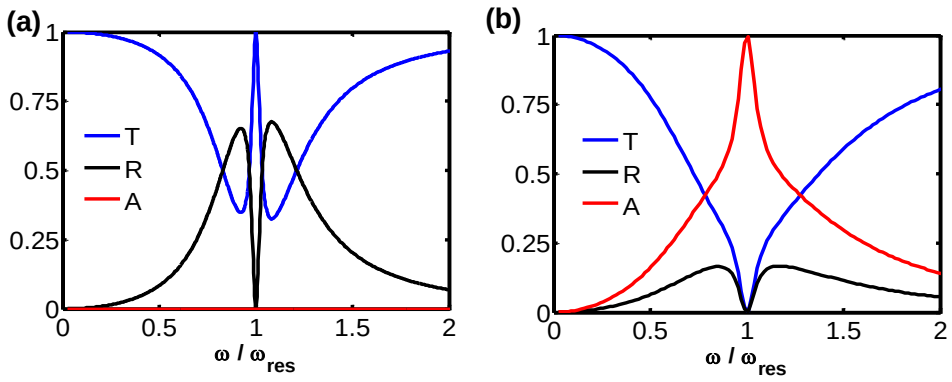

Figure 2.3.6: (a) The transmission, reflection, and absorption as a function of normalized frequency for the lossless nanoantennas, i.e. $\gamma_{\rm ee} = 0$ and $\gamma_{\rm mm} = 0$. (b) The same plot as (a) for the complete absorption case that requires, i.e. $\gamma_{\rm ee} = \frac{\alpha_{0\rm ee}}{2\Lambda^2 c_0}$ and $\gamma_{\rm mm} = \frac{\alpha_{0\rm mm}}{2\Lambda^2 c_0}$. We assumed that the $\Lambda = \lambda_{\rm res}/5$ and $\alpha_{0\rm ee} = 8\alpha_{0\rm mm} = \Lambda \times c_0^2$.

Now, in to order to understand the complete absorption for an array of electric and magnetic dipole moments in details, let us assume that the dispersive characteristics of the effective polarizabilities of the nanoantenna can be described by a Lorentzian line-shape that read as [33]

$$\frac{1}{\alpha_{\rm mm}} = \frac{\omega_{0\rm mm}^2 - \omega^2 - i\omega\gamma_{\rm mm}}{\alpha_{0\rm mm}} - i\frac{k^3}{6\pi}, \tag{2.3.42}$$

$$\frac{1}{\alpha_{\rm ee}} = \frac{\omega_{0\rm ee}^2 - \omega^2 - i\omega\gamma_{\rm ee}}{\alpha_{0\rm ee}} - i\frac{k^3}{6\pi}, \tag{2.3.43}$$

where $\omega_{0\rm ee}$ and $\omega_{0\rm mm}$ are the electric and magnetic resonance frequencies. $\gamma_{0\rm ee}$ and $\gamma_{0\rm mm}$ are the Ohmic losses and $\alpha_{0\rm ee}$ and $\alpha_{0\rm mm}$ are the corresponding oscillator amplitudes. By using Eq. 2.3.20 and the inter-particle interaction constant, i.e. $\beta_{\rm ee} = \beta_{\rm mm} = \Re\left(\beta_{\rm ee}\right) - i\frac{k^3}{6\pi} + i\frac{k}{2\Lambda^2}$ one can calculate the reflection coefficient

$$\begin{aligned} r &= \frac{ik}{2\Lambda^2}\left(\frac{1}{\frac{1}{\alpha_{\rm ee}} - \beta_{\rm ee}} - \frac{1}{\frac{1}{\alpha_{\rm mm}} - \beta_{\rm mm}}\right) \\ &= \frac{ik}{2\Lambda^2}\left(\frac{\alpha_{0\rm ee}}{\omega_{0\rm ee}'^2 - \omega^2 - i\omega\left(\gamma_{\rm ee} + \frac{\alpha_{0\rm ee}}{2\Lambda^2 c_0}\right)} - \frac{\alpha_{0\rm mm}}{\omega_{0\rm mm}'^2 - \omega^2 - i\omega\left(\gamma_{\rm mm} + \frac{\alpha_{0\rm mm}}{2\Lambda^2 c_0}\right)}\right) \\ &= \frac{ik}{2\Lambda^2}\left(\alpha_{\rm ee}^{\rm eff} - \alpha_{\rm mm}^{\rm eff}\right), \end{aligned}$$

where $\omega_{0\rm mm}' = \omega_{0\rm mm} - \Re\left(\beta_{\rm mm}\right)\alpha_{0\rm mm}$ and $\omega_{0\rm ee}' = \omega_{0\rm ee} - \Re\left(\beta_{\rm ee}\right)\alpha_{0\rm ee}$ are the reso-

nance frequency of the electric and magnetic dipoles in the array. The transmission coefficient will be

$$t = 1+\frac{ik}{2\Lambda^2}\left(\frac{1}{\frac{1}{\alpha_{\rm ee}}-\beta_{\rm ee}}+\frac{1}{\frac{1}{\alpha_{\rm mm}}-\beta_{\rm mm}}\right)=1+\frac{ik}{2\Lambda^2}\left(\alpha_{\rm ee}^{\rm eff}+\alpha_{\rm mm}^{\rm eff}\right).$$

Therefore, complete light absorption occurs if the following conditions are satisfied:

$$\begin{aligned}\alpha_{0\rm ee}\gamma_{\rm mm} &= \alpha_{0\rm mm}\gamma_{\rm ee},\\ \omega_{\rm res} &= \frac{\omega_{0\rm mm}'^2\alpha_{0\rm ee}-\omega_{0\rm ee}'^2\alpha_{0\rm mm}}{\alpha_{0\rm ee}-\alpha_{0\rm mm}},\\ \frac{\alpha_{0\rm ee}}{\omega_{0\rm ee}'^2-\omega_{\rm res}^2-i\omega_{\rm res}\left(\gamma_{\rm ee}+\frac{\alpha_{0\rm ee}}{2\Lambda^2c_0}\right)} &= \frac{i\Lambda^2}{k}.\end{aligned}$$

Here, we study in detail two cases, namely a lossless scenario that of maximum absorption (known as critical coupling). We assume that $\omega_{0\rm ee}^{'}=\omega_{0\rm mm}^{'}=\omega_{\rm res}$. Let us start with the lossless case. Figure 2.3.6 (a) shows the transmission, reflection, and absorption as a function of normalized frequency when the nanoantenna is lossless, i.e. $\gamma_{\rm ee}=\gamma_{\rm mm}=0$. In this case, the transmission is similar to possesses features known in the context of electromagnetically induced transparency (EIT) [55]. The array shows zero absorption and the reflection vanishes at the resonance frequency.

In the case of complete absorption, the Ohmic loss for the electric and magnetic dipoles are $\gamma_{\rm ee}=\frac{\alpha_{0\rm ee}}{2\Lambda^2c_0}$, $\gamma_{\rm mm}=\frac{\alpha_{0\rm mm}}{2\Lambda^2c_0}$, respectively. Figure 2.3.6 (b) depicts the spectral dependency of the optical coefficients in such situation. At the resonance frequency, we observe complete absorption. It is interesting to mention that one may achieve the electromagnetically induced absorption (EIA) by proper tuning of the electric and magnetic dipole moments [56, 57]. This can be seen in Fig. 2.3.6 (b). In the next chapter, we will investigate an actual example for an array of nanoantennas made from nonidentical coupled nanopatches, which exhibit balanced electric and magnetic dipole moments.

2.4 Complete light absorption: Physical mechanisms

As shown in the previous sections, *an array of electric or magnetic dipole moments* can only absorb 50 percent of the impinging light [Fig. 2.3.7 (a) and (b)]. One of

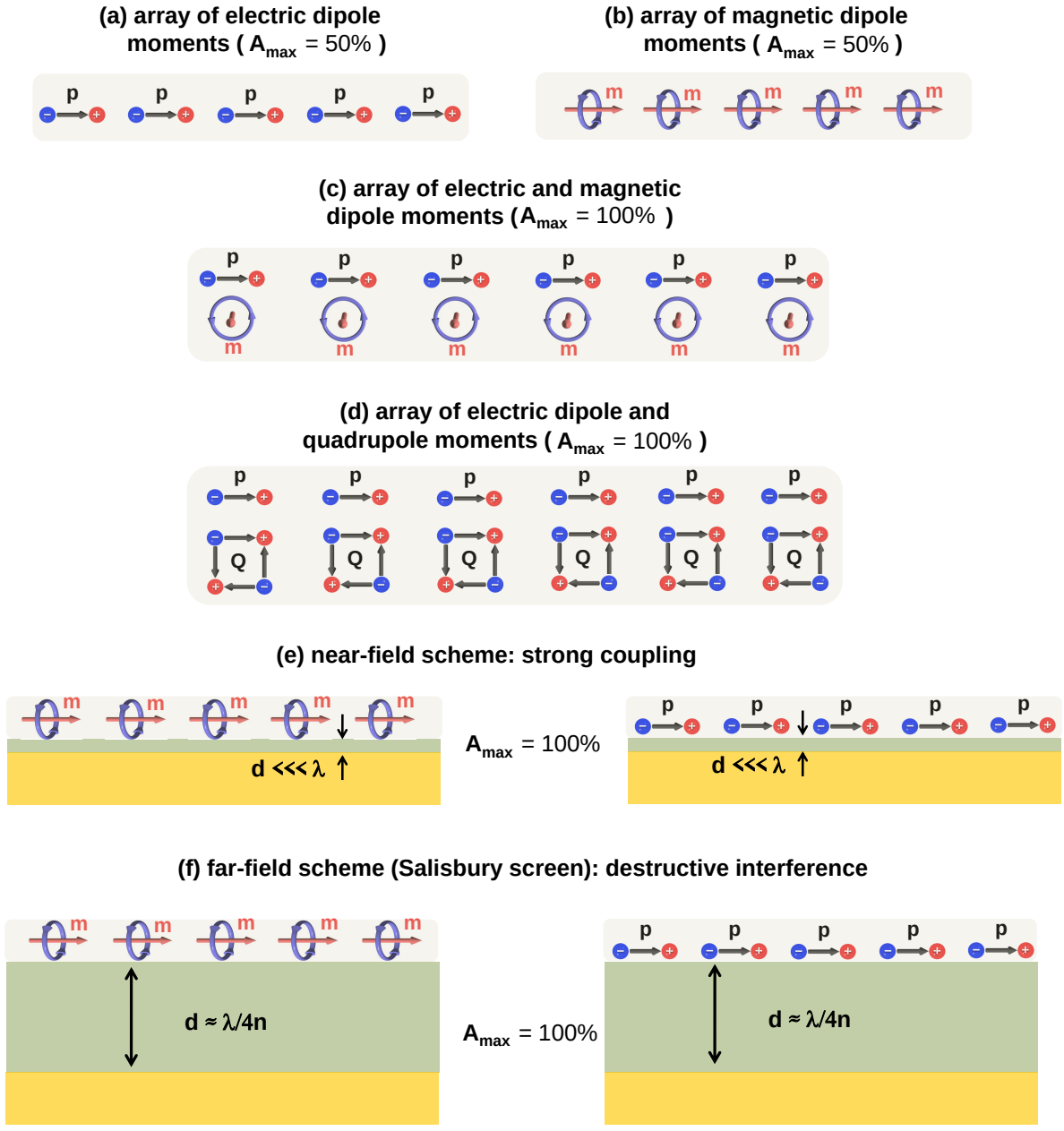

Figure 2.3.7: Schematic view of different approaches to enhance the absorption. (a) and (b) Array of electric/magnetic dipole moments. (c) Array of electric and magnetic dipole moments. (d) Array of electric dipole and electric quadrupole moments. (e) and (f) Array of electric/magnetic dipole moments on top of a metallic ground plate separated by a dielectric spacer with a near-field coupling and far-field interference schemes, respectively.

the questions that we aim to properly address in this thesis is *how to increase the absorption of an array of plasmonic nanoantennas beyond the limits imposed when considering nanoantennas that sustain only an electric or a magnetic dipole moment?* In this section, we briefly review some of the fundamental approaches that can be used for this purpose [Fig. 2.3.7]. They can be summarized as follows:

- Using an *array of electric and magnetic dipole moments*: As shown in previous sections, an array of electric and magnetic dipole moments can fully absorb the impinging light [Fig. 2.3.7 (c)]. We will discuss it in details in Chapter 3. In particular, we will show that an array of nonidentical coupled nanopatches can act as a perfect absorber.

- Using an *array of electric or magnetic dipole moments on top of a metallic ground plate*: Complete light absorption can be achieved by using two different schemes, namely near-field scheme or far-field interference scheme [Fig. 2.3.7 (e) and (f)]. This will be discussed in Chapter 4.

- Using an *array of electric dipole and electric quadrupole moments*: Complete light absorption can be achieved if the amplitude and phase of both moments are properly balanced [Fig. 2.3.7 (d)]. We will discuss that in Chapter 5.

3 Bianisotropic nanoantennas

3.1 Introduction

In the previous chapter, we introduced an analytical tool to quantify the scattering response of a single nanoantenna based on the multipole expansion of its scattered field. We also derived some universal limitations for nanoantennas, which exhibit only an electric or a magnetic dipole moment. We showed that an array composed of such nanoantennas can absorb at most 50 percent of impinging light. We also analytically showed that for an array of nanoantennas, which support both electric and magnetic dipole moments, it would be possible to achieve a complete light absorption. In this chapter, we study in detail an experimentally feasible metasurface that entirely absorbs the incident illumination and which relies on nanoantennas that sustain both an electric and a magnetic dipole moment.

In the first part of this chapter, we explore the optical properties of three different plasmonic nanoantennas made of nanopatches, i.e. a single nanopatch, coupled identical nanopatches, and coupled nonidentical nanopatches [Fig. 3.1.1]. We start the analysis by considering the simplest plasmonic nanoantenna, i.e. a single nanopatch. We show that such a nanoantenna exhibits only an electric dipole response. This response occurs because of the excitation of the localized surface plasmon polariton [Fig. 3.1.1 (a)]. The forward and backward scattering response of such nanoantenna are identical. Afterwards, we investigate a nanoantenna made of two identical coupled nanopatches, which possesses a magnetic response beside the electric one [Fig. 3.1.1 (b)]. This magnetic response is linked to the antisymmetric mode in the coupled system. Its existence can be explained by hybridization theory [58,59]. The additional excitation of this magnetic response provides more degrees of freedom to control the optical response of the nanoantenna. The radiation pattern of such a nanoantenna can be tuned from a dipole-like to a more directive one by varying the dielectric spacer between the two nanopatchs [Fig. 3.1.1 (b) and (d)]. This directive radiation pattern is occurs because of to an interference between the radiated far-fields of the induced electric and magnetic dipole moments. However, it offers an identical optical response, when illuminated from forward and backward directions. In particular, we show that the absorption/scattering cross section of such a nanoan-

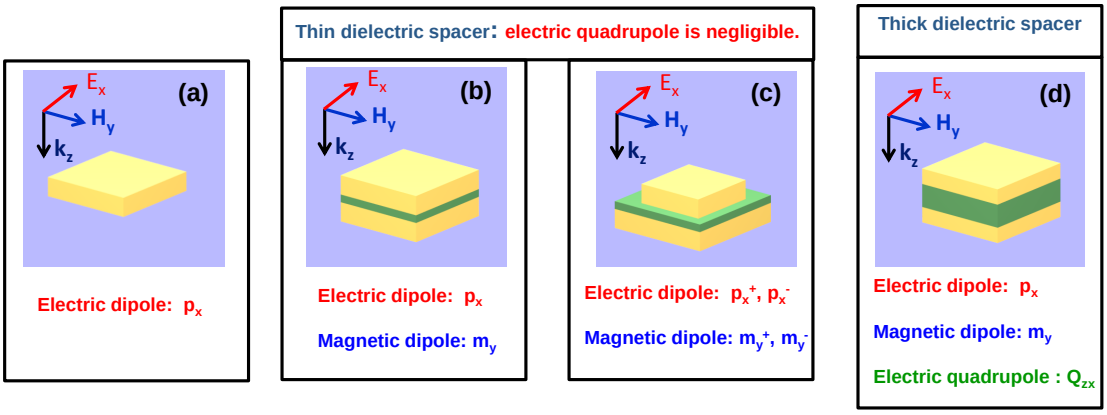

Figure 3.1.1: Schematic view of the investigated plasmonic nanoantennas in this chapter and the corresponding induced moments, when illuminated by an x-polarized plane wave (E_x, H_y). (a) Single nanopatch, (b) identical coupled nanopatches with a thin dielectric spacer, (c) nonidentical coupled nanopatches with a thin dielectric spacer, and (d) identical coupled nanopatches with a thick dielectric spacer.

tenna is independent of the illumination directions. Next, we study a nanoantenna made of two coupled nanopatches with different lateral dimentions [Fig. 3.1.1 (c)]. We will show that such a nanoantenna exhibits a resonant *magneto-electric (bianisotropic) coupling*, in addition to the resonant electric and magnetic coupling. Bianisotropic coupling occurs whenever an electric or a magnetic response is induced by the local magnetic/electric field. This causes different induced electric and magnetic dipole moments when the nanoantenna is illuminated by a plane wave from opposite directions [Fig. 3.1.2 (a)-(b)]. This asymmetric nanoantenna possesses an optical response similar to the omega-particle at microwave frequencies (or in the microwave regime) [27, 60]. However, it has the unique advantage that frequency and strength of its magneto-electric resonance can be tuned with respect to the corresponding values of the electric resonance. We show that the proposed bianisotropic nanoantenna possesses a directive radiation pattern with a vanishing scattering into the backward direction. The bianisotropic coupling also provides an additional remarkable feature in the optical response of an array of such nanoantennas. In particular, it enables an asymmetric reflection and transmission, i.e. the optical properties explicitly and strongly depend on the illumination direction. Finally, we introduce a novel nanoantenna with tunable radiation pattern. This is done by considering a phase change material (PCM) as a dielectric spacer of the nonidentical nanoantenna. We show that the pattern of such nanoantenna can be tuned by an external laser pulse, which changes the state of the PCM from an amorphous to a crystalline state. This causes an strong change in the permittivity of the PCM and allows to tune the radiation

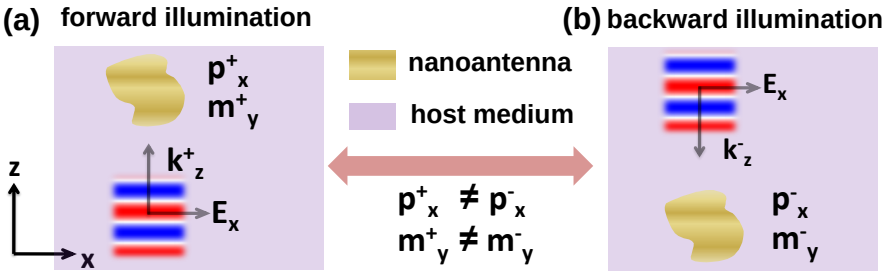

Figure 3.1.2: Schematic view in the x-z-plane of a bianisotropic nanoantenna illuminated from forward (a) and backward directions (b), respectively. The induced dipole moments in forward (p_x^+, m_y^+) and backward (p_x^-, m_y^-) directions are different, i.e. $p_x^+ \neq p_x^-, m_y^+ \neq m_y^-$.

pattern of the nanoantenna; i.e. from a purely dipole-like to a directive one.

In the second part of the present chapter, we investigate the optical properties of a lossless high-index dielectric nanoantenna, i.e. silicon nanodisk. This nanoantenna possesses an electric and magnetic dipole response. This permits to achieve interesting optical features such as a directive radiation pattern; known as the first Kerker condition [20,26,61]. More sophisticated features such as super-scattering and super-directivity can be achieved by using higher order multipole moments [28,37,39]. However, they are more complicated from a theoretical point of view. Therefore, we propose a novel high-index dielectric nanoantenna with bianisotropic coupling which offers an additional degree of freedom. This offers more control on the scattering features in the *dipolar approximation*. This is done by introducing a cylindrical air hole in a high index dielectric cylinder. The bianisotropic coupling can be tuned by varying the geometrical parameters of the cylindrical air hole. This allows to have a dielectric nanoantenna with different backscattering or radiation patterns when illuminated from forward or backward directions. Finally, we show that a proper geometrical tuning of such a nanoantenna is capable of providing a 2π phase change in the reflection spectrum with a rather large amplitude. This renders such nanoantennas to be interesting ingredients for potential reflectarrays.

We note that most of the findings of this chapter have been previously published in Ref. [47, 62, 63].

3.2 Bianisotropic nanoantennas: Theory

In this section, we present a simple approach to retrieve all the relevant polarizability components of an arbitrary bianisotropic nanoantenna [47, 64–68]. They link the induced dipole moments to the local external electric and magnetic field. We

analytically deduce the scattering, absorption, and extinction cross sections of a bianisotropic nanoantenna in dipole approximation. This suggests that the nanoantenna only supports electric and magnetic dipole moments and all the higher-order moments are negligible. We assume that the electric/magnetic moment is induced by incident electric and magnetic fields of the plane wave. The relation between the induced electric dipole moment vector $\mathbf{p} = (p_\mathrm{x}, p_\mathrm{y}, p_\mathrm{z})^T$, magnetic dipole moment vector $\mathbf{m} = (m_\mathrm{x}, m_\mathrm{y}, m_\mathrm{z})^T$and the incident field $\mathbf{E}^\mathrm{inc} = \left(E_\mathrm{x}^\mathrm{inc}, E_\mathrm{y}^\mathrm{inc}, E_\mathrm{z}^\mathrm{inc}\right)^T$, $\mathbf{H}^\mathrm{inc} = \left(H_\mathrm{x}^\mathrm{inc}, H_\mathrm{y}^\mathrm{inc}, H_\mathrm{z}^\mathrm{inc}\right)^T$read as

$$\begin{pmatrix} \frac{\mathbf{p}}{\epsilon_0} \\ Z\mathbf{m} \end{pmatrix} = \overline{\overline{\alpha}} \begin{pmatrix} \mathbf{E}^\mathrm{inc} \\ Z\mathbf{H}^\mathrm{inc} \end{pmatrix}. \tag{3.2.1}$$

$\overline{\overline{\alpha}}$ is the polarizability tensor and defined as:

$$\overline{\overline{\alpha}} = \begin{pmatrix} \overline{\overline{\alpha}}^\mathrm{ee} & \overline{\overline{\alpha}}^\mathrm{em} \\ \overline{\overline{\alpha}}^\mathrm{me} & \overline{\overline{\alpha}}^\mathrm{mm} \end{pmatrix}. \tag{3.2.2}$$

Here $\overline{\overline{\alpha}}^\mathrm{ee}$/$\overline{\overline{\alpha}}^\mathrm{mm}$ and $\overline{\overline{\alpha}}^\mathrm{em}$/$\overline{\overline{\alpha}}^\mathrm{me}$ are the electric/magnetic and electro-magnetic/magneto-electric polarizability dyadic of individual nanoantennas, respectively. Equation 3.2.1 in matrix form can be denoted as

$$\begin{pmatrix} \frac{p_\mathrm{x}}{\epsilon_0} \\ \frac{p_\mathrm{y}}{\epsilon_0} \\ \frac{p_\mathrm{z}}{\epsilon_0} \\ Zm_\mathrm{x} \\ Zm_\mathrm{y} \\ Zm_\mathrm{z} \end{pmatrix} = \begin{pmatrix} \alpha_\mathrm{xx}^\mathrm{ee} & \alpha_\mathrm{xy}^\mathrm{ee} & \alpha_\mathrm{xz}^\mathrm{ee} & \alpha_\mathrm{xx}^\mathrm{em} & \alpha_\mathrm{xy}^\mathrm{em} & \alpha_\mathrm{xz}^\mathrm{em} \\ \alpha_\mathrm{yx}^\mathrm{ee} & \alpha_\mathrm{yy}^\mathrm{ee} & \alpha_\mathrm{yz}^\mathrm{ee} & \alpha_\mathrm{yx}^\mathrm{em} & \alpha_\mathrm{yy}^\mathrm{em} & \alpha_\mathrm{yz}^\mathrm{em} \\ \alpha_\mathrm{zx}^\mathrm{ee} & \alpha_\mathrm{zy}^\mathrm{ee} & \alpha_\mathrm{zz}^\mathrm{ee} & \alpha_\mathrm{zx}^\mathrm{em} & \alpha_\mathrm{zy}^\mathrm{em} & \alpha_\mathrm{zz}^\mathrm{em} \\ \alpha_\mathrm{xx}^\mathrm{me} & \alpha_\mathrm{xy}^\mathrm{me} & \alpha_\mathrm{xz}^\mathrm{me} & \alpha_\mathrm{xx}^\mathrm{mm} & \alpha_\mathrm{xy}^\mathrm{mm} & \alpha_\mathrm{xz}^\mathrm{mm} \\ \alpha_\mathrm{yx}^\mathrm{me} & \alpha_\mathrm{yy}^\mathrm{me} & \alpha_\mathrm{yz}^\mathrm{me} & \alpha_\mathrm{yx}^\mathrm{mm} & \alpha_\mathrm{yy}^\mathrm{mm} & \alpha_\mathrm{yz}^\mathrm{mm} \\ \alpha_\mathrm{zx}^\mathrm{me} & \alpha_\mathrm{zy}^\mathrm{me} & \alpha_\mathrm{zz}^\mathrm{me} & \alpha_\mathrm{zx}^\mathrm{mm} & \alpha_\mathrm{zy}^\mathrm{mm} & \alpha_\mathrm{zz}^\mathrm{mm} \end{pmatrix} \begin{pmatrix} E_\mathrm{x}^\mathrm{inc} \\ E_\mathrm{y}^\mathrm{inc} \\ E_\mathrm{z}^\mathrm{inc} \\ ZH_\mathrm{x}^\mathrm{inc} \\ ZH_\mathrm{y}^\mathrm{inc} \\ ZH_\mathrm{z}^\mathrm{inc} \end{pmatrix}, \tag{3.2.3}$$

According to Eq. 3.2.3, the polarizability tensor has 36 components. In order to retrieve all the components, it is necessary to use six different illuminations (three pairs of numerical calculation with mutually perpendicular plane wave illuminations). This is illustrated exemplary in Fig. 3.2.1(a), where an arbitrary nanoantenna is illuminated by an x-polarized plane wave at normal incident for both illumination directions ($\pm$). $E_\mathrm{x}^\mathrm{inc}$ and $H_\mathrm{y}^\mathrm{inc} = E_\mathrm{x}^\mathrm{inc}/Z$ are the electric and magnetic field amplitudes, respectively. The corresponding electric and magnetic dipole moments for both illumination directions are given by:

$$\begin{aligned}
\frac{p_{\mathrm{x}}^{\pm}}{\epsilon_0} &= \alpha_{\mathrm{xx}}^{\mathrm{ee}} E_{\mathrm{x}}^{\mathrm{inc}} \pm \alpha_{\mathrm{xy}}^{\mathrm{em}} Z H_{\mathrm{y}}^{\mathrm{inc}}, \\
\frac{p_{\mathrm{y}}^{\pm}}{\epsilon_0} &= \alpha_{\mathrm{yx}}^{\mathrm{ee}} E_{\mathrm{x}}^{\mathrm{inc}} \pm \alpha_{\mathrm{yy}}^{\mathrm{em}} Z H_{\mathrm{y}}^{\mathrm{inc}}, \\
\frac{p_{\mathrm{z}}^{\pm}}{\epsilon_0} &= \alpha_{\mathrm{zx}}^{\mathrm{ee}} E_{\mathrm{x}}^{\mathrm{inc}} \pm \alpha_{\mathrm{zy}}^{\mathrm{em}} Z H_{\mathrm{y}}^{\mathrm{inc}},
\end{aligned} \tag{3.2.4}$$

$$\begin{aligned}
Z m_{\mathrm{x}}^{\pm} &= \alpha_{\mathrm{xx}}^{\mathrm{me}} E_{\mathrm{x}}^{\mathrm{inc}} \pm \alpha_{\mathrm{xy}}^{\mathrm{mm}} Z H_{\mathrm{y}}^{\mathrm{inc}}, \\
Z m_{\mathrm{y}}^{\pm} &= \alpha_{\mathrm{yx}}^{\mathrm{me}} E_{\mathrm{x}}^{\mathrm{inc}} \pm \alpha_{\mathrm{yy}}^{\mathrm{mm}} Z H_{\mathrm{y}}^{\mathrm{inc}}, \\
Z m_{\mathrm{z}}^{\pm} &= \alpha_{\mathrm{zx}}^{\mathrm{me}} E_{\mathrm{x}}^{\mathrm{inc}} \pm \alpha_{\mathrm{zy}}^{\mathrm{mm}} Z H_{\mathrm{y}}^{\mathrm{inc}}.
\end{aligned} \tag{3.2.5}$$

Now, by adding and subtracting Eqs. 3.2.4 and 3.2.5, we can obtain the following equations for twelve components of the polarizability matrix:

$$\begin{aligned}
\alpha_{\mathrm{xx}}^{\mathrm{ee}} = \frac{p_{\mathrm{x}}^{+} + p_{\mathrm{x}}^{-}}{2\epsilon_0 E_{\mathrm{x}}^{\mathrm{inc}}} \quad , \quad \alpha_{\mathrm{xy}}^{\mathrm{em}} = \frac{p_{\mathrm{x}}^{+} - p_{\mathrm{x}}^{-}}{2\epsilon_0 E_{\mathrm{x}}^{\mathrm{inc}}}, \\
\alpha_{\mathrm{yx}}^{\mathrm{ee}} = \frac{p_{\mathrm{y}}^{+} + p_{\mathrm{y}}^{-}}{2\epsilon_0 E_{\mathrm{x}}^{\mathrm{inc}}} \quad , \quad \alpha_{\mathrm{yy}}^{\mathrm{em}} = \frac{p_{\mathrm{y}}^{+} - p_{\mathrm{y}}^{-}}{2\epsilon_0 E_{\mathrm{x}}^{\mathrm{inc}}}, \\
\alpha_{\mathrm{zx}}^{\mathrm{ee}} = \frac{p_{\mathrm{z}}^{+} + p_{\mathrm{z}}^{-}}{2\epsilon_0 E_{\mathrm{x}}^{\mathrm{inc}}} \quad , \quad \alpha_{\mathrm{zy}}^{\mathrm{em}} = \frac{p_{\mathrm{z}}^{+} - p_{\mathrm{z}}^{-}}{2\epsilon_0 E_{\mathrm{x}}^{\mathrm{inc}}}, \\
\alpha_{\mathrm{xx}}^{\mathrm{me}} = \frac{m_{\mathrm{x}}^{+} + m_{\mathrm{x}}^{-}}{2H_{\mathrm{y}}^{\mathrm{inc}}} \quad , \quad \alpha_{\mathrm{xy}}^{\mathrm{mm}} = \frac{m_{\mathrm{x}}^{+} - m_{\mathrm{x}}^{-}}{2H_{\mathrm{y}}^{\mathrm{inc}}}, \\
\alpha_{\mathrm{yx}}^{\mathrm{me}} = \frac{m_{\mathrm{y}}^{+} + m_{\mathrm{y}}^{-}}{2H_{\mathrm{y}}^{\mathrm{inc}}} \quad , \quad \alpha_{\mathrm{yy}}^{\mathrm{mm}} = \frac{m_{\mathrm{y}}^{+} - m_{\mathrm{y}}^{-}}{2H_{\mathrm{y}}^{\mathrm{inc}}}, \\
\alpha_{\mathrm{zx}}^{\mathrm{me}} = \frac{m_{\mathrm{z}}^{+} + m_{\mathrm{z}}^{-}}{2H_{\mathrm{y}}^{\mathrm{inc}}} \quad , \quad \alpha_{\mathrm{zy}}^{\mathrm{mm}} = \frac{m_{\mathrm{z}}^{+} - m_{\mathrm{z}}^{-}}{2H_{\mathrm{y}}^{\mathrm{inc}}}.
\end{aligned} \tag{3.2.6}$$

In the numerical calculation, we assume that the plane wave has $E_{\mathrm{x}}^{\mathrm{inc}} = 1\,\frac{V}{m}$ and $H_{\mathrm{y}}^{\mathrm{inc}} = E_{\mathrm{x}}^{\mathrm{inc}}/Z$. Finally By applying the aforementioned procedure for two remaining pairs of illuminations, i.e. for plane waves propagating in $\pm$x and $\pm$y illumination directions [Fig. 3.2.1 (b) and (c) respectively], we can obtain all components of the polarizability tensor.

Having all the polarizabilities components of an arbitrary bianisotropic nanoantenna, we can calculate its scattering, extinction, and absorption cross sections. Let us start with the definition of scattered power

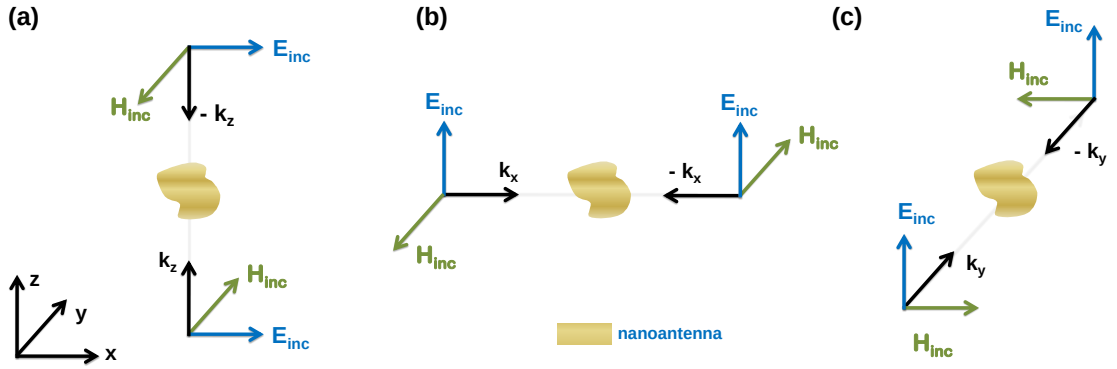

Figure 3.2.1: Sketches of plane waves for three pairs of illuminations to retrieve all the components of the polarizability tensor, where k_x, k_y, and k_z are the propagation constants along the x, y, and z axis, respectively.

$$
\begin{aligned}
P_{\text{sca}} &= \frac{1}{2}\text{Re}\oiint_S \left(\mathbf{E}_{\text{sca}} \times \mathbf{H}^*_{\text{sca}}\right)\cdot \mathbf{n}\text{d}s, \\
&= \frac{c^2 Z k^4}{12\pi}\left(|\mathbf{p}|^2 + \left|\frac{\mathbf{m}}{c}\right|^2\right) = \frac{c^2 Z k^4}{12\pi}\begin{pmatrix}\mathbf{p}\\ \frac{\mathbf{m}}{c}\end{pmatrix}^{\dagger}\cdot\begin{pmatrix}\mathbf{p}\\ \frac{\mathbf{m}}{c}\end{pmatrix}, \\
&= \frac{k^4}{12\pi Z}\begin{pmatrix}\mathbf{E}_{\text{inc}}\\ Z\mathbf{H}_{\text{inc}}\end{pmatrix}^{\dagger}\cdot\begin{pmatrix}\overline{\overline{\alpha}}_{\text{ee}} & \overline{\overline{\alpha}}_{\text{em}}\\ \overline{\overline{\alpha}}_{\text{me}} & \overline{\overline{\alpha}}_{\text{mm}}\end{pmatrix}^{\dagger}\cdot \qquad (3.2.7)\\
&\quad \begin{pmatrix}\overline{\overline{\alpha}}_{\text{ee}} & \overline{\overline{\alpha}}_{\text{em}}\\ \overline{\overline{\alpha}}_{\text{me}} & \overline{\overline{\alpha}}_{\text{mm}}\end{pmatrix}\cdot\begin{pmatrix}\mathbf{E}_{\text{inc}}\\ Z\mathbf{H}_{\text{inc}}\end{pmatrix}, \qquad (3.2.8)
\end{aligned}
$$

where the dagger symbol (i.e. †) denotes the Hermitian (conjugate transpose). On the other hand, the extinction cross section can be calculated from

$$
\begin{aligned}
P_{\text{ext}} &= -\frac{1}{2}\text{Re}\oiint_S \left(\mathbf{E}_{\text{inc}} \times \mathbf{H}_{\text{sca}}{}^* + \mathbf{E}_{\text{sca}} \times \mathbf{H}^*_{\text{inc}}\right)\cdot \mathbf{n}\text{d}s, \\
&= -\frac{\omega}{2}\text{Im}\left\{\mathbf{p}^*\cdot\mathbf{E}_{\text{inc}} + \mu_0\mathbf{m}^*\cdot\mathbf{H}^*_{\text{inc}}\right\}, \qquad (3.2.9)\\
&= -\frac{\omega}{2}\text{Im}\left\{\begin{pmatrix}\mathbf{p}\\ \frac{\mathbf{m}}{c}\end{pmatrix}^{\dagger}\cdot\begin{pmatrix}\mathbf{E}_{\text{inc}}\\ Z\mathbf{H}_{\text{inc}}\end{pmatrix}\right\}, \qquad (3.2.10)\\
&= -\frac{\omega}{2}\epsilon_0\text{Im}\left\{\begin{pmatrix}\mathbf{E}_{\text{inc}}\\ Z\mathbf{H}_{\text{inc}}\end{pmatrix}^{\dagger}\cdot\begin{pmatrix}\overline{\overline{\alpha}}_{\text{ee}} & \overline{\overline{\alpha}}_{\text{em}}\\ \overline{\overline{\alpha}}_{\text{me}} & \overline{\overline{\alpha}}_{\text{mm}}\end{pmatrix}^{\dagger}\cdot\begin{pmatrix}\mathbf{E}_{\text{inc}}\\ Z\mathbf{H}_{\text{inc}}\end{pmatrix}\right\}.
\end{aligned}
$$

Note that, in this thesis, we are only interested in the bianisotropic nanoantenna that preserve the polarization and do not produce the cross-polarized dipole moments,

known as omega-type bianisotropic [60]. Therefore, for an x-polarized plane wave (i.e. $E_{\mathrm{x}}^{\mathrm{inc}}$) illumination the induce dipole moments are given by

$$\begin{pmatrix} \frac{p_{\mathrm{x}}}{\epsilon_0} \\ Zm_{\mathrm{y}} \end{pmatrix} = \begin{pmatrix} \alpha_{\mathrm{xx}}^{\mathrm{ee}} & \alpha_{\mathrm{xy}}^{\mathrm{ey}} \\ \alpha_{\mathrm{yx}}^{\mathrm{me}} & \alpha_{\mathrm{yy}}^{\mathrm{mm}} \end{pmatrix} \begin{pmatrix} E_{\mathrm{x}}^{\mathrm{inc}} \\ ZH_{\mathrm{y}}^{\mathrm{inc}} \end{pmatrix}. \tag{3.2.11}$$

All the other dipole moments should be zero, i.e. $p_{\mathrm{y}} = p_{\mathrm{z}} = 0$ and $m_{\mathrm{x}} = m_{\mathrm{z}} = 0$. By using Eq. 3.2.7 and the time averaged Poynting-vector for the illuminating plane wave (intensity) $I_0 = \frac{|\mathbf{E}_{\mathrm{inc}}|^2}{2Z}$, the scattering cross section can be expressed as

$$C_{\mathrm{sca}}^{\pm} = \frac{k^4}{6\pi} \left(\left| \alpha_{\mathrm{xx}}^{\mathrm{ee}} \pm \alpha_{\mathrm{xy}}^{\mathrm{em}} \right|^2 + \left| \alpha_{\mathrm{yx}}^{\mathrm{me}} \pm \alpha_{\mathrm{yy}}^{\mathrm{mm}} \right|^2 \right). \tag{3.2.12}$$

Here, $\pm$ indicate different illumination directions (forward and backward). By using Eq. 3.2.9 and Eq. 3.2.11, the extinction cross section of a bianisotropic nanoantenna for both forward and backward illumination directions is given by

$$C_{\mathrm{ext}}^{\pm} = k \, \mathrm{Im} \left(\alpha_{\mathrm{xx}}^{\mathrm{ee}} \pm \alpha_{\mathrm{xy}}^{\mathrm{em}} \pm \alpha_{\mathrm{yx}}^{\mathrm{me}} + \alpha_{\mathrm{yy}}^{\mathrm{mm}} \right). \tag{3.2.13}$$

It is interesting to mention that for lossless nanoantennas, i.e. $C_{\mathrm{abs}} = 0$, the scattering cross section is identical to the extinction cross section for both illuminations $C_{\mathrm{sca}}^{\pm} = C_{\mathrm{ext}}^{\pm}$. This leads to the following interesting relations between different polarizability components

$$\begin{aligned} \mathrm{Im} \left(\frac{\alpha_{\mathrm{xx}}^{\mathrm{ee}}}{\alpha_{\mathrm{xx}}^{\mathrm{ee}} \alpha_{\mathrm{yy}}^{\mathrm{mm}} - \alpha_{\mathrm{xy}}^{\mathrm{em}} \alpha_{\mathrm{yx}}^{\mathrm{me}}} \right) &= -\frac{k^3}{6\pi}, \\ \mathrm{Im} \left(\frac{\alpha_{\mathrm{yy}}^{\mathrm{mm}}}{\alpha_{\mathrm{xx}}^{\mathrm{ee}} \alpha_{\mathrm{yy}}^{\mathrm{mm}} - \alpha_{\mathrm{xy}}^{\mathrm{em}} \alpha_{\mathrm{yx}}^{\mathrm{me}}} \right) &= -\frac{k^3}{6\pi}, \\ \mathrm{Re} \left(\frac{\alpha_{\mathrm{xy}}^{\mathrm{em}}}{\alpha_{\mathrm{xx}}^{\mathrm{ee}} \alpha_{\mathrm{yy}}^{\mathrm{mm}} - \alpha_{\mathrm{xy}}^{\mathrm{em}} \alpha_{\mathrm{yx}}^{\mathrm{me}}} \right) &= 0. \end{aligned} \tag{3.2.14}$$

These equations are known as the generalized Sipe-Kranendonk [33, 64]. They hold only for lossless nanoantennas. Till now, we discussed the scattering properties of individual nanoantennas. Let us calculate the optical properties of an array of such nanoantennas from the induced polarizabilities. We can start from the relation between the induced electric and magnetic dipole moments in the array and local fields

$$\begin{pmatrix} \frac{p_x}{\epsilon_0} \\ Zm_y \end{pmatrix} = \begin{pmatrix} \alpha_{xx}^{ee} & \alpha_{xy}^{ey} \\ \alpha_{yx}^{me} & \alpha_{yy}^{mm} \end{pmatrix} \begin{pmatrix} E_x^{loc} \\ ZH_y^{loc} \end{pmatrix},$$

where $E_x^{loc}$and H_y^{loc} are the local field. They can be defined as $E_x^{loc} = E_x^{inc} + E_x^{int}$, $H_y^{loc} = H_y^{inc} + H_y^{int}$. Here, $E_x^{int} = \beta^{ee} p_x$ and $H_y^{int} = \beta^{mm} m_y$ are the interaction electric/magnetic field created by all other electric dipoles in the array. By using the generalized boundary condition and the averaged electric and magnetic current density (i.e. Eq. 2.3.11), we can deduce the reflection and transmission coefficients for an array of bianisotropic nanoantennas that is given by

$$r = \frac{ik}{2\Lambda^2 \Delta_t} \left[\alpha_{xx}^{ee} \pm \alpha_{xy}^{em} \mp \alpha_{yx}^{me} - \alpha_{yy}^{mm}\right], \tag{3.2.15}$$

$$t = 1 + \frac{ik}{2\Lambda^2 \Delta_t} \left[\alpha_{xx}^{ee} \pm \alpha_{xy}^{em} \mp \alpha_{yx}^{me} - \alpha_{yy}^{mm} \right. \tag{3.2.16}$$
$$\left. - \left(\alpha_{xx}^{ee} \alpha_{yy}^{mm} - \alpha_{xy}^{em} \alpha_{yx}^{me}\right) \left(\beta^{ee} + \beta^{mm}\right)\right],$$

where $\Delta_t = 1 - \alpha_{xx}^{ee}\beta^{ee} - \alpha_{yy}^{mm}\beta^{mm} - (\alpha_{xy}^{em}\alpha_{yx}^{me} - \alpha_{xx}^{ee}\alpha_{yy}^{mm})\beta^{ee}\beta^{mm}$ [47, 69, 70].

3.3 Plasmonic nanoantennas

In this section, we numerically and analytically investigate the optical properties of three different nanoantennas made of nanopatches. In particular, we show that a single nanopatch possesses only an electric response. The identical coupled nanopatches can provide additionally a magnetic response [50, 71, 72]. This allows to have better control on the optical response of a single nanoantenna as well as an array. To obtain even higher control, we propose a nanoantenna made of two nonidentical coupled nanopatches, which leads to an additional magneto-electric coupling. This coupling, in dipole approximation, provides the most comprehensive control on the reflection and transmission spectra of the array as well as the scattering of the individual nanoantennas [60]. We show that it can offer remarkable optical features such as a directional radiation pattern, asymmetric reflection, and perfect absorption [47].

3.3.1 Single nanopatches

We start with the simplest nanoantenna that has been extensively investigated in the literature [49]. That is a gold nanopatch as shown in Fig. 3.2.2 (a). Note that the discussion in this subsection is independent of the geometry of the nanoantenna and

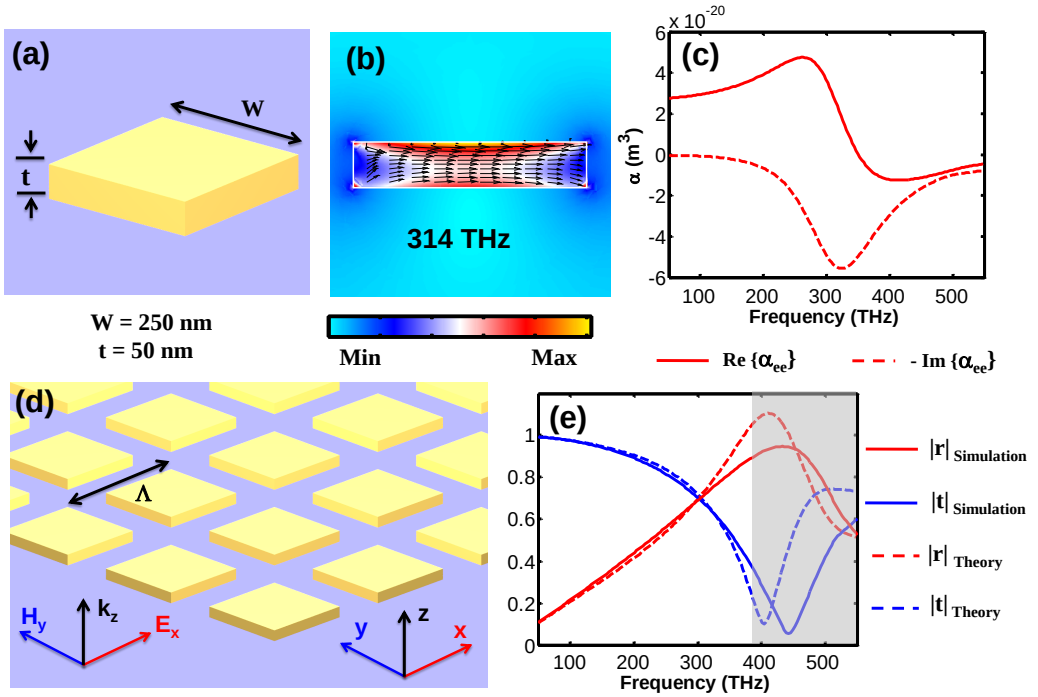

Figure 3.2.2: (a) Schematic of nanopatches antenna. (b) Current distributions at electric resonance frequency. (c) Extracted electric polarizability component of the investigated nanoantenna. (e) Analytical [using Eq. 2.3.20 and 2.3.22] and full wave simulation results for reflection and transmission spectra of the array shown in (d). The period of the array is $\Lambda = 400$ nm, the dielectric spacer has a refractive index of $n = 1.46$. The host medium is air.

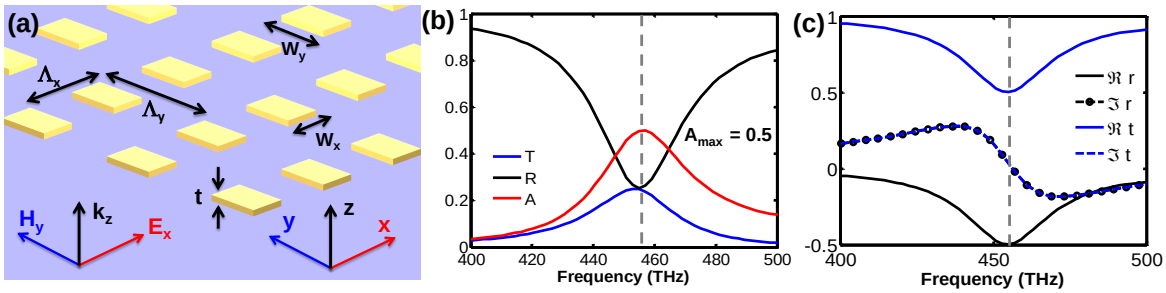

Figure 3.2.3: (a) Schematic view of the rectangular nanopatches designed for maximum absorption, i.e. $A_{\max} = \frac{1}{2}$. (b) The reflection, transmission and absorption spectra. (c) The reflection and transmission coefficients. Note that at resonance, $r|_{\text{res}} = -\frac{1}{2}$ and $t|_{\text{res}} = \frac{1}{2}$. The period in x and y directions are $\Lambda_x = 320$ nm and $\Lambda_y = 500$ nm. The gold nanopatch has a thickness $t = 15$ nm and a width of $W_x = 100$ nm and $W_y = 145$ nm.

holds for different type of nanoantennas such as nanodisks, nanostrips, nanospheres, nanocylinders, and nanorings. We will investigate in details the optical properties of different type of nanoantennas made of nanorings in the last chapter. The electric polarizability α_{xx}^{ee} of the investigated nanoantenna is depicted in Fig. 3.2.2 (c). The gold nanopatch supports an electric resonance in response to an incident electromagnetic field whenever a localized surface plasmon polariton is excited [Fig. 3.2.2 (b)]. Notice that all the other polarizability components of the nanopatch are negligible. As a result, a planar array composed of nanopatches should also provide an electric resonance behavior in response to a plane wave illumination. This is done by using the introduced theoretical model in the previous chapter and full wave simulation [Fig. 3.2.2 (e)]. The electric resonance is the only mechanism which can be used to control the optical response of the array response. In other words, the response can be controlled by changing the patch dimensions, i.e. resonance frequency of the nanopatch and the distance between the nanopatches; i.e. interaction constants β^{ee} [Fig. 3.2.2 (e)]. However, with such simple nanopatches, only very limited control over the level of reflection and transmission spectra can be achieved. Note that, the optical response of the array is identical when illuminated from opposite directions. This is true for an array with only electric/magnetic response without bianisotropy.

It can be seen that the absorption of the array is small at the resonance frequency due to the notably smaller absorption losses when compared to scattering losses [Fig. 3.2.2 (e)]. By proper tuning the geometry of nanopatches, the absorption of the array can be enhanced. As explained in the previous chapter, the maximum absorption is limited to 50 percent. This occurs when the reflection and transmission of the array are $r = -\frac{1}{2}$ and $t = \frac{1}{2}$, respectively [Fig. 3.2.3 (c)]. In order to prove that we also optimized the array such that it can absorb 50 percent of the impinging plane wave [Fig. 3.2.3 (c)]. This is shown in Fig. 3.2.3 (b). The dimensions of the optimized nanopatches are given in the legend of the Fig. 3.2.3. Note that the results [Fig. 3.2.3] are in good agreement with the analytical findings explained in the previous chapter [Fig. 2.3.3].

3.3.2 Coupled identical nanopatches

In the previous subsection, we have shown that a single nanopatch possesses an electric response. In order to have more control over the optical response of nanoantennas, an additional magnetic response is essential. This is feasible by adding an identical, closely spaced nanopatch on top of the first one [Fig. 3.3.1 (a)]. As shown in Fig.3.3.1 (b) and (c), in addition to the previous broad electric resonance a new magnetic mode is also supported by the coupled nanopatches [47, 50, 71, 73, 74]. This oc-

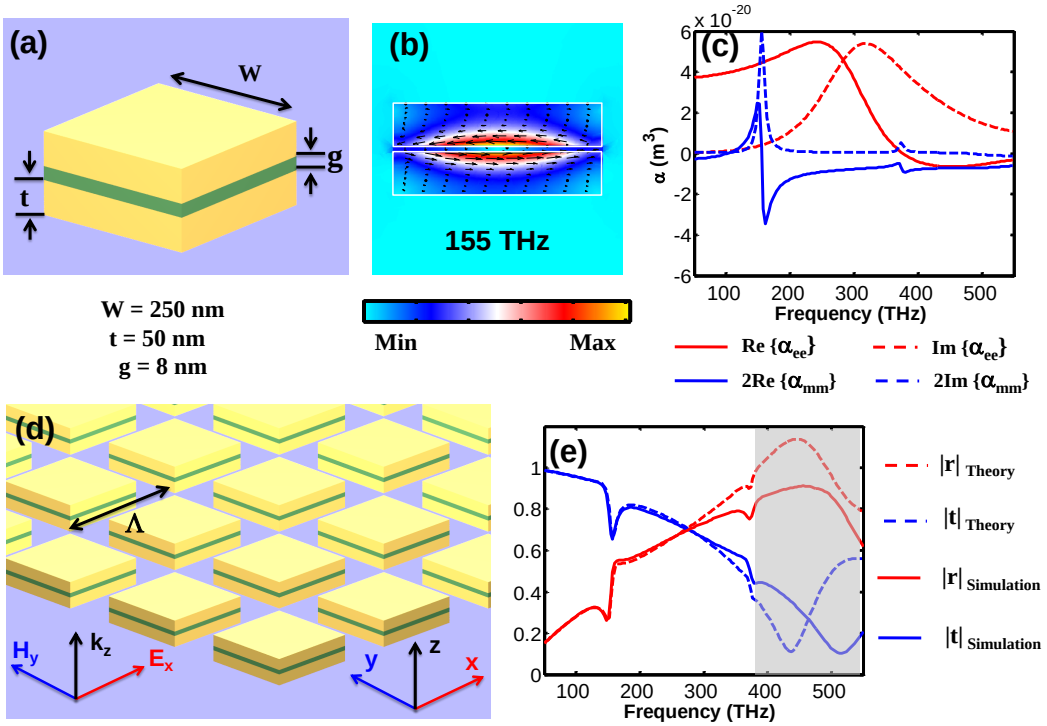

Figure 3.3.1: (a) Schematic of coupled nanopatches. (b) Current distribution at the magnetic resonance frequency. (c) Extracted electric polarizability electric and magnetic polarizability components of the investigated nanoantenna. (e) Analytical [using Eq. 2.3.36 and 2.3.37] and full wave simulation results for reflection and transmission spectra of the array shown in (d). The period of the array is $\Lambda = 400$ nm, the dielectric spacer has a refractive index of $n = 1.46$. Ambient material is air.

curs due to the hybridization of the modes, supported by the individual nanopatches, to form an anti-symmetric (bonding, low energy) and a symmetric (anti-bonding, high energy) mode [50]. The current distribution of the magnetic mode (anti-symmetric mode) is shown in Fig. 3.3.1 (b). The magnetic response can be seen from the nanoantenna polarizabilities shown in Fig. 3.3.1 (c). The electric and magnetic responses (α_{xx}^{ee} and α_{yy}^{mm}) in the coupled nanopatches permit to control the radiation pattern of the nanoantenna. The magneto-electric coupling, i.e. α_{xy}^{em} and α_{xy}^{me}, are still zero due to the fact that the nanoantenna is symmetric will respect to the top and bottom illumination directions.

Similar structures like the investigated coupled nanopatches, such as nanodiscs, are widely used in the literature as one of the simplest building blocks in periodic arrays to obtain a magnetic response [50, 71, 72, 75, 76]. In dipole approximation, both strength and frequency of the magnetic resonance can be tuned by varying the distance between two nanopatches (dielectric spacer). However, the magnetic resonance is always spectrally separated from the electric one. Therefore, although the magni-

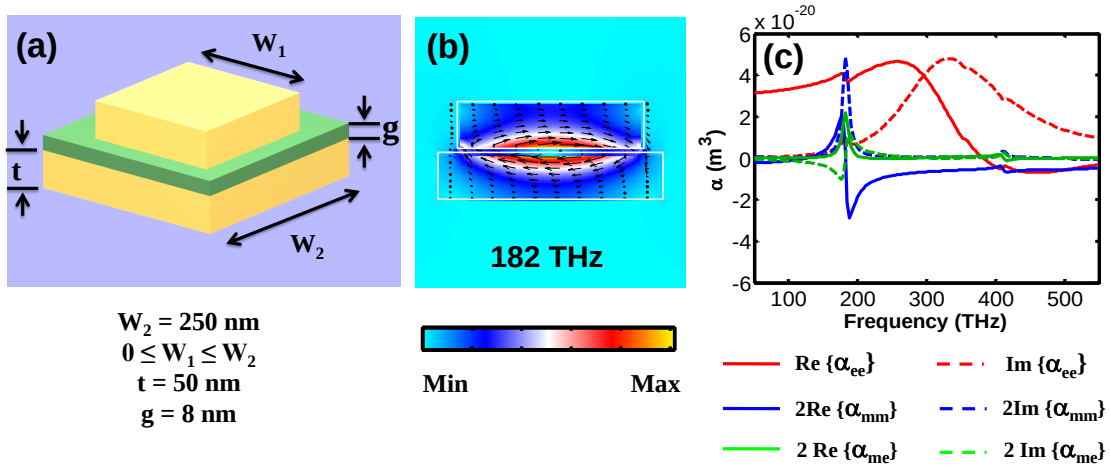

Figure 3.3.2: (a) Schematic of coupled nonidentical nanopatches. (b) Current distributions at the magnetic resonance frequencies. (c) Extracted electric polarizability electric, magnetic and magneto-electric polarizability components of the investigated nanoantenna. The dielectric spacer has a refractive index of $n = 1.46$. Ambient material is air.

tude of the achievable electric polarization at the magnetic resonance is comparable to the magnetic polarization, it is not possible to balance the scattering contribution from the different dipole polarizabilities. The analytical [using Eqs. 2.3.36, and 2.3.37] and full wave simulation results for reflection and transmission are shown in Fig. 3.3.1 (e). There is good agreement between the analytical and full wave simulation results below 400 THz. The grey shadow in Fig. 3.3.1 (e) represent spectral domains where the individual nanoantenna is not optically small and contributions of higher order modes are no longer negligible. Moreover, since the bianisotropy is absent in the present nanoantenna, there is no control of the directional scattering response; i.e. the array behaves identically for forward and backward illumination directions. It might be possible to achieve total absorption if the nanoantenna is in balanced condition (i.e. $p_{\mathrm{x}} = \frac{m_{\mathrm{y}}}{c}$).

3.3.3 Coupled nonidentical nanopatches: Bianisotropic nanoantennas

In this subsection we introduce an experimentally feasible bianisotropic nanoantenna based on coupled nonidentical nanopatches. The geometry of the proposed bianisotropic nanoantenna is shown in Fig. 3.3.2 (a). In order to achieve a notable bianisotropic response, the symmetry of the structure has to be broken. This allows to obtain more control over the optical spectra as well as to achieve a directional dependent response. To achieve such a notable bianisotropy, we consider is the same

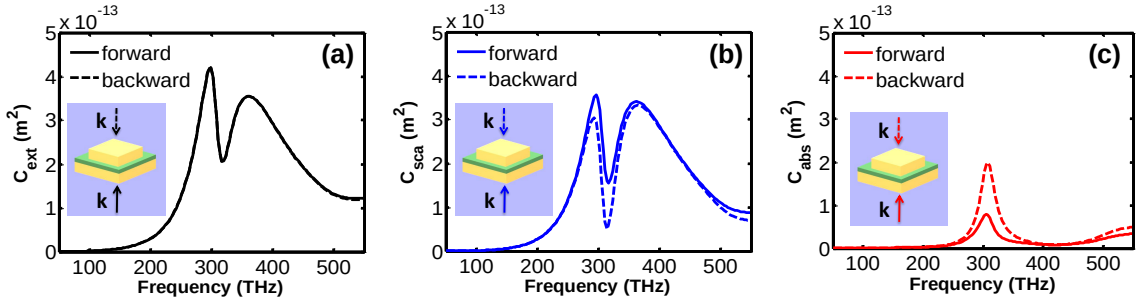

Figure 3.3.3: Extinction (a), scattering (a), and absorption, (b) and cross sections for the nonidentical nanopatches for both illumination directions for $W_1 = 100$ nm. The absorption and scattering cross sections are different at the magneto-electric resonance for opposite illumination directions whereas the extinction cross section is identical.

double nanopatch topology as before but now with different lateral dimensions for each nanopatch [Fig. 3.3.3 (a)]. Fig. 3.3.1 (c) shows the extracted electric polarizability electric, magnetic and magneto-electric polarizability components of the investigated nanoantenna. Note that the magneto-electric response is different from the magneto-electric response of a wire omega particle at microwave frequency [77]. There, the resonance frequencies in the dispersion of all polarizabilities, i.e. the electric, magnetic and magneto-electric polarizability, are identical since they are linked to the same mode sustained by the wire omega particle [77]. In contrast, the magnetic and the magneto-electric resonance frequencies are identical in the considered coupled nonidentical nanopatches, but the electric resonance frequency is different. However, since the magnetic and electric dipole moments, which are created by the electric and magnetic fields in the plane of the array, respectively, are perpendicular to each other, the presented nanoantenna scheme can be generally considered as an omega-type particle as well [60]. We note that most of the findings of this section have been previously published in Ref. [47].

It is clear from Fig. 3.3.2 (b) that the current distribution of the proposed nanoantenna shown at the low frequency resonance produces a magnetic response, comparable to the situation of identical nanopatches [Fig. 3.3.1 (a)]. However, for nonidentical nanopatches the induced currents are no longer symmetric with respect to the geometrical origin of these two nanopatches. This results in a magneto-electric/electromagnetic response.

To explain the scattering properties of the investigated bianisotropic nanoantenna, we can start from the definition of the extinction cross section, i.e. Eq. 3.2.13 and given by [15, 64, 67, 78]

$$C_{\text{ext}}^{\pm} = k\text{Im}\left(\alpha_{\text{xx}}^{\text{ee}} \pm \alpha_{\text{xy}}^{\text{em}} \pm \alpha_{\text{yx}}^{\text{me}} + \alpha_{\text{yy}}^{\text{mm}}\right). \tag{3.3.1}$$

As already highlighted, the plus/minus ($\pm$) sign corresponds to the propagation direction of the incident plane waves in forward/backward direction. For a reciprocal nanoantenna [60], i.e. $\alpha_{\text{xy}}^{\text{em}} = -\alpha_{\text{yx}}^{\text{me}}$, we can conclude that the extinction cross sections for both illuminations are identical, i.e. $C_{\text{ext}} = C_{\text{ext}}^{+} = C_{\text{ext}}^{-}$, and read as

$$C_{\text{ext}} = k\,\text{Im}\left(\alpha_{\text{xx}}^{\text{ee}} + \alpha_{\text{yy}}^{\text{mm}}\right). \tag{3.3.2}$$

As a confirmation the extinction cross sections of the proposed nanoantenna for both illumination directions are calculated and shown in Fig. 3.3.3 (a). However, the scattering/absorption cross sections are not identical when the nanoantenna is illuminated from opposite directions [Fig. 3.3.3 (b) and (c)]. This can be shown analytically by using the definition of the scattering cross sections for both illuminations, i.e. Eq. 3.2.12 for the reciprocal nanoantenna

$$C_{\text{sca}}^{\pm} = \frac{k^4}{6\pi}\left(\left|\alpha_{\text{xx}}^{\text{ee}} \pm \alpha_{\text{xy}}^{\text{em}}\right|^2 + \left|\alpha_{\text{xy}}^{\text{em}} \mp \alpha_{\text{yy}}^{\text{mm}}\right|^2\right). \tag{3.3.3}$$

According to Eq. (3.3.3), the scattering cross sections are not the same for both illumination directions, i.e. $C_{\text{sca}}^{-} \neq C_{\text{sca}}^{+}$ due to the bianisotropic coupling (i.e. α_{me} and α_{em}). Using the relation between absorption, scattering and extinction cross sections, i.e. $C_{\text{abs}}^{\pm} = C_{\text{ext}} - C_{\text{sca}}^{\pm}$, it can be concluded that the absorption cross sections also depend on the illumination directions, i.e. $C_{\text{abs}}^{+} \neq C_{\text{abs}}^{-}$. Our numerical results for scattering and absorption cross sections are also shown in Fig. 3.3.3 (b) and (c). The difference between forward and backward directions is obviously due to the bianisotropy and this occurs around the magneto-electric (bianisotropic) coupling. Note that at resonance frequency, for the backward direction the nanoantenna is at critical coupling, i.e. $C_{\text{abs}}^{-}|_{\text{res}} = C_{\text{sca}}^{-}|_{\text{res}}$.

3.3.3.1 Directive nanoantennas: Multipolar interference

In this subsection, we investigate the radiation patterns of three different nanoantennas, i.e. the single nanopatch, the coupled identical nanopatches, and the coupled nonidentical nanopatches. We show that it is possible to design a nanoantenna with a directive radiation pattern due to an interference between the radiated far-fields of the induced electric and magnetic dipole moments. In general, in order to have a nanoantenna with a directive pattern, a balanced contribution of both electric and magnetic

polarizabilities is required; known as the first Kerker condition [19, 20, 79, 80]. This condition can be achieved for nanoantennas without bianisotropic response. However, having a nanoantenna with a bianisotropic response adds at least two degrees of freedom. The first degree of freedom provides the ability to design a nanoantenna which possesses different far field patterns when illuminated from opposite (forward and backward) directions. This means that one can design a nanoantenna which exhibits a directive pattern for one direction but a non-directive pattern for the opposite direction [Fig. 3.3.5 (e,f)]. The second relates to the fact that for some nanoantennas it is not possible to achieve the balanced condition between the electric and magnetic polarizabilities. Therefore, breaking the symmetries of the nanoantennas will introduce an additional bianisotropic coupling which might be a proper solution to eventually satisfy the Kerker condition. In the following, we try to address these issues.

Let us consider a nanoantenna that possesses an induced electric p_{x} and magnetic m_{y} dipole moment. The radiated far-field of the nanoantenna reads as [22]

$$\begin{aligned} \mathbf{E}_{\mathrm{far}}(\mathbf{r}) &= \frac{k^2}{4\pi\epsilon} p_{\mathrm{x}} \frac{e^{ikr}}{r}\left(-\sin\varphi\,\hat{\varphi} + \cos\theta\cos\varphi\,\hat{\theta}\right), \\ &\quad -\frac{Zk^2}{4\pi} m_{\mathrm{y}} \frac{e^{ikr}}{r}\left(\cos\theta\sin\varphi\,\hat{\varphi} - \cos\varphi\,\hat{\theta}\right), \end{aligned} \tag{3.3.4}$$

where, r is radial distance, ϕ is azimuthal angle and θ is polar angle in spherical coordinate. $k = \sqrt{\epsilon_r}\omega/c$ is the wavenumber for an angular frequency ω in a homogeneous isotropic background material characterized by a relative permittivity ϵ_r, and c is the speed of light. Using Eq. (3.3.4), the normalized backward radar scattering cross section of the nanoantenna can be defined as

$$Q_{\mathrm{RBS}} = \frac{C_{\mathrm{RBS}}}{A} = \lim_{r\to\infty} \frac{4\pi r^2}{A} \frac{\left|\mathbf{E}_{\mathrm{far}}(\varphi = 0, \theta = \pi)\right|^2}{\left|\mathbf{E}_{\mathrm{inc}}\right|^2} \tag{3.3.5}$$

$$= \frac{k^4}{4\pi\epsilon^2 A \left|\mathbf{E}_{\mathrm{inc}}\right|^2} \left| p_{\mathrm{x}} - \frac{\sqrt{\epsilon_r} m_{\mathrm{y}}}{c} \right|^2, \tag{3.3.6}$$

where $|\mathbf{E}_{\mathrm{inc}}|$ is the amplitude of the incident electric field. $A = W^2$ is the geometrical cross section. According to Eq. (3.3.5), zero backscattering field occurs if the Kerker condition

$$p_{\mathrm{x}} - \frac{\sqrt{\epsilon_r} m_{\mathrm{y}}}{c} = 0, \tag{3.3.7}$$

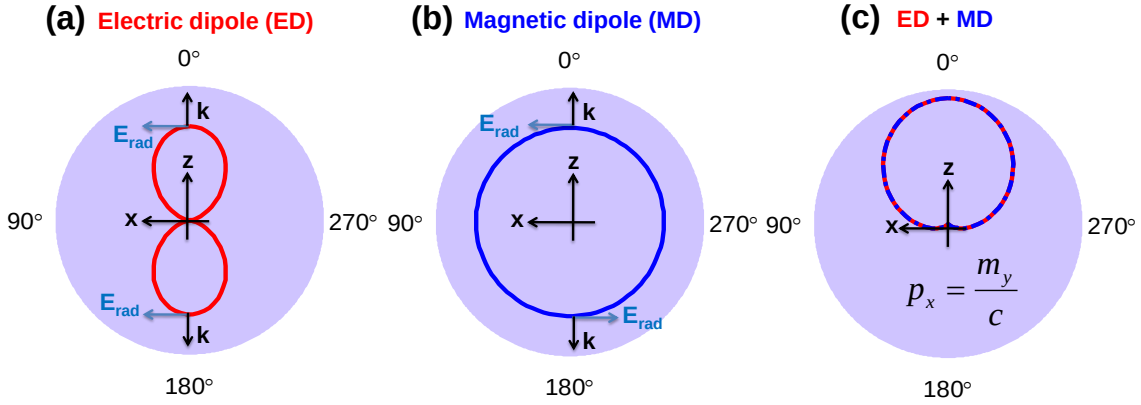

Figure 3.3.4: Radiation pattern for different multipole moments in the xz-plane. (a) Electric dipole moment (p_x), i.e. $|\mathbf{E}_{\mathrm{far}}|^2 \propto |p_{\mathrm{x}}|^2 \cos^2\theta$. The blue arrows indicate the phase of the radiated field. (b) Magnetic dipole moment (m_{y}), i.e. $|\mathbf{E}_{\mathrm{far}}|^2 \propto |\frac{m_y}{c}|^2$. (c) Superposition of electric and magnetic dipole moments, i.e. $|\mathbf{E}_{\mathrm{far}}|^2 \propto |p_{\mathrm{x}}|^2(1+\cos\theta)^2$, when the Kerker condition is fulfilled, i.e. $p_{\mathrm{x}} = \frac{m_y}{c}$.

is fulfilled. To illustrate the physical mechanism behind the Kerker condition, the radiation pattern of an electric dipole moment p_{x} and a magnetic moment m_{y} in the xz-plane ($\varphi = 0$) are shown in Fig. 3.3.4 (a) and (b). If Eq. (3.3.7) holds, the electric field radiated by an electric dipole and magnetic dipole interfere constructively at $\theta = 0$ [Fig. 3.3.4 (c)], i.e. the radiated fields are in phase in forward direction [Fig. 3.3.4 (a) and (b)]. On the other hand, there is no scattering in backward direction ($\theta = \pi$) because of the destructive interference in this direction.

For a reciprocal bianisotropic nanoantenna, the normalized backward radar scattering cross sections for both illumination directions [66, 79, 81, 82] $Q^{\pm}_{\mathrm{RBS}}$ can be calculated Eq. 3.3.5 and are given by

$$Q^{\pm}_{\mathrm{RBS}} = \frac{k^4}{4\pi A}\left|\alpha^{\mathrm{ee}}_{\mathrm{xx}} \pm \alpha^{\mathrm{em}}_{\mathrm{xy}} \mp \alpha^{\mathrm{me}}_{\mathrm{yx}} - \alpha^{\mathrm{mm}}_{\mathrm{yy}}\right|^2. \tag{3.3.8}$$

Equation 3.3.8 shows that only for one direction the nanoantenna can fulfill the Kerker condition. In other words, the Kerker condition can be satisfied for a backward illumination, $Q^{-}_{\mathrm{RBS}} = 0$, i.e. $\alpha^{\mathrm{ee}}_{\mathrm{xx}} - 2\alpha^{\mathrm{em}}_{\mathrm{xy}} - \alpha^{\mathrm{mm}}_{\mathrm{yy}} = 0$. However, for the forward illumination $Q^{+}_{\mathrm{RBS}} \neq 0$, i.e. $\alpha^{\mathrm{ee}}_{\mathrm{xx}} + 2\alpha^{\mathrm{em}}_{\mathrm{xy}} - \alpha^{\mathrm{mm}}_{\mathrm{yy}} \neq 0$.

Notice, the normalized forward radar scattering cross sections for both illumination

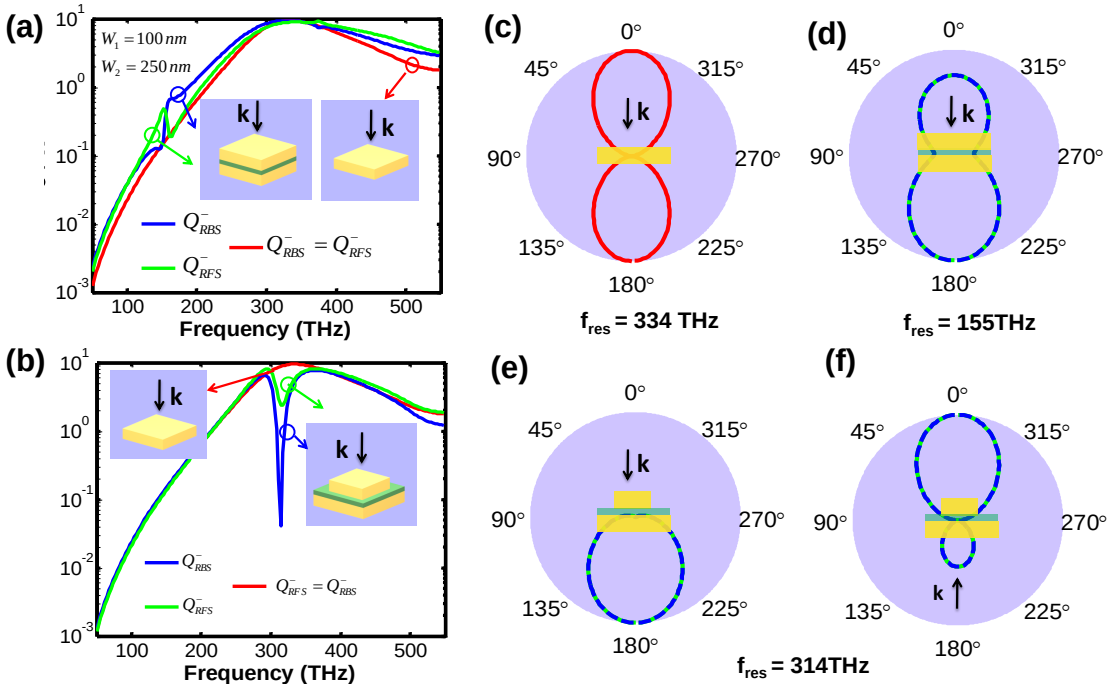

Figure 3.3.5: (a) and (b) Comparison between forward and backward normalized radar scattering cross sections for a single nanopatch (shown only in red since backward and forward normalized radar scatterings are identical), two identical coupled nanopatches (a) and two nonidentical nanopatches (b) (shown in green and blue) with $W_1/W_2 = 0.4$. Illumination occurs as shown in the inset. Radiation patterns of (c) a single nanopatch and (d) two identical coupled nanopatches at resonance. (e) Corresponding radiation pattern of two nonidentical coupled nanopatches illuminated from top at the frequency when $Q^-_{\mathrm{RBS}} \approx 0$. (e) Same as (f) but illuminated from opposite illuminations.

directions read as

$$\begin{aligned} Q^{\pm}_{\mathrm{RFS}} &= \frac{C^{\pm}_{\mathrm{RFS}}}{A} = \lim_{r\to\infty} \frac{4\pi r^2}{A} \frac{|\mathbf{E}_{\mathrm{sca}}\left(\varphi = 0, \theta^{\pm} = 0, \pi\right)|^2}{|\mathbf{E}_{\mathrm{inc}}|^2} \\ &= \frac{k^4}{4\pi A} \left|\alpha^{\mathrm{ee}}_{\mathrm{xx}} \pm \alpha^{\mathrm{em}}_{\mathrm{xy}} \pm \alpha^{\mathrm{me}}_{\mathrm{yx}} + \alpha^{\mathrm{mm}}_{\mathrm{yy}}\right|^2 \\ &= \frac{k^4}{4\pi A} \left|\alpha^{\mathrm{ee}}_{\mathrm{xx}} + \alpha^{\mathrm{mm}}_{\mathrm{yy}}\right|^2 . \end{aligned} \tag{3.3.9}$$

Equation 3.3.9 explicitly shows that the forward scattering is independent of the illumination directions, i.e. $Q^{-}_{\mathrm{RFS}} = Q^{+}_{\mathrm{RFS}}$.

Figure 3.3.5 (a) and (b) show the normalized forward and backward scattering cross sections for three different nanoantennas: a single nanopatch, two identical, and nonidentical coupled nanopatches. It is obvious from Fig. 3.3.5 (a) and (b) that the backscattered fields are canceled for the two nonidentical coupled nanopatches at the design frequency (314 THz) while there is no cancellation for a single nanopatch as well as two identical coupled nanopatches. This cancellation is obviously a consequence of destructive interference between the electric and magnetic dipole moments [Fig. 3.3.4 (c) and 3.3.5 (e)]. It is important to mention that for the identical coupled nanopatches in the limit of dipole approximation [83] (small dielectric spacer, i.e. $g < 10$ nm) zero backscattering regime is not achievable due to the fact that the electric and magnetic dipole moments can not be in balance [Fig. 3.3.5 (a) and (d)]. However, with the help of an additional electric quadrupole moment (larger dielectric spacer, e.g. $g = 50$ nm), it might be possible to realize a directive nanoantenna with zero backscattering for the identical coupled nanopatches. Notice that the directive pattern occurs due to the coherent interference of the electric and magnetic dipoles as well as the electric quadrupole [19]. We will explain that in chapter 5 for a nanoring antenna. Normalized polar field patterns at resonance are also plotted in Fig. 3.3.5 (c)-(f) to illustrate zero backscattering as well as the directivity of corresponding antennas. Notice that for the backscattering cancellation of fields, both the strength and resonance frequency of the magneto-electric coupling have to be tuned. The proposed design is a promising nominee for directive plasmonic antennas coupled to quantum emitters [84].

3.3.3.2 Asymmetric reflection

In the previous subsection, we introduced some of the interesting optical features of an individual bianisotropic nanoantenna. Here, we will investigate the optical response of an array of such nanoantennas and will show that it is possible to realize the complete light absorption by proper tuning of all polarizability components.

Moreover, we will show that due to the bianisotropic coupling it is possible to achieve a strong asymmetric reflection/absorption for opposite illumination directions. By using Eq. 3.2.16, the reflection for an array of reciprocal bianisotropic nanoantennas (i.e. $\alpha_{xy}^{em} = -\alpha_{yx}^{me}$) can be expressed as

$$r^{\pm} = \frac{ik}{2\Lambda^2\Delta_t}\left(\alpha_{xx}^{ee} \pm 2\alpha_{xy}^{em} - \alpha_{yy}^{mm}\right). \tag{3.3.10}$$

The bianisotropic coupling provides more control over the transmission and reflection coefficients (r and t) by using four complex polarizabilities components instead of only the electric and magnetic polarizability component. Moreover, it is clear from Eq. (3.3.10) that due to the different signs of α_{xy}^{em} and α_{yx}^{me} a different optical response is obtained when illuminating the array from opposite directions, i.e. $r^+ \neq r^-$. An important design criterion will be that the coefficients α_{xy}^{em} and α_{yx}^{me} should exhibit a comparable strength to the electric and magnetic polarizabilities at the same frequencies rather than being only nonzero. The schematic view of the periodic array is shown in Fig. 3.3.6 (a). Figure 3.3.6 shows the transmission and reflection for both numerical and analytical results [using Eqs. 3.2.15 and 3.2.16]. The difference between forward and backward reflection spectra can be calculated by using Eq. 3.3.10 and is given by

$$\begin{aligned} R^+ - R^- &= \left|r^+\right|^2 - \left|r^-\right|^2 \\ &= \frac{2k^2}{\Lambda^2\left|\Delta_t\right|^2}\Re\left\{\left(\alpha_{xx}^{ee} - \alpha_{yy}^{mm}\right)\left(\alpha_{xy}^{em} - \alpha_{xy}^{me}\right)^*\right\}, \end{aligned}$$

where $*$ denotes the complex conjugate. Therefore, it is expected to achieve a maximum contrast between the reflection spectra for the forward and backward illuminations when $\Re\left\{\left(\alpha_{xx}^{ee} - \alpha_{yy}^{mm}\right)\left(\alpha_{xy}^{em} - \alpha_{xy}^{me}\right)^*\right\}$ is maximum. However, it should be noted that the presence of losses are essential to get asymmetric reflection for the investigated nanopatches. In the next section, we will show that for a high-index dielectric bianisotropic nanoantenna, the reflection amplitudes are identical for both illumination direction (i.e. $|r^-| = |r^+|$) and only the phase is different, i.e. $r^+ \neq r^-$.

A parametric study illustrated in Fig. 3.3.7 (a) and (b) reveals that the maximum difference between the amplitude of reflection coefficients upon illumination from opposite directions occurs at a ratio of $\frac{W_1}{W_2} \approx 0.4$. Furthermore, the numerical and analytical results are in good agreement at lower frequencies. It is important to state that the analytical model presented here proves as a very reliable tool to correctly explain the array behavior. Notice that the grey shadows in Fig. 3.3.7 (a) and (b)

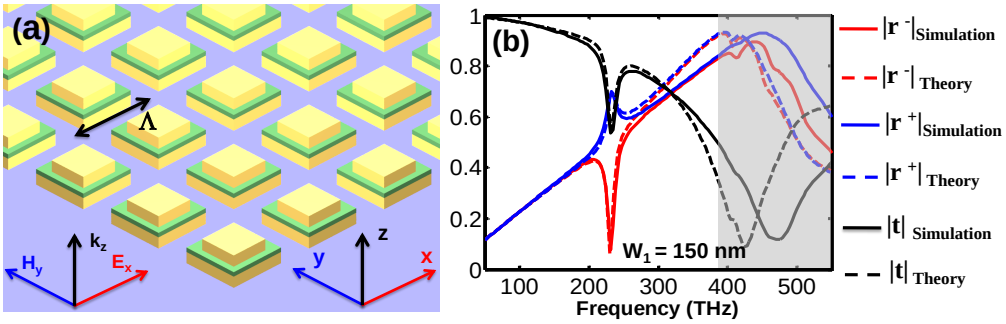

Figure 3.3.6: (a) Schematic view of the array of coupled nonidentical nanopatches. (b) Analytical [using Eq. 3.2.15 and 3.2.16] and full wave simulation results of reflection and transmission spectra of the investigated array for both illumination directions, where r^- and r^+ are reflections for the backward and forward illumination directions. The periodicity is chosen to be $\Lambda = 400$ nm, the dielectric spacer has a refractive index of $n = 1.46$.

represent spectral domains where contributions of higher order modes are no longer negligible. Consequently, the analytical model is less predictive there. However, the model presented here is fully sufficient to explain the reflection and transmission coefficients at the desired frequency band qualitatively, but full wave simulations are necessary to quantitatively predict the optical response from the array. In the next subsection, we show that the magneto-electric response can be modified by changing the lateral dimension of the upper nanopatch. With that, we can obtain a perfect absorber for the array.

3.3.3.3 Complete light absorption

In this subsection, we present an interesting example for an application where light is nearly complete absorbed in an array with a subwavelength thickness ($\approx \lambda/10$) at a specific resonance band for a specific illumination direction. The proposed array is not anymore a total reflector from the other direction far from the resonance band, because it consists of an array of isolated particles rather than, as usually considered, of an array of particles on top of a metallic ground plate. In general, complete light absorption can be achieved by suppressing transmission and reflection (i.e. $R = 0$ and $T = 0$) from one direction only. According to Eqs. 3.3.10, conditions for total absorption in terms of individual polarizability components for backward illumination can be expressed as:

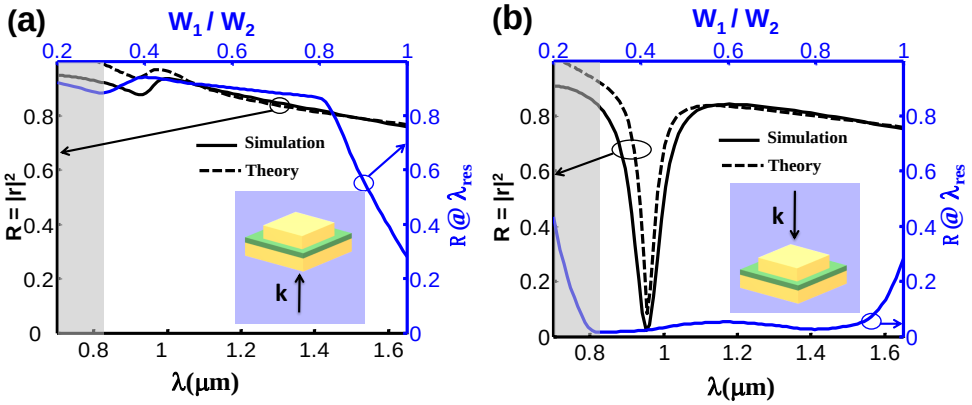

Figure 3.3.7: (a) and (b) Full wave simulations and analytical predictions for the reflection spectra (black lines) when illuminating the array with a forward (a) or a backward (b) propagating plane wave. The ratio of W_1/W_2 is chosen to be 0.4 and the absolute size of W_2 is kept fixed at 250 nm. We see a dramatically different response if the array is illuminated from different directions. In forward direction (a) the reflection is nearly constant in the entire spectrum. In backward direction (b) a pronounced resonance occurs with a well developed dip. By changing the ratio of W_1/W_2 the resonance frequency changes but the optical response is robust. This can be seen in the plot of the reflection at the resonance wavelength as function of this ratio (blue curves in both figures). The period of the array is fixed to be $\Lambda = 275$ nm.

$$\begin{aligned} \alpha_{xx}^{ee} &= 2\alpha_{xy}^{em} + \alpha_{yy}^{mm}, \\ \frac{2c\Lambda^2\Delta_t}{ik} &= \alpha_{xx}^{ee} + \alpha_{yy}^{mm} - \left(\alpha_{xx}^{ee}\alpha_{yy}^{mm} - \alpha_{xy}^{em}\alpha_{yx}^{me}\right)\left(\beta^{ee} + \beta^{mm}\right). \end{aligned} \tag{3.3.11}$$

Figures 3.3.8 (a) and (b) show the real and imaginary parts of the left and right sides of Eq. 3.3.11 at resonance as a function of W_1/W_2 for backward illumination. It shows that the nearly complete absorption can be achieved when both conditions are satisfied and this is indicated by the red shaded areas in Figs. 3.3.8 (a) and (b). Figure 3.3.8 (c) shows a parametric study of the maximum absorbed power (that is maximum at resonance frequency) for different ratios of $\frac{W_1}{W_2}$ with illumination from the backward direction. Note that the maximum absorption for a varying ratio of $\frac{W_1}{W_2}$ takes place at different wavelengths (λ_{max}). The wavelength dependent response for the situation where the maximum share of light is absorbed is also illustrated in Fig. 3.3.8 (c). The nearly total absorption occurs for a ratio of $\frac{W_1}{W_2} \approx 0.4$ for an array period of $\Lambda = 275$ nm (g and t are fixed to be 8 nm and 50 nm).

To conclude, in this subsection, we introduced a simple design for a plasmonic

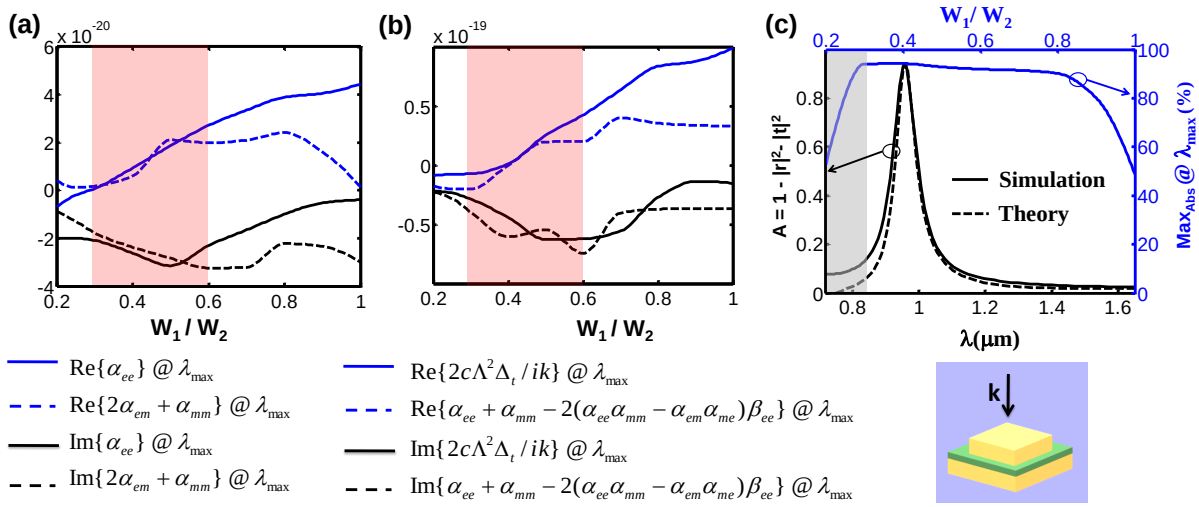

Figure 3.3.8: (a) and (b) The real (blue lines) and imaginary (black lines) parts of the left and right sides of Eq. 3.3.11 at resonance frequency as a function of W_1/W_2 for a backward illumination. The red sections represent spectral domains where nearly total absorption can be achieved. (c) Full wave simulations and analytical predictions for the absorption spectra (black lines) when backward illumination is applied to the array. We see that we have nearly perfect absorption at resonance. The period of the array is fixed to $\Lambda = 275$ nm.

bianisotropic nanoantenna. It provides a control over the electric, magnetic, and magneto-electric responses. The magneto-electric coupling is achieved by a pair of separated nanopatches which allows to obtain balanced condition, i.e. the equivalence of the electric and magnetic polarizations. At visible frequencies, this balanced condition has been earlier achieved only for non-bianisotropic nanoantennas (between the electric and magnetic Mie resonances of silicon spheres or spheroids) [26, 61, 82]. In the present case the amplitudes of three effective polarizabilities, i.e. electric, magnetic and magneto-electric, can be engineered with same strength. The presence of the bianisotropic response provides the asymmetry of reflectance for opposite illumination directions. A very strong asymmetry of reflection as well as nearly perfect absorption for the suggested nanoantennas have been shown. Moreover, an individual nanoantenna can operate as a very directive nanoantenna with zero backscattered fields known as Huygens' scatterer.

3.3.4 Tunable bianisotropic nanoantennas

The optical response of plasmonic devices mainly depends on their geometries and materials. The operational frequencies of these devices are mostly fixed. In order to achieve tunable devices, tunable materials are required. Recently, tunable plasmonic

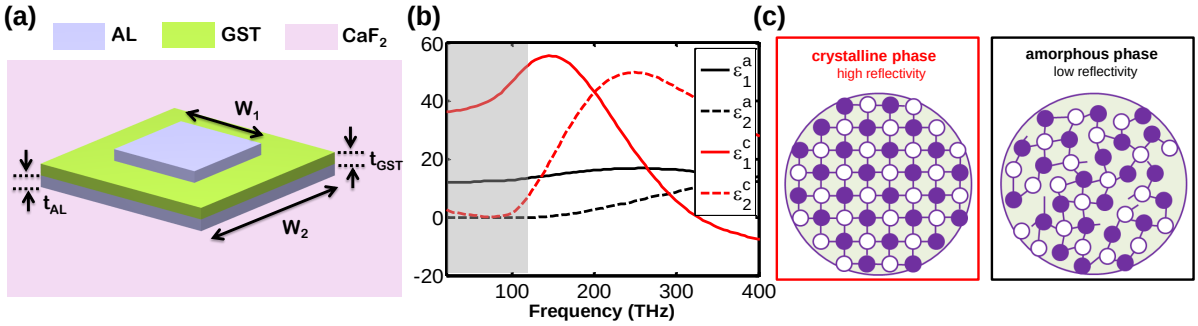

Figure 3.3.9: (a) Geometry of the tunable nanoantenna. The spacer is made of germanium antimony telluride (GeSbTe or GST). The thickness of the aluminum patch is $t_{\mathrm{AL}} = 50$ nm, the width of the upper and the lower patch are $W_1 = 350$ nm, and $W_2 = 800$ nm, respectively. The thickness of the GST spacer is $t_{\mathrm{GST}} = 70$ nm. The refractive index of an embedding material (i.e. CaF_2) is 1.4. (b) Real $(\epsilon_1^{\mathrm{a}}, \epsilon_1^{\mathrm{c}})$ and imaginary $(\epsilon_2^{\mathrm{a}}, \epsilon_2^{\mathrm{c}})$ parts of the relative permittivity of the GST as a function of frequency for crystalline $\epsilon^{\mathrm{c}} = \epsilon_1^{\mathrm{c}} + i\epsilon_2^{\mathrm{c}}$ and amorphous $\epsilon^{\mathrm{a}} = \epsilon_1^{\mathrm{a}} + i\epsilon_2^{\mathrm{a}}$ phases, respectively [86–88]. Notice that the grey shadow represents a spectral domains for which the absorption is considerably small for both phases. c) Crystalline (red box) and amorphous (black box) phases [87].

devices have been demonstrated by employing different materials such as graphene and liquid crystals [74, 85]. Moreover, phase change materials (PCMs) are viable candidates to design tunable plasmonic devices. There are many PCMs that can be used to obtain a tunable optical response. However, very few materials have a pronounced difference in their optical properties when switched between different phases. The germanium antimony telluride ($Ge_3Sb_2Te_6$ or short GST) is a phase change material that is mainly used in rewritable optical discs and phase-change memory applications [86, 87]. Its optical properties change significantly between amorphous and crystalline phases [Fig. 3.3.9 (c)]. The pronounced optical contrast might be due to the strong change in the atomic arrangement of two phases (i.e. amorphous and crystalline) [86]. The main characteristics that make GST useful for plasmonic applications are related to its fast switching speed with laser pulses and drastic changes of optical properties [88]. The switching between stable amorphous and crystalline phases is in the order of nanoseconds.

In the following, we suggest a tunable plasmonic antenna that possesses fascinating optical properties, i.e. fast switching between its far-field patterns. The proposed tunable antenna is similar to the previous section. However, in order to have a tunable optical response, we utilize GST as the dielectric spacer material [Fig. 3.3.9 (a)]. The antenna is made of aluminum instead of gold. This reflects the fact that gold is an impractical material to be combined with GST since it strongly diffuses into

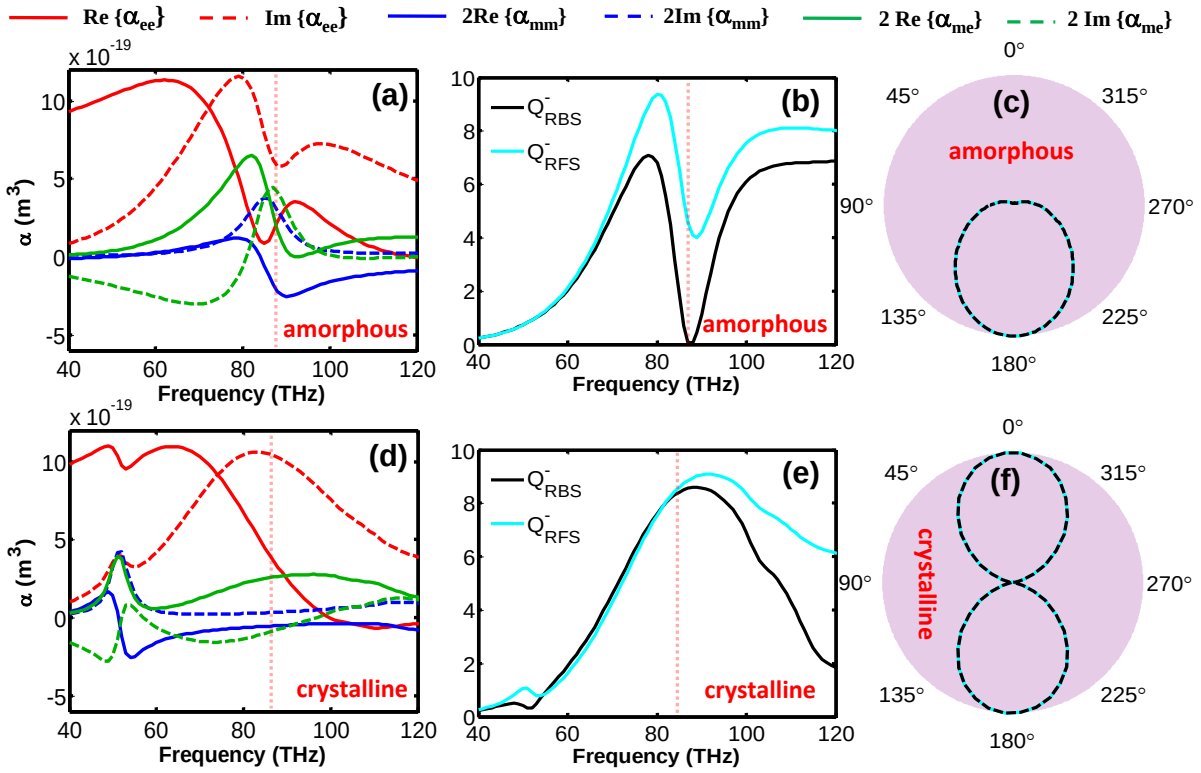

Figure 3.3.10: (a) and (d) Polarizability components of the nanoantenna in amorphous and crystalline phases, respectively. (b) and (e) Normalized forward and backward radar cross section in both phases, respectively. (c) and (f) The pattern of a tunable antenna at 86 THz for both phases.

the GST layer during thermal crystallization [87]. The dispersive real (solid lines) and imaginary (dashed lines) permittivity of GST for both amorphous "a" (red) and crystalline "c" (black) phases are depicted in Fig. 3.3.9 (b). It can be seen that the real part of the permittivity is considerably large in the mid infrared. For example, at 90 THz, the permittivity for the crystalline phase is $\epsilon^c = 40{+}0.8\mathrm{i}$ and the permittivity for the amorphous phase is $\epsilon^c = 12.8{+}0.01\mathrm{i}$ [86–88]. Moreover, the imaginary part is considerably small in the mid infrared due to the fact that it is below the optical band gap. In the following, we will show that this huge tunability of the permittivity (between the amorphous and crystalline phases) can be extremely useful to design antennas with tunable patterns.

We demonstrated, already in previous sections, that the asymmetric antenna can support two distinct modes, i.e. electric and magnetic modes. Therefore, it is possible to achieve two different radiation patterns by a proper design; a) a purely electric dipole resonance which leads to a dipole-like pattern [Fig. 3.3.10 (c)] b) when the electric and magnetic response are in balance which provides a directive pat-

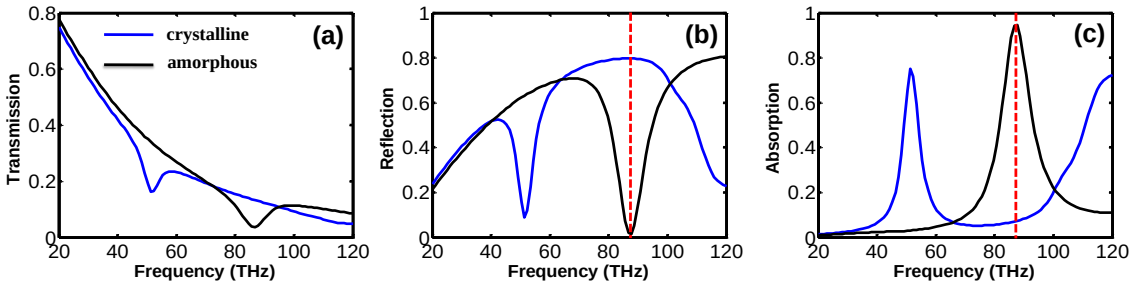

Figure 3.3.11: (a)-(c) Transmission, reflection and absorption of the array of investigated structure for both phases. The response of device changes from a reflector to a perfect absorber at resonance frequency 86 THz.

tern [Fig. 3.3.10 (a)]. The polarizability components of the tunable antenna in the amorphous phase is depicted in Fig. 3.3.10 (a). At resonance (red dashed line) i.e. 86 THz the antenna shows strong electric, magnetic and magneto-electric responses. The normalized forward (Q^{-}_{RFS}) and backward (Q^{-}_{RBS}) radar cross sections are shown in Fig. 3.3.10 (b) for the amorphous phase. It can be seen that the antenna possesses zero backscattering at 86 THz. Therefore, the corresponding far-field pattern of the antenna should be directive as shown in Fig. 3.3.10 (c). The directive pattern as well as zero backscattering are due to a destructive interference between the radiated fields of the electric and magnetic dipole moments at backward direction. However, at crystalline phase (at 86 THz), the antenna supports only an electric response [Fig. 3.3.10 (d)]. As a result, the forward and backward scattering response is identical [red dashed line in Fig. 3.3.10 (e)]. This implies that the pattern of the antenna should be entirely different compared to the amorphous phase [3.3.10 (f)].

The optical response of a periodic array of these tunable nanoantennas can lead to interesting and practical devices. Figure 3.3.11 (a)-(c) represents the transmission, reflection, and absorption of the proposed tunable device for both amorphous (black lines) and crystalline (blue lines) phases. At 86 THz, the device shows significantly different optical responses for two phases due to significant change of the individual polarizabilities [Fig. 3.3.10 (a) and (c)]. It behaves as a good reflector in the crystalline phase whereas in the amorphous phase it operates as a nearly perfect absorber [Fig. 3.3.11 (c)]. It is important to note that switching between perfect absorber and reflector can be achieved in the order of nanoseconds with an external laser pulse.

All the investigated nanoantennas in the previous sections were made of plasmonic materials (metals). We used their intrinsic losses to design interesting devices such as perfect absorbers. It would be interesting to investigate the optical properties of lossless nanoantennas. Therefore, in the next section, we try to focus on the lossless

cases and propose a bianisotropic nanoantenna made out of a high-index dielectric (e.g. silicon).

3.4 High-index dielectric nanoantennas

Plasmonic nanoantennas have attracted enormous research interests due to its potential applications [25, 78, 89–92]. However, its applications are notably limited by Ohmic losses at optical frequencies [30, 93–95]. Recently, an alternative strategy has been introduced to overcome this problem. Basically, the suggestion is to use high-index dielectric materials as building blocks of devices that control light-matter interaction [39,55,61,96–102]. A high-index dielectric nanoantenna can support both electric and magnetic resonant responses [26,61,103]. Interesting optical features such as directional scattering pattern with zero backscattering can be achieved by proper tuning of these responses [20,26,61,82,103,104]. Nanoantennas with higher multipolar responses, e.g. electric and magnetic quadrupoles may provide even higher control on the intriguing scattering features, e.g. super-scattering, and super-directivity [28,38] compared to nanoantennas with only dipolar responses. However, they require more complicated theoretical considerations. Therefore, it is very demanding to achieve more control over the scattering features of nanoantennas without adding such theoretical complexities. The *bianisotropy* might be the only suitable solution to control the scattering properties of nanoantennas in the context of *dipolar* responses [47,60].

In this section we introduce a novel high-index dielectric nanoantenna with bianisotropic coupling. We start by considering a cylindrical dielectric nanoantenna. We show that it can support both electric and magnetic responses which leads to interesting optical features, e.g. zero backscattering. It fulfills the Sipe−Kranendonk condition (i.e. Eq. 3.2.14) due to the fact that the antenna is lossless. Finally, we show that breaking the symmetry (with respect to the illumination directions) of the cylindrical dielectric nanoantenna leads to an additional magneto-electric coupling which offers interesting optical features. We note that most of the findings of this section have been previously published in Ref. [63].

3.4.1 Cylindrical nanoantennas

Let us start with a cylindrical high-index dielectric nanoantenna as shown in Fig. 3.4.1 (a). The antenna is illuminated by a plane wave with an electric field polarized along the x-axis that propagates in the positive z-direction. The total scattering cross section and contributions of the different Cartesian multipoles are depicted in Fig. 3.4.1 (b). It shows that the higher order multipoles are negligible below 450 THz

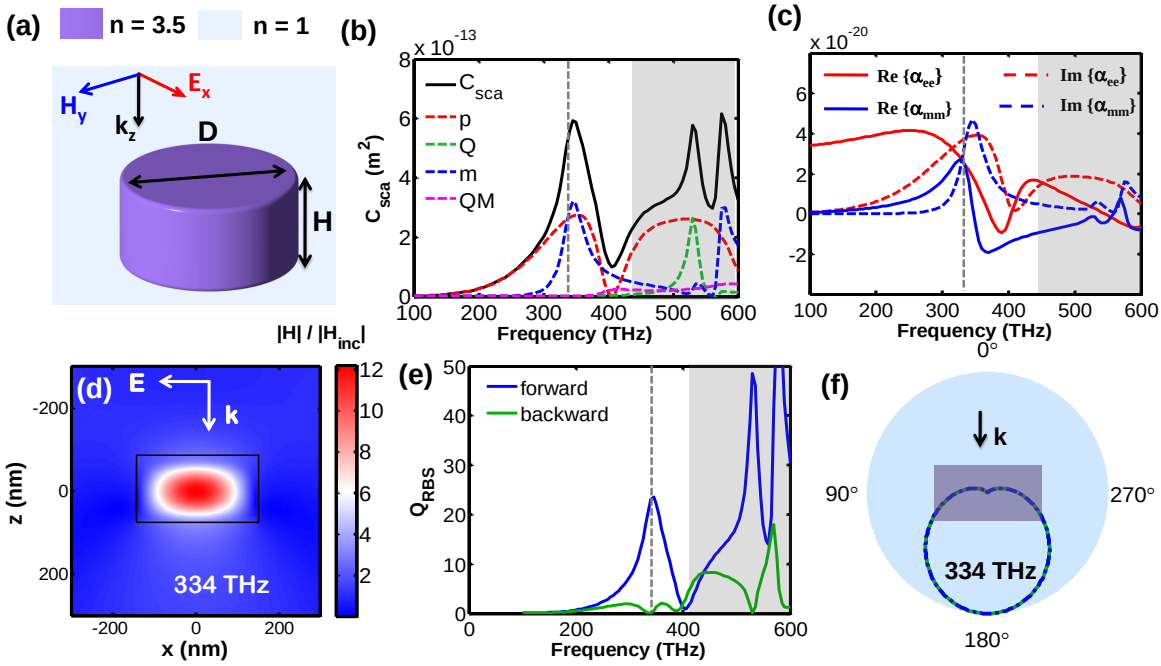

Figure 3.4.1: (a) Schematic view of a high-index dielectric nanoantenna with a height of $H = 150$ nm and diameter of $D = 300$ nm. The dielectric cylinder has a refractive index of $n = \sqrt{\epsilon_r} = 3.5$. (b) The corresponding total scattering cross sections and contributions from different Cartesian multipole moments as a function of frequency. (c) Calculated electric (red lines) and magnetic (blue lines) polarizabilities as a function of frequency. The grey dashed line shows the balanced condition, i.e. $\alpha_{xx}^{ee} = \alpha_{yy}^{mm}$. (d) Normalized magnetic field distributions at the balanced condition. (e) Normalized forward and backward radar cross sections. (f) Far-field radiation pattern at the balanced condition.

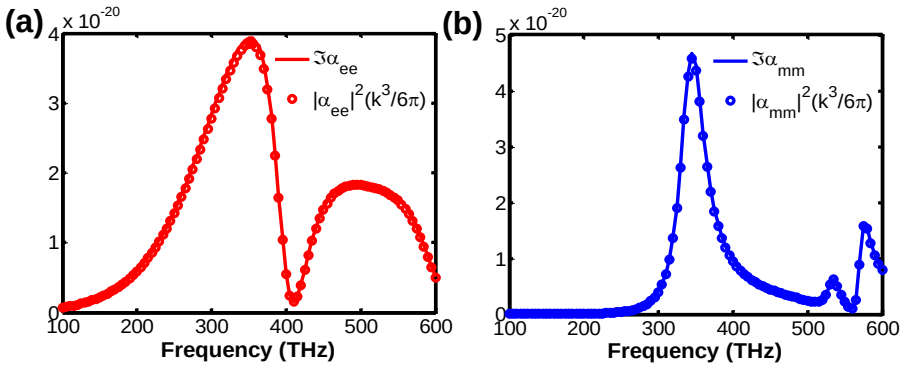

Figure 3.4.2: The Sipe–Kranendonk condition for the lossless high-index dielectric nanoantenna. There is a great agreement for electric and magnetic moments, i.e. the Sipe–Kranendonk condition is satisfied.

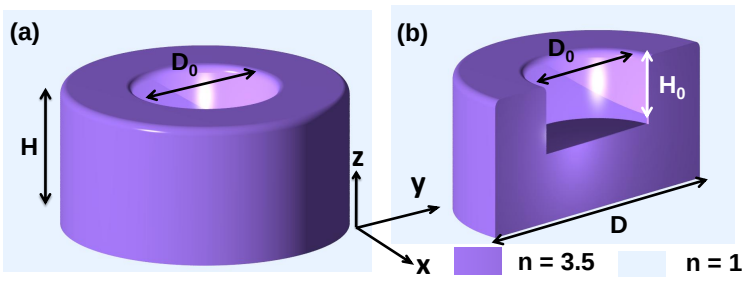

Figure 3.4.3: Schematic of the proposed bianisotropic high-index dielectric meta-atom. The dielectric cylinder has a diameter $D = 300$ nm and height $H = 150$ nm with a cylindrical hole inside it which has the diameter $D_0 = 150$ nm and height $H_0 = 10 - 140$ nm with a refractive index 1 (air). The dielectric cylinder has a refractive index of $n = \sqrt{\epsilon_r} = 3.5$.

and the antenna can be fully described by electric and magnetic dipole moments. Interestingly, at 334 THz, the contribution of electric and magnetic dipole moments to the total scattering cross section is identical, i.e. $C^{\mathrm{m}}_{\mathrm{sca}} = C^{\mathrm{p}}_{\mathrm{sca}}$ [Fig. 3.4.1 (b)]. It can be shown that the electric and magnetic moments are at the balanced condition (i.e. $p_{\mathrm{x}} = \frac{m_{\mathrm{y}}}{c}$). To confirm that, we calculated the electric and magnetic polarizability components of the nanoantenna as shown in Fig. 3.4.1 (c). The interesting point is that the amplitude of the magnetic resonance of the nanoantenna is comparable to the electric one. The balanced condition i.e. $\alpha^{\mathrm{ee}}_{\mathrm{xx}} = \alpha^{\mathrm{mm}}_{\mathrm{yy}}$ is fulfilled and it can be seen in Fig. 3.4.1 (c) at 334 THz. It is important to mention that the geometry of the nanoantenna was properly tuned such that it satisfies the balanced condition. Its a selected geometry and meeting the balanced condition cannot be satisfied by every possible geometry.

As already highlighted and shown, the nanoantenna supports both an electric and a magnetic response. The latter is due to a strong displacement current, which circulating in the nanoantenna. The strong magnetic field enhancement can be seen in Fig. 3.4.1 (d). Since the nanoantenna is lossless (no Ohmic losses), it should also satisfy the Sipe−Kranendonk condition [27, 33, 64, 105], i.e. Eq. 3.2.14 that can be simplified as

$$\Im\alpha^{\mathrm{ee}}_{\mathrm{xx}} = \left|\alpha^{\mathrm{ee}}_{\mathrm{xx}}\right|^2 \frac{k^3}{6\pi}, \tag{3.4.1}$$

$$\Im\alpha^{\mathrm{mm}}_{\mathrm{yy}} = \left|\alpha^{\mathrm{mm}}_{\mathrm{yy}}\right|^2 \frac{k^3}{6\pi}. \tag{3.4.2}$$

Figure 3.4.2 (a) and (b) present the Sipe−Kranendonk conditions for both the electric and magnetic dipole moments. It can be seen that there is a great agreement for both moments.

The normalized forward and backward radar cross sections of a nanoantenna are shown in Fig. 3.4.1 (e). As highlighted already, the antenna shows zero backscattering fields at 334 THz, i.e. $Q_{\mathrm{RBS}} = \frac{k^4}{4\pi A}\left|\alpha_{\mathrm{xx}}^{\mathrm{ee}} - \alpha_{\mathrm{yy}}^{\mathrm{mm}}\right|^2 = 0$ due to the fact that it satisfies the balanced condition, i.e. $\alpha_{\mathrm{xx}}^{\mathrm{ee}} = \alpha_{\mathrm{yy}}^{\mathrm{mm}}$. The physical mechanism to achieve an antenna with zero backscattering is a destructive interference between the radiated fields of the electric and magnetic dipole moments in backward direction. Whereas, the forward scattering will be enhanced due to constructive interference between the radiated fields of the induced moments [Fig. 3.3.4]. At lower frequencies (below 450 THz), the forward scattering can be calculated by using $Q_{\mathrm{FBS}} = \frac{k^4}{4\pi A}\left|\alpha_{\mathrm{xx}}^{\mathrm{ee}} + \alpha_{\mathrm{yy}}^{\mathrm{mm}}\right|^2$.

3.4.2 Bianisotropic nanoantennas

In this subsection, we suggest a feasible approach to realize a magneto-electric (bianisotropic) coupling in a high-index dielectric nanoantenna. We show that this property can be achieved by breaking the symmetry of a cylindrical nanoantenna, i.e. a high-index dielectric cylinder into which partially a cylindrical hole is drilled [Figs. 3.4.3 (a) and (b)]. Such a nanoantenna supports electric and magnetic dipole moments with different strength when illuminated by a plane wave in forward or backward directions [Fig. 3.4.4 (a) and (b)]. In particular, we show that the bianisotropic coupling in the proposed nanoantenna causes different backscattering responses as well as radiation patterns for the opposite illumination directions. This coupling can be tuned by controlling geometrical parameters of the nanoantenna. We also demonstrate that an infinite periodic planar array of such lossless nanoantennas provides different resonant reflection phases for different illumination directions. This is certainly due to the proposed magneto-electric coupling and it is not possible with only an electric and/or magnetic response. We also demonstrate that the investigated nanoantenna is an excellent candidate for unit-cells of reflectarrays [106]. Indeed, this nanoantenna in its reflection resonance band provides a 2π phase change while it maintains a considerable amplitude. Moreover, since there is no metallic ground plate contained in the proposed reflectarray, it will be transparent out of its resonance band.

The geometry of the proposed bianisotropic high-index dielectric nanoantenna is shown in Figs. 3.4.3 (a) and (b). The suggested nanoantenna is not symmetric with respect to the forward and backward illumination directions [Fig. 3.4.3 (a)]. Material and geometrical parameters of the nanoantenna are given in Fig. 3.4.3. Using the multipole expansion of the scattered field, we have computed the total scattering cross section and the contribution of each multipole moment when the nanoantenna is illuminated by a plane wave in forward and backward directions [Figs. 3.4.5 (a) and (c)]. The higher order multipole moments, i.e. the electric quadrupole Q and

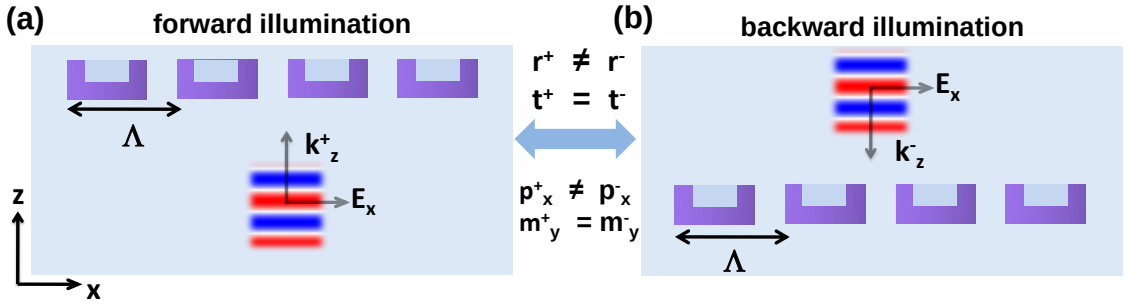

Figure 3.4.4: Sketch of forward and backward illuminations. The array supports different reflections coefficients due to bianisotropic coupling, i.e. $r^{+} \neq r^{-}$.

magnetic quadrupole QM moemnts are not negligible above 450 THz [grey shadows in Figs. 3.4.5 (a) and (c)]. As mentioned earlier, we are interested in a spectral domain where the optical response of the nanoantenna can be only described by its electric and magnetic dipole contributions. This corresponds to frequencies below 450 THz. Therefore, we concentrate in the following on this frequency range.

As already highlighted, for a reciprocal nanoantenna (i.e. $\alpha_{xy}^{em} = -\alpha_{yx}^{me}$), the extinction cross sections for both illuminations are identical, i.e. $C_{ext} = C_{ext}^{+} = C_{ext}^{-}$. Moreover, the extinction cross section C_{ext} for a lossless reciprocal nanoantenna is identical to the scattering cross section C_{sca}, i.e. $C_{ext} = C_{sca}$ due to the fact that the absorption cross section is zero, i.e. $C_{abs} = C_{ext} - C_{sca} = 0$. This explains why the scattering cross sections are identical for the proposed nanoantenna when illuminated from opposite directions, i.e. $C_{sca} = C_{sca}^{+} = C_{sca}^{-}$ [see black solid lines in Figs. 3.4.5 (a) and (c)]. Note that the equality between extinction and scattering cross sections for the lossless bianisotropic nanoantenna leads to the Sipe–Kranendonk condition [27, 33, 64, 105], i.e. Eq. 3.2.14.

It is important to note that for a plasmonic bianisotropic nanoantenna, due to the intrinsic Ohmic losses of metals, the scattering and absorption cross sections will be different for forward and backward illuminations [47, 107]. Furthermore, a planar periodic array of lossy bianisotropic nanoantennas possesses a strong asymmetric reflectance and perfect absorption. These effects have been studied in the previous sections [47, 72].

Although the scattering/extinction cross sections are similar for different illumination directions in the proposed nanoantenna, the contributions of the electric and magnetic dipole moments to the total scattering cross sections are not, i.e. $\mathrm{p}^{+} \neq \mathrm{p}^{-}$ and $\mathrm{m}^{+} \neq \mathrm{m}^{-}$ [see red and blue dashed lines in Figs. 3.4.5 (a) and (c)]. It can also be seen from Figs. 3.4.5 (b) and (d) that the magnetic field distributions are significantly different when the nanoantenna is illuminated from froward and backward

directions. This is obviously due to the presence of magneto-electric coupling, which is provided by the asymmetry in the nanoantenna.

In order to prove this, we have also calculated the individual polarizability components of the nanoantenna [Figs. 3.4.6 (a)-(c)] [16,47,65,68,108]. The magneto-electric coupling $\alpha_{\mathrm{xy}}^{\mathrm{em}}$ is comparable with the electric $\alpha_{\mathrm{xx}}^{\mathrm{ee}}$ and magnetic α_{mm} couplings for the proposed nanoantenna [Figs. 3.4.6 (a)-(c)]. The level of this coupling can be tuned by changing the geometrical parameters of the nanoantenna, i.e. the height H_0 and diameter D_0 of the partially drilled cylindrical air hole inside the high-index dielectric cylinder. Figure 3.4.6(d) presents the magnitude of electric, magnetic, and magneto-electric polarizabilities of the nanoantenna at the maximum of magneto-electric coupling ($|\alpha_{\mathrm{xy}}^{\mathrm{em}}|^{\mathrm{max}}$) as a function of the height of cylindrical air hole H_0. It confirms that the amplitude of the magneto-electric coupling can be tuned and its maximum occurs when the height of hole H_0 is appropriately half of the dielectric cylinder H, i.e. $H_0 \approx \frac{H}{2}$=75 nm. Notice that the magneto-electric coupling can also be tuned by changing the diameter of the cylindrical air hole D_0.

As highlighted before, a lossless bianisotropic nanoantenna possesses identical scattering cross sections for both forward and backward illumination directions. However, the backward radar cross section depends on the illumination directions [Fig. 3.4.7 (a)] and is given by

$$Q_{\mathrm{RBS}}^{\pm} = \frac{k^4}{4\pi A}\left|\alpha_{\mathrm{xx}}^{\mathrm{ee}} \pm 2\alpha_{\mathrm{xy}}^{\mathrm{em}} - \alpha_{\mathrm{yy}}^{\mathrm{mm}}\right|^2, \tag{3.4.3}$$

where $A = \pi\left(\frac{D}{2}\right)^2$ is the geometrical cross section and D is the diameter of the nanoantenna [Fig. 3.4.3]. Consequently, due to bianisotropy, the backscattering responses $Q_{\mathrm{RBS}}^{\pm}$ are different when the nanoantenna is illuminated from opposite directions, i.e. $Q_{\mathrm{RBS}}^{+} \neq Q_{\mathrm{RBS}}^{-}$. Note that the forward radar cross section as shown in Fig. 3.4.7 (a) is identical for both illumination directions according to the definition of normalized forward radar cross section Eq. 3.3.9 [47]. Hence, we expect that the nanoantenna should support different radiation patterns for opposite illumination directions as depicted in Fig. 3.4.7 (b). In summary, the following relations hold for the proposed lossless bianisotropic nanoantenna:

$$C_{\mathrm{sca}} = C_{\mathrm{ext}} = C_{\mathrm{scat}}^{\pm} = C_{\mathrm{ext}}^{\pm}, \quad Q_{\mathrm{RFS}}^{+} = Q_{\mathrm{RFS}}^{-}, \tag{3.4.4}$$

$$p^{+} \neq p^{-}, \quad m^{+} \neq m^{-}, \quad Q_{\mathrm{RBS}}^{+} \neq Q_{\mathrm{RBS}}^{-}. \tag{3.4.5}$$

In the next subsection, we start to demonstrate its interesting characteristics when used in a planar periodic array.

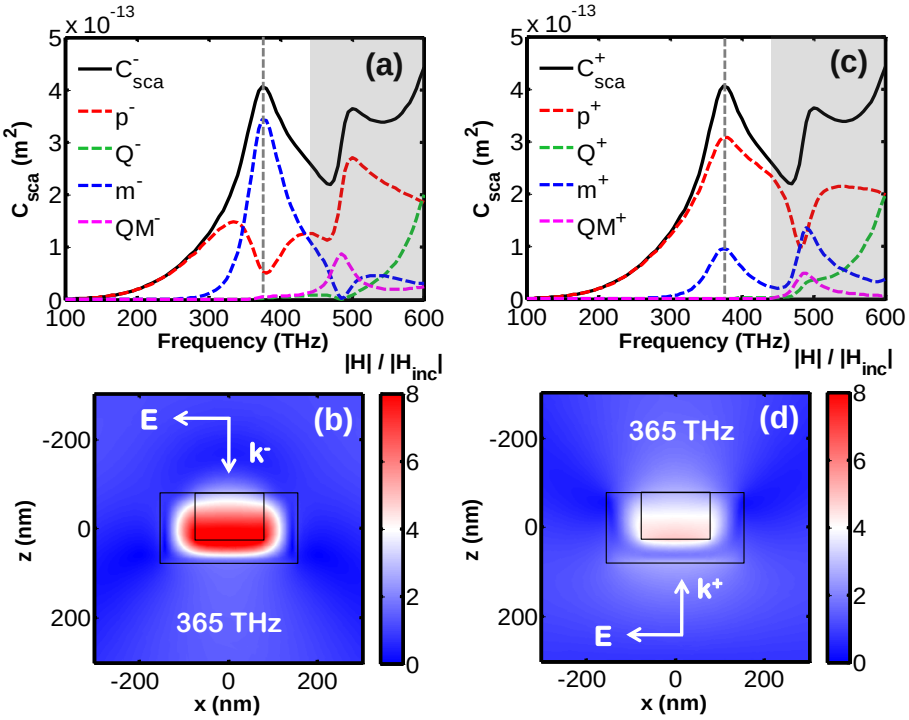

Figure 3.4.5: (a) and (c) Total scattering cross sections $C_{sca}^{\pm}$ and contributions from different Cartesian multipole moments as a function of frequency for forward (+) and backward (−) illumination directions; electric dipole moment $p^{\pm}$ (red dashed line), magnetic dipole moment $m^{\pm}$ (blue dashed line), electric quadrupole moment $Q^{\pm}$ (green dashed line) and magnetic quadrupole moment $QM^{\pm}$ (purple dashed line). The height of the air hole is $H_0 = 100$ nm. (b) and (d) Normalized magnetic field distributions at 365 THz [grey dashed line in (a) and (c)] for both illumination directions.

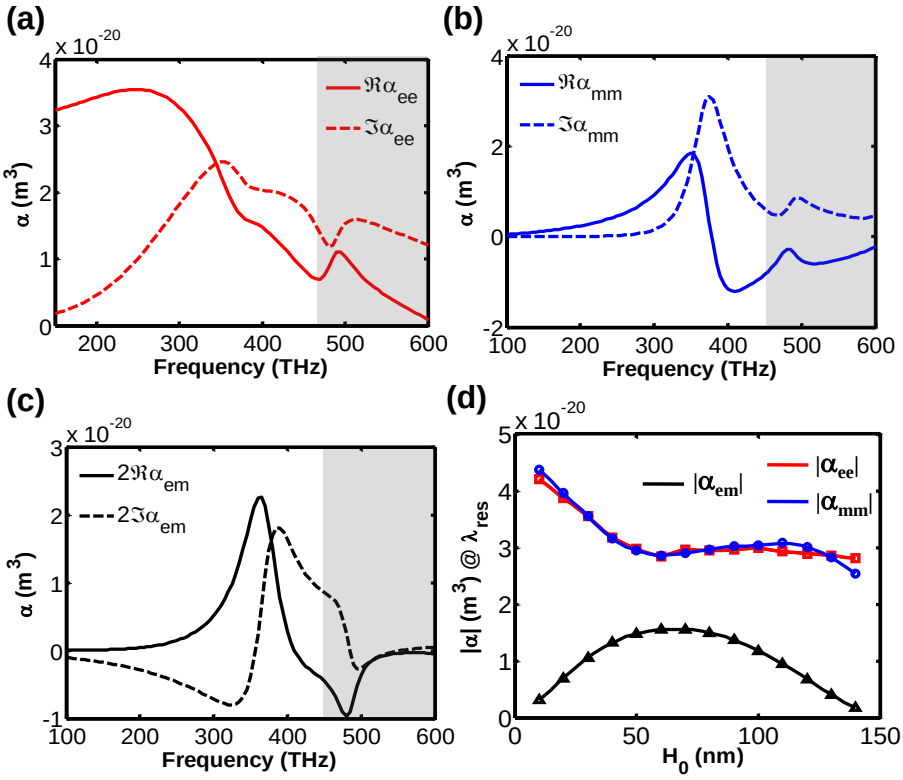

Figure 3.4.6: (a)-(c) Individual polarizability components of the proposed nanoantenna. The geometrical parameters are: the height of the cylinder H = 150 nm, the height of cylindrical air hole H_0 = 100 nm, and its diameter D_0 = 150 nm. (d) Comparison between the amplitude of the individual polarizability components at maximum of the magnetoelectric coupling. The maximum bianisotropy happens when the height of the air hole is approximately half of the dielectric cylinder, i.e. $H_0 \approx \frac{H}{2}$=75 nm and this corresponds to half of the height.

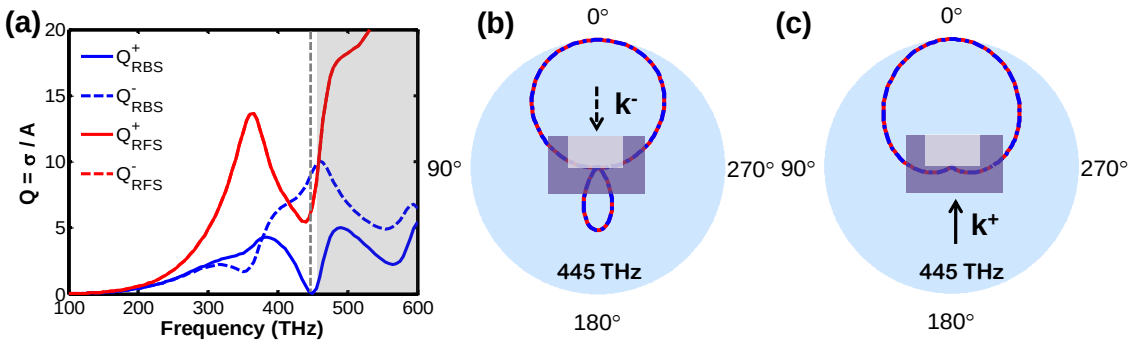

Figure 3.4.7: (a) Normalized backward (blue lines) and forward (red lines) radar cross sections when the nanoantenna is illuminated from backward (dashed lines) and forward (solid lines) directions for H_0 = 75 nm. (b) and (c) Radiation patterns for backward (b) and forward (c) illumination directions at 445 THz, respectively.

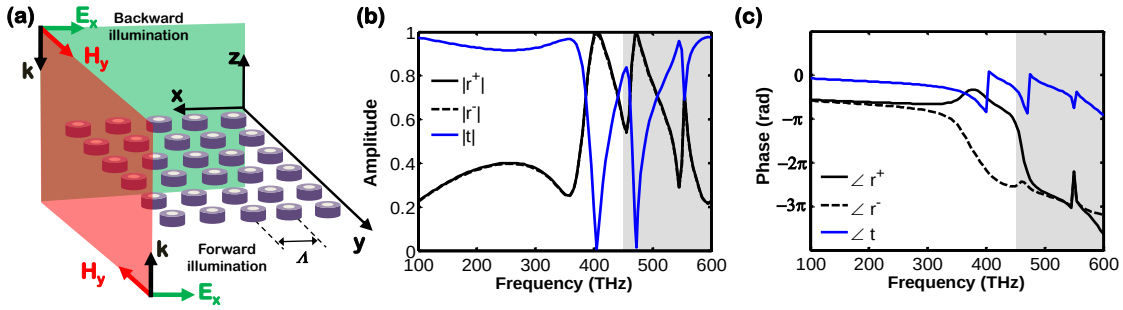

Figure 3.4.8: (a) A periodic planar array composed of the proposed bianisotropic nanoantennas with $H_0 = 75$ nm. (b) Reflection and transmission amplitude for two illumination directions shown in (a). (c) The same plots as in (b) for phases. The reference plane for phase is considered at $z = 0$ plane.

3.4.3 Bianisotropic nanoantenna in planar arrays

In this subsection, we consider a periodic array composed of the proposed bianisotropic nanoantenna that is arranged along a planar surface, here the xy−plane [Fig. 3.4.8 (a)]. Since the nanoantennas are assumed to be lossless, the Ohmic losses of the proposed array are also zero. The array is illuminated at normal incidence from two directions, i.e. forward and backward directions [Figs. 3.4.4(a) and (b) for the definition of forward and backward illumination]. The reflection and transmission amplitudes and phases for these two illumination cases are depicted in Figs. 3.4.8(b) and (c). It is obvious that the amplitudes for the reflection and transmission for the different illumination directions are identical since there are no losses. The phase in transmission is equally identical due to reciprocity. On the contrary, the phase in reflection is not identical. This is due to the presence of bianisotropy in the proposed array [Figs. 3.4.4(a) and (b)].

Now, we claim that the proposed nanoantenna is a proper candidate as a unit cell in reflectarrays. Indeed, a unit cell must provide a 2π phase change prior being applicable in reflectarrays [106, 109–112]. This 2π phase change can be obtained by a suitable geometrical tuning. Moreover, it has to maintain a high reflection amplitude across the considered geometrical configuration. Figure 3.4.8 shows the amplitude and phase variations versus different height and diameter of the air hole inside the dielectric cylinder when the proposed nanoantenna is used in a square array with period $\Lambda = 400$ nm.

As can be seen from Fig. 3.4.9(a), the proposed nanoantenna satisfies the required condition for the phase variation of the reflection coefficient for both illumination directions when we fix the height $H_0 = 75$ nm and change the diameter $D_0 = 20 - 280$ nm. The amplitude of the reflection coefficient is close to unity within

an acceptable range while it drops down to one half at both ends of the diameter variations. The situation is a bit worse for the case when we fix the diameter $D_0 = 150$ nm and vary the height $H_0 = 10 - 140$ nm. In this case, we obtain a phase variation of 2π only for the forward illumination direction while the amplitude of the reflection coefficient, in some region, drops down to 20 percent [Fig. 3.4.9(b)]. We should mention that better results might be obtained if the geometry is carefully optimized. The presented example only serves the purpose to demonstrate the idea.

Another important point is that the proposed nanoantenna in the array provides asymmetric phase variations. That is, the variation of reflection phases are different for different illumination directions. It means that we may properly design a reflectarray with two different properties when looking from different directions onto the plane. This is impossible using symmetrical structures which do not provide bianisotropic properties.

The most important point about the proposed reflectarray is its transparency out of the resonance band. Indeed, in the investigated reflectarray, we do not rely on a metallic back reflector [110,113,114]. Instead, we have offered resonant nanoantennas with bianisotropic properties to obtain a full reflection. This gives us the possibility to preserve transparency outside the resonance band in the reflectarray. This transparency is very important when combining multiple receiving/transmitting systems. Then, we need a reflectarray at a frequency band while we do not want to prevent signals to get transmitted out of that frequency band.

In a short summary of this section, we proposed a high-index dielectric nanoantenna which supports a bianisotropic (magneto-electric) coupling in addition to its electric and magnetic couplings. We demonstrated that the magneto-electric coupling can be tuned by geometrical parameters of the proposed nanoantenna. The nanoantenna possesses different backward radar cross sections when illuminated by a plane wave from opposite directions while it exhibits an identical forward radar cross sections. Moreover, the extinction and scattering cross sections are identical for both illumination direction. For a periodic planar array of such a bianisotropic nanoantenna, we observed interesting optical features, e.g. asymmetric reflection phases for opposite illumination directions. We illustrated that the array provides a 2π phase variation together with an acceptable reflection amplitude over the whole phase spectrum by tuning the geometrical parameters of the nanoantenna. Finally, we demonstrated that the employment of the proposed resonant nanoantenna together with the absence of a fully reflective metallic screen gives the opportunity of *out-of-band transparency* in reflectarrays. All the mentioned effects are the direct outcomes of the suggested *bianisotropy*. The observed lossless bianisotropic effect might open a new direction to the design of high-index nanoantennas and metasurfaces;

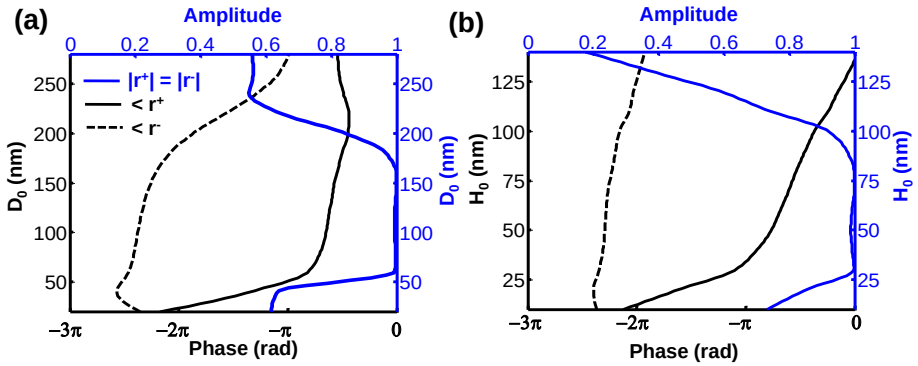

Figure 3.4.9: (a) The phase of the reflection coefficient of an array of nanoantennas versus the diameter of the air hole at resonance frequency $f = 405$ THz for two different illumination directions denoted by r^+ and r^-. H_0 is fixed to 75 nm. (b) The same plot as in (a) for variation of air hole height. D_0 is fixed to 150 nm.

e.g, reflectarrays, transmitarrays, and Huygens sources.

3.5 Concluding remarks

In this chapter, we introduced two bianisotropic nanoantennas made of different materials, namely, plasmonic nanoantennas (made of gold) and high-index dielectric nanoantenna (e.g. silicon). Our findings can be summarized as following :

Plasmonic bianisotropic nanoantennas- we introduced nonidentical coupled nanopatches separated by a dielectric spacer, which exhibit a strong magneto-electric (bianisotropic) coupling. This coupling is achieved by breaking the symmetry of a nanoantenna, i.e. using two coupled nanopatches with different lateral dimensions. The magneto-electric coupling can be tuned by changing the geometrical dimensions. We have shown that this strong magneto-electric coupling can offer interesting optical features such as directional radiation pattern, complete light absorption, and strong asymmetric reflections when illuminated from opposite directions. Finally, it would be interesting to summarize all the scattering properties of such nanoantennas as following [Table. 3.1]:

- *Scattering, absorption and extinction cross sections*: Scattering/absorption cross section depends on the illumination directions (forward and backward), i.e. $C^+_{\text{abs}} \neq C^-_{\text{abs}}$, $C^+_{\text{sca}} \neq C^-_{\text{sca}}$. However, according to the optical theorem, the extinction cross section for both (any) illumination directions should be identical, i.e. $C^+_{\text{ext}} = C^-_{\text{ext}}$.

- *Forward and backward radar scattering cross sections*: The backward scattering

cross section depends on the illumination directions, i.e. $Q^{+}_{\mathrm{RBS}} \neq Q^{-}_{\mathrm{RBS}}$. However, the forward cross section is independent of the illumination directions, i.e. $Q^{+}_{\mathrm{RFS}} = Q^{-}_{\mathrm{RFS}}$. This is a direct consequence of the optical theorem.

- *Transmission, reflection, and absorption*: Reflection/absorption depends on illumination directions, i.e. $R^{+} \neq R^{-}$, $A^{+} \neq A^{-}$. However, the transmission is independent of the illumination directions, i.e. $T^{+} = T^{-}$.

High-index dielectric bianisotropic nanoantennas- we introduced an all dielectric nanoantenna with a strong magneto-electric coupling. The key to obtain this magneto-electric coupling is breaking the symmetry of a high-index dielectric cylinder by drilling an air hole inside. We showed that the magneto-electric coupling will lead to interesting features for both individual nanoantennas as well as for an array of such nanoantennas. For instance, the individual nanoantenna shows different radiation patterns when illuminated from opposite directions. It also provide different phases in the reflected amplitude for an array made of such nanoantennas. Finally, it would be interesting to summarize all the scattering properties of a high-index (lossless) bianisotropic nanoantenna as following [Table. 3.1]:

- *Scattering, absorption and extinction cross sections*: All of them are independent of the illumination directions, i.e. $C^{\pm}_{\mathrm{abs}} = C^{\pm}_{\mathrm{sca}} = C^{\pm}_{\mathrm{ext}}$.

- *Forward and backward scattering cross sections*: The backward scattering cross section depends on the illumination directions, i.e. $Q^{+}_{\mathrm{RBS}} \neq Q^{-}_{\mathrm{RBS}}$. However, the forward cross section does not depend of the illumination directions, i.e. $Q^{+}_{\mathrm{RFS}} = Q^{-}_{\mathrm{RFS}}$.

- *Transmission, reflection, and absorption*: Reflection and transmission are independent of the illumination directions. $R^{+} = R^{-}$, $T^{+} = T^{-}$ and the absorption is zero, i.e. $A^{\pm} = 0$. However, the reflection coefficients show different phases for opposite illumination directions, i.e. $r^{+} \neq r^{-}$.

Table 3.1: Comparison between optical properties of plasmonic and dielectric nanoantennas for forward (+) and backward (−) illumination directions.

Optical response	Individual nanoantenna		Array of nanoantennas	
	Dielectric	Plasmonic	Dielectric	Plasmonic
Scattering cross section	$C^+_{\mathrm{sca}} = C^-_{\mathrm{sca}}$	$C^+_{\mathrm{sca}} \neq C^-_{\mathrm{sca}}$	-	-
Absorption cross section	$C^+_{\mathrm{abs}} = C^-_{\mathrm{abs}}$	$C^+_{\mathrm{abs}} \neq C^-_{\mathrm{abs}}$	-	-
Extinction cross section	$C^+_{\mathrm{ext}} = C^-_{\mathrm{ext}}$	$C^+_{\mathrm{ext}} = C^-_{\mathrm{ext}}$	-	-
Forward radar cross section	$C^+_{\mathrm{RFS}} = C^+_{\mathrm{RFS}}$	$C^+_{\mathrm{RFS}} = C^+_{\mathrm{RFS}}$	-	-
Backward radar cross section	$C^+_{\mathrm{RBS}} \neq C^+_{\mathrm{RBS}}$	$C^+_{\mathrm{RBS}} \neq C^+_{\mathrm{RBS}}$	-	-
Transmission	-	-	$T^+ = T^-$	$T^+ = T^-$
Reflection	-	-	$R^+ = R^-(r^+ \neq r^-)$	$R^+ \neq R^-$
Absorption	-	-	$A^+ = A^-$	$A^+ \neq A^-$

4 Nanoantennas as perfect absorbers: Near-field and far-field schemes

4.1 Introduction

In the previous chapters, it is shown that an array of electric dipole moments can absorb at most 50 percent of impinging light. The important question is: How to increase the absorption of an array of nanoantennas, which support electric or magnetic moments? In chapter 3, we suggested an array of nonidentical coupled nanopatches, which exhibit both electric and magnetic dipole moments. The total absorption is explained by a balanced condition between the induced electric and magnetic dipole moments. In this chapter, we will focus on the optical properties of an array of gold nanoantennas on top of a gold ground plate in two different regimes, i.e.a near-field and a far-field scheme. We will show that it is possible to achieve complete light absorption for both regimes.

In the first scheme, we will explore the strong near-field coupling between the nanoantennas and the metallic ground plate. We will introduce concept of the extreme coupling in order to obtain deep subwavelength nanoantennas or nanocavitites that can fully absorb the incident light at a set of discrete frequencies [Fig. 4.1.1 (a)]. The *extreme coupling* occurs when the dielectric spacer is only a few nanometers. We will explain it in details later. The perfect absorber in the extreme coupling regime possesses a robust response over a large angle incident. We will use a simple analytical model to predict the resonance frequency of the coupled system consisting of the nanoantenna coupled to the ground plate. The system is studied analytically and numerically, but also experimental results are presented here for completeness. These results come from a collaboration with various groups at the Friedrich-Schiller Universität Jena and were provided by co-workers. All the results are self-consistent and in good agreement.

In the far-field scheme, the dielectric spacer between the nanoantennas and the

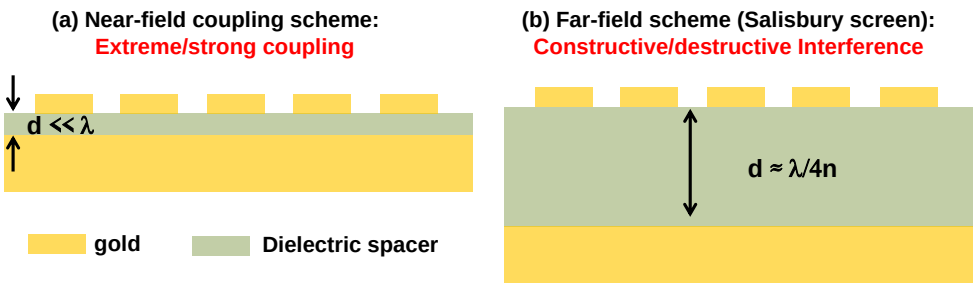

Figure 4.1.1: Schematic view of a perfect absorber made of gold nanopatches and gold ground plate separated by a dielectric spacer. (a) Near-field scheme. (b) Far-field scheme

metallic ground plate is considerably large such that near-field coupling can be neglected [Fig. 4.1.1 (b)]. In this case, the underlying physical mechanism of the perfect absorber can be understood by a simple asymmetric Fabry-Perot model with two mirrors, the upper one is the array of gold nanoantennas and the lower one is the metallic ground plate. The total absorption occurs when the reflection coefficient is fully suppressed due to the destructive interference.

We note that most of the findings of this chapter have been previously published in Ref. [51, 74, 83, 91].

4.2 Near-field scheme: Extreme Coupling

Plasmonic perfect absorbers have tremendous applications in, e.g. thermal emitters [9, 115–117], plasmonic sensors [9, 118] and solar cells [89, 119]. The canonical structure that is usually used to achieve total absorption is shown in Fig. 4.1.1 (a). It consists of an array of nanoantennas with arbitrary shapes on top of a metallic ground plate. Both constituents are separated by a dielectric spacer. The metallic ground plate can suppress the transmission $T = 0$. Perfect absorption can be achieved when the structure is at critical coupling, which causes also a vanishing reflection [31, 49]. Therefore, the entire energy of the incoming wave can be absorbed by the structure. The majority of the suggested perfect absorbers in the literature does not operate in a deep-subwavelength regime [5]. This is due to the fact that these perfect absorbers possess thick dielectric spacers, i.e. in the order of tens of nanometers. Therefore, the absorption changes strongly when illuminated at oblique incidence. We note that most of the findings of this section have been previously published in Ref. [91].

In this section, we will introduce the concept of extreme coupling, which allows to achieve a deep-subwavelength perfect absorber. Afterwards, we propose a semi-analytical model to predict the resonance frequencies of the proposed perfect ab-

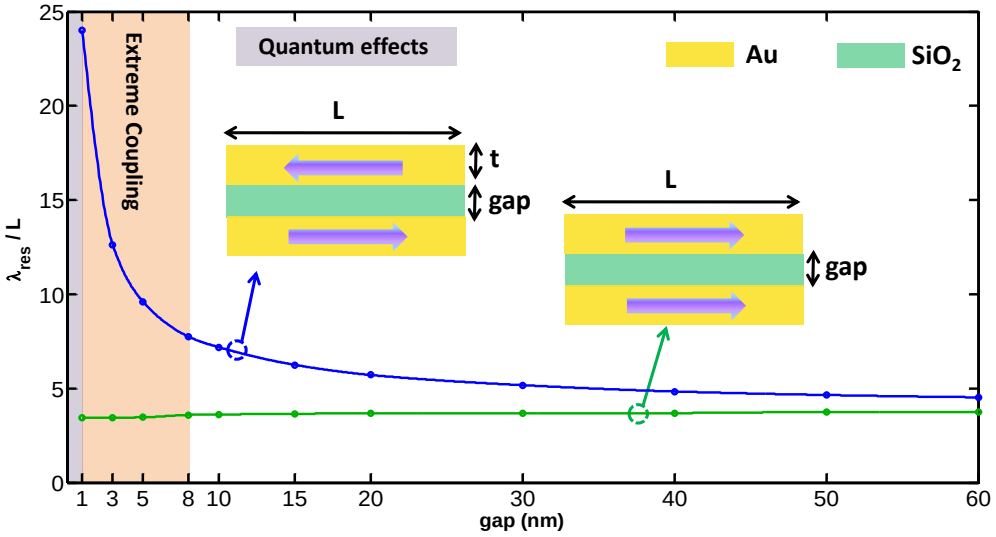

Figure 4.2.1: The resonance position for both symmetric and antisymmetric modes of coupled nanopatches as a function of the thickness of the dielectric spacer (gap). The length of the nanopatches is $L = 250$ nm and the thickness of the gold nanopatches is t = 50 nm. The extreme coupling occurs when the spacer is ultra-thin, i.e. in the order of few nanometers. Note that the dielectric spacer smaller than 1 nm leads to quantum effects, which is beyond the scope of this thesis.

sorber [Fig. 4.1.1 (a)]. The semi-analytical model can predict all the supported modes of the structure. The predicted resonance frequencies of the model are in good agreement with the numerical one. Finally, we will compare the theoretical and experimental results of the proposed absorber. The small deviation will be explained by surface roughness of the thick metallic ground plate.

4.2.1 Extreme Coupling

To understand the concept of extreme coupling, we first will focus on the resonance frequency of a simple structure made of two coupled nanopatches. This structure is similar to the perfect absorber shown in the inset of Fig. 4.2.1. As already mentioned in the previous chapter, it supports localized modes, namely, symmetric and antisymmetric modes [see inset of Fig. 4.2.1]. The resonance frequency (normalized wavelength, i.e. λ_{res}/L , L is the width of nanopatches) of the coupled nanopatches as a function of the dielectric spacer (gap) is also shown in Fig. 4.2.1. They are calculated by a full wave simulation. However, a simple analytical model can also predict the resonance position which we will show later. The resonance position of the symmetric mode only marginally changes upon decreasing the spacer [green line in Fig. 4.2.1]. In contrast, the resonance position of the antisymmetric mode

changes significantly [blue line in Fig. 4.2.1]. *Extreme coupling* occurs whenever the structure has an ultra-thin dielectric spacer, i.e. in the order of few nanometers. In other word, *extreme coupling* allows to obtain resonances in the deep-subwavelength domain, i.e. $\lambda_{\mathrm{res}}/L > 10$ [51, 91, 120]. In following subsections, we will show that the ultra-thin dielectric spacer can be realized experimentally by the atomic layer deposition techniques [14, 51, 91].

Note that for dielectric spacers below 1 nm quantum effects are expected to emerge that cannot be explained on the grounds of the classical theory as considered in the context of this thesis [121–123]. Therefore, we would like to not consider these effects here. It is important to mention that not just the spectral position of the resonances but also the field enhancement in this structure depends on the thickness of the dielectric spacer [5, 9, 12, 50, 124, 125]. The ultimate field enhancement can only be obtained in the extreme coupling regime [91, 126]. The concept of extreme coupling that relies on very thin dielectric spacers is universal and can be applied to any type of structures [50, 120, 126–128]. We believe that many applications can directly benefit from this concept, e.g. deep-subwavelength nanocavities and truly homogenous metamaterials [51, 83, 129].

4.2.2 Theory: Fabry-Perot model

In this subsection, we explain a semi-analytical approach (known as Fabry-Perot model) to predict the resonance frequencies of a perfect absorber in near-field coupling regime [130–134]. This analytical approach is powerful and offers a proper understanding on the behavior of the perfect absorber in the extreme coupling regime. Fig. 4.2.2 shows the schematic view of the perfect absorber made of gold nanowires and gold ground plate separated by a dielectric spacer. The resonances of the perfect absorber occur whenever the phase accumulation per round trip due to the propagation (i.e. $2\beta L = 2k_0 n_{\mathrm{eff}} L$) and the reflection (i.e. $2\phi_{\mathrm{r}}$) is an integer multiple of 2π, i.e.

$$2k_0 n_{\mathrm{eff}} L + 2\phi_{\mathrm{r}} = 2m\pi \quad \rightarrow \quad \lambda_{res} = \frac{2\pi n_{\mathrm{eff}} L}{m\pi - \phi_r} \tag{4.2.1}$$

where, $m = 1, 2, 3, ...$ is the order of resonance, and ϕ_r is the phase of the reflection coefficient at the structure termination, L is the size of the nanoantenna, k_0 is the free space wavenumber, and n_{eff} is the effective index of the guided mode. The origin of the resonance can be traced back to the constructive interference of light which is reflected back and forth at the termination of the structure [91, 134, 135].

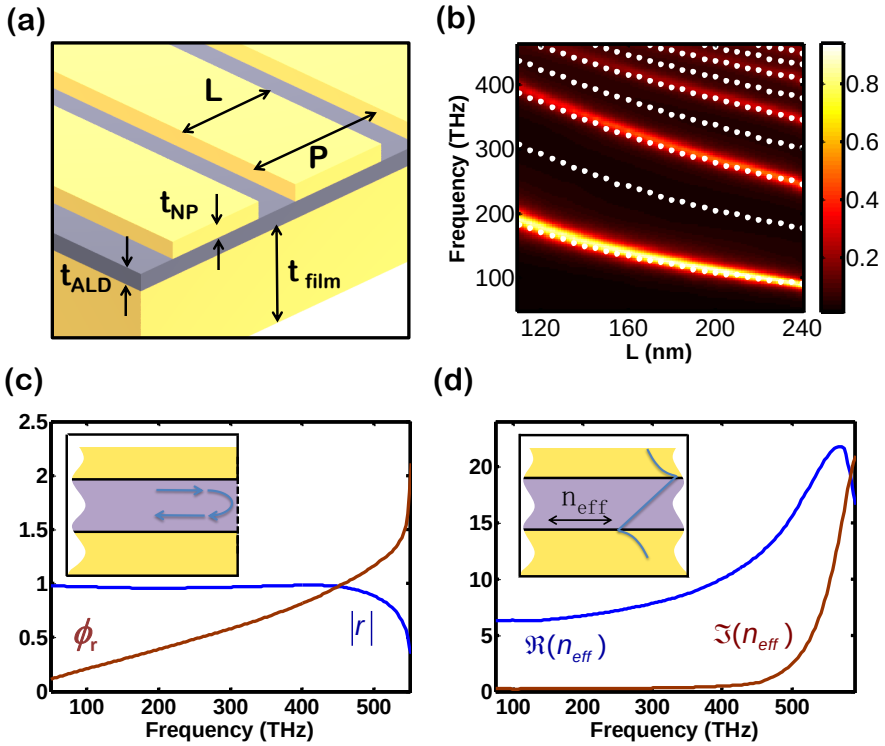

Figure 4.2.2: (a) Schematic of the investigated two-dimensional perfect absorber. (b) The simulated absorption as a function of nanowire width and frequency at normal incidence. The predicted resonance positions of all supported modes by the perfect absorber are shown with white doted curves. The modes are calculated by the semi-analytical model. (c) Phase and modulus of the reflection coefficient as a function of frequency. (d) Real and imaginary parts of the effective index of the guided mode as a function of frequency. The geometrical parameters are $P = 250\,\text{nm}$, $L = 100 - 240\,\text{nm}$, $t_{\text{film}} = 200\,\text{nm}$, $t_{\text{ALD}} = 3\,\text{nm}$, $t_{\text{NP}} = 30\,\text{nm}$. (c)

It is important to mention that the physical origin of the resonances of the perfect absorber are propagating surface plasmon polaritons (PSPPs).

In order to use Eq. 4.2.1, we should calculate the effective index $n_{\text{eff}}(\omega)$ and the phase of the reflection coefficient at the structure termination ϕ_{r}. First, we calculate the dispersion relation of the guided eigenmodes, i.e. $n_{\text{eff}}(\omega)$. Then, this mode is considered as an illumination at the termination of the finite structure (perfect absorber). Finally, the total field in a plane normal to the x axis and located at $x = 0$ was calculated. The complex reflection coefficient of this mode at the termination is extracted by employing the orthogonality relations obtained by the unconjugated reciprocity theorem [91, 134], which yields an expression for the reflection coefficient as

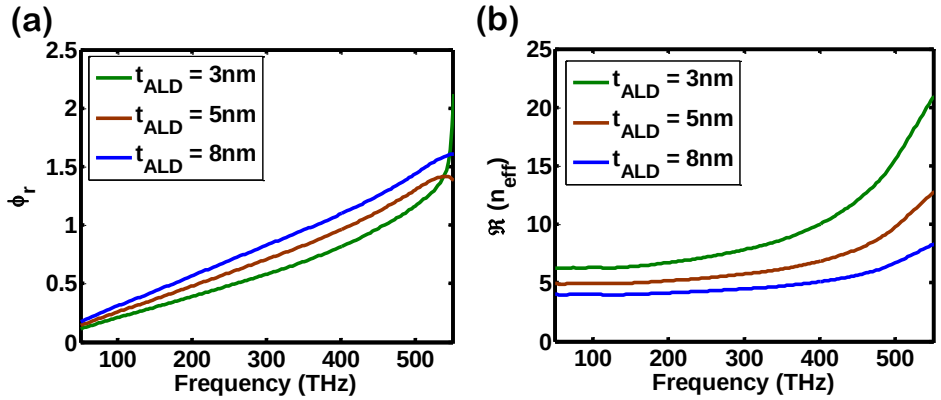

Figure 4.2.3: (a) The phase of reflection as a function of frequency for different dielectric spacers. (b) The real part of the effective index as a function of frequency and the thickness of the dielectric spacer.

$$r = -\exp^{-i2\beta L} \frac{\int_{-\infty}^{\infty} E_{0z}(0,z)\left[H_y(0,z) - H_{0y}(0,z)\right] \mathrm{d}z}{\int_{-\infty}^{\infty} E_{0z}(0,z) H_{0y}(0,z)\, \mathrm{d}z}, \tag{4.2.2}$$

where $H_y(0,z)$, and $E_z(0,z)$ are the magnetic and the electric field components of the incident propagating surface plasmon polariton mode at $x = 0$, and $\beta = k_0 n_{\mathrm{eff}}$ is the propagation constant of the antisymmetric mode. All quantities, except the nanowire geometry, depend on frequency. Note that the reflection coefficient is complex and strongly depends on the shape of the nanowire termination. The modulus ($|r|$) as well as the phase (ϕ_r) of the reflection coefficient of the antisymmetric mode is shown in Fig 4.2.2.

Let us focus on a two-dimensional perfect absorber. This means that the structure is infinitely extended in y-direction [Fig. 4.2.2]. A schematic view of the two-dimensional perfect absorber is shown in Fig. 4.2.2 (a). All the geometrical parameters are shown in the figure caption. Note that the resonance frequencies of a two-dimensional perfect absorber are almost identical to the three-dimensional one [31, 136]. This similarity occurs because the physical behavior of the three-dimensional perfect absorber is similar to the two-dimensional one.

At lower frequencies, the metal can be considered as a perfect electric conductor and the phase ϕ_{r} in Fig. 4.2.2 (c) can be neglected. Our numerical result also confirms that the modulus $|r|$ is close to unity and the phase is quite small. At higher frequencies the phase will increase because the metal behaves as a strongly coupled plasma [17]. This allows to obtain a deep-subwavelength structure. Figure 4.2.2 (d) shows the real and imaginary parts of the effective index of the structure as a function of frequency. It can be seen that the effective index increases by increasing

the frequency. The imaginary part is almost zero for lower frequencies (smaller than 300 THz). This ensures pronounced and narrow resonances for the perfect absorber. However, the real part of the effective index is larger than 6 at all frequencies and rises up to 20 in the visible frequencies. The effective index of the structure increases strongly while decreasing the thickness of dielectric spacer (i.e. t_{ALD}). To understand the effect of the thickness of dielectric spacer, the effective index of the structure is calculated for different dielectric thickness, i.e. $t_{\mathrm{ALD}} = 3, 5, 8$ nm. The simulation results also show that the phase of reflection will slightly increase by increasing the thickness of dielectric spacer [Fig. 4.2.3 (a)]. This large effective index is eventually the key to achieve deep sub-wavelength resonances. The phase pick up in reflection just increases linearly with frequency and it is very similar for all thicknesses. However, the effective index of the structure n_{eff} will decrease by increasing the thickness of dielectric spacer [Fig. 4.2.3 (b)] [54].

The simulated absorption at normal incidence for the two-dimensional structure as a function of frequency and wire width (L) is shown in Fig. 4.2.2 (b). The white dotted lines are calculated by the semi-analytical model. The simulated absorption peaks and the estimated resonance frequencies of the excited modes based on a semi-analytical model are in excellent agreement. The resonance frequencies of all supported modes by the structure shift to lower frequencies by increasing the width L [Fig. 4.2.2]. Note that the odd modes can be excited only at oblique incidence whereas the even modes can be excited for both normal and oblique incidence. This will be discussed in detail in the next subsection. However, all the even and odd modes can be simultaneously predicted by the semi-analytical model [Fig. 4.2.8 (b)]. Therefore, we can conclude that the Fabry-Perot model properly predicts the resonance position of all the supported modes of the perfect absorber. In the next subsection, we will numerically and experimentally investigate a three-dimensional perfect absorber in the near-field scheme. We will show that the concept of the extreme coupling allows to achieve deep-subwavelength perfect absorber. We will show that the measured and simulated absorption are in good agreement [Fig. 4.2.6].

4.2.3 Array of nanopatches on top of a metallic ground plate

The investigated perfect absorber consists of an array of gold nanopatches on top of a gold metallic ground plate and separated by a thin dielectric spacer. The investigated structure and a SEM image of a sample fabricated by colleagues at the Friedrich-Schiller Universität Jena are shown in Fig. 4.2.5 (a) and (b). Figure 4.2.4 also shows an artistic view of the structure. The geometrical parameters of the perfect absorber are selected such that the structure possesses well-pronounced resonances with large

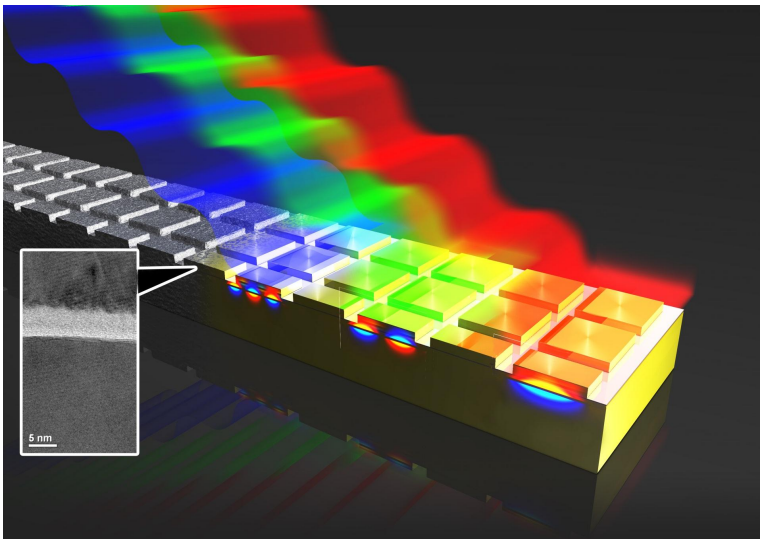

Figure 4.2.4: Schematic of the perfect absorber in the extreme coupling regime. The perfect absorber consists of a gold nanopatch deposited on a gold ground plate and separated by an ultrathin dielectric spacer. The ultrathin dielectric spacer is fabricated with ALD technique. The structure supports different modes (indicated with the different colors). The current distributions as well as a TEM image of a cross section of the fabricated sample are shown in the figure.

absorption. The proposed structure will support a fundamental as well as higher-order antisymmetric modes. The perfect absorber is periodic in x and y directions with a periodicity of $P_{\mathrm{x}} = P_{\mathrm{y}} = 250$ nm. An extremely thin layer of fused silica with dielectric index of $\varepsilon = 2.25$ is used as a dielectric spacer on top of the metallic ground plates. This thin spacer has been fabricated by using atomic layer deposition (ALD). The patch nanoantennas as well as the ground plate are made of gold and the permittivity is taken from Ref. [137]. The semi-analytical approach known as Fabry-Perot model can predict the resonance position of the proposed structure [shown for two-dimensional absorber in Fig. 4.2.2 (b)]. In order to avoid the emergence of quantum plasmonic effects, we consider dielectric spacers thicker than 3 nm. Note that the quantum effect investigation is out of scope of this thesis and established very well in the literature . However, we will show that the limiting factor for the suggested perfect absorber is the unavoidable surface roughness that contributes to a degradation of resonances.

We would like to mention that the deep subwavelength perfect absorber in this chapter have been fabricated by Dr. Hüebner, Institute of Photonic Technology (IPHT), Jena, Germany and measured by Dr. Ekaterina Pshenay-Severin at Institute of Applied Physics Friedrich-Schiller-University Jena. The fabrication of the structure starts on the wafer level by using a 4 inch fused silica wafer. At first,

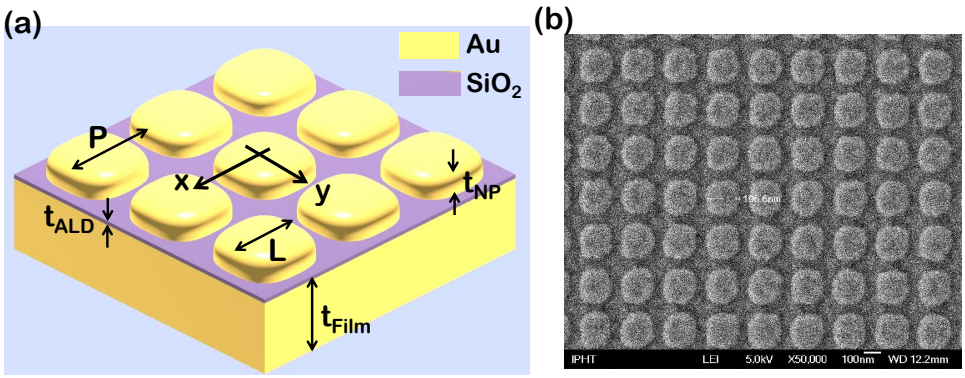

Figure 4.2.5: (a) Schematic view of the plasmonic perfect absorber with an extremely thin dielectric spacer. b) SEM image of a fabricated perfect absorber. Geometrical parameters are chosen as $P = 250\,\mathrm{nm}$, $W = 100 - 200\,\mathrm{nm}$, $t_{\mathrm{film}} = 200\,\mathrm{nm}$, $t_{\mathrm{ALD}} = 3 - 8\,\mathrm{nm}$, $t_{\mathrm{NP}} = 30\,\mathrm{nm}$.

the 200 nm thick gold ground plates were prepared. Sliced in chips the samples were individually coated with ultrathin SiO_2-films (in the range of 3 to 8 nm) by means of ALD. Eventually, the thin 2D-gold grating nanostructure was prepared on top of the ALD layer by using aligned electron beam lithography, Ti/Au - evaporation and lift-off-technique. The optical measurements were performed by a FTIR Bruker spectrometer connected to a microscope in reflection mode. Reflection spectra were measured for both principle polarizations in the spectral range from 75 THz to 600 THz. Measurements in such a broad spectral range were realized using specific detectors for certain spectral ranges. The reflection for two angles of incidence was investigated. The measurements of the reflection for normal incidence were conducted with a 15 x objective (NA=0.40) that corresponds to the half cone opening angle of 24 degrees. The reflection measurements for oblique incidence were performed with Bruker's grazing angle objective. More details about the measurement and experiment can be found in Ref. [91].

The reflection spectra for both measurement and simulation are shown in Fig. 4.2.6 (a) and (b) for normal ($\theta = 0^o$) as well as oblique incidence ($\theta = 70^o$) for TM polarization, respectively. The length of the nanopatch is $L = 195\,\mathrm{nm}$ and the dielectric spacer has a thickness of 3 nm. This thin dielectric spacer between the gold plates of the structure will lead to a large propagation constant and, hence, effective index. This allows to achieve a perfect absorber which supports multiple resonances [4.2.6 (a) and (b)]. At normal incidence, the plane wave illumination can excite only even order modes. The current distributions of such modes are sketched in Fig. 4.2.6 (e), i.e. the fundamental mode (FM) and second order mode. In order to excite odd modes in addition to the even modes, one need to break the symmetry by an oblique illumination. The first three modes, i.e. the fundamental,

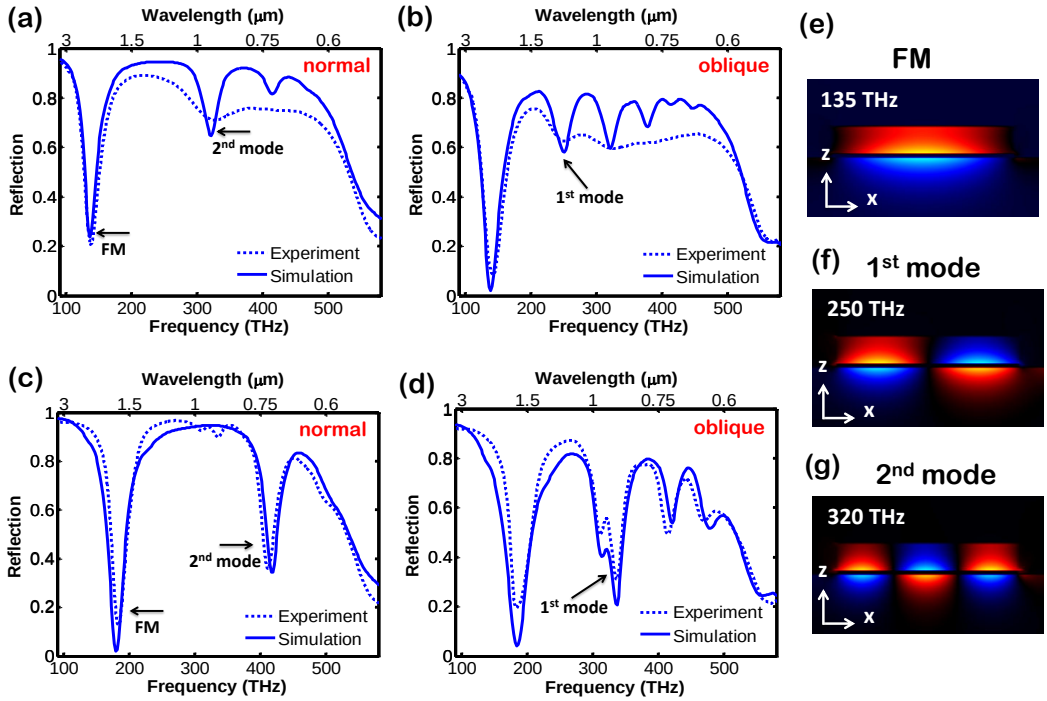

Figure 4.2.6: (a) and (b) experimental and numerical reflection spectra at normal and oblique incidence ($\theta = 70^o$) for $L = 195$ nm with 3 nm gap, respectively. (c) and (d) show experimental and numerical reflection spectra for $L = 200$ nm with an 8 nm gap at normal and oblique incidence, respectively. (e)-(g) Current distribution (x-component) of the fundamental, first, and second modes for $L = 195$ nm with 3 nm gap. The perfect absorber is illuminated by a TM polarized plane wave. The magnetic field is along the y direction.

the first, and the second order mode appear at 135, 250 and 320 THz, respectively, with negligible dependence on the incidence angle [4.2.6 (a) and (b)]. It can be seen that the fundamental mode is red shifted (2.25 μm) due to an extreme near-field coupling between the gold nanopatches and the ground plate. This provides a deep-subwavelength perfect absorber with an aspect ratio of resonance wavelength to period of roughly $\lambda/P \approx 10$. This is considered huge in comparison with any conventional plasmonic perfect absorbers. Note that typical values for this ratio as achievable with a spacer of 30 nm are around 3 [9].

The numerical results are in excellent agreement with the measured reflection at lower frequencies. At higher frequencies, the measured reflection is generally smaller and the resonances are less pronounced and broader. These small discrepancies can be fully explained by the surface roughness of the thick metallic ground plate. We will discuss it in details later. At fundamental mode (FM), the absorption is $A > 0.75$ at both normal and oblique incidence. Note that the absorption is less pronounced for higher order modes (i.e. first and second mode) due to an impedance mismatch

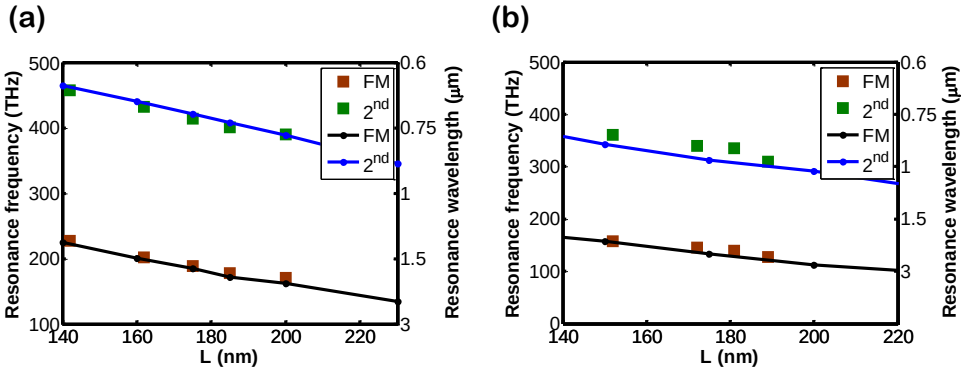

Figure 4.2.7: (a) shows the measured (dots) and simulated (solid lines) resonance frequencies of the perfect absorber as a function of its length (L) for the fundamental and second order mode. (a) 3 nm spacer; (b) 8 nm spacer.

between the incoming wave and the structure.

Figure 4.2.6 (e) shows the current distribution of the first three excited modes of the structure. From these current distributions it can be concluded that all the supported modes by the structure can be fully understood from the fundamental mode of the metal-insulator-metal (MIM) waveguide. The fundamental mode is antisymmetric with respect to the current in the upper and the lower metallic plate and sometimes called the magnetic dipolar one [138, 139]. Note that the symmetric MIM-waveguide mode which is usually identified with the electric dipolar mode occurs at very high frequencies.

Figure 4.2.6 (c) and (d) show the measured and simulated reflection spectra of the structure with a length of the nanopatch of $L = 200\,\text{nm}$ at normal ($\theta = 0^o$) and oblique incidence ($\theta = 70^o$), respectively. In this case, the dielectric spacer is considerably thick and fabricated with ALD, i.e. $t_{\text{ALD}} = 8\,\text{nm}$. It can be seen that there is an excellent agreement between the measured and simulated reflection spectra [Fig. 4.2.6 (c) and (d)] at all frequencies of interest. This better agreement compared to $t_{\text{ALD}} = 3$ nm can be attributed to the marginal impact of the surface roughness for a thicker dielectric spacer. We will explain it in detail later.

As already explained in the previous subsection, the effective index of the structure (i.e. $t_{\text{ALD}} = 8\,\text{nm}$ dielectric spacer) will decrease compared to a $t_{\text{ALD}} = 3\,\text{nm}$. This allows to achieve a better impedance matching and also the resonances shift to higher frequencies. Furthermore, less modes can be excited in the investigated spectral range. Nonetheless, we can easily identify all the supported modes, i.e. the fundamental, the first, second, and third one in the measured spectra at 180, 335, 415 and 480 THz, respectively. The measured absorption for the fundamental mode

is roughly 0.9 at normal incidence. In fact, this is due to the fact that the structure with thicker dielectric spacer can offer better impedance matching with impinging light.

Similar spectra to those shown in 4.2.6 are measured at normal incidence for the proposed structure with a different length L while maintaining the spacer thickness. The dependence of the resonance positions of the fundamental and the second order mode extracted from the measured and simulated spectra as a function of the length of the structure (L) for $t_{\mathrm{ALD}} = 3\,\mathrm{nm}$ and $t_{\mathrm{ALD}} = 8\,\mathrm{nm}$ are shown in Fig. 4.2.7, respectively. The resonance frequency ω_{res} of the structure depends on the length of nanopatches L, i.e. it decreases by increasing the length of the nanopatches ($\omega_{\mathrm{res}} \propto 1/L$). Our numerical predictions show an excellent agreement between the experimentally measured resonance frequencies for thick as well as very thin spacers. The results show that for the small ALD gap of 3 nm, the resonance frequency of the fundamental mode will shift to extremely long wavelengths when compared to the size of nanopatches.

4.2.4 Surface roughness

As already highlighted in the previous subsection, the minor deviation between the experiment and numerical results can be addressed to the surface roughness [91]. In order to properly quantify the surface roughness, we used only two parameters, namely the maximum height and modulation frequency. An AFM measurement was conducted at the metallic ground plate before the deposition of the ALD layer to be able to estimate both quantities. Figure 4.2.8 (c) shows an a selected cut over the distance of a 4 period super-cell. The measured surface roughness is not too large (maximum modulation height is 10 nm). However, this modulation height is almost equal to the dielectric spacer (e.g. $t_{\mathrm{ALD}} = 10$ nm). This should affect the optical response of the perfect absorber strongly. TEM measurements are conducted to determine the surface roughness of each layer [Fig. 4.2.8 (b)]. The large modulation height is due to the large overall thickness of 200 nm of the evaporated ground plate. This can be significantly reduced for thinner plates or by using crystalline grown gold.

The surface roughness considered in the simulations is shown in Fig. 4.2.8 (d). The maximum modulation height is assumed to be 10 nm and the modulation frequency is chosen such that the roughness distribution resembles the measured one [Fig. 4.2.8 (b)]. The ALD layer as well as the upper metallic nanowires are assumed to be conformably deposited. Figure 4.2.8 (e) and (f) show the simulated reflection spectra of the structure as a function of frequency for $t_{\mathrm{ALD}} = 3$ and 8 nm. Fist, we

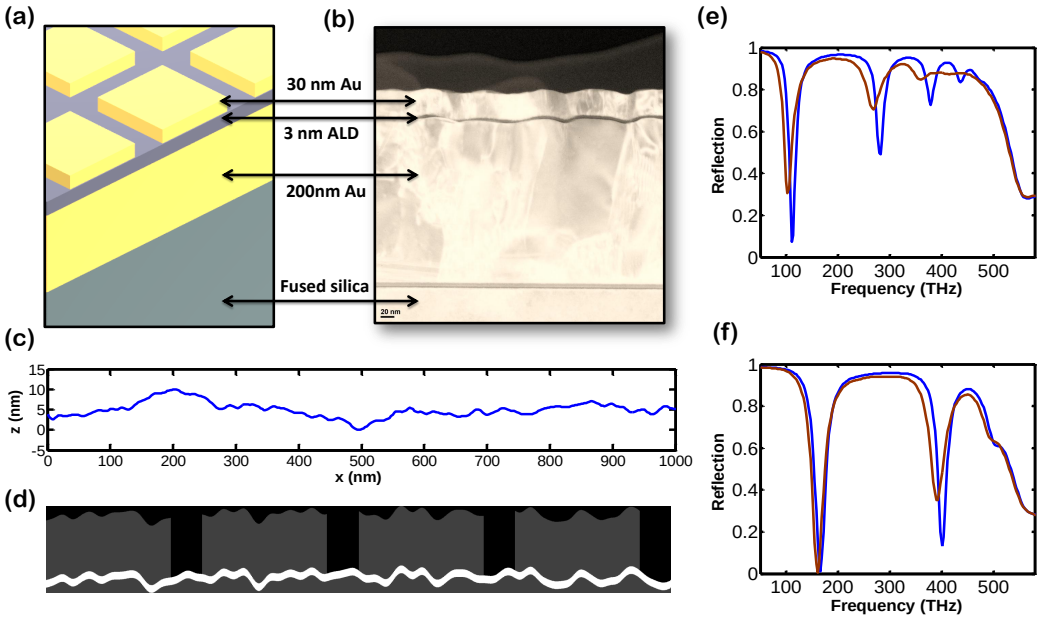

Figure 4.2.8: (a) Schematic view of the plasmonic perfect absorber. (b) Cross-sectional TEM picture of a fabricated sample. (c) The surface topology based on AFM measurement of a fabricated sample. (d) The surface roughness of a two-dimensional perfect absorber for 4 unit cells. (e) and (f) The reflection as function of frequency without (blue line) and with (brown line) surface roughness for thin and thick dielectric spacers ($t_{\mathrm{ALD}} = 3, 8$ nm), respectively.

investigate a thin ALD gap, i.e. $t_{\mathrm{ALD}} = 3$ nm, all resonance frequencies are slightly shifted to lower frequencies [Fig 4.2.8 (e)]. Moreover, the resonance dip of the structure with surface roughness is less pronounced compared to the ideal case. At higher frequencies, the surface roughness leads to spectral broadening. This will explain the small deviation between numerical and experimental results. However, for the thick gap ($t_{\mathrm{ALD}} = 8$ nm), the spectral broadening is almost negligible which is similar to the experimental observations. Note that the surface roughness is the dominating effect for the investigated structure and quantum effects can be fully neglected.

In this section, we proposed a deep-subwavelength perfect absorber based on extreme coupling. We showed that the extreme coupling can be obtained by a thin dielectric spacer, in the order of few nanometers, which is experimentally achieved by an atomic layer deposition (ALD). We used a semi-analytical approach based on Fabry-Perot model to predict the resonance frequencies of the perfect absorber. The predicted resonance frequencies are in a good agreement with numerical results. Most of the theoretical and numerical findings of this section are fully supported by experimental results. The small deviation between the numerical and experimental results is explained by surface roughness.

4.3 Far-field scheme: Destructive/constructive interference

In Chapter 2, we have shown that the absorption of an array of rectangular nanopatches is limited to 50 percent. Note that this is a universal limitation as long as the nanopatches can be only described by an electric dipole moment, i.e. all higher orders are negligible. One of the simplest and practical approaches to enhance the absorption is using a metallic ground plate in order to suppress the transmission [Fig. 4.3.1 (a)]. In fact, complete light absorption can occur when the reflection goes to zero ($R = 0$) due to the fact that the transmission is zero ($T = 0$) (thick metallic ground plate). In order to achieve zero reflection the dielectric spacer should be properly tuned such that the directly reflected light interferes destructively with the light that experiences multiple reflections in the layer [Fig. 4.3.1 (a)]. In the next subsection, we will show that the optical response of the structure can be fully explained by a simple Fabry-Perot model. This model is only valid for considerably thick dielectric spacers (i.e. far-field scheme).

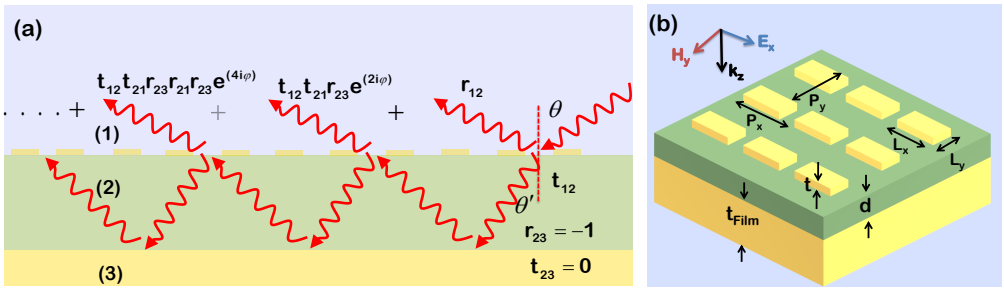

Figure 4.3.1: (a) Asymmetric Fabry-Perot cavity model for a perfect absorber in far-field interference scheme. (b) Schematic of the proposed perfect absorber. The geometrical parameters of the structure are: $t_{\mathrm{Film}} = 300$ nm, $d = 20 - 1500\,\mathrm{nm}$, $L_x = 400\,\mathrm{nm}$, $L_y = 100\,\mathrm{nm}$, $P_X = P_y = 500$ nm and $t = 20$ nm.

4.3.1 Theory: Asymmetric Fabry-Perot cavity

Let us focus on the underlying mechanism of the perfect absorption of a perfect absorber in the far-field scheme [Fig. 4.3.1 (a)]. As already mentioned, the perfect absorber consists of an array of nanoantennas on top of a metallic ground plate separated by a thick dielectric spacer. To simplify the structure and also to provide a physical explanation, we consider the structure as an asymmetric Fabry-Perot cavity with two mirrors, i.e. the metallic ground plate as the bottom mirror and the array

of nanoantennas as the top mirror. The total reflection and transmission coefficients of the cavity can be expressed as using Airys formula that reads [74, 140, 141]:

$$r = r_{12} + r_{\mathrm{m}} = r_{12} + \frac{t_{12}t_{21}r_{23}e^{(2i\varphi)}}{1 - r_{21}r_{23}e^{(2i\varphi)}}, \tag{4.3.1}$$

$$t = \frac{t_{12}t_{23}e^{(2i\varphi)}}{1 - r_{21}r_{23}e^{(2i\varphi)}}, \tag{4.3.2}$$

where t_{12}, t_{21}, r_{12}, r_{21}, r_{23} are complex-valued reflection and transmission coefficients at both interface, $\varphi = k_0 nd\cos\theta'$ is the phase accumulated upon a cavity transfer, k_0 is the free space wavenumber, n is the refractive index of the dielectric, and d is its thickness. In principle, the array of nanoantennas fully can be modeled only by its reflection and transmission coefficients. A full wave simulation can be used to calculate the reflection and transmission coefficients (r_{12}, t_{12}, r_{21}, and t_{21}). This can be done by assuming that the nanoantennas are sandwiched between two semi-infinite half-spaces, i.e. air and dielectric and illuminated by a linearly polarized incident plane wave either from the top air or from dielectric [74].

As already mentioned, the total absorption can be obtained if the reflection as well as transmission of the structure vanishes. The transmission of the structure is totally suppressed $T = |t| = 0$. This is due to sufficiently thick metallic ground plate (i.e. $t_{23} = 0$). To achieve total absorption ($A = 1 - T - R \simeq 1$) the reflection should be zero as well ($R = |r|^2 = |r_{12} + r_m|^2 \simeq 0$). The reflection is the sum of the direct reflection coefficient r_{12} and the multiple reflection coefficient r_m [as sketched in Fig. 4.3.1 (a)]. Therefore, in the far-field scheme, the condition of the perfect absorption read as

$$r_{12} = -r_m. \tag{4.3.3}$$

In the next subsection, we will show that the total absorption occurs whenever Eq. 4.3.3 is fulfilled.

4.3.2 Array of nanopatches on top of a metallic ground plate

The schematic view of the proposed perfect absorber is depicted in Fig. 4.3.1 (b). It consists of an array of rectangular gold nanopatches on top of a metallic ground plate separated by a thick dielectric spacer. The structure is periodic in x and y directions and the periods are $P_x = P_y = 500$ nm. The refractive index of the dielectric spacer is $n = \sqrt{\varepsilon_{\mathrm{d}}} = 1.5$. To explore the underlying physics of the proposed perfect absorber, we calculated the absorption A as a function of the thickness of the dielectric spacer d

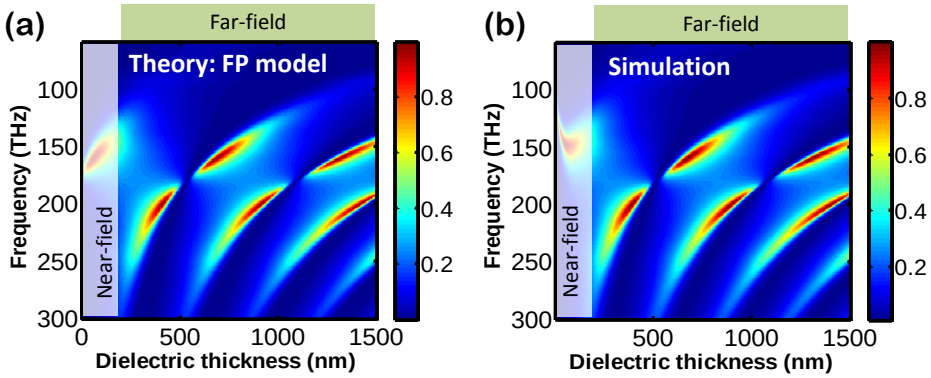

Figure 4.3.2: (a) and (b) Theoretical and simulation absorption spectra as a function of frequency and dielectric thickness (d) for a gold nanopatches perfect absorber at normal incidence

and the frequency [Fig. 4.3.2 (b)]. The dielectric spacer is varied from $20-1500$ nm. To be able to compare it with the Fabry-Perot model, the simulated result is divided into two distinct parts, namely, far-field and near-field [Fig. 4.3.2 (a) and (b)]. The numerical result shows that the perfect absorption ($A=1$) can be achieved at various dielectric spacer d, periodically spaced around a frequency of operation. Moreover, the resonance frequency of maximum absorption is slightly changing for different dielectric spacer. Note that the hybridization of the localized eigenmode of the gold nanopatches with the Fabry-Perot resonance of the cavity can be clearly seen in Fig. 4.3.2 (a) and (b). This will lead to a strong Rabi splitting and avoid crossing [Fig. 4.3.2 (a) and (b)].

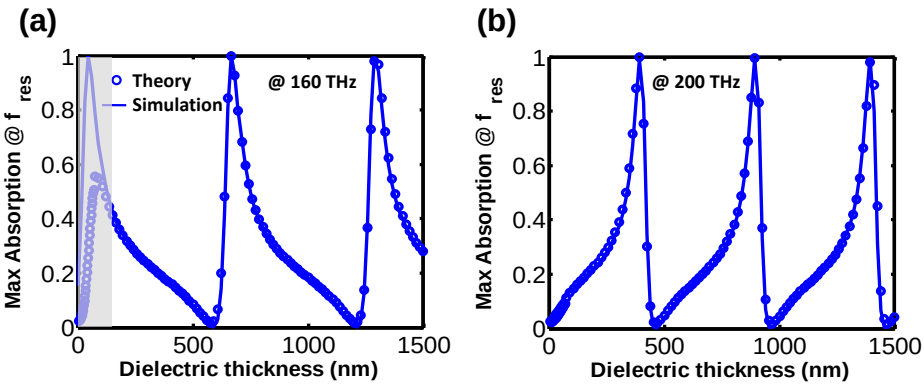

Figure 4.3.3: (a) and (b) Maximum absorption as a function of dielectric thickness calculated from semi-analytical approach and full wave simulation for two different frequencies 160 THz and 200 THz, respectively.

The absorption spectra as a function of the dielectric spacer thickness d and resonance frequency is calculated by using the Airy's formula. It can be seen that it shows similar behavior compared to the simulated results [Fig. 4.3.2 (a) and (b)]. As

already highlighted, the analytical result can not predict the simulated result for thin dielectric spacers due to the strong coupling between nanopatches and the metallic ground plate. This can be better seen in Fig. 4.3.3 for two different resonance frequencies 160 THz (a) and 180 THz (b). It can be seen that the absorption is shown at those discrete frequencies as a function of the thickness of the dielectric spacer.

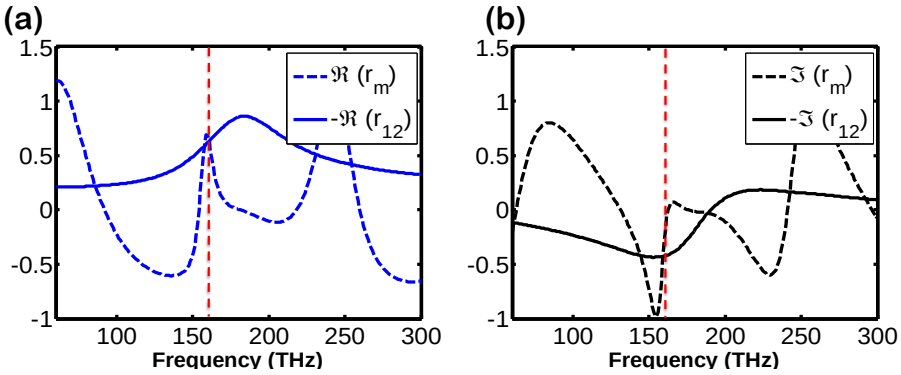

Figure 4.3.4: (a) and (b) Real and imaginary parts of direct reflection coefficient (r_{12}) as well as multiple reflection coefficient (r_m) with dielectric thickness $d = 370$ nm. The red hashed lines represent the crossing point when real and imaginary parts of reflection coefficients have the same magnitude but opposite sign, i.e. $r_{12} = -r_m$.

In order to compare the numerical and analytical results, they are displayed in the same figure [Fig. 4.3.3 (a) and (b)]. For thick dielectric spacers, i.e. $d > 250$ nm, there is a perfect agreement between the numerical and proposed analytical results. However, for thin dielectric spacers, there is a huge deviation between the metallic ground plate and the nanopatches due to strong coupling. We investigated this in detail in the previous section (i.e. near-field coupling scheme). In order to fully understand the absorption mechanism in the proposed structure, the real and imaginary parts of the direct reflection coefficient r_{12} and the multiple reflection coefficient r_m are calculated at the resonance frequency $f = 160$ THz for a spacer thickness $d = 370$ nm [Fig. 4.3.4 (a) and 4.3.4 (b)]. It can be easily seen that due to the constructive interference between the both coefficients r_m and r_{12}, i.e. $r_{12} = -r_m$, the total reflection coefficient is completely suppressed, i.e. $r = r_{12} + r_m = 0$. Therefore, the absorption reaches nearly 100 percent for the investigated frequency.

In this section, we proposed a perfect absorber (Salisbury screen) in the mid-infrared regime based on a periodic array of gold nanopatches. Moreover, we used a simple semi-analytical approach based on an asymmetric Fabry-Perot model in order to predict the optical responses of the perfect absorber. We showed that this model is only valid for thick dielectric spacers (i.e. no near-field coupling). The

proposed structure provided a complete absorption for various dielectric thicknesses d. The underlying mechanism of the total absorption is fully explained by destructive interference.

4.4 Concluding remarks

To conclude, in this chapter we have studied complete light absorption in two different schemes, i.e. near-field coupling scheme and far-field interference scheme. For both cases, the perfect absorber is made of an array of nanoantennas on top of a gold ground plate which is separated by a dielectric spacer.

In the first scheme (near-field coupling), we have introduced the concept of the *extreme coupling*. This only occurs for a dielectric spacer in the order of few nanometers. The experimental realization of the structure is achieved by taking advantage of atomic layer deposition (ALD) in order to fabricate thin dielectric spacers. We have experimentally shown that a deep-subwavelength nanoantenna, with a ratio of resonance wavelength to period of $\lambda/P \approx 10$. This is only possible when the perfect absorber operates at extreme coupling. An analytical approach based on a Fabry-Perot model is used to predict the resonance position of the investigated structure. Small deviations between the experimental, numerical, analytical results for the extremely thin dielectric spacers (3 nm) are explained by the surface roughness of the metallic ground layer. Finally, it is important to note that the concept of the extreme coupling might be useful to obtain an ultimate field enhancement, truly homogenous metamaterials, and omnidirectional perfect absorbers.

In the second scheme (far-field interference), the dielectric spacer between the metallic ground plate and the array of nanoantennas is considerably thick ($d \sim \lambda$) such that there is no near-field coupling between them. In this case, we have shown that the only mechanism to obtain the complete light absorption for an array of nanoantennas (the absorption is limited to 50 percent) is using the concept of interference. A simple asymmetric Fabry-Perot cavity with two mirrors (the metallic ground plate as the bottom mirror and the nanoantennas array as the top mirror) has been used to predict the response of the perfect absorber. The total absorption occurs when the reflection is completely suppressed by a destructive interference between the direct reflection coefficient and the multiple reflection coefficients.

5 Plasmonic ring nanoantennas

5.1 Introduction

In Chapter 3, we investigated the light scattering by nanoantennas such as identical and nonidentical coupled nanopatches, which exhibit electric and magnetic dipole moments. We showed that one can achieve a different optical response, i.e. reflection and absorption, when the array of nanoantennas is illuminated in forward and backward directions. This was due to the bianisotropic response of the nanoantenna which is achieved by breaking the symmetry of nanopatches. This bianisotropic response provides interesting optical features such as designing a nanoantenna with vanishing backscattering. Moreover, we found that it is possible to design a metasurface which completely absorbs the incident light.

In this chapter, we will discuss the optical response of new types of nanoantennas made of gold nanorings. As we will show, they have unique properties that make them appealing for a larger number of applications. This concerns in particular the field enhancement in the vicinity of the metallic nanoantennas [18, 25]. The enhanced field can be used to boost the efficiency of optoelectronic devices ranging from light-emitting diodes to solar cells [89]. It also has the potential to increase the sensitivity of Raman scattering or infrared absorption spectroscopy. The physical origin of field enhancement is the excitation of localized surface plasmon resonances (LSPRs) [25]. In principle, the properties of the LSPR are dictated by the geometry of the nanoantenna; i.e. its size and shape and the optical properties of the materials. Light interaction with various plasmonic nanoantennas with different geometries such as nanopatches, nanorodes, and nanospheres have been extensively investigated numerically and experimentally [49]. For most of the aforementioned nanoantennas the enhanced field is localized outside the nanostructure and in a rather small volume in the vicinity of the nanoantennas. However, for some applications, it is essential to have plasmonic nanostructures with a uniform field enhancement that stretches along extended spatial domains. It has been shown that a plasmonic nanoring is a good candidate for providing such a uniform field enhancement [142–146]. Nanoring antennas attracted a lot attentions due to its potential for enhancing nonlinear effects and boosting the solar cell efficiency [147, 148]. Therefore, it is essential to

understand and describe the optical response of a gold nanoring in order to design nanoantennas for a specific application.

The first goal of the present chapter is to investigate a metasurface made of gold nanorings and discuss its optical properties based on the simple analytical method developed in the previous chapters. Predictions are compared to full wave simulations. To link the study from the very first beginning to experiments conducted in close proximity to the thesis, we present results of these experiments in parallel. All structures of the present chapter have been fabricated and measured by Dennis Lehr at the group of Prof. Kley, University of Jena.

The second goal of this chapter is to investigate plasmonic nanoantennas with interesting optical features for desired applications. We show that one can obtain a nanoantenna based on a gold nanoring with a directional pattern. As already explained in the previous chapters, such directionality can be achieved for nanoantennas with balanced electric and magnetic dipole moments; the so called first Kerker condition [20, 26, 82]. In this chapter, we first introduce a generalized Kerker condition, beyond considering only dipole moments, i.e. for an electric and magnetic dipole moment and an electric quadrupole moment. A gold nanoring with high aspect ratio ($D \sim H$, where D is the inner diameter, H is the height of nanoring) is a prototypical nanoantenna that fortunately supports electric dipole and quadrupole moments. We will discuss the scattering response of a nanoring that fulfills the balanced condition. We show that at the balanced condition a ring nanoantenna possesses a directive pattern with suppressed back scattering and enhanced forward scattering. This is due to the destructive interference of the radiated far-fields emitted from the electric dipole and quadrupole moments in the backward direction and their constructive interference in the forward direction. Moreover, we investigate the optical response of a periodic array of such nanoantennas. For such a metasurface, it would be possible to achieve a perfect absorption beyond dipole approximation by a proper tuning of the electric dipole and quadrupole moments. The mechanism of total absorption is different from the suggested approaches in the previous chapters.

Since the seminal theoretical work of Ugo Fano on scattering line-shape of inelastic scattering of electrons from helium, tremendous efforts have been made to observe the same resonant scattering phenomenon in atomic but also in many other physical systems [79]. The Fano resonance type of features are found in various studies, e.g. superconductors optics, and scattering in photonics crystals [79]. In general, a Fano resonance is a resonant scattering phenomenon that gives rise to an asymmetric line-shape. Interference between two resonant scattering states or modes, i.e. a background state (broad resonance or bright mode) and a discrete state (that possesses a sharp resonance or dark mode) produces the asymmetric line-shape. Recently, Fano

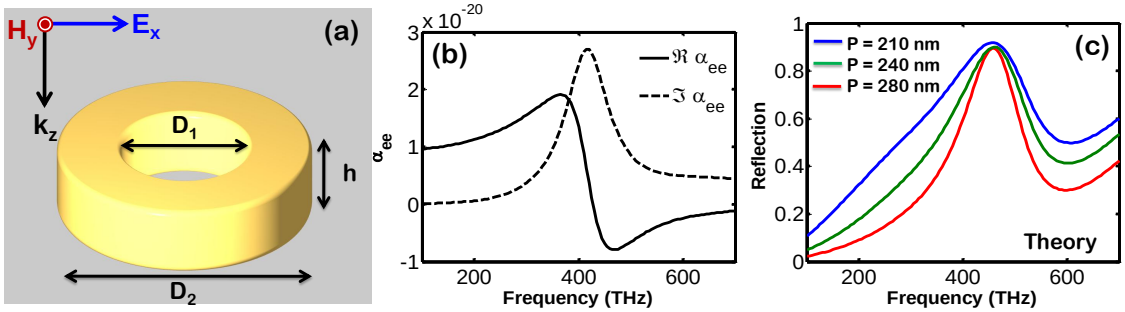

Figure 5.1.1: (a) Plasmonic nanoring with the inner diameter $D_1 = 65$ nm, the outer diameter D_2=195 nm and height $h = 50$ nm. (b) Electric polarizabilty of an individual gold nanoring. (c) The array response (reflection) calculated analytically from the individual polarizabilty for different periods. All the geometrical parameters of the nanoring is also shown in the Fig.

resonances in various plasmonic nanostructures have been studied because of interesting application perspectives [79, 149–154]. In particular, they can be used for sensing applications that benefit from the extreme field enhancement and sharp spectral features. In most of the plasmonic nanostructures, the bright mode is the electric dipole moment and the dark mode is a higher multipole, e.g. electric quadrupole moment. The last goal of this chapter is to design multi-resonant plasmonic nanoantennas made of gold nanorings with some exotic optical response such as scattering dark states and Fano resonances. This is achieved by using a concentric multi-nanoring.

We note that most of the findings of this chapter have been previously published in Ref. [147, 155, 156].

5.2 Strongly coupled nanorings

In this section, we briefly discuss the optical properties of an individual nanoantenna made of a plasmonic nanoring as well as of an array of such nanoantennas. The schematic of the investigated structure is depicted in Fig. 5.1.1 (a). It can be characterized by three geometrical parameters, i.e. the inner diameter D_1, the outer diameter D_2, and the height h. Due to this large number of degrees of freedom, the optical response of the nanoantenna can be easily tuned by varying the geometry of the nanoring. The nanoantennas are made up of gold and assumed to be embedded in air. The are illuminated by a plane wave with an electric field polarized along the x-axis that propagates in the positive z-direction. The investigated nanoring shows only an electric response in the entire spectral region, i.e. all higher order multipole moments can be neglected [Fig. 5.1.1]. Notice that this is valid only for the selected geometrical parameters. In the next section, we will present nanorings with consider-

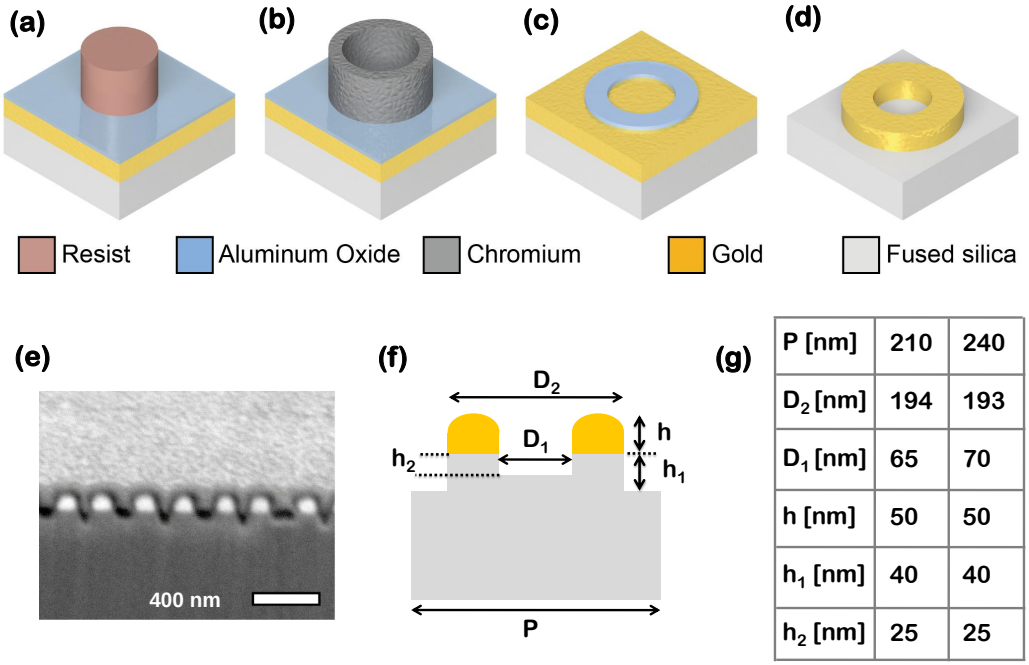

(g)

P [nm]	210	240
D_2 [nm]	194	193
D_1 [nm]	65	70
h [nm]	50	50
h_1 [nm]	40	40
h_2 [nm]	25	25

Figure 5.2.1: Sketches of intermediate fabrication steps. a) Template for double patterning, b) chromium ring after double patterning, c) Al_2O_3 ring after Ion Beam Etching (IBE) and removal of the chromium mask, d) gold nanoring after Oxygen Reactive Ion Beam Etching (O2-RIBE) and stripping of the Al_2O_3 mask. e) Cross section of fabricated sample, f) sketch of nanoring model, g) measured geometrical parameters of the nanoring arrays

ably larger height that can support a new mode (i.e. an electric quadrupole response) in addition to the electric dipole response. The retrieved electric polarizability of the nanoring is depicted in Fig. 5.1.1 (b).

Before presenting the experimental results, we briefly explain the basic process to fabricate such nanoantennas. Details can be found in Ref. [157]. First, resist pillars are generated on a fused silica substrate by using character projection electron beam lithography (EBL) on a 50 nm gold and 10 nm aluminum oxide layers [Fig. 5.2.1 (a)]. Then, the resist pattern is converted into a chromium ring by double patterning (DP) [157], i.e. homogeneous coating with chromium by ion beam deposition and subsequent ion beam etching to remove the chromium from horizontal surfaces [Fig. 5.2.1 (b)]. This chromium ring is transferred into the underlying aluminum oxide layer [Fig. 5.2.1 (c)] and then, into the gold layer [Fig. 5.2.1 (d)] by ion beam etching.

As already mentioned, the gold nanoring can be modeled by the inner diameter D_2, the outer diameter D_1, and the height h. However, the cross section of the fabricated sample shows slight distortions with respect to Fig. 5.1.1 (a). Therefore,

it is necessary to model the rings with two more parameters, i.e. h_1 and h_2 [Figs. 5.2.1 (e)-(f)]. The geometry of the gold nanorings is also simulated according to the model illustrated in [Fig. 5.2.1 (f)]. All the measured parameters for the nanorings are shown in the table contained in Fig. 5.2.1 (g). In the simulation the permittivity of the gold was taken from ellipsometric measurements of a bare gold layer. In order to evaluate the optical properties of the gold nanoring, several spectral measurements performed and compared them to the numerical simulations. The numerical and experimental results are depicted in Fig. 5.2.2 (a) and (b). The numerical (solid lines) and measurement (dashed lines) are in extraordinary agreement with respect to the spectral resonance position, width, and amplitude [157]. We also calculated the field distributions for two different periods. It can be seen there is a uniform field enhancement inside the gold nanoring [Fig. 5.2.2 (c) and (d)]. This uniform field enhancement is due to the dipolar resonance of the ring [146] which has a great potential to design practical devices such as a plasmonic sensor for the DNA detection or a plasmonic color filter [158, 159]. It can also be used to boost nonlinear effects [147].

Experimental and numerical results show that decreasing the period of the nanoring leads to a small spectral blueshift and spectral broadening [Fig. 5.2.2 (a) and (b)]. In order to understand the impact of the period, we calculated the optical response from an array of such nanoantennas, i.e. reflection and transmission spectra, by applying the analytical approaches which were explained in Chapter 2 [see Eq. 2.3.20 and Eq. 2.3.22]. This can be done because the scattering response of an isolated nanoanetnna is dominated by an electric dipole moment [Fig. 5.2.1 (b)]. The theoretical results are shown in Fig 5.1.1 (c) for different periods, i.e. P =210, 240, 280 nm. Here, the gold nanoring has an inner diameter of $D_1 = 65$ nm, the outer diameter $D_2 = 195$ nm and the height of $h_1 = 50$ nm. The theoretical results also confirm that broadening of spectra will occur by decreasing the period of array [Fig 5.1.1 (c)]. This is simply due to the dipole-dipole interaction between nanorings in the array and depends on the period of the array. The electric field will enhance by decreasing the period of the array because of the inter-particle coupling in the array [Fig. 5.2.2 (c) and (d)].

To this end, we investigated the optical response of a dense array of nanorings. We have shown that there is a great agreement between numerical, experimental, and theoretical result. The optical properties of the plasmonics nanorings can be tuned, by varying the plasmonic material, substrate, and filling material, and the nanoring's size. We believe that plasmonic nanorings can offer interesting optical features which we will try to explore to some extent in this chapter. In particular, in the next section, we want to explore a nanoantenna based on a gold nanoring

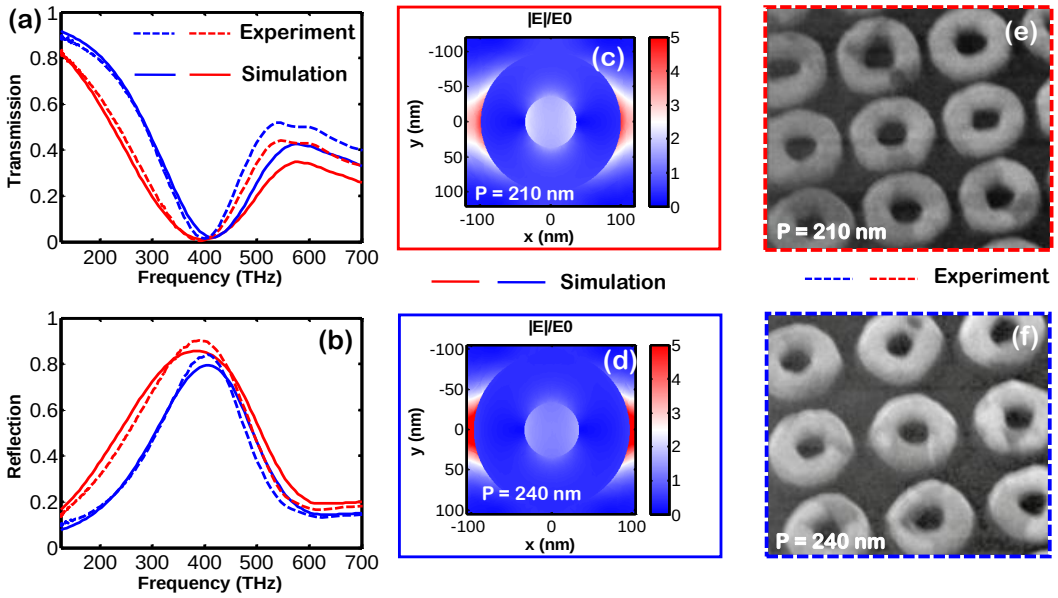

Figure 5.2.2: (a) and (b) Simulated (blue and red solid lines) and measured (blue and red dashed lines) transmission and reflection for gold nanoring arrays with different geometrical parameters (period $P = 210$ nm (red) and $P = 240$ nm (blue)). (c) and (d) The field distribution for two different periods. Smaller periods, i.e. small ring to ring distance leads to larger field enhancement. (e) and (f) Images of the fabricated samples for two periods.

with a directional pattern. In order to do that, we first introduce a generalized Kerker condition for a nanoantenna which supports an electric quadrupole moment in addition to the electric and magnetic dipole moments. The antenna will show a directional pattern whenever all these moments are in balanced condition. We will show that a nanoantenna made of gold nanorings can be tuned such that it meets this condition.

5.3 Directive nanoring: Multipole interference

Engineering the scattering of optical nanoantennas is a fast-growing field which attracts tremendous attentions [39, 84, 108, 160, 161]. The ability to engineer the scattering response can be attributed to the fact that nanoantennas can support different multipole modes, not only electric dipole ones [28, 38, 91, 162]. A proper tuning of size, shape and material of nanoantennas leads to intriguing scattering effects such as superscattering [28, 37, 38], cloaking [163, 164], and controllable scattering direction [61, 82, 165–169].

In the previous section, we discussed the optical properties of a gold nanoring theoretically, numerically, and experimentally. Such nanoantennas [Fig. 5.3.1(a)]

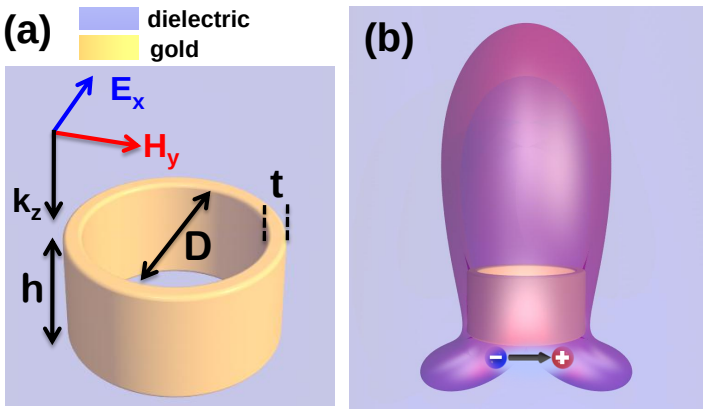

Figure 5.3.1: (a) Schematic representation of the investigated gold nanoring. The nanoantenna is embedded in a homogenous host medium with refractive index of $n = \sqrt{\epsilon_r} = 1.5$. (b) Artistic view of the radiation pattern of the nanoantenna.

have been investigated theoretically and numerically due to their promising applications [142, 145–147, 154, 170–172]. It is shown that they generally support only an electric dipolar mode with a uniform field enhancement inside. This dipolar mode exhibits an identical scattering in forward and backward direction. Therefore, an interesting question is: *Is it possible to achieve directional scattering from a plasmonic nanoring?* To achieve a directional pattern with zero backscattered field for magneto-dielectric spheres, Kerker suggested to use an interference of their electric and magnetic dipole modes [20]. Recently, the so-called Kerker condition have been attracted considerable attention both theoretically and experimentally in order to realize directional emission for dielectric and metallic nanoantennas [61,82,104,166–168,173,174].

In order to address the aforementioned question, we introduce in this section a more general approach to design directive nanoantennas with zero backscattering based on a generalization of this Kerker condition [174]. Particularly, we include electric quadrupole modes as well. In particular, we discuss the scattering properties of a single nanoring which possess two modes with a notable amplitude in the same spectral region, i.e. an electric dipole and an electric quadrupole mode. We show that this can occur whenever the nanoring has a large height compared to the inner diameter (i.e. $D \simeq h$) [Fig. 5.3.1 (a)]. Such a nanoantenna possesses a directive radiation pattern with zero backscattering [Fig. 5.3.1 (b)]. The generalized Kerker condition is used to predict and explain the suppression of the nanoring's scattering in backward direction. Moreover, a constructive interference leads to an enhanced forward scattering which provides the desirable directional scattering properties [Fig. 5.3.1 (b)]. We show that all these findings can be used to explain the far-field emission of a dipole emitter close to such a nanoring as well. A similar approach is also used to

discuss the scattering properties of few coupled nanorings which radiate the light in a desired direction.

5.3.1 Single nanoring

This subsection is organized as follows: first we introduce the theory of the generalized Kerker condition. Afterwards, we confirm the applicability of the condition at the example of a specifically designed plasmonic nanoring [Fig. 5.3.1 (a)]. Finally, we demonstrate how this nanoantenna can be used for directive and enhanced emission of a close-by dipole emitter. We note that most of the findings of this section have been previously published in Ref. [155].

Let us consider a nanoantenna with an induced electric moment p_{x}, a magnetic dipole moment m_{y} and an electric quadrupole moment Q_{xz}. The radiated far-field of the nanoantenna reads as [22]

$$\begin{aligned}\mathbf{E}_{\mathrm{far}}(\mathbf{r}) &= \frac{k^2}{4\pi\epsilon}p_{\mathrm{x}}\frac{e^{ikr}}{r}\left(-\sin\varphi\,\hat{\varphi}+\cos\theta\cos\varphi\,\hat{\theta}\right) \\ &\quad -\frac{Zk^2}{4\pi}m_{\mathrm{y}}\frac{e^{ikr}}{r}\left(\cos\theta\sin\varphi\,\hat{\varphi}-\cos\varphi\,\hat{\theta}\right) \\ &\quad -\frac{ik^3}{24\pi\epsilon}Q_{\mathrm{xz}}\frac{e^{ikr}}{r}\left(-\sin\,\varphi\cos\,\theta\,\hat{\varphi}+\cos\,2\theta\cos\,\varphi\,\hat{\theta}\right),\end{aligned} \tag{5.3.1}$$

where r is radial distance, ϕ is azimuthal angle and θ is the polar angle, in spherical coordinates. $k=\sqrt{\epsilon_r}\omega/c$ is the wavenumber for an angular frequency ω, and c is the speed of light. ϵ_r is the host medium relative permittivity. Using Eq. (5.3.1), the backward radar scattering cross section of the nanoantenna can be defined as

$$\sigma_{\mathrm{Backward}} = \lim_{r\to\infty}4\pi r^2\frac{\left|\mathbf{E}_{\mathrm{far}}(\varphi=0,\theta=\pi)\right|^2}{\left|\mathbf{E}_{\mathrm{inc}}\right|^2}, \tag{5.3.2}$$

$$= \frac{k^4}{4\pi\epsilon^2\left|\mathbf{E}_{\mathrm{inc}}\right|^2}\left|p_{\mathrm{x}}-\frac{\sqrt{\epsilon_r}m_{\mathrm{y}}}{c}+\frac{ik}{6}Q_{\mathrm{xz}}\right|^2. \tag{5.3.3}$$

where $|\mathbf{E}_{\mathrm{inc}}|$ is the the amplitude of the incident electric field. According to Eq. (5.3.2), zero backscattering field occurs if the so-called generalized Kerker condition

$$p_{\mathrm{x}}-\frac{\sqrt{\epsilon_r}m_{\mathrm{y}}}{c}+\frac{ik}{6}Q_{\mathrm{xz}} = 0 \tag{5.3.4}$$

is fulfilled. Note that Eq. (5.3.4) reduces to the well-known Kerker condition $p_{\mathrm{x}}-\frac{\sqrt{\epsilon_r}m_{\mathrm{y}}}{c}=0$ [20], if the quadrupole moment is not considered. To take higher order multipole moments into account, Eq. (5.3.4) can be extended. Furthermore, the

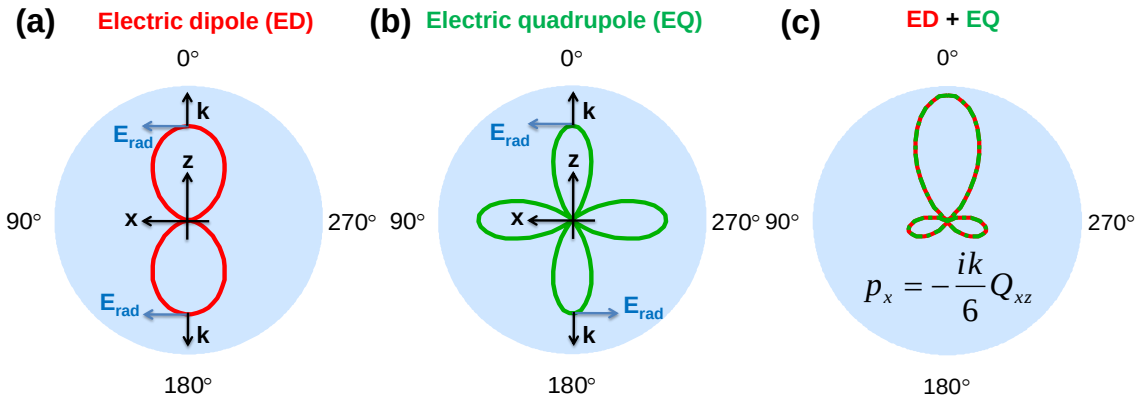

Figure 5.3.2: Radiation pattern for different multipole moments in the xz-plane. (a) Electric dipole moment (p_x), i.e. $|\mathbf{E}_{\mathrm{far}}|^2 \propto \cos^2\theta$. The blue arrows indicate the phase of the radiated field. (b) Electric quadrupole moment (Q_{xz}), i.e. $|\mathbf{E}_{\mathrm{far}}|^2 \propto \cos^2 2\theta$. (c) Superposition of electric dipole and quadrupole moments, i.e. $|\mathbf{E}_{\mathrm{far}}|^2 \propto (\cos\theta + \cos 2\theta)^2$, when the generalized Kerker condition is fulfilled [see Eq. (5.3.4) with $m_y = 0$], i.e. $p_{\mathrm{x}} = -i\frac{k}{6}Q_{\mathrm{xz}}$.

forward radar scattering cross section of the nanoantenna reads as

$$\begin{aligned}\sigma_{\mathrm{Forward}} &= \lim_{r\to\infty} 4\pi r^2 \frac{|\mathbf{E}_{\mathrm{far}}(\varphi=0,\theta=0)|^2}{|\mathbf{E}_{\mathrm{inc}}|^2} \\ &= \frac{k^4}{4\pi\epsilon^2 |\mathbf{E}_{\mathrm{inc}}|^2}\left|p_{\mathrm{x}} + \frac{\sqrt{\epsilon_r} m_{\mathrm{y}}}{c} - \frac{ik}{6}Q_{\mathrm{xz}}\right|^2 . \end{aligned} \tag{5.3.5}$$

Hence, if Eq. (5.3.4) is fulfilled, a constructive interference in forward direction is achieved in addition to the destructive one in backward direction.

To illustrate the physical mechanism behind the generalized Kerker condition, the radiation pattern of an electric dipole moment p_{x} and an electric quadrupole moment Q_{xz} in the xz-plane ($\varphi = 0°$) are shown in Fig. 5.3.2 (a) and (b). Here, we consider $m_{\mathrm{y}} = 0$, since the nanoring investigated later supports a negligible magnetic response. Then, if Eq. (5.3.4) holds, the electric field radiated by an electric dipole and electric quadrupole interfere constructively at $\theta = 0°$ [Fig. 5.3.2 (c)], i.e. the radiated fields are in phase in forward direction [Fig. 5.3.2 (a) and (b)]. On the other hand, there is no scattering backwards ($\theta = 180°$) because of the destructive interference in this direction.

Equation (5.3.4) provides a general guideline to design nanoantennas without backscattering and enhanced forwardscattering on the base of multipolar interference. To demonstrate its applicability, the scattering response of a plasmonic nanoring will be investigated now. A schematic of the investigated nanoring which fulfills

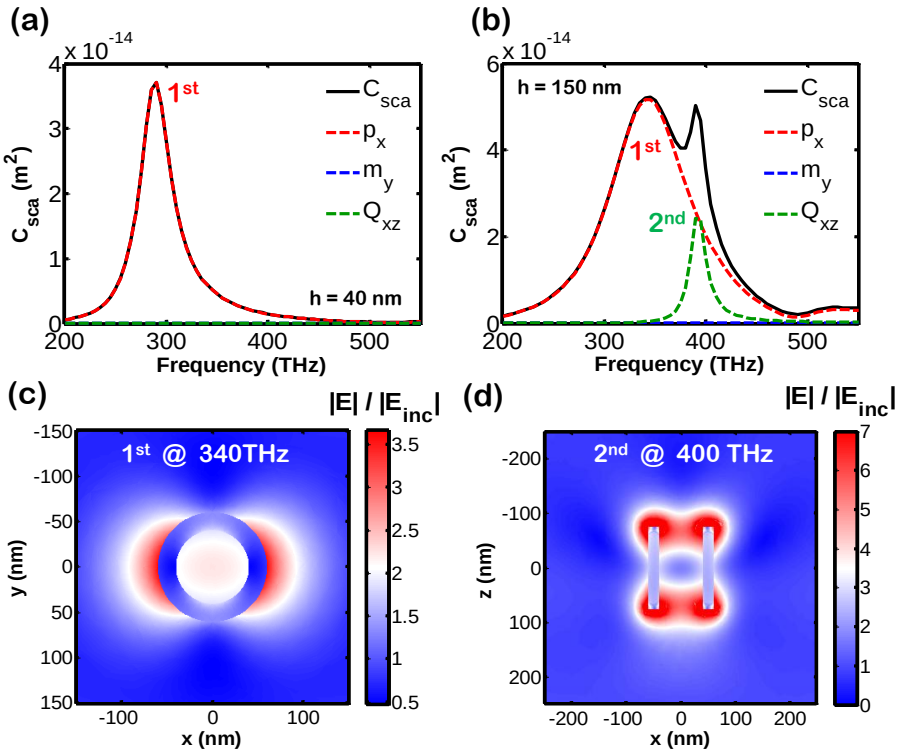

Figure 5.3.3: Plane wave excitation nanorings. (a) and (b) Total scattering cross sections and contributions from different multipole moments as a function of frequency for nanorings with two different heights, $h = 40\,\text{nm}$ [(a)] and $h = 150\,\text{nm}$ [(b)]; electric dipole moment p_x (red dashed line), magnetic dipole moment m_y (blue dashed line), and and electric quadrupole moment Q_xz (green dashed line). (c) and (d) Field distributions of the nanoring with $h = 150\,\text{nm}$ for the first [$\nu_1 \approx 340\,\text{THz}$, (c)] and second mode [$\nu_2 \approx 400\,\text{THz}$, (d)].

the generalized Kerker condition is depicted in Fig. 5.3.1. The thickness of the gold layer is $t = 20\,\text{nm}$ with a height of ($h = 40$ and $150\,\text{nm}$). The inner diameter of the nanoring is $D = 80\,\text{nm}$. The nanoring is illuminated by an x-polarised plane wave propagating in the z-direction [Fig. 5.3.1 (a)]. It is embedded in a homogenous host medium with refractive index of $n = \sqrt{\epsilon_r} = 1.5$.

The scattering cross sections of nanorings for two different heights ($h = 40$ and $150\,\text{nm}$) are shown in Fig. 5.3.3 (a) and (b). For the nanoring with small height, i.e. $h = 40\,\text{nm}$, the scattering response can be fully described by an electric dipole resonance around a frequency of 290 THz [Fig. 5.3.3 (a)]. This nanoring ($h = 40\,\text{nm}$) exhibits an identical forward and backward scattering response. However, for the nanoring with a height of $h = 150\,\text{nm}$, a second mode can be observed around a frequency of 400 THz in addition to the dipole mode which is at 340 THz [Fig. 5.3.3 (b)]. Note that the dipole resonance is slightly blue-shifted. The second mode might be

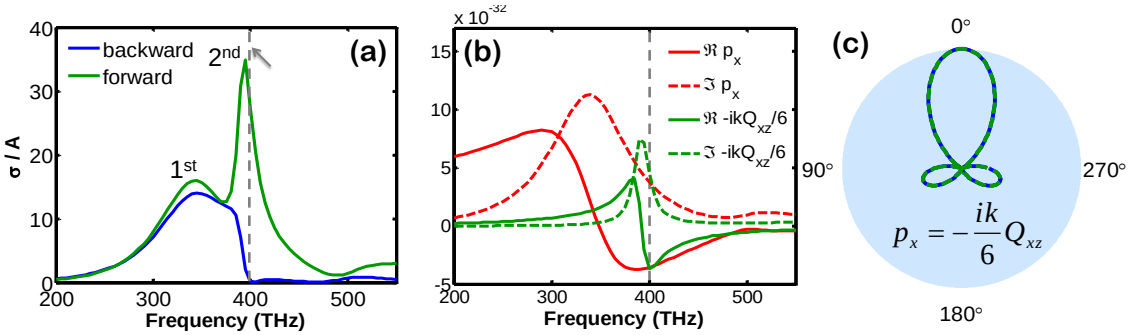

Figure 5.3.4: Plane wave excitation of the nanoring with $h = 150\,\text{nm}$, radiation pattern. (a) Normalized forward (green line) and backward (blue line) scattering cross sections. (b) The real and imaginary parts of the electric dipole moment (p_x) and the rescaled electric quadrupole moment ($-i\frac{k}{6}Q_{\text{xz}}$). Note that, Eq. (5.3.4) should hold for both imaginary and real parts at second mode (grey dashed line). (c) The radiated far-field pattern at second mode, i.e. 400 THz (grey dashed line). This pattern is identical to the theoretically predicted one [Fig. 5.3.2 (c)].

explained by a Fabry-Perot oscillation of surface plasmons from top to bottom of the nanoring [130, 175]. According to the multipole expansion, the new mode is dominated by an electric quadrupole moment (green dashed line). Nevertheless, the first mode has a strong contribution to the scattering cross section C_{sca} at the resonance frequency of the second mode as well. In fact, C_{sca} is enhanced at the second mode which is known as superscattering [28, 37, 38]. Note that the antenna is designed such that contribution of magnetic dipoles is negligible in the entire scattering cross section.

We will only consider the nanoring with large height, i.e. $h = 150\,\text{nm}$ due to the fact that it supports two modes. This allows to obtain interesting optical features, i.e. directive radiation pattern. Figure 5.3.3 (c) and (d) shows the field distributions of the first and second mode for the nanoring with $h = 150\,\text{nm}$, respectively. The first mode (340 THz) shows a uniform field enhancement inside the nanoring [142,157,171]. This is similar to that observed for nanorings with small heights [Fig. 5.2.2 (c) and (d)]. However, the second mode (400 THz) represents a strong field enhancement around the upper and lower terminations of the nanoring. Moreover, the field strongly varies inside the nanoring, which may be utilized to couple to dipole-forbidden transitions of quantum systems [176].

The forward and backward radar scattering cross sections for the considered nanoring are sketched in Fig 5.3.4 (a). At lower frequencies (below 330 THz), the forward and backward scattering cross sections are very similar due to the dominating electric dipolar response. However, at higher frequency (above 400 THz), the backward

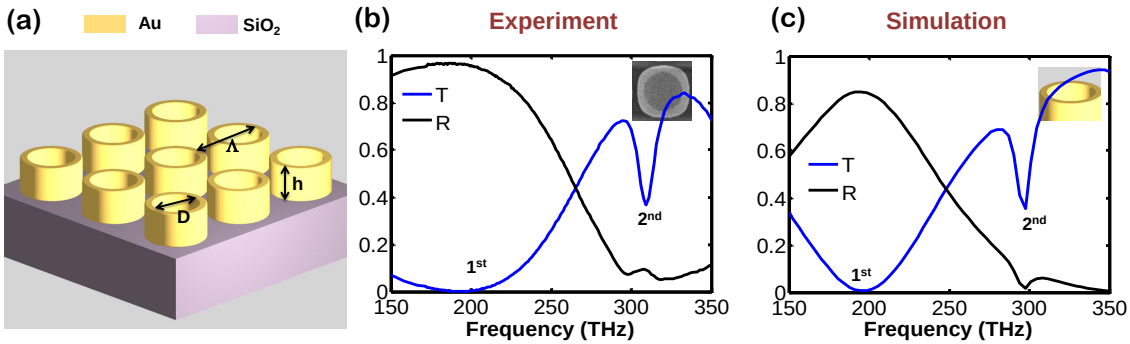

Figure 5.3.5: (a) Schematic view of an array of nanorings on top of a dielectric substrate. (b) Experimental transmission and reflection spectra. (c) Numerical transmission and reflection spectra. The Kerker condition is fulfilled since the reflection of the array reaches zero at the quadrupole mode. The geometrical parameters of the nanorings are $H = 245$ nm, $D = 360$ nm, $t = 20$ nm, and $\Lambda = 560$ nm.

scattering is significantly suppressed while the forward scattering is considerably enhanced. We already claimed that the generalized Kerker condition [Eq. (5.3.4)] can fully describe the enhancement of the forward scattering and suppression of the backward scattering due to the coherent interference of the involved multipoles. To confirm that, the real and imaginary parts of the electric dipole and quadrupole moments of the investigated nanoring are shown in Fig. 5.3.4 (b). It can be seen that Eq. (5.3.4) [$p_\mathrm{x} = -i\frac{k}{6}Q_\mathrm{xz}$ for $m_\mathrm{y} = 0$] holds for $\nu = \nu_2$. Therefore, the Kerker condition can fully explain the scattering properties due to the fact that it agrees perfectly with the theoretical predictions [Fig. 5.3.4 and Fig. 5.3.2].

Eventually, we have presented the possibility to design plasmonic nanorings which fulfill the generalized Kerker condition [Eq. (5.3.4)]. The condition is suitable to describe its scattering properties. However, the electric dipole and quadrupole moments are very sensitive to the actual geometrical parameters of the nanorings. In the investigated case, nanorings of sufficient height are needed to realize a properly strong Fabry-Perot resonance with quadrupolar multipole moment. We have shown that a nanoring exhibits zero backscattering if its satisfies the generalized Kerker condition ($p_\mathrm{x} = -i\frac{k}{6}Q_\mathrm{xz}$). Therefore, one can show that an array of such nanoantennas possesses a vanishing reflection, i.e. $R \propto \left|p_\mathrm{x} + i\frac{k}{6}Q_\mathrm{xz}\right|^2 \approx 0$ (more details can be found in the next section). To confirm that, we calculated the numerical transmission and reflection spectra of a periodic array of such nanoantennas [Fig. 5.3.5 (a) and (c)]. It can be seen that the array supports two modes, i.e. the electric dipole and quadrupole modes [Fig. 5.3.5 (c)]. Figure 5.3.5 (c) shows almost zero reflection due to the destructive interference of multipoles. The effect is less pronounced in

the experiment compared to the numerical result due to the geometrical deviations [Fig. 5.3.5 (b)]. In fact, the second mode is really sensitive to geometrical parameters, especially to the height of the ring. More details of the array response will be given in the following sections. In particular, we will show that it is possible to obtain complete light absorption by proper varying the geometry of the nanoring and the period of the structure.

Till now, we only discussed a plane wave excitation scheme. The question is what will happen if we excite the nanoantenna in the near-field excitation scheme, i.e. by a close-by dipole emitter. In general, it is not possible to transfer all the results from far-field excitation to near-field ones for two reasons: (a) emitters in the near-field may couple to dark modes that are not excitable from the far-field, (b) spectral shifts between these two excitation schemes [177, 178]. Nevertheless, the results from the far-field excitation may be used as a rule of thumb to achieve a directive nanoantennas for near-field excitation. In the case of the application of the generalized Kerker condition on plasmonic nanorings, it would be desirable to use the directivity of these nanoantennas for close-by emitters as well combined with an enhancement of their spontaneous emission rate. In Fig. 5.3.6, the results for a dipole excitation of the nanoring is shown. The dipole is placed centered at the bottom of the nanoring [Fig. 5.3.6 (a)]. The scattered field intensities in back- and forward direction are displayed in Fig. 5.3.6 (a). They show that the scattering is mostly in the forward direction at $\nu_{\mathrm{dip}} \approx 380\,\mathrm{THz}$, see also the inset for the radiation pattern at ν_{dip}. The redshift of the spectral position of highest directivity can be explained by the difference between near- and far-field illumination [177, 178]. The calculated emission rate enhancement in the far-field, usually termed Purcell factor F, is calculated by the enhancement of the emitted power to the far-field compared to its emission without nanoantenna, $F = P_{\mathrm{na}}^{\mathrm{rad}}/P_{\mathrm{fs}}^{\mathrm{rad}}$ [176]. The radiation efficiency η is calculated as the fraction of emitted power that is not dissipated by the nanoring to the total power emitted by the dipole [Fig. 5.3.6 (b)] [176]. Moderate Purcell factors around 12 are calculated for ν_{dip} with respect to efficiencies around 0.6. The efficiency dip around $\nu_2 \approx 400\,\mathrm{THz}$ can be attributed to the coupling to the quadrupolar mode of the nanoring. Hence, even though this coupling is necessary to achieve the high directivity, it leads to a comparably low efficiency for such large nanoantennas [179].

We have shown that the nanorings designed with the help of the generalized Kerker condition, i.e. Eq. (5.3.4), can be used to enhance the emission of dipole emitters while sustaining the directional character of the radiation. However, the connection between near-field and far-field investigations is not straight forward, but Eq. (5.3.4) might be seen as a valuable guideline to design directional nanoantennas for a coupling to close-by emitters. To conclude, in this subsection we introduced a novel con-

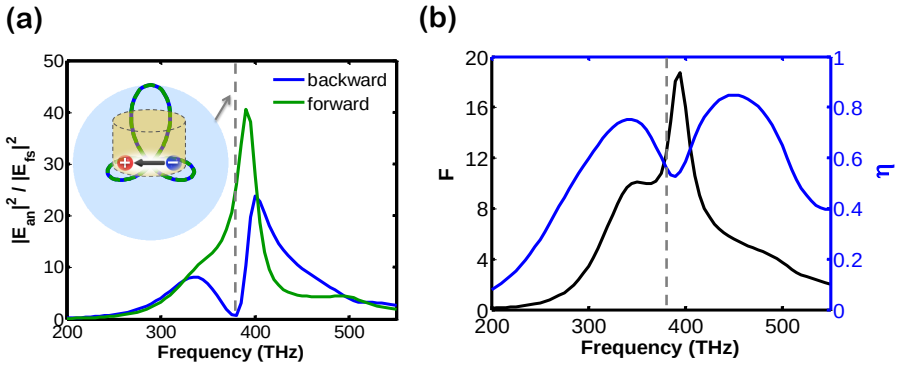

Figure 5.3.6: Electric dipole excitation. (a) Normalized forward and backward far-fields: E_{fs} is the radiated electric field by a point electric dipole without nanoantenna and E_{an} the same quantity in the presence of the nanoring. Inset: Highly directive radiation pattern at $\nu_{\mathrm{dip}} \approx 380\,\mathrm{THz}$. (b) Purcell factor F (black line) and nanoantenna efficiency η (blue line).

dition to achieve highly directional plasmonic nanoantennas. The generalized Kerker condition is based on the constructive/destructive interference of different multipole moments in forward/backward direction. It has been verified for plasmonic nanorings in the case of plane-wave excitations and shows a predictive character for close-by dipoles as well. These findings provide a powerful guideline for the design of highly directive plasmonic nanoantennas.

5.3.2 Coupled nanorings

In the previous subsection, we introduced a ring nanoantenna that can enhance light in forward direction and suppress in the backward direction. This allows to design a nanoantenna with zero backscattered field whenever the higher order multipoles are excited. In this subsection, we will show that by a proper design of a few coupled nanoantennas one can tune the scattering field in a desired direction. As an example, we investigate three strongly coupled nanorings (trimer) separated by a small dielectric spacer. The scattering cross section of the coupled nanoantennas can form a different pattern with respect to the isolated one. The geometry of the coupled nanorings is shown in Fig. 5.3.7 (a). The nanoantennas are strongly coupled and produce a hot-spot between nanorings. The scattering cross section of the nanorings and the contribution of different multipole moments are calculated based on multipole expansion and shown in Fig. 5.3.7 (b). Note that the single nanoring (with the dimensions depicted in Fig. 5.3.7) exhibits only an electric dipole moment. However, the coupled nanorings supports electric quadrupole response in addition to the electric dipole of a single nanorings. The contribution of the magnetic dipole is

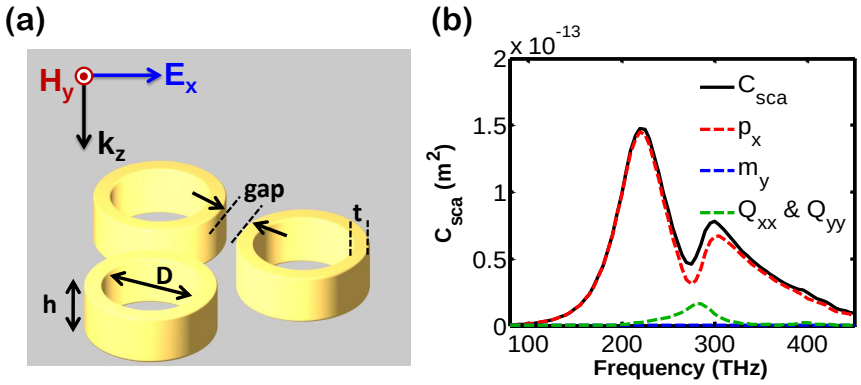

Figure 5.3.7: (a) Geometry of the coupled nanorings. The height and inner diameter of the nanoring are $h = 50$ nm and $D = 100$ nm, respectively. The thickness of the gold nanoring is assumed to be $t = 30$ nm. The coupled nanorings are embedded in a homogeneous host medium with refractive index 1.5. (b) Scattering cross section of the structure as a function of frequency. Individual contributions by the electric dipole moment $\mathrm{p_x}$ (red dashed line), magnetic dipole moment $\mathrm{m_y}$ (blue dashed line), and electric quadrupole moment Q_{xx} and Q_{yy} (green dashed line).

almost negligible. Note that the induced electric quadrupole moment in the coupled nanorings antenna (Q_{xx}) is different from previous section (i.e. single nanoring with considerably large height Q_{xz}). Therefore, it might offer a different radiation pattern compared to a single nanoring at the electric quadrupole resonance at 275 THz. In order to understand the far-field radiation pattern, we focus on the radiated far-field of a nanoantenna with an induced electric dipole moment p_{x} and an electric quadrupole moment Q_{xx} , Q_{yy} which is given by

$$\begin{aligned}\mathbf{E}_{\mathrm{far}}(\mathbf{r}) &= \frac{k^2}{4\pi\epsilon}\frac{e^{ikr}}{r}p_{\mathrm{x}}\left(-\sin\varphi\hat{\varphi}+\cos\theta\cos\varphi\hat{\theta}\right) \\ &\quad -\frac{ik^3}{24\pi\epsilon}\frac{e^{ikr}}{r}Q_{\mathrm{xx}}\left(-\sin\theta\cos\varphi\sin\phi\hat{\phi}+\sin\theta\cos\theta\left(1+\cos^2\varphi\right)\hat{\theta}\right) \\ &\quad -\frac{ik^3}{24\pi\epsilon}\frac{e^{ikr}}{r}Q_{\mathrm{yy}}\left(\sin\theta\cos\phi\sin\varphi\hat{\phi}+\sin\theta\cos\theta\left(1+\sin^2\varphi\right)\hat{\theta}\right).\end{aligned} \tag{5.3.6}$$

Since we are interested in the electric radiated far-field at xz-plane ($\varphi = 0$) that can be written as

$$\begin{aligned}\mathbf{E}_{\mathrm{far}}(\mathbf{r}) &= \frac{k^2}{4\pi\epsilon}p_{\mathrm{x}}\frac{e^{ikr}}{r}\cos\theta\hat{\theta} \\ &\quad -\frac{ik^3}{24\pi\epsilon}\frac{e^{ikr}}{r}\left(2Q_{\mathrm{xx}}+Q_{\mathrm{yy}}\right)\sin\theta\cos\theta\hat{\theta}.\end{aligned} \tag{5.3.7}$$

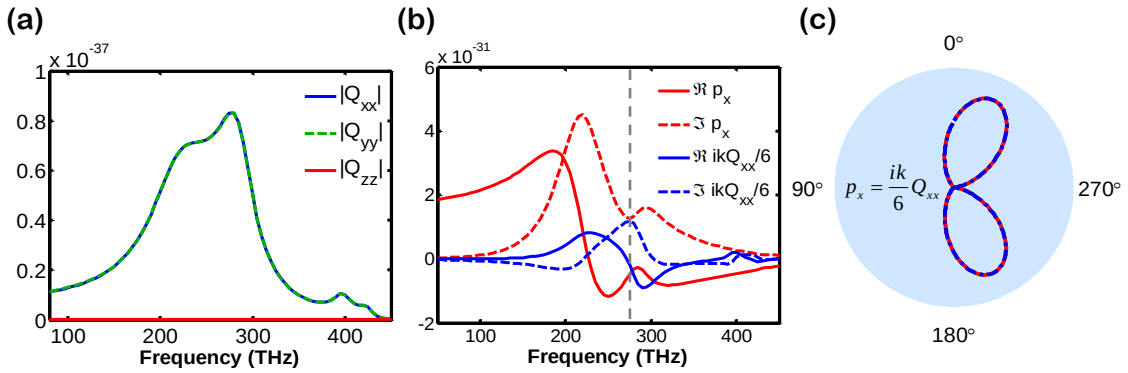

Figure 5.3.8: (a) The amplitude of different electric quadrupole components ($Q_{\mathrm{xx}}, Q_{\mathrm{yy}}, Q_{\mathrm{zz}}$). (b) The real and imaginary parts of the electric dipole (p_{x}) and quadrupole ($\frac{ik}{6}Q_{\mathrm{xx}}$). The grey dashed line shows the frequency at which the balanced condition, i.e. $p_{\mathrm{x}} = \frac{ik}{6}Q_{\mathrm{xx}}$, is fulfilled . (c) Radiation pattern of the coupled nanorings at 275 THz.

Using the traceless properties of the quadrupole matrix, i.e. $Q_{\mathrm{xx}} + Q_{\mathrm{yy}} + Q_{\mathrm{zz}} = 0$, and the fact that the coupled nanorings has considerably small $Q_{\mathrm{zz}} \approx 0$, we can conclude that $Q_{xx} = -Q_{yy}$. To confirm that, we calculated Cartesian quadrupole moments of the coupled nanorings in Fig. 5.3.8 (a). It can be seen that the Q_{zz} is almost negligible. Therefore, for the investigated nanoantenna [Fig. 5.3.7 (a)], the radiated far-field in xz-plane ($\varphi = 0$) for dominated moments can be expressed as

$$\mathbf{E}_{\mathrm{far}}(\mathbf{r}) = \frac{k^2}{4\pi\epsilon}\frac{e^{ikr}}{r}\left[p_x - \frac{ik}{6}Q_{xx}\sin\theta\right]\cos\theta\hat{\theta}.$$

The real and imaginary parts of electric dipole and electric quadrupole are shown in Fig. 5.3.8(b). It can be seen that at 275 THz, the electric dipole and quadrupole are in balanced condition, i.e. $p_{\mathrm{x}} = i\frac{k}{6}Q_{\mathrm{xx}}$ for both real and imaginary parts. Therefore, the radiation pattern of the coupled nanoantenna is governed by $|\mathbf{E}_{\mathrm{far}}|^2 \propto (1-\sin\theta)^2\cos^2 2\theta$. This simply means that at $\theta = \frac{5\pi}{3}, \frac{4\pi}{3}$ the electric dipole p_{x} and electric quadrupole Q_{xx} should interfere constructively [Fig. 5.3.9(b)-(c)]. However, at $\theta = \frac{\pi}{3}, \frac{2\pi}{3}$ there is a constructive interference between the electric dipole p_{x} and the electric quadrupole Q_{xx} [Fig. 5.3.9(b)-(c)]. Moreover, from the far-field expression, we can conclude that the nanoantenna does not radiate at $\theta = \frac{\pi}{2}, \frac{3\pi}{2}$. The far-field radiated pattern of the coupled nanoanetnna is sketched in Fig. 5.3.8 (c) that is in great agreement with the theoretical prediction [Fig. 5.3.9 (c)].

To conclude this section, we introduced a generalized Kerker condition which can be used to explain the radiation pattern of arbitrary nanoantennas. In particular, we used nanoantennas based on nanorings such that they fulfill the balanced condition

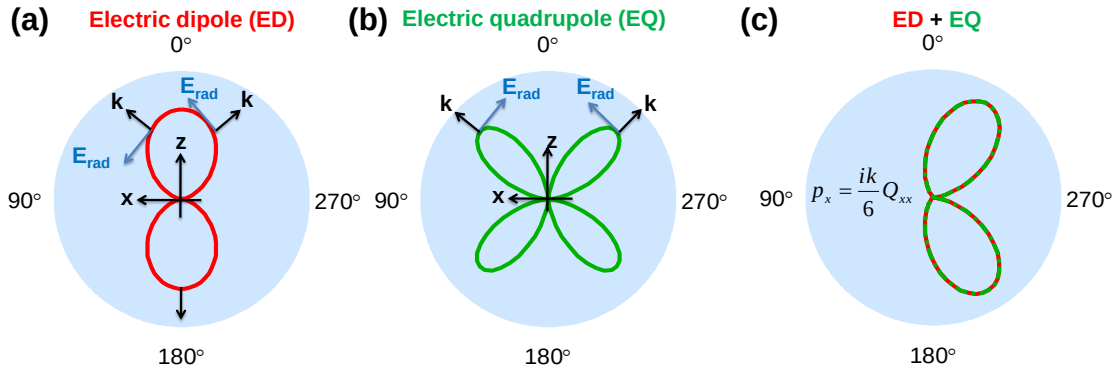

Figure 5.3.9: Radiation pattern for different multipole moments in the xz-plane. (a) Electric dipole moment (p_x), i.e. $|\mathbf{E}_{\text{far}}|^2 \propto \cos^2\theta$. The blue arrows indicate the phase of the radiated field. (b) Electric quadrupole moment (Q_{xx}), i.e. $|\mathbf{E}_{\text{far}}|^2 \propto \cos^2\theta \sin^2\theta$. (c) Superposition of electric dipole and quadrupole moments, i.e. $|\mathbf{E}_{\text{far}}|^2 \propto (1-\sin\theta)^2 \cos^2\theta$, when the balanced condition is fulfilled, i.e. $p_x = i\frac{k}{6}Q_{xx}$.

between the electric dipole and quadrupole moment to obtain the desired radiation pattern. In the next section, we will show that we can achieve a complete light absorption for an array of nanoantennas which operate in balanced condition.

5.4 Single nanorings: Complete light absorption

In chapter 2, we introduced various physical mechanisms to increase the light interaction with an array of nanoantennas made from optically small resonant nanoantennas, i.e. electric and magnetic dipoles. It has been shown that complete light absorption can be achieved if the effective electric and magnetic dipoles are in balanced condition. One might ask *what happens if the nanoantennas support higher order multipole moments (beyond the electric and magnetic dipoles)*? In this section, we aim to address this question properly by using an array of nanoantennas that supports multipole moments beyond the dipole one, i.e. electric dipole and quadrupole moments. In the previous subsection, it has been shown that by controlling the height of a single nanoring, it is possible to achieve a nanoantenna with two modes (i.e. electric dipole and quadrupole modes) which allows to obtain a directional radiation pattern. This occurs whenever the electric dipole and quadrupole moments fulfill the balanced condition ($p_x = -\frac{ik}{6}Q_{xz}$). We also proved experimentally and numerically that this condition will lead to a zero reflection for an array of nanoantennas which fulfill the balanced condition. In order to show that let us start with the average current density of a periodic array of electric dipole and quadrupole moments [60, 180]

$$J_{\mathrm{x}} = \frac{-i\omega}{\Lambda^2}\left(p_{\mathrm{x}}^{\mathrm{eff}} + \frac{ik}{6}Q_{\mathrm{xz}}^{\mathrm{eff}}\right), \tag{5.4.1}$$

where $p_{\mathrm{x}}^{\mathrm{eff}}$ and $Q_{\mathrm{xz}}^{\mathrm{eff}}$ are the effective electric dipole and quadrupole moments of the array. To calculate the array response, we can use the relation between the reflected electric field and electric current density, i.e.

$$\mathbf{E}_{\mathrm{r}} = -\frac{1}{2}\left(Z_0\mathbf{J}_e^s\right). \tag{5.4.2}$$

Finally, the reflection coefficient can be found as

$$r = \frac{i\omega}{2\Lambda^2}Z_0\frac{\left(p_{\mathrm{x}}^{\mathrm{eff}} + \frac{ik}{6}Q_{\mathrm{xz}}^{\mathrm{eff}}\right)}{E_{\mathrm{inc}}}, \tag{5.4.3}$$

where E_{inc} is the amplitude of the incident electric field. To obtain a zero reflection, the relation between electric dipole and quadrupole moments, i.e. $p_{\mathrm{x}}^{\mathrm{eff}} = -\frac{ik}{6}Q_{\mathrm{xz}}^{\mathrm{eff}}$, should be satisfied. Note that this is also true for the individual moments, i.e. $p_{\mathrm{x}} = -\frac{ik}{6}Q_{\mathrm{xz}}$. Similarly, to calculate the the transmission coefficient, we applied the relation between transmitted electric field and electric current density, i.e.

$$\mathbf{E}_{\mathrm{t}} = \mathbf{E}_i - \frac{1}{2}\left(Z_0\mathbf{J}_e^s\right), \tag{5.4.4}$$

and the transmission coefficient can be found as

$$t = 1 + \frac{i\omega}{2\Lambda^2}Z_0\frac{\left(p_{\mathrm{x}}^{\mathrm{eff}} - \frac{ik}{6}Q_{\mathrm{xz}}^{\mathrm{eff}}\right)}{E_{\mathrm{inc}}}. \tag{5.4.5}$$

Now to achieve an array with total absorption, both reflection and transmission coefficients should be zero ($t = r = 0$). This leads to the following relation between the electric dipole moment and the incident electric field

$$p_{\mathrm{x}}^{\mathrm{eff}} = -\frac{ik}{6}Q_{\mathrm{xz}}^{\mathrm{eff}} = \frac{i\Lambda^2}{\omega Z_0}E_{\mathrm{inc}}. \tag{5.4.6}$$

By using the relation between the effective electric polarizibility and electric dipole moment, i.e. $p_{\mathrm{x}}^{\mathrm{eff}} = \epsilon_0\alpha_{\mathrm{x}}^{\mathrm{eff}}E_{\mathrm{inc}}$, we can find the effective electric polarizability of the

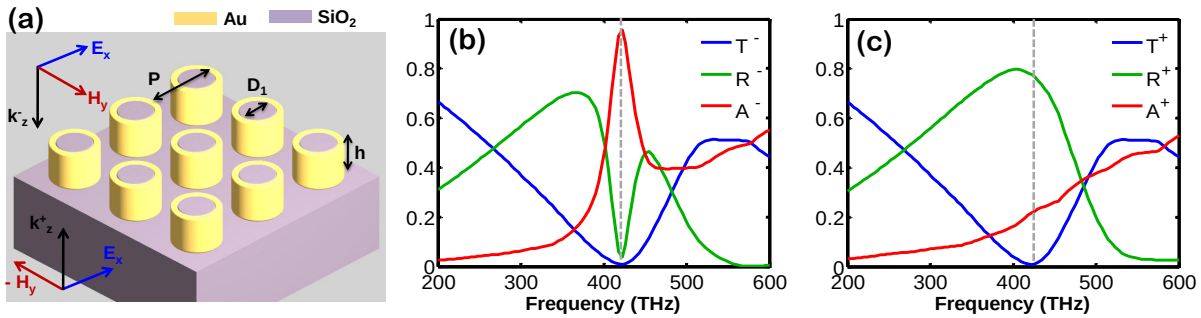

Figure 5.4.1: Schematic of the nanoring perfect absorber. The reflection, transmission and absorption of an array of nanoring's with period P = 180 nm, inner diameter diameter D_1= 100 nm, the height of nanoring h = 150 nm, and the gold thickness t = 20 nm. The gold nanorings are deposited on a dielectric substrate with refractive index n = 1.5.

array for the complete absorption condtion, i.e. $\alpha_{\mathrm{x}}^{\mathrm{eff}} = i\frac{\Lambda^2}{k}$.

The schematic of the investigated perfect absorber based on nanorings is shown in Fig 5.4.1 (a). It consists of an array of nanorings filled with refractive index n =1.5. The absorption, reflection, transmission spectra are shown in Fig 5.4.1 (b). It can be seen that the reflection and transmission reaches zero at the resonance of the electric quadrupole moment [grey dashed line in Fig. 5.4.1] and the impinging light is fully absorbed by the nanorings. The interesting point about this perfect absorber compared to the perfect absorbers with metallic ground plate (which discussed in chapter 4) is that it shows out of band transmission. Note that the response of the perfect absorber will change significantly by changing the angle of incidence (not shown here). This is due to the fact that at oblique incident the electric dipole and electric quadrupole are not in balanced condition. Finally, we should mention that the array of nanorings is deposited on a substrate that might increase the complexity of the investigated aforementioned theoretical model. In other words, the substrate might lead to an induced bianisotropic response since the height of nanorings are really large compared to the wavelength. This effect can be seen in Fig. 5.4.1 (b) and (c) where the array is illuminated from opposite directions. In fact, it shows that the induced moments are entirely different for forward and backward illumination directions. More details about the substrate induced bianisotropy (SIB) can be found in Ref. [181]. This is beyond the scope of this thesis.

5.5 Multi-nanorings: Scattering dark states

Multi-resonant plasmonic nanostructures offer possibilities for broadband sensor devices [12,91], efficient solar cell upconversion [89], coherent control [182], optical tag-

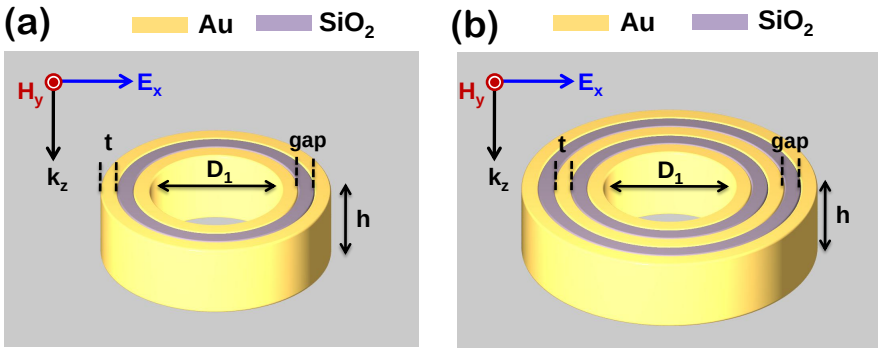

Figure 5.4.2: Schematic view of the investigated nanoantennas in air made of multiple concentric plasmonic nanorings. (a) two nanorings (b) three nanorings. The height of the nanoring is h=75 nm, the inner dimater is D_1 = 100 nm, the gold and dielectric thickness are t = gap = 20 nm.

ging [183] and enhanced nonlinear interactions [184]. For some of these applications, e.g. sensor devices, it is essential to have nanoantennas which offer Fano resonances. In general, Fano resonances originate from a coupling of dark and bright modes. In conventional plasmonic nanoantennas, the continuum (bright) mode is usually an electric dipole and the discrete (dark) mode is typically an electric quadrupole (or another higher order multipole mode) [28, 79, 149, 151, 161, 174, 185]. The coherent interference of these two modes leads to an asymmetric line-shape in the scattering response of a single nanoantenna or in the reflectance and transmittance spectra of an array. In this section, we introduce a new type of multi-resonant plasmonic nanoantennas based on multi-rings which exhibits entirely which exhibits a Fano resonance that does not rely on modes characterized by higher order multipole moments [Fig. 5.4.2 (a) and (b)]. The proposed nanoantenna supports only electric dipole resonances. In fact, the bright and dark modes are only electric dipoles. This allows to achieve interesting features such as an enhanced transmission, suppressed reflection, and scattering dark state [186]. We note that most of the findings of this section have been previously published in Ref. [156].

We already considered the basic geometry of a multi-ring, i.e. a single nanoring and its optical responses. We found that for a single nanoring with considerably small height, the dominant mode is electric dipolar. We will show that this mode also exists when multiple rings are nested [Fig. 5.4.2]. We focus on multi-nanorings with two and three concentric nanorings, but this is by no means a restriction. The schematic of the multi-nanoring is depicted in Fig. 5.4.2. The dielectric spacer between consecutive rings are made of glass (SiO_2) and the nanorings are made of gold. Here, we assumed that the thickness of the different nanorings (gold/dielectric) is 20 nm. The inner diameter of the nanoring is D_1 = 100 nm. The height of all concentric nanorings is

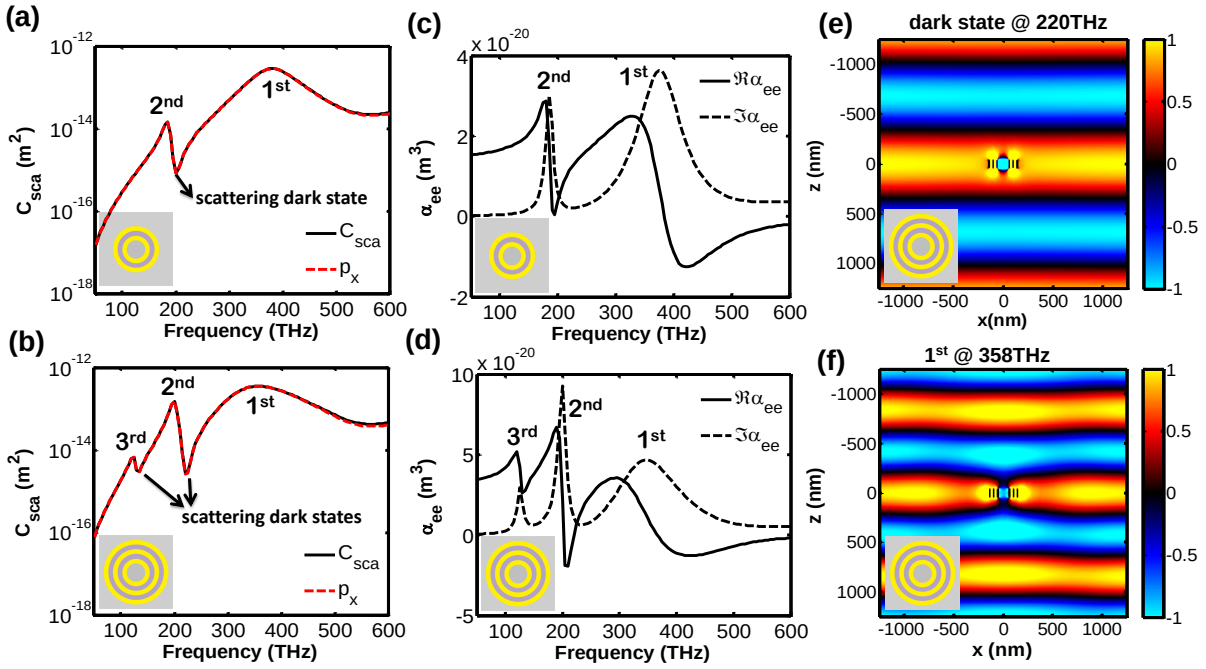

Figure 5.5.1: (a) and (b) Scattering cross sections as a function of frequency for two and three concentric nanorings, respectively. (c) and (d) The corresponding individual electric polarizabilities calculated by multipole expansion of the scattered field. (e) and (f) Field distributions (E_x) for the scattering dark state (220 THz) and the 1$^{\mathrm{nd}}$ mode (358 THz) of the multi-rings consisting of three gold rings.

$h = 75$ nm. The structure is embedded in vacuum and illuminated by a plane wave as sketched in Fig 5.4.2 (a) and (b).

Before a periodic array of multi-rings is considered, the numerically calculated scattering response of individual multi-rings shall be investigated first. The total scattering cross section versus frequency ν for multi-rings with two and three gold nanorings is shown in Fig. 5.5.1 (a) and (b). The scattering response of the nanoantennas is readily explained by its electric dipole moment [red dashed lines in Fig. 5.5.1 (a) and (b)]; all higher-order multipoles are negligible.

For an x-polarized plane wave illumination, the induced electric dipole moment of the investigated nanoantennas can be calculated as $p_\mathrm{x} = \epsilon_0 \alpha_\mathrm{ee} E_\mathrm{x}$, since no cross-polarized electric dipole moments are induced. The real and imaginary parts of the electric polarizability α_ee are shown in Fig. 5.5.1 (c) and (d). The electric polarization indicates the existence of two and three modes for two and three gold rings, respectively. The 1$^{\mathrm{st}}$ mode is spectrally very broad compared to the higher modes. Consequently, the 1$^{\mathrm{st}}$ mode can be denominated as continuum mode and the higher modes as discrete modes with a higher quality factor. The resonance positions are clearly encountered as peaks in the total scattering cross section spectrum. Between

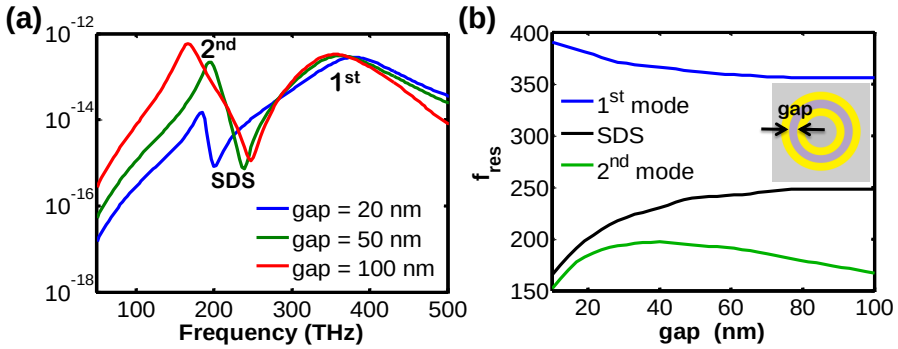

Figure 5.5.2: (a) Total scattering cross sections for different dielectric spacer (gap) of the two concentric nanorings. (b) The resonance position of different modes as a function of dielectric spacer.

those peaks, the scattering response is suppressed by a coherent interference between the continuum and a discrete mode. This phenomenon is known as a scattering dark state, which always appears between two scattering peaks [186] and can be due to a Fano resonance [79]. It is important to note that the Fano resonance in the investigated multi-rings is only due to electric dipole modes, which is entirely different from usually discussed plasmonic Fano resonances [145,183,186,187]. Scattering dark states exhibit a strongly suppressed scattering response in the far field. For example, the three-ring nanoantenna is hardly visible at $\nu = 220\,\mathrm{THz}$. At this frequency, the illumination causes a field enhancement in the near-field, but the far-field remains almost unperturbed [Fig. 5.5.1 (e)]. In contrast, the illumination is considerably scattered for the 1st mode at 358 THz [Fig. 5.5.1 (f)]. This suppression of the scattering response is related to the scattering cancellation technique [183, 187–189].

In order to investigate the robustness of the observed optical features, i.e. the scattering dark state and the asymmetric Fano like-shape, we calculated the scattering cross sections of the two concentric nanorings for different dielectric spacer (gap). Figure. 5.5.2 (a) depicts the scattering cross sections as a function of frequency for different dielectric spacer, i.e. gap= 20, 50, 100 nm. The amplitude and bandwidth of the 2nd mode can be largely tuned and enhanced by increasing the gap. However, the amplitude of the 1st mode is almost fixed. This allows to tune the position of the scattering dark state over a broad range of frequency [Fig. 5.5.2 (b)].

The scattering response of the isolated multi-rings at normal incidence can be solely explained by their electric polarizability α_{ee}. In this case, dense array theory can be used to calculate the reflection r and transmission t coefficients of a periodic

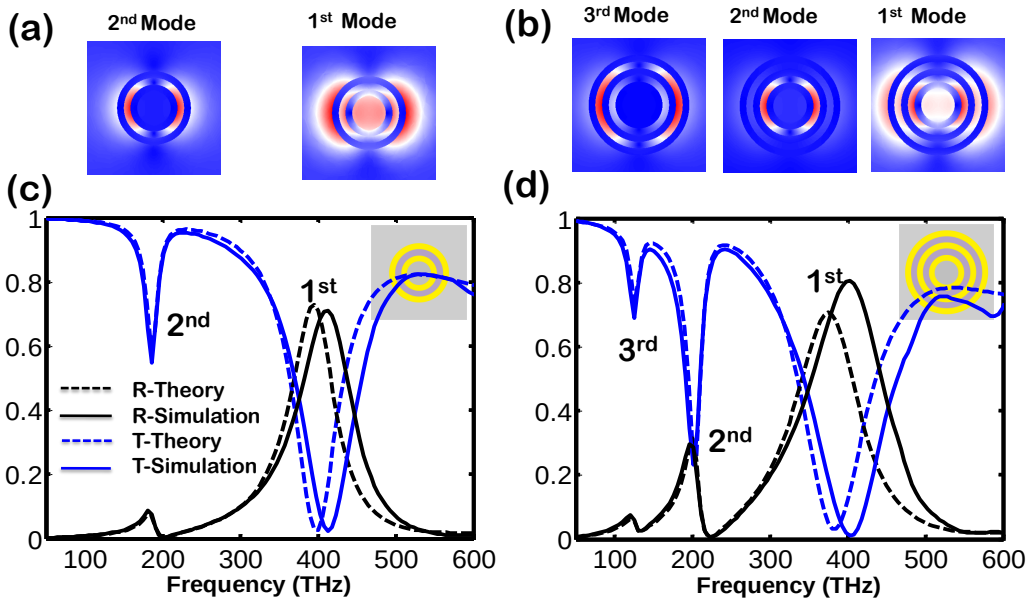

Figure 5.5.3: (a) and (b) The electric field distributions ($|E|/|E_{\text{inc}}|$) for all modes of the two and three concentric nanorings, respectively. (c) and (d) Simulation (solid lines) and theoretical [dashed lines, based on dense array theory] transmission and reflection spectra for the array of such multi-rings with period $\Lambda = 500\,\text{nm}$.

array of these multi-rings [16, 27, 47, 83]:

$$r = \frac{ik}{2\Lambda^2}\frac{\alpha_{\text{ee}}}{1-\alpha_{\text{ee}}\beta_{\text{ee}}}, \tag{5.5.1}$$

$$t = 1 + r\ . \tag{5.5.2}$$

Reflection and transmission are sketched in Fig. 5.5.3 (c) and (d) based on Eq. (5.5.1) and Eq. (5.5.2), and compared with rigorous numerical simulations. At lower frequencies, the numerical results are in good agreement to the theory. A redshift of the numerical results occurs at higher frequencies, because the wavelength gets comparable to the actual size of the multi-rings and retardation effects become more pronounced. The asymmetric line-shape of the reflection and transmission is due to interference of different dipole modes as highlighted earlier. It is remarkable that in a small frequency range, e.g. for the three gold ring structure between 200-220 THz, the transmission and reflection of the array changes drastically. Besides the Fano resonances, this is a direct evidence of enhanced transmission of the scattering dark states as well.

The electric field distributions for all modes are shown in Fig. 5.5.3 (a) and (b). The continuum mode is due to an electric dipolar response of the whole nanoantenna, which leads to a uniform field enhancement inside the innermost nanoring. This

mode has been extensively studied for single nanoring nanoantennas [142, 144, 146, 157,171]. The higher modes are localized inside the dielectric spacer between two gold nanorings. These highly concentrated gap modes might be used for coherent control [182], to boost nonlinear effects [147, 184] or to access dipole-forbidden transitions of quantum systems [176].

For an experimental verification, colleagues at the Friedrich-Schiller Universität Jena fabricated and characterized devoted samples with the same methodology as described in the previous sections. Figure 5.5.5 (b) and (c) shows the experimentally measured and numerically calculated transmission and reflection for an array made from nanoantennas possessing two concentric plasmonic nanorings, respectively. The basic of the fabrication process has been explained in details in Ref. [157]. Figure 5.5.5 (a) shows an SEM image of a fabricated sample. The experimental results agree well with numerical predictions. The small discrepancies between experimental and numerical results can be attributed to gold impurities [171]. The onset of an asymmetric lineshape and enhanced transmission can be observed in Fig. 5.5.5. In order to fit the measured reflection spectra, we used a well-known fitting function which is a product of the Fano line-shape spectra and the Lorentzian line-shape spectra and is given by

$$C_{\mathrm{Fano}}(\omega) = \left[\left(\frac{\omega}{\omega_a}\right)^4 \frac{a^2}{\left(\frac{\omega^2-\omega_s^2}{2W_s\omega_s}\right)^2+1}\right]\left[\frac{\left(\frac{\omega^2-\omega_a^2}{2W_a\omega_a}+q\right)^2+b}{\left(\frac{\omega^2-\omega_a^2}{2W_a\omega_a}\right)^2+1}\right], \qquad (5.5.3)$$

where q is the Fano (asymmetric) parameter, ω_a is the central frequency of the asymmetric resonance with a spectral width of W_a and b is the modulation damping. ω_s is the central frequency of the Lorentzian resonance with spectral width of W_s, and a is the maximum amplitude of the resonance. Note that the measured transmission spectra is fitted by $1 - R_{\mathrm{Fit}}$. All the fitting parameters can be found in Table 5.5.4. These asymmetric parameters (i.e. q and b) confirm that the spectra possess notable asymmetric line-shape.

However, the traces of the scattering dark state are less pronounced than in the numerical investigations [Fig. 5.5.3]. This is in fact related to the huge absorption of a 3 nm Cr-SiO_2 layer (mixture of silicon dioxide and chromium layer) (not shown here). This layer is a residue of the etching process and a nuisance. It can be however avoided by using another fabrication technique [147]. Moreover, the substrate also partially diminishes these features. It can be only restored by embedding the whole structure in a uniform medium with the same refractive index as the substrate, e.g. SiO_2. Note that our simulation result (not shown here) confirms that these two fea-

Figure 5.5.4: Fitting parameters for Fig. 5.5.5.

	a^2	ω_s (THz)	W_s (THz)	ω_a (THz)	W_a (THz)	q	b
Fig. 5.5 (b)	1.05	210	136	196	38	−0.57	0.62
Fig. 5.5 (c)	0.98	216	210	194	38	−0.55	−0.23

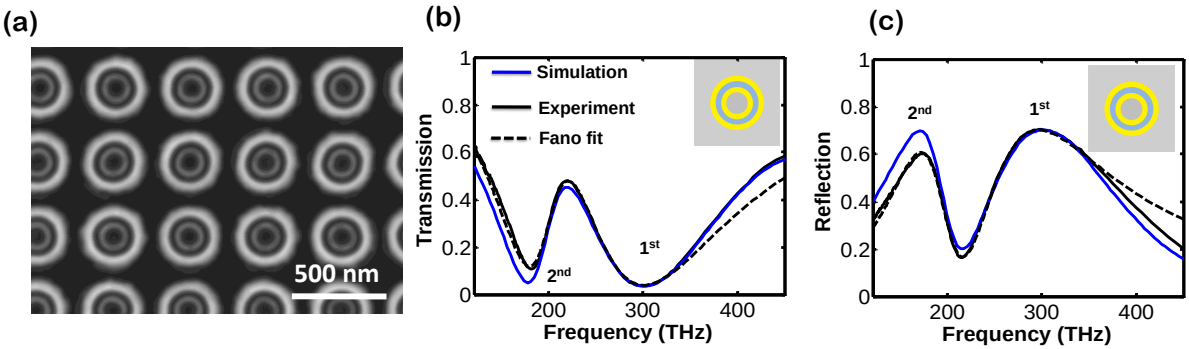

Figure 5.5.5: (a) SEM image of a fabricated sample. (b) Simulated, measured, and the corresponding Fano fit of the transmission spectra for two concentric gold nanorings. (c) The same for the reflection spectra. The dimensions of the two concentric nanorings are $D_1 = 100$ nm, $t_1 = 23$ nm , gap= 36 nm, $t_2 = 66$ nm. The array is placed on a dielectric substrate (fused silica) with a refractive index of $n = 1.46$.

tures (scattering dark state and enhanced transmission) are much more pronounced for an ideal structure (i.e. without the 3 nm Cr-SiO_2 layer) which is embedded in homogenous media.

In conclusion, in this section we introduced a new type of multi-resonant plasmonic nanoantenna based on concentric nanorings that shows some remarkable optical features, i.e. Fano resonances that enhance and also fully suppress scattering at selected frequencies. Dense-array theory can be applied to the investigated concentric nanorings and predict the optical response of an associated array based on the polarizability of the isolated nanoantenna. The numerically calculated response of such arrays agrees well with dense-array predictions and experimental data. The distinguished field concentration of the modes inside of the dielectric spacer makes concentric nanorings an interesting platform for enhanced light-matter-interactions, especially for multiresonant systems. Furthermore, the introduced fabrication method is compatible to industry processes. It enables a large-scale, deterministic, and re-

producible fabrication of multiresonant nanostructures with nanometric gaps.

5.6 Concluding remarks

The focus of this chapter was on plasmonic rings nanoantennas and their possible applications. We demonstrated that nanoantennas made of gold nanroings can offer various remarkable optical features such as directional light emission, complete light absorption, scattering dark states, and Fano resonances.

As already highlighted in the previous chapters, a nanoantenna with balanced electric and magnetic dipole moments exhibits a directive pattern with zero backscattering, known as the first Kerker condition. In this chapter, we introduced a generalized Kerker condition for a nanoantenna which supports electric and magnetic dipole moments and electric quadrupole moments. We demonstrated that a plasmonic nanoring can support such modes, i.e. electric dipole and quadrupole moments and constitutes an antenna with a directive pattern. The key for achieving this desired pattern was a constructive interference between the radiated far-fields of the induced moments in the forward and a destructive one in the backward direction. Moreover, we also managed to design an antenna consisting of few coupled nanorings to control the radiation pattern that might be useful for some applications.

There are different approaches in order to achieve the complete light absorption for a periodic array of plasmonic nanoantennas. Among all of them, a basic approach is using an array of nanoantennas which supports both electric and magnetic dipole moments. These moments should be at balanced conditions and this is extensively discussed in the previous chapters. In this chapter, we suggested a new approach to realize a complete light absorption for an array of nanoantennas which supports higher order multiples, i.e. *beyond dipolar response*. We showed that a periodic array of gold nanorings which exhibits electric dipole and quadrupole moments can provide a nearly complete light absorption.

Finally, we introduced a multi-resonant plasmonic nanoantenna based on concentric nanorings separated by thin dielectric spacers that provides some fascinating optical features such as scattering dark states and Fano resonances. The Fano resonance in the proposed concentric nanorings has different physical origin with respect to the conventional plasmonic Fano resonance. In general, the Fano resonance occurs when a nanostructure exhibits multiple resonances with different moments, e.g. an electric dipole moment and electric quadrupole moment. However, we observed a purely electric dipole response for the proposed concentric nanorings but yet Fano features. Eventually we exploited the spectral interference of different electric dipolar

modes with a largely disparate losses, that caused their line width to be substantially different. Fano features. Eventually we exploited the spectral interference of different electric dipolar modes with a largely disparate losses, that caused their line width to be substantially different. This allows to predict the optical response of a periodic array made of such nanoantennas by using a simple analytical approach. The numerical results calculated for an array of proposed nanoantennas agree well with analytical predictions and experimental results.

6 Summary and outlook

Nanophotonics is a rapidly developing field, which aims to control light-matter interaction at the nanoscale. Nanoantennas, as a canonical element in this field, can provide a fundamental role due to its notable electric and magnetic response. In this thesis, we aimed to theoretically investigate optical properties of various nanoantennas which help to further develop this field. In particular, remarkable optical features such as directional radiation pattern, Fano resonance, scattering dark state, extreme coupling, strong bianisotropic response, asymmetric reflection, and complete light absorption were exploited.

In Chapter 2, we investigated a theoretical framework to understand the underlying scattering mechanism of an arbitrary shaped nanoantenna. We studied a universal limitation on the scattering/absorption cross section of an individual nanoantenna that supports an electric/magnetic dipole moment. This leads to a universal limitation on the absorption (i.e. 50 percent of the impinging light) of an array of nanoantennas. To overcome this universal limitation, we theoretically presented various approaches, namely, using an array of both electric and magnetic dipole moments, an array of electric/magnetic dipole moments on top of a metallic ground plate (both near-field and far-field schemes), and an array of electric dipole and quadrupole moments. Furthermore, we presented a simple analytical approach to obtain the array response from the individual polarizabilities nanoantenna.

In Chapter 3, we explored bianisotropic coupling in two distinct nanoantennas, namely, high-index dielectric nanoantennas and plasmonic nanoantennas. The key to achieve this coupling is breaking the symmetry of the nanoantennas. In particular, to obtain plasmonic nanoantennas with bianisotropic coupling, we proposed coupled gold nanopatches with different lateral dimensions. The electric and magnetic dipole moments of such a structure are entirely different for forward and backward illumination directions. In fact, this was related to a strong bianisotropic coupling. This coupling can be tuned by varying the lateral dimensions of the nanoantenna. This provides a directional radiation pattern when the electric and magnetic dipole moments are in balanced condition. Moreover, for an array of such nanoantennas, we presented intriguing optical features such as perfect absorption and asymmetric reflection. We also proposed a tunable nanoantenna by using a phase change material

as a dielectric spacer between the nanopatches. This allows to achieve entirely different radiation patterns by applying an external laser pulse or heating the sample. In the second part of this chapter, we focused on high-index dielectric nanoantennas with tunable bianisotropic response. In general, a dielectric nanoantenna supports both electric and magnetic modes. However, these modes are not coupled when the antennas are symmetric with respect to the illumination directions. We proposed an experimentally feasible nanoantenna with notable bianisotropic (magneto-electric) coupling. This provides different optical responses for opposite illumination directions, i.e. namely asymmetric radiation pattern and asymmetric reflection coefficients.

In Chapter 4, we presented a perfect absorber which consists of an array of nanopatches on top of a metallic ground plate separated by a dielectric spacer. The complete light absorption is achieved in two entirely different schemes. The first scheme (i.e. near-field coupling) occurs when the dielectric spacer is considerably small compared to the operating wavelength. In fact, in this scheme we introduced the concept of *extreme coupling* by using an atomic layer deposition (ALD) to obtain few nanometers dielectric spacer. This allows to achieve deep-subwavelength nanoantennas, extreme field enhancement, local magnetic metamaterials, and omnidirectional perfect absorbers. Finally, we applied a simple analytical model to predict the resonance frequencies of the investigated nanostructure that shows excellent agreement with experiment and numerical results. The second scheme (far-field interference) occurs when the dielectric spacer is really large compared to the wavelength. In this scheme, the optical response of the perfect absorber can be fully predicted by a simple Fabry-Perot model. The underlying mechanism of complete light absorption is explained by a destructive interference of the directly reflected light and the light that has been experiencing multiple reflections.

In Chapter 5, we focused on various plasmonic nanoantennas made of nanorings. We showed that a plasmonic nanoring can provide a uniform field enhancement that is essential for various applications, e.g. boosting the nonlinear effect, enhancing the solar cell efficiency, and plasmonic nanosensors. We introduced a generalized Kerker condition for an arbitrary nanoantenna beyond the dipole moments, i.e. electric and magnetic dipole moments and electric quadrupole moment. This condition is examined for a nanoring which supports both modes and highly directional radiation patterns with zero backscattering field is achieved. Furthermore, complete light absorption is attained for an array of nanorings with a balanced electric dipole and quadrupole moments. We also investigated a nanoantenna made of multiple concentric plasmonic nanorings with exotic optical features. The concept of scattering dark state is introduced for such nanoantennas. Most of the theoretical and numerical

findings of this chapter are fully supported by experimental results.

Many new insights have been obtained in the course of the thesis but much science actually could be done and awaits an exploration. Particularly, the thesis can be extended towards the following directions::

- *Directive radiation*: We have shown that it is possible to achieve a directive radiation for nanoantennas with balanced multipole moments. In particular, the balanced condition has been discussed for electric and magnetic dipole moments and electric quadrupole moment. In order to obtain even better directive nanoantenna, one can investigate the balanced condition that takes higher order multipole moments into account.

- *Multipolar excitation*: We mainly focused on the interaction of a plane wave with nanoantennas. It would be interesting to investigate the interaction of sources that emit radiation corresponding to a well defined multipole moment (e.g. electric and magnetic dipole moments or even higher orders) as an external excitation of the nanoantennas. This helps to better understand the interaction between quantum emitters and nanoantennas.

- *Fano resonances*: In this thesis, we briefly discussed the Fano response for some of the investigated nanoantennas. One may extensively investigate the Fano resonance based on the multiple expansion.

- *Analytical model (oblique incidence)*: In this thesis, we mainly focus on the optical properties of the array at normal incidence. One may extend the analytical model to oblique incident. This might help to study interesting optical features at oblique incidence.

- *Analytical model (interaction constant)*: The interaction constant in the analytical model [i.e. Eqs. 2.3.15 and 2.3.20] is obtained with the quasi-static approximation. Therefore, the prediction of the analytical model is accurate as long as the nanoantennas are small compared to the wavelength. One may investigate the modification to the effects when the interaction constant is considered beyond the quasi-static approximation.

- *Perfect absorbers based on higher multipole moments*: In this thesis, we achieved complete light absorption for an array of nanoantennas with a balanced electric and magnetic dipole moments and electric quadrupole moment. One may investigate even higher order multipoles to achieve complete light absorption. The absorption for such array might be extremely sensitive to the angle of incidence. Therefore, it might be possible to switch between electromagnetically

induced absorption (EIA) [56,57] and electromagnetically induced transmission (EIT) [37] by changing the angle of incidence.

All these aspects constitute reasonable extensions for the present thesis work. Some of them are of technical nature but some of them also allow to probe for a more ultimate limits of the control of light as long as complicated nanoantennas are considered. Nanooptics, in general, promises to provide control on the scattering response of nanoantennas in an unprecedented manner. The question is, what to do with this ability and how to actually achieve predefined configurations. This issue was touched in this thesis but there is much more to do in the future.

Bibliography

[1] B. A. Munk. *Frequency selective surfaces: theory and design*. John Wiley & Sons, 2005.

[2] W. Dallenbach and W. Kleinsteuber. Reflection and absorption of decimeter-waves by plane dielectric layers. *Hochfreq. u Elektroak*, 51:152–156, 1938.

[3] W. W. Salisbury. Absorbent body for electromagnetic waves, June 10 1952. US Patent 2,599,944.

[4] H. Severin. Nonreflecting absorbers for microwave radiation. *Antennas and Propagation, IRE Transactions on*, 4(3):385–392, 1956.

[5] C. M. Watts, X. Liu, and W. J. Padilla. Metamaterial electromagnetic wave absorbers. *Advanced Materials*, 24(23):OP98–OP120, 2012.

[6] N. Landy, S. Sajuyigbe, J. Mock, D. Smith, and W. Padilla. Perfect metamaterial absorber. *Physical Review Letters*, 100(20):207402, 2008.

[7] N. Engheta. Thin absorbing screens using metamaterial surfaces. In *Antennas and Propagation Society International Symposium, 2002. IEEE*, volume 2, pages 392–395. IEEE, 2002.

[8] Y. Avitzour, Y. A. Urzhumov, and G. Shvets. Wide-angle infrared absorber based on a negative-index plasmonic metamaterial. *Phys. Rev. B*, 79:045131, Jan 2009.

[9] N. Liu, M. Mesch, T. Weiss, M. Hentschel, and H. Giessen. Infrared perfect absorber and its application as plasmonic sensor. *Nano Lett.*, 10(7):2342–2348, June 2010.

[10] R. Alaee, C. Menzel, C. Rockstuhl, and F. Lederer. Perfect absorbers on curved surfaces and their potential applications. *Opt. Express*, 20(16):18370–18376, Jul 2012.

[11] M. Albooyeh, D. Morits, and S. Tretyakov. Effective electric and magnetic properties of metasurfaces in transition from crystalline to amorphous state. *Physical Review B*, 85(20):205110, 2012.

[12] K. Aydin, V. E. Ferry, R. M. Briggs, and H. A. Atwater. Broadband polarization-independent resonant light absorption using ultrathin plasmonic super absorbers. *Nat Commun*, 2:517–, November 2011.

[13] C. Hu, Z. Zhao, X. Chen, and X. Luo. Realizing near-perfect absorption at visible frequencies. *Opt. Express*, 17(13):11039–11044, Jun 2009.

[14] U. Huebner, E. Pshenay-Severin, R. Alaee, C. Menzel, M. Ziegler, C. Rockstuhl, F. Lederer, T. Pertsch, H.-G. Meyer, and J. Popp. Exploiting extreme coupling to realize a metamaterial perfect absorber. *Microelectronic Engineering*, 111(0):110 – 113, 2013.

[15] D. R. H. Craig F. Bohren. *Absorption and Scattering of Light by Small Particles*. Wiley-VCH, 1998.

[16] S. Mühlig, C. Menzel, C. Rockstuhl, and F. Lederer. Multipole analysis of meta-atoms. *Metamaterials*, 5(2):64–73, 2011.

[17] L. Novotny. Effective wavelength scaling for optical antennas. *Phys. Rev. Lett.*, 98:266802, Jun 2007.

[18] L. Novotny. Nano-optics: Optical antennas tuned to pitch. *Nature*, 455(7215):887–887, October 2008.

[19] L. Novotny and N. van Hulst. Antennas for light. *Nat Photon*, 5(2):83–90, February 2011.

[20] M. Kerker, D.-S. Wang, and C. L. Giles. Electromagnetic scattering by magnetic spheres. *J. Opt. Soc. Am.*, 73(6):765–767, Jun 1983.

[21] C. Multiphysics. 4.3 user's guide, 2012.

[22] J. D. Jackson. *Classical Electrodynamics*. Wiley, 3rd edition, 1998.

[23] E. E. Radescu and G. Vaman. Exact calculation of the angular momentum loss, recoil force, and radiation intensity for an arbitrary source in terms of electric, magnetic, and toroid multipoles. *Phys. Rev. E*, 65:046609, Apr 2002.

[24] V. Savinov, V. A. Fedotov, and N. I. Zheludev. Toroidal dipolar excitation and macroscopic electromagnetic properties of metamaterials. *Phys. Rev. B*, 89:205112, May 2014.

[25] S. A. Maier. *Plasmonics: Fundamentals and Applications.* Springer, 2007.

[26] A. I. Kuznetsov, A. E. Miroshnichenko, Y. H. Fu, J. Zhang, and B. Lukyanchuk. Magnetic light. *Sci. Rep.*, 2:–, July 2012.

[27] S. Tretyakov. *Analytical modeling in applied electromagnetics.* Artech House, 2003.

[28] Z. Ruan and S. Fan. Superscattering of light from subwavelength nanostructures. *Phys. Rev. Lett.*, 105:013901, Jun 2010.

[29] S. Tretyakov. Maximizing absorption and scattering by dipole particles. *Plasmonics*, 9(4):935–944, 2014.

[30] D. S. Filonov, A. E. Krasnok, A. P. Slobozhanyuk, P. V. Kapitanova, E. A. Nenasheva, Y. S. Kivshar, and P. A. Belov. Experimental verification of the concept of all-dielectric nanoantennas. *Applied Physics Letters*, 100(20):–, 2012.

[31] C. Wu, B. Neuner, G. Shvets, J. John, A. Milder, B. Zollars, and S. Savoy. Large-area wide-angle spectrally selective plasmonic absorber. *Phys. Rev. B*, 84:075102, Aug 2011.

[32] C. F. Bohren. How can a particle absorb more than the light incident on it? *American Journal of Physics*, 51(4):323–327, 1983.

[33] J. E. Sipe and J. V. Kranendonk. Macroscopic electromagnetic theory of resonant dielectrics. *Phys. Rev. A*, 9:1806–1822, May 1974.

[34] M. Husnik, M. W. Klein, N. Feth, M. Konig, J. Niegemann, K. Busch, S. Linden, and M. Wegener. Absolute extinction cross-section of individual magnetic split-ring resonators. *Nat Photon*, 2(10):614–617, October 2008.

[35] M. Husnik, S. Linden, R. Diehl, J. Niegemann, K. Busch, and M. Wegener. Quantitative experimental determination of scattering and absorption cross-section spectra of individual optical metallic nanoantennas. *Phys. Rev. Lett.*, 109:233902, Dec 2012.

[36] M. Husnik, J. Niegemann, K. Busch, and M. Wegener. Quantitative spectroscopy on individual wire, slot, bow-tie, rectangular, and square-shaped optical antennas. *Opt. Lett.*, 38(22):4597–4600, Nov 2013.

[37] L. Verslegers, Z. Yu, Z. Ruan, P. B. Catrysse, and S. Fan. From electromagnetically induced transparency to superscattering with a single structure: A coupled-mode theory for doubly resonant structures. *Phys. Rev. Lett.*, 108:083902, Feb 2012.

[38] Z. Ruan and S. Fan. Design of subwavelength superscattering nanospheres. *Applied Physics Letters*, 98(4):–, 2011.

[39] A. E. Krasnok, C. R. Simovski, P. A. Belov, and Y. S. Kivshar. Superdirective dielectric nanoantennas. *Nanoscale*, 6(13):7354–7361, 2014.

[40] C. L. Holloway, M. A. Mohamed, E. F. Kuester, and A. Dienstfrey. Reflection and transmission properties of a metafilm: With an application to a controllable surface composed of resonant particles. *Electromagnetic Compatibility, IEEE Transactions on*, 47(4):853–865, 2005.

[41] C. L. Holloway, E. F. Kuester, and A. Dienstfrey. Characterizing metasurfaces/metafilms: The connection between surface susceptibilities and effective material properties. *Antennas and Wireless Propagation Letters, IEEE*, 10:1507–1511, 2011.

[42] C. Strachan. The reflexion of light at a surface covered by a monomolecular film. In *Mathematical Proceedings of the Cambridge Philosophical Society*, volume 29, pages 116–130. Cambridge Univ Press, 1933.

[43] M. Albooyeh. Electromagnetic characterization of metasurfaces. 2015.

[44] R. E. Collin. *Field theory of guided waves*. McGraw-Hill, 1960.

[45] C. R. Simovski, M. S. Kondratjev, P. A. Belov, and S. A. Tretyakov. Interaction effects in two-dimensional bianisotropic arrays. *Antennas and Propagation, IEEE Transactions on*, 47(9):1429–1439, 1999.

[46] D. M. Pozar. *Microwave engineering*. Wiley. com, 2009.

[47] R. Alaee, M. Albooyeh, M. Yazdi, N. Komjani, C. Simovski, F. Lederer, and C. Rockstuhl. Magnetoelectric coupling in nonidentical plasmonic nanoparticles: Theory and applications. *Phys. Rev. B*, 91:115119, Mar 2015.

[48] D.-H. Kwon and D. M. Pozar. Optimal characteristics of an arbitrary receive antenna. *Antennas and Propagation, IEEE Transactions on*, 57(12):3720–3727, 2009.

[49] F. G. De Abajo. Colloquium: Light scattering by particle and hole arrays. *Reviews of Modern Physics*, 79(4):1267, 2007.

[50] N. J. Halas, S. Lal, W.-S. Chang, S. Link, and P. Nordlander. Plasmons in strongly coupled metallic nanostructures. *Chemical Reviews*, 111(6):3913–3961, 2011.

[51] C. Menzel, R. Alaee, E. Pshenay-Severin, C. Helgert, A. Chipouline, C. Rockstuhl, T. Pertsch, and F. Lederer. Genuine effectively biaxial left-handed metamaterials due to extreme coupling. *Optics Letters*, 37(4):596–598, 2012.

[52] T. W. Ebbesen, H. J. Lezec, H. F. Ghaemi, T. Thio, and P. A. Wolff. Extraordinary optical transmission through sub-wavelength hole arrays. *Nature*, 391(6668):667–669, February 1998.

[53] L. Martín-Moreno, F. J. Garc'iia-Vidal, H. J. Lezec, K. M. Pellerin, T. Thio, J. B. Pendry, and T. W. Ebbesen. Theory of extraordinary optical transmission through subwavelength hole arrays. *Phys. Rev. Lett.*, 86:1114–1117, Feb 2001.

[54] H. Liu and P. Lalanne. Microscopic theory of the extraordinary optical transmission. *Nature*, 452(7188):728–731, April 2008.

[55] Y. Yang, I. I. Kravchenko, D. P. Briggs, and J. Valentine. All-dielectric metasurface analogue of electromagnetically induced transparency. *Nat Commun*, 5:–, December 2014.

[56] R. Taubert, M. Hentschel, J. Kästel, and H. Giessen. Classical analog of electromagnetically induced absorption in plasmonics. *Nano Letters*, 12(3):1367–1371, 2012. PMID: 22273467.

[57] R. Taubert, M. Hentschel, and H. Giessen. Plasmonic analog of electromagnetically induced absorption: simulations, experiments, and coupled oscillator analysis. *J. Opt. Soc. Am. B*, 30(12):3123–3134, Dec 2013.

[58] P. Nordlander, C. Oubre, E. Prodan, K. Li, and M. I. Stockman. Plasmon hybridization in nanoparticle dimers. *Nano Lett.*, 4(5):899–903, 2004.

[59] E. Prodan, C. Radloff, N. J. Halas, and P. Nordlander. A hybridization model for the plasmon response of complex nanostructures. *Science*, 302(5644):419–422, 2003.

[60] A. Serdyukov. *Electromagnetics of bi-anisotropic materials: Theory and applications*, volume 11. Taylor & Francis, 2001.

[61] I. Staude, A. E. Miroshnichenko, M. Decker, N. T. Fofang, S. Liu, E. Gonzales, J. Dominguez, T. S. Luk, D. N. Neshev, I. Brener, et al. Tailoring directional scattering through magnetic and electric resonances in subwavelength silicon nanodisks. *ACS Nano*, 7(9):7824–7832, 2013.

[62] M. Yazdi, M. Albooyeh, R. Alaee, V. Asadchy, N. Komjani, C. Rockstuhl, C. Simovski, and S. Tretyakov. A bianisotropic metasurface with resonant asymmetric absorption. *Antennas and Propagation, IEEE Transactions on*, PP(99):1–1, 2015.

[63] R. Alaee, M. Albooyeh, A. Rahimzadegan, M. S. Mirmoosa, Y. S. Kivshar, and C. Rockstuhl. All-dielectric reciprocal bianisotropic nanoparticles. *Phys. Rev. B*, 92:245130, Dec 2015.

[64] P. Belov, S. Maslovski, K. Simovski, and S. Tretyakov. A condition imposed on the electromagnetic polarizability of a bianisotropic lossless scatterer. *Technical Physics Letters*, 29(9):718–720, 2003.

[65] Y. E. Terekhov, A. Zhuravlev, and G. Belokopytov. The polarizability matrix of split-ring resonators. *Moscow University Physics Bulletin*, 66(3):254–259, 2011.

[66] J. Vehmas, Y. Ra'di, A. O. Karilainen, and S. A. Tretyakov. Eliminating electromagnetic scattering from small particles. *Antennas and Propagation, IEEE Transactions on*, 61(7):3747–3756, 2013.

[67] I. Liberal, Y. Ra'di, R. Gonzalo, I. Ederra, S. Tretyakov, and R. Ziolkowski. Least upper bounds of the powers extracted and scattered by bi-anisotropic particles. *Antennas and Propagation, IEEE Transactions on*, 62(9):4726–4735, Sept 2014.

[68] V. S. Asadchy, I. A. Faniayeu, Y. Radi, and S. A. Tretyakov. Determining polarizability tensors for an arbitrary small electromagnetic scatterer. *Photonics and Nanostructures - Fundamentals and Applications*, 12(4):298 – 304, 2014. Metamaterials-2013 Congress.

[69] T. Niemi, A. Karilainen, and S. Tretyakov. Synthesis of polarization transformers. *Antennas and Propagation, IEEE Transactions on*, 61(6):3102–3111, 2013.

[70] Y. Ra'di, V. Asadchy, and S. Tretyakov. Total absorption of electromagnetic waves in ultimately thin layers. *Antennas and Propagation, IEEE Transactions on*, 61(9):4606–4614, Sept 2013.

[71] G. Dolling, C. Enkrich, M. Wegener, J. Zhou, C. M. Soukoulis, and S. Linden. Cut-wire pairs and plate pairs as magnetic atoms for optical metamaterials. *Optics Letters*, 30(23):3198–3200, 2005.

[72] C. Menzel, C. Helgert, C. Rockstuhl, E.-B. Kley, A. Tünnermann, T. Pertsch, and F. Lederer. Asymmetric transmission of linearly polarized light at optical metamaterials. *Physical Review Letters*, 104(25):253902, 2010.

[73] S. Weitemeyer, M. Husnik, and M. Wegener. Observation of unusual absorption and scattering cross-section line shapes of individual optical double-wire antennas. *Applied Physics Letters*, 104(3):031111, 2014.

[74] R. Alaee, M. Farhat, C. Rockstuhl, and F. Lederer. A perfect absorber made of a graphene micro-ribbon metamaterial. *Opt. Express*, 20(27):28017–28024, Dec 2012.

[75] V. M. Shalaev. Optical negative-index metamaterials. *Nature Photonics*, 1(1):41–48, 2007.

[76] N. Liu, H. Guo, L. Fu, S. Kaiser, H. Schweizer, and H. Giessen. Plasmon hybridization in stacked cut-wire metamaterials. *Advanced Materials*, 19(21):3628–3632, 2007.

[77] C. Simovski, S. Tretyakov, A. Sochava, B. Sauviac, F. Mariotte, and T. Kharina. Antenna model for conductive omega particles. *Journal of Electromagnetic Waves and Applications*, 11(11):1509–1530, 1997.

[78] L. Novotny and B. Hecht. *Principles of Nano-Optics*. Cambridge University Press, 2006.

[79] A. E. Miroshnichenko, S. Flach, and Y. S. Kivshar. Fano resonances in nanoscale structures. *Rev. Mod. Phys.*, 82:2257–2298, Aug 2010.

[80] E. Rusak, I. Staude, M. Decker, J. Sautter, A. E. Miroshnichenko, D. A. Powell, D. N. Neshev, and Y. S. Kivshar. Hybrid nanoantennas for directional emission enhancement. *Applied Physics Letters*, 105(22):–, 2014.

[81] I. V. Lindell, A. Sihvola, P. Yla-Oijala, and H. Wallén. Zero backscattering from self-dual objects of finite size. *Antennas and Propagation, IEEE Transactions on*, 57(9):2725–2731, 2009.

[82] S. Person, M. Jain, Z. Lapin, J. J. Saenz, G. Wicks, and L. Novotny. Demonstration of zero optical backscattering from single nanoparticles. *Nano Letters*, 13(4):1806–1809, 2013. PMID: 23461654.

[83] C. Menzel, E. Hebestreit, R. Alaee, M. Albooyeh, S. Mühlig, S. Burger, C. Rockstuhl, C. Simovski, S. Tretyakov, F. Lederer, and T. Pertsch. Extreme coupling: A route towards local magnetic metamaterials. *Phys. Rev. B*, 89:155125, Apr 2014.

[84] A. G. Curto, G. Volpe, T. H. Taminiau, M. P. Kreuzer, R. Quidant, and N. F. van Hulst. Unidirectional emission of a quantum dot coupled to a nanoantenna. *Science*, 329(5994):930–933, 2010.

[85] D. Shrekenhamer, W.-C. Chen, and W. Padilla. Liquid crystal tunable metamaterial absorber. *Phys. Rev. Lett.*, 110:177403, Apr 2013.

[86] M. Wuttig and N. Yamada. Phase-change materials for rewriteable data storage. *Nat Mater*, 6(11):824–832, November 2007.

[87] A.-K. U. Michel, D. N. Chigrin, T. W. W. Maß, K. Schänauer, M. Salinga, M. Wuttig, and T. Taubner. Using low-loss phase-change materials for mid-infrared antenna resonance tuning. *Nano Letters*, 13(8):3470–3475, 2013. PMID: 23742151.

[88] A.-K. U. Michel, P. Zalden, D. N. Chigrin, M. Wuttig, A. M. Lindenberg, and T. Taubner. Reversible optical switching of infrared antenna resonances with ultrathin phase-change layers using femtosecond laser pulses. *ACS Photonics*, 1(9):833–839, 2014.

[89] H. A. Atwater and A. Polman. Plasmonics for improved photovoltaic devices. *Nat Mater*, 9(3):205–213, March 2010.

[90] D. K. Gramotnev and S. I. Bozhevolnyi. Plasmonics beyond the diffraction limit. *Nat Photon*, 4(2):83–91, February 2010.

[91] R. Alaee, C. Menzel, U. Huebner, E. Pshenay-Severin, S. Bin Hasan, T. Pertsch, C. Rockstuhl, and F. Lederer. Deep-subwavelength plasmonic nanoresonators exploiting extreme coupling. *Nano Letters*, 13(8):3482–3486, 2013. PMID: 23805879.

[92] J. A. Schuller, E. S. Barnard, W. Cai, Y. C. Jun, J. S. White, and M. L. Brongersma. Plasmonics for extreme light concentration and manipulation. *Nat Mater*, 9(3):193–204, March 2010.

[93] A. Boltasseva and H. A. Atwater. Low-loss plasmonic metamaterials. *Science*, 331(6015):290–291, 2011.

[94] P. Tassin, T. Koschny, M. Kafesaki, and C. M. Soukoulis. A comparison of graphene, superconductors and metals as conductors for metamaterials and plasmonics. *Nat Photon*, 6(4):259–264, April 2012.

[95] P. Moitra, Y. Yang, Z. Anderson, I. I. Kravchenko, D. P. Briggs, and J. Valentine. Realization of an all-dielectric zero-index optical metamaterial. *Nat Photon*, 7(10):791–795, October 2013.

[96] A. Ahmadi and H. Mosallaei. Physical configuration and performance modeling of all-dielectric metamaterials. *Phys. Rev. B*, 77:045104, Jan 2008.

[97] A. B. Evlyukhin, C. Reinhardt, A. Seidel, B. S. Luk'yanchuk, and B. N. Chichkov. Optical response features of si-nanoparticle arrays. *Phys. Rev. B*, 82:045404, Jul 2010.

[98] A. B. Evlyukhin, S. M. Novikov, U. Zywietz, R. L. Eriksen, C. Reinhardt, S. I. Bozhevolnyi, and B. N. Chichkov. Demonstration of magnetic dipole resonances of dielectric nanospheres in the visible region. *Nano Letters*, 12(7):3749–3755, 2012. PMID: 22703443.

[99] A. E. Krasnok, A. E. Miroshnichenko, P. A. Belov, and Y. S. Kivshar. All-dielectric optical nanoantennas. *Opt. Express*, 20(18):20599–20604, Aug 2012.

[100] I. Staude, V. V. Khardikov, N. T. Fofang, S. Liu, M. Decker, D. N. Neshev, T. S. Luk, I. Brener, and Y. S. Kivshar. Shaping photoluminescence spectra with magnetoelectric resonances in all-dielectric nanoparticles. *ACS Photonics*, 2(2):172–177, 2015.

[101] D. Lin, P. Fan, E. Hasman, and M. L. Brongersma. Dielectric gradient metasurface optical elements. *Science*, 345(6194):298–302, 2014.

[102] M. L. Brongersma, Y. Cui, and S. Fan. Light management for photovoltaics using high-index nanostructures. *Nat Mater*, 13(5):451–460, May 2014.

[103] J. A. Schuller, R. Zia, T. Taubner, and M. L. Brongersma. Dielectric metamaterials based on electric and magnetic resonances of silicon carbide particles. *Phys. Rev. Lett.*, 99:107401, Sep 2007.

[104] X. Zambrana-Puyalto, I. Fernandez-Corbaton, M. L. Juan, X. Vidal, and G. Molina-Terriza. Duality symmetry and kerker conditions. *Opt. Lett.*, 38(11):1857–1859, Jun 2013.

[105] I. Sersic, M. A. van de Haar, F. B. Arango, and A. F. Koenderink. Ubiquity of optical activity in planar metamaterial scatterers. *Physical Review Letters*, 108(22):223903, 2012.

[106] J. Huang. *Reflectarray antenna*. Wiley Online Library, 2005.

[107] D. L. Sounas and A. Alu. Extinction symmetry for reciprocal objects and its implications on cloaking and scattering manipulation. *Opt. Lett.*, 39(13):4053–4056, Jul 2014.

[108] F. Bernal Arango, T. Coenen, and A. F. Koenderink. Underpinning hybridization intuition for complex nanoantennas by magnetoelectric quadrupolar polarizability retrieval. *ACS Photonics*, 1(5):444–453, 2014.

[109] M. Decker, I. Staude, M. Falkner, J. Dominguez, D. N. Neshev, I. Brener, T. Pertsch, and Y. S. Kivshar. High-efficiency dielectric huygens surfaces. *Advanced Optical Materials*, 2015.

[110] A. V. Kildishev, A. Boltasseva, and V. M. Shalaev. Planar photonics with metasurfaces. *Science*, 339(6125), 2013.

[111] J. Cheng, D. Ansari-Oghol-Beig, and H. Mosallaei. Wave manipulation with designer dielectric metasurfaces. *Opt. Lett.*, 39(21):6285–6288, Nov 2014.

[112] M. Albooyeh, N. Komjani, and M. S. Mahani. A circularly polarized element for reflectarray antennas. *Antennas and Wireless Propagation Letters, IEEE*, 8:319–322, 2009.

[113] N. Yu and F. Capasso. Flat optics with designer metasurfaces. *Nature Materials*, 13(2):139–150, 2014.

[114] M. Farmahini-Farahani and H. Mosallaei. Birefringent reflectarray metasurface for beam engineering in infrared. *Optics Letters*, 38(4):462–464, 2013.

[115] F. B. Niesler, J. K. Gansel, S. Fischbach, and M. Wegener. Metamaterial metal-based bolometers. *Appl. Phys. Lett.*, 100(20):203508–203508, 2012.

[116] I. Celanovic, D. Perreault, and J. Kassakian. Resonant-cavity enhanced thermal emission. *Phys. Rev. B*, 72(7):075127, 2005.

[117] I. Puscasu and W. L. Schaich. Narrow-band, tunable infrared emission from arrays of microstrip patches. *Applied Physics Letters*, 92(23):233102–233102, 2008.

[118] J. N. Anker, W. P. Hall, O. Lyandres, N. C. Shah, J. Zhao, and R. P. Van Duyne. Biosensing with plasmonic nanosensors. *Nature materials*, 7(6):442–453, 2008.

[119] C. Hägglund and S. P. Apell. Plasmonic near-field absorbers for ultrathin solar cells. *J. Phys. Chem. Lett.*, 3(10):1275–1285, 2012.

[120] Y. Kurokawa and H. T. Miyazaki. Metal-insulator-metal plasmon nanocavities: Analysis of optical properties. *Phys. Rev. B*, 75:035411, Jan 2007.

[121] R. Esteban, A. G. Borisov, P. Nordlander, and J. Aizpurua. Bridging quantum and classical plasmonics with a quantum-corrected model. *Nature Communications*, 3:825, 2012.

[122] K. J. Savage, M. M. Hawkeye, R. Esteban, A. G. Borisov, J. Aizpurua, and J. J. Baumberg. Revealing the quantum regime in tunnelling plasmonics. *Nature*, 491(7425):574–577, 2012.

[123] G. Toscano, S. Raza, A.-P. Jauho, N. A. Mortensen, and M. Wubs. Modified field enhancement and extinction by plasmonic nanowire dimers due to nonlocal response. *Opt. Express*, 20(4):4176–4188, Feb 2012.

[124] J. Yang, C. Sauvan, A. Jouanin, S. Collin, J.-L. Pelouard, and P. Lalanne. Ultrasmall metal-insulator-metal nanoresonators: impact of slow-wave effects on the quality factor. *Opt. Express*, 20(15):16880–16891, Jul 2012.

[125] H. Choo, M.-K. Kim, M. Staffaroni, T. J. Seok, J. Bokor, S. Cabrini, P. J. Schuck, M. C. Wu, and E. Yablonovitch. Nanofocusing in a metal-insulator-metal gap plasmon waveguide with a three-dimensional linear taper. *Nature Photonics*, 6(12):838–844, 2012.

[126] C. Ciracì, R. T. Hill, J. J. Mock, Y. Urzhumov, A. I. Fernández-Domínguez, S. A. Maier, J. B. Pendry, A. Chilkoti, and D. R. Smith. Probing the ultimate limits of plasmonic enhancement. *Science*, 337(6098):1072–1074, 2012.

[127] H. Ditlbacher, A. Hohenau, D. Wagner, U. Kreibig, M. Rogers, F. Hofer, F. R. Aussenegg, and J. R. Krenn. Silver nanowires as surface plasmon resonators. *Phys. Rev. Lett.*, 95(25):257403, 2005.

[128] H. T. Miyazaki and Y. Kurokawa. Squeezing visible light waves into a 3-nm-thick and 55-nm-long plasmon cavity. *Phys. Rev. Lett.*, 96(9):97401, 2006.

[129] R. Alaee, C. Menzel, A. Banas, K. Banas, S. Xu, H. Chen, H. O. Moser, F. Lederer, and C. Rockstuhl. Propagation of electromagnetic fields in bulk terahertz metamaterials: A combined experimental and theoretical study. *Phys. Rev. B*, 87:075110, Feb 2013.

[130] R. Gordon. Light in a subwavelength slit in a metal: Propagation and reflection. *Phys. Rev. B*, 73:153405, Apr 2006.

[131] S. I. Bozhevolnyi and T. Søndergaard. General properties of slow-plasmon resonant nanostructures: nano-antennas and resonators. *Optics Express*, 15(17):10869–10877, 2007.

[132] A. Chandran, E. S. Barnard, J. S. White, and M. L. Brongersma. Metal-dielectric-metal surface plasmon-polariton resonators. *Phys. Rev. B*, 85(8):085416, 2012.

[133] J. Dorfmüller, R. Vogelgesang, R. T. Weitz, C. Rockstuhl, C. Etrich, T. Pertsch, F. Lederer, and K. Kern. Fabry-pérot resonances in one-dimensional plasmonic nanostructures. *Nano Lett.*, 9(6):2372–2377, 2009. PMID: 19472987.

[134] S. B. Hasan, R. Filter, A. Ahmed, R. Vogelgesang, R. Gordon, C. Rockstuhl, and F. Lederer. Relating localized nanoparticle resonances to an associated antenna problem. *Phys. Rev. B*, 84:195405, Nov 2011.

[135] S. Zhang, Y.-S. Park, Y. Liu, T. Zentgraf, and X. Zhang. Far-field measurement of ultra-small plasmonic mode volume. *Opt. Express*, 18(6):6048–6055, 2010.

[136] A. Moreau, C. Ciracì, J. J. Mock, R. T. Hill, Q. Wang, B. J. Wiley, A. Chilkoti, and D. R. Smith. Controlled-reflectance surfaces with film-coupled colloidal nanoantennas. *Nature*, 492(7427):86–89, 2012.

[137] P. B. Johnson and R. W. Christy. Optical constants of the noble metals. *Phys. Rev. B*, 6:4370–4379, Dec 1972.

[138] J. Hao, J. Wang, X. Liu, W. J. Padilla, L. Zhou, and M. Qiu. High performance optical absorber based on a plasmonic metamaterial. *Appl. Phys. Lett.*, 96(25):251104–251104, 2010.

[139] J. Hao, L. Zhou, and M. Qiu. Nearly total absorption of light and heat generation by plasmonic metamaterials. *Phys. Rev. B*, 83(16):165107, 2011.

[140] B. E. A. Saleh and M. C. Teich. *Fundamentals of Photonics*. Wiley Series in Pure and Applied Optics. Wiley-Interscience, 2nd edition, 2007.

[141] R. Yu, R. Alaee, F. Lederer, and C. Rockstuhl. Manipulating the interaction between localized and delocalized surface plasmon-polaritons in graphene. *Phys. Rev. B*, 90:085409, Aug 2014.

[142] J. Aizpurua, P. Hanarp, D. S. Sutherland, M. Käll, G. W. Bryant, and F. J. Garcia-Etxarri, A.a de Abajo. Optical properties of gold nanorings. *Phys. Rev. Lett.*, 90:057401, Feb 2003.

[143] F. Hao, P. Nordlander, M. T. Burnett, and S. A. Maier. Enhanced tunability and linewidth sharpening of plasmon resonances in hybridized metallic ring/disk nanocavities. *Phys. Rev. B*, 76:245417, Dec 2007.

[144] F. Hao, Y. Sonnefraud, P. V. Dorpe, S. A. Maier, N. J. Halas, and P. Nordlander. Symmetry breaking in plasmonic nanocavities: Subradiant lspr sensing and a tunable fano resonance. *Nano Letters*, 8(11):3983–3988, 2008. PMID: 18831572.

[145] F. Hao, P. Nordlander, Y. Sonnefraud, P. V. Dorpe, and S. A. Maier. Tunability of subradiant dipolar and fano-type plasmon resonances in metallic ring/disk cavities: Implications for nanoscale optical sensing. *ACS Nano*, 3(3):643–652, February 2009.

[146] P. Nordlander. The ring: A leitmotif in plasmonics. *ACS Nano*, 3(3):488–492, 2009.

[147] D. Lehr, J. Reinhold, I. Thiele, H. Hartung, K. Dietrich, C. Menzel, T. Pertsch, E.-B. Kley, and A. Tünnermann. Enhancing second harmonic generation in gold nanoring resonators filled with lithium niobate. *Nano Letters*, 15(2):1025–1030, 2015. PMID: 25584636.

[148] E. M. Larsson, J. Alegret, M. Käll, and D. S. Sutherland. Sensing characteristics of nir localized surface plasmon resonances in gold nanorings for application as ultrasensitive biosensors. *Nano Letters*, 7(5):1256–1263, 2007. PMID: 17430004.

[149] B. Lukyanchuk, N. I. Zheludev, S. A. Maier, N. J. Halas, P. Nordlander, H. Giessen, and C. T. Chong. The fano resonance in plasmonic nanostructures and metamaterials. *Nature Materials*, 9(9):707–715, 2010.

[150] H. Chen, L. Shao, Y. C. Man, C. Zhao, J. Wang, and B. Yang. Fano resonance in (gold core)-(dielectric shell) nanostructures without symmetry breaking. *Small*, 8(10):1503–1509, 2012.

[151] B. Gallinet and O. J. F. Martin. *Ab initio* theory of fano resonances in plasmonic nanostructures and metamaterials. *Phys. Rev. B*, 83:235427, Jun 2011.

[152] B. Gallinet and O. J. F. Martin. Influence of electromagnetic interactions on the line shape of plasmonic fano resonances. *ACS Nano*, 5(11):8999–9008, 2011. PMID: 22026329.

[153] S. N. Sheikholeslami, A. Garcia-Etxarri, and J. A. Dionne. Controlling the interplay of electric and magnetic modes via fano-like plasmon resonances. *Nano Letters*, 11(9):3927–3934, 2011. PMID: 21819059.

[154] Y. Sonnefraud, N. Verellen, H. Sobhani, G. A. Vandenbosch, V. V. Moshchalkov, P. Van Dorpe, P. Nordlander, and S. A. Maier. Experimental realization of subradiant, superradiant, and fano resonances in ring/disk plasmonic nanocavities. *ACS Nano*, 4(3):1664–1670, 2010. PMID: 20155967.

[155] R. Alaee, R. Filter, D. Lehr, F. Lederer, and C. Rockstuhl. A generalized kerker condition for highly directive nanoantennas. *Opt. Lett.*, 40(11):2645–2648, Jun 2015.

[156] R. Alaee, D. Lehr, R. Filter, F. Lederer, E.-B. Kley, C. Rockstuhl, and A. Tünnermann. Scattering dark states in multiresonant concentric plasmonic nanorings. *ACS Photonics*, 2(8):1085–1090, 2015.

[157] D. Lehr, R. Alaee, R. Filter, K. Dietrich, T. Siefke, C. Rockstuhl, F. Lederer, E.-B. Kley, and A. Tünnermann. Plasmonic nanoring fabrication tuned to pitch: Efficient, deterministic, and large scale realization of ultra-small gaps for next generation plasmonic devices. *Applied Physics Letters*, 105(14):–, 2014.

[158] G. Si, Y. Zhao, H. Liu, S. Teo, M. Zhang, T. Jun Huang, A. J. Danner, and J. Teng. Annular aperture array based color filter. *Applied Physics Letters*, 99(3):–, 2011.

[159] C. Huang, J. Ye, S. Wang, T. Stakenborg, and L. Lagae. Gold nanoring as a sensitive plasmonic biosensor for on-chip dna detection. *Applied Physics Letters*, 100(17):173114, 2012.

[160] I. Liberal, I. Ederra, R. Gonzalo, and R. Ziolkowski. A multipolar analysis of near-field absorption and scattering processes. *Antennas and Propagation, IEEE Transactions on*, 61(10):5184–5199, Oct 2013.

[161] L. Wei, A. E. Miroshnichenko, and Y. S. Kivshar. Control of light scattering by nanoparticles with optically-induced magnetic responses. *Chinese Physics B*, 23(4):047806, 2014.

[162] S. Linden, C. Enkrich, M. Wegener, J. Zhou, T. Koschny, and C. M. Soukoulis. Magnetic response of metamaterials at 100 terahertz. *Science*, 306(5700):1351–1353, 2004.

[163] W. Cai, U. K. Chettiar, H.-K. Yuan, V. C. de Silva, A. V. Kildishev, V. P. Drachev, and V. M. Shalaev. Metamagnetics with rainbow colors. *Optics Express*, 15(6):3333–3341, 2007.

[164] A. Alu and N. Engheta. Multifrequency optical invisibility cloak with layered plasmonic shells. *Phys. Rev. Lett.*, 100:113901, Mar 2008.

[165] R. K. Rodriguez, S. F. B. Arango, P. Steinbusch, T. A. Verschuuren, M. F. Koenderink, A. and J. G. Rivas. Breaking the symmetry of forward-backward light emission with localized and collective magnetoelectric resonances in arrays of pyramid-shaped aluminum nanoparticles. *Phys. Rev. Lett.*, 113:247401, Dec 2014.

[166] M. Nieto-Vesperinas, R. Gomez-Medina, and J. J. Saenz. Angle-suppressed scattering and optical forces on submicrometer dielectric particles. *J. Opt. Soc. Am. A*, 28(1):54–60, Jan 2011.

[167] T. Coenen, F. Bernal Arango, A. Femius Koenderink, and A. Polman. Directional emission from a single plasmonic scatterer. *Nat Commun*, 5:–, February 2014.

[168] Y. H. Fu, A. I. Kuznetsov, A. E. Miroshnichenko, Y. F. Yu, and B. Luk/'yanchuk. Directional visible light scattering by silicon nanoparticles. *Nat Commun*, 4:1527–, February 2013.

[169] T. Pakizeh and M. Kall. Unidirectional ultracompact optical nanoantennas. *Nano Letters*, 9(6):2343–2349, 2009.

[170] C.-Y. Tsai, S.-P. Lu, J.-W. Lin, and P.-T. Lee. High sensitivity plasmonic index sensor using slablike gold nanoring arrays. *Applied Physics Letters*, 98(15):–, 2011.

[171] D. Lehr, K. Dietrich, C. Helgert, T. Käsebier, H.-J. Fuchs, A. Tünnermann, and E.-B. Kley. Plasmonic properties of aluminum nanorings generated by double patterning. *Opt. Lett.*, 37(2):157–159, Jan 2012.

[172] A. Rakovich, P. Albella, and S. A. Maier. Plasmonic control of radiative properties of semiconductor quantum dots coupled to plasmonic ring cavities. *ACS Nano*, 0(0):null, 0. PMID: 25602764.

[173] B. Rolly, B. Stout, and N. Bonod. Boosting the directivity of optical antennas with magnetic and electric dipolar resonant particles. *Opt. Express*, 20(18):20376–20386, Aug 2012.

[174] I. M. Hancu, A. G. Curto, M. Castro-Lopez, M. Kuttge, and N. F. van Hulst. Multipolar interference for directed light emission. *Nano Letters*, 14(1):166–171, 2013.

[175] R. Filter, J. Qi, C. Rockstuhl, and F. Lederer. Circular optical nanoantennas: an analytical theory. *Phys. Rev. B*, 85:125429, Mar 2012.

[176] R. Filter, S. Mühlig, T. Eichelkraut, C. Rockstuhl, and F. Lederer. Controlling the dynamics of quantum mechanical systems sustaining dipole-forbidden transitions via optical nanoantennas. *Phys. Rev. B*, 86:035404, Jul 2012.

[177] C. Menzel, E. Hebestreit, S. Mühlig, C. Rockstuhl, S. Burger, F. Lederer, and T. Pertsch. The spectral shift between near-and far-field resonances of optical nano-antennas. *Optics express*, 22(8):9971–9982, 2014.

[178] P. Alonso-Gonzalez, P. Albella, F. Neubrech, C. Huck, J. Chen, F. Golmar, F. Casanova, L. E. Hueso, A. Pucci, J. Aizpurua, and R. Hillenbrand. Experimental verification of the spectral shift between near- and far-field peak intensities of plasmonic infrared nanoantennas. *Phys. Rev. Lett.*, 110:203902, May 2013.

[179] R. Filter, K. Słowik, J. Straubel, F. Lederer, and C. Rockstuhl. Nanoantennas for ultrabright single photon sources. *Opt. Lett.*, 39(5):1246–1249, Mar 2014.

[180] P. Grahn, A. Shevchenko, and M. Kaivola. Theoretical description of bifacial optical nanomaterials. *Opt. Express*, 21(20):23471–23485, Oct 2013.

[181] M. Albooyeh, R. Alaee, C. Rockstuhl, and C. Simovski. Revisiting substrate-induced bianisotropy in metasurfaces. *Phys. Rev. B*, 91:195304, May 2015.

[182] G. leveque and O. Martin. Narrow-band multiresonant plasmon nanostructure for the coherent control of light: an optical analog of the xylophone. *Physical review letters*, 100(11):117402, 2008.

[183] F. Monticone, C. Argyropoulos, and A. Alu. Layered plasmonic cloaks to tailor the optical scattering at the nanoscale. *Sci. Rep.*, 2, December 2012.

[184] B. Metzger, T. Schumacher, M. Hentschel, M. Lippitz, and H. Giessen. Third harmonic mechanism in complex plasmonic fano structures. *ACS Photonics*, 1(6):471–476, 2014.

[185] R. Singh, I. A. I. Al-Naib, M. Koch, and W. Zhang. Sharp fano resonances in thz metamaterials. *Opt. Express*, 19(7):6312–6319, Mar 2011.

[186] C. W. Hsu, B. G. DeLacy, S. G. Johnson, J. D. Joannopoulos, and M. Soljacic. Theoretical criteria for scattering dark states in nanostructured particles. *Nano Letters*, 14(5):2783–2788, 2014. PMID: 24805881.

[187] F. Monticone, C. Argyropoulos, and A. Alù. Multilayered plasmonic covers for comblike scattering response and optical tagging. *Phys. Rev. Lett.*, 110:113901, Mar 2013.

[188] P.-Y. Chen, J. Soric, and A. Alu. Invisibility and cloaking based on scattering cancellation. *Advanced Materials*, 24(44):OP281–OP304, 2012.

[189] S. Mühlig, A. Cunningham, J. Dintinger, M. Farhat, S. B. Hasan, T. Scharf, T. Bürgi, F. Lederer, and C. Rockstuhl. A self-assembled three-dimensional cloak in the visible. *Sci. Rep.*, 3:–, August 2013.

Acknowledgments

First of all, I wish to express my sincere thanks to Prof. Dr. Falk Lederer and Prof. Dr. Carsten Rockstuhl for giving me the unique opportunity to carry out my PhD at their group. Thanks for providing me with all the necessary tools for the research. This work would not have been possible without your constructive advice. Special thanks goes to Prof. Carsten Rockstuhl. I have been amazingly fortunate to have a supervisor who gave me the freedom to explore on my own, and at the same time the guidance to recover when my steps faltered. Thank you so much for all the things that you have taught me.

I would like to acknowledge Prof. Dr. Martin Wegener for being the second referee of my thesis.

I would like to thank Dr. Christoph Menzel for his extraordinary support and excellent guidance during my PhD study at the Institute of Condensed Matter Theory and Solid State Optics at the Friedrich-Schiller Universität Jena. You are an amazing scientist with immense knowledge in metamaterials and plasmonics. I am indebted to you for teaching me how to do research. I really enjoyed working with you. I want to thank you for everything.

I would like to acknowledge my theoretical collaborators at the Alto university in Espoo: Prof. Constantin Simovski, Mohammad S. Mirmoosa, and Dr. Mohammad Albooyeh. I would like to specially thank my friend, Mohammad, for his excellent scientific support. I would also like to thank my experimental collaborators at the Friedrich-Schiller Universität Jena, Dennis Lehr, Dr. Uwe Hübner, Dr. Ekaterina Pshenay-Severin, Matthias Falkner and Dr. Stefanie Kroker for the experimental supports. Special thanks goes to Dennis from the Institute of Applied Physics for his supportive experiment and perfect collaboration.

I would like to acknowledge all my colleagues in Jena and Karlsruhe for their helps and perfect supports. I also would like to thank Dr. Robert Filter, Dr. Shakeeb Bin Hasan, Renwen Yu, Dr. Mohamed Farhat, Dr. Giuseppe Toscano, Dr. Ivan Fernandez-Corbaton, Dr. Panagiotis Kotetes, Martin Fruhnert, Jakob Straubel and Andreas Vetter for their nice friendship. My sincere thanks goes to Szilvia Mammel for her endless support.

I would like to specially thank Andreas Vetter, Renwen Yu, Ghassem Alaee, and

my wife for proof-reading of the thesis.

Apart from my colleagues, I would like to acknowledge my wonderful friends, Zahra Lotfi and Reza Momeni. I will never forget these amazing years that we spent together. I really enjoyed being with you. Please stay friend with me.

My heart-felt appreciation goes to my family. I have an amazing family, unique in many ways. It is quite impossible to truly acknowledge you for your warm-heartedness and unconditional supports. Special thanks goes to my wonderful parents for supporting me in everything. I would like to deeply appreciate my beloved wife, Zeinab, who cares about me with her endless love.